DISS. ETH No. 22372

Damage evolution in wood and layered wood composites monitored in situ by acoustic emission, digital image correlation and synchrotron based tomographic microscopy

A thesis submitted to attain the degree of

DOCTOR OF SCIENCES of ETH ZURICH

(Dr. Sc. ETH Zurich)

presented by

Franziska Baensch (nee Ritschel)

Dipl. Ing., TU Dresden

born 01/05/1983

citizen of

Germany

Accepted on the recommendation of

Prof. Dr.-Ing. habil. Dr. h. c. P. Niemz, ETH Zurich, examiner

Prof. Dr. habil. I. Burgert, ETH Zurich, co-examiner

Prof. Dr.-Ing. habil. Dipl.-Geophys. C. U. Große, TU Munich, co-examiner

Dr. phil. II A. J. Brunner, Empa Dübendorf, co-examiner

2015

Abstract

Wood is one of the oldest building materials in the world, however some recent construction materials are also based on wood, such as Laminated Veneer Lumber (LVL). Bearing in mind the changes in fire regulations that now allow the construction of multi-level wooden buildings, wood products such as plywood, cross laminated timber (CLT), LVL or oriented strand board (OSB), are becoming increasingly more important in construction. To avoid critical situations and to maintain safety standards when applying wood based materials, more detailed information on damage accumulation and interaction is required for adequate design and durable implementation of wood materials in load bearing elements in building constructions.

Compared with solid wood, there is still limited knowledge on damage and failure mechanisms in these materials, especially at the microscopic scale. The damage progress in wood involves several length scales of the wooden hierarchical structure, complying with the growth rings at the mesoscopic scale, that occur on account of the composition of chemical constituents and the arrangement of cell types and cell wall structures at the microscopic level. In the case of the plywood, which is focused on in the studies presented here, the failure behavior differs from that of solid wood due to the additional length scale introduced by the layered structure of bonded veneers. Thus, the material behavior is mainly influenced by the orientation of the veneers as well as the used adhesive.

The detailed behavior of these materials under load, with the complex interactions between size and properties of the microstructural units, their interfaces, and the micro-and mesoscopic stress distributions yielding the observed macroscopic failure, is focused on. To this aim, the tensile failure of several plywood materials consisting of three up to six layers was monitored by the Acoustic Emission (AE) method, which provides high time-resolution (µs - ms) for damage initiation and accumulation on all length-scales. AE is the phenomenon of generating transient or continuous elastic waves by releasing stored elastic energy in materials by means of, e.g., plastic deformation or crack propagation, and hence, the detection of AE by means of piezo-electric sensors mounted on the material's surfaces facilitates recording multi-scale information on damage progress covering almost the whole specimen volume. Furthermore, to facilitate the interpretation of the AE results, the specimen's surfaces were monitored by CCD cameras for post-calculations of strain field formations by applying the method of digital image correlation (DIC).

Compared to the damage accumulation in solid spruce, a more distinctive exponential increase in damage growth was determined for the plywood materials. Hence, it is demonstrated that the destruction of plywood undergoes two damage growth rates clearly generated by the layered structure. The first damage growth rate is mainly restricted to the single layers releasing only about 30% of the total fracture energy, whereby the defect growth is larger the more layers constitute the plywood structure. Furthermore, a larger number of defects occurring during the first defect growth rate are found to predict a higher tensile strength of the material. The second rate of defect growth starting at about 70% of the ultimate stress indicates the path of lowest resistance sought through all layers.

The comparison of model layered wood made of clear spruce lamella and industrially produced plywood comprising to process-related pre-damages (lathe checks) has proven that the presence of pre-damages decreases the detected amount of AE. Besides, the model layered wood reveals a relatively higher share of microscopic scale damages than the industrial plywood materials.

Furthermore, the unsupervised pattern recognition (UPR) method for frequency based AE signal classification, originally developed for fiber-reinforced composite laminates, was applied to wood and layered wood materials for the first time. This implementation is straightforward, since these composites and wood both have distinct microstructures with anisotropic elastic properties. Firstly, to validate this cluster technique, tensile tests on miniature specimens made of spruce wood were monitored by AE and, simultaneously, by synchrotron radiation micro computed tomography (SRµCT). Analogous to the different grain orientation of the veneers in the plywood, stress was applied parallel and perpendicular to the grain. By means of the UPR method, two classes of AE signals were identified, whereby one class of AE signals is characterized by a relatively high share of low frequency components and the opposite is true for the second class. Correlations of this cluster formation with the details of the crack propagation extracted from the SRµCT tomograms led to the hypothesis that the signature of relatively slow cell separation mechanisms and rapid cell wall cracks might be the origin. The same tests were performed on bonded miniature specimens that consist of two clear spruce wood lamellae joined together, which yielded similar cluster results that were also assigned to separation mechanisms and cell wall cracks. A third cluster exclusively attributed to the failure in the adhesive layers was not identified. However, based on the combination of SRµCT images and related AE cluster patterns, it is assumed that AE signals generated by crack mechanisms of the adhesive might be among the signals of the low frequency

cluster assigned to separation mechanisms. This may also be true for the laboratory scale specimens made of model layered wood and industrial plywood, since the UPR technique subsequently applied to the AE detected while tensile testing the different layered structures of plywood also yielded only two AE signal clusters. Similar to the results of the miniature tests, the clusters differ in signals of relatively high shares of low frequency and high frequency content and are thus assumed to also be caused by separation or by shear mechanisms and cell wall cracks, respectively, which essentially occur over the whole test duration. Furthermore, the broad range in AE energy of the detected events over the whole test duration proves that multi-scaled damages are present during both damage growth rates.

The knowledge gained on the microscopic as well as on the mesoscopic scale failure behavior and fracture pattern for different layered plywood materials enables an improved understanding of the complex interactions between dimension and function of the structural elements for failure evolution. Beside further clarification of the damage micromechanics of wood-based materials, new advances in test and monitoring methodology and in experimental characterization, analysis and evaluation were obtained, regarding the combination of AE and SRμCT monitoring as well as adaptation of the new UPR approach.

Zusammenfassung

Holz ist einer der ältesten Baustoffe der Welt und zugleich der Rohstoff für noch junge, neu entwickelte Materialien wie beispielsweise dem Furnierschichtholz „Laminated Veneer Lumber" (LVL). Seit im Rahmen der europäischen Harmonisierung der Bauvorschriften die Brandschutzvorgaben Änderungen unterliegen, erleben insbesondere holzbasierte Baustoffprodukte wie Sperrholz, „Cross laminated timber" (CLT), LVL und „Oriented Strand Board" (OSB) einen Aufschwung im Bausektor. Um kritische Situationen zu vermeiden und die Sicherheit bei der Verbauung von Holzwerkstoffen gewährleisten zu können, ist es unerlässlich deren Schädigungsverhalten, die Ausbildung, Ansammlung und Wechselwirkung auftretender Schädigungen im Detail zu kennen. Nur so können spezialisierte Produkte für Konstruktionen entwickelt und die Tragfähigkeit lasttragender Holz-Elemente verbessert werden.

Verglichen mit dem umfangreichen Kenntnisstand zum Verhalten von Vollholz, besteht für viele Holzwerkstoffe noch Aufklärungsbedarf, insbesondere hinsichtlich des Schädigungsverlaufs im mikroskopischen Bereich. Bedingt durch die hierarchische Struktur, erfolgt die Schadensausbildung im Vollholz auf verschiedenen Größenskalen, beispielsweise an den Jahrringsgrenzen (mesoskopische Ebene) wo verschiedene Zelltypen (mikroskopische Ebene) einen Schwachpunkt in der Struktur darstellen können. Bei Holzwerkstoffen wird das Materialverhalten zusätzlich beeinflusst durch die Holzpartikelgröße, Ausrichtung und Anteil an verarbeitetem Holz sowie Bindematerial und Klebstoff. Im Falle des hier schwerpunktmäßig untersuchten Furnierwerkstoffes Sperrholz, sind die Furniere, deren Faserorientierung und Qualität sowie der verwendete Klebstoff von Bedeutung.

Ziel dieser Arbeit ist es, die Versagensentwicklung von Sperrholz unter Belastung detailliert zu beschreiben. Dabei werden die komplexen Wechselwirkungen zwischen Größe und Funktion der mikro-strukturellen Elemente und deren Grenzflächen untersucht und die zum makroskopischen Versagen führenden mikro- und mesoskopischen Spannungsverteilungen analysiert. Zu diesem Zweck wurden verschiedene Sperrholzmaterialien, bestehend aus drei bis sechs Furnierlagen, auf Zug bis zum endgültigen Versagen belastet und die auftretende Schallemission (AE, *aus dem Engl.: Acoustic Emission*) gemessen. Das Phänomen AE ist die Ausbreitung transienter und kontinuierlicher elastischer Wellen im Material, welche beispielsweise durch plastische Verformungen oder Rissbildung verursacht werden. Mit Hilfe von piezoelektrischen Sensoren, die auf der Materialoberfläche befestigt werden, sind

diese Wellen detektierbar. Auf diese Weise wird die mehrskalige, über das gesamte Probenvolumen auftretende Schadensausbildung und -ansammlung, in hoher Zeitauflösung (ms-μs) erfasst. Da die Informationen aus der AE schwer zu interpretieren sind, wurden die Probenoberflächen während der Belastungstests zusätzlich mit CCD Kameras aufgenommen. Die generierten Bilder, nachträglich mittels Digitaler Bildkorrelation (DIC, *aus dem Engl.: Digital Image Correlation*) ausgewertet, liefern die Dehnungsfelder an der Probenoberfläche.

Während Vollholz eine eher lineare Schadensansammlung unter fortschreitender Belastung aufweist, wurde für die untersuchten Sperrhölzer ein exponentieller Zuwachs an Schädigungen festgestellt. Dementsprechend konnten für Sperrhölzer zwei Defekt-Zuwachsraten bestimmt werden, die eindeutig auf den Einfluss der Lagenstruktur zurückzuführen sind. Die erste Defekt-Zuwachsrate wird hauptsächlich durch die Schwachstellen in den einzelnen Lagen verursacht, wobei etwa 30% der insgesamt auftretenden Bruchenergie (anhand der Korrelation zwischen Bruchenergie und Energie der AE Signale ermittelt) freigesetzt wurden. Eine größere erste Defekt-Zuwachsrate korreliert tendenziell mit einer höheren Festigkeit, und ermöglicht somit eine grobe Vorhersage zur Materialfestigkeit. Die zweite Defekt-Zuwachsrate setzt bei etwa 70% der maximalen Last ein, wobei dann der Weg des geringsten Widerstandes „global" über alle Lagen des Sperrholz-Prüfkörpers gesucht wird. Gegenüber dem „idealisierten" Lagenholz, welches aus fehlerfreien, auf-Dicke-gehobelten Fichtenholzlamellen hergestellt wurde, generierte das industriell gefertigte Sperrholz mit seinen typischen, verarbeitungsbedingten Vorschädigungen (Schälrisse) eine niedrigere Anzahl AE Signale. Es wurde festgestellt, dass der Schadensverlauf im idealisierten Lagenholz einen vergleichsweise hohen Anteil an mikroskopischen Schäden aufweist.

Mit Hilfe eines Ansatzes zur Mustererkennung wurden die gemessenen AE Signale klassifiziert. Die verwendete Methode wurde ursprünglich für Untersuchungen an polymeren Faserverstärkten Verbundwerkstoffen (FVW) entwickelt. Es werden ausschließlich frequenzbasierte Parameter der AE Signale ausgewertet. Für die Grundlagenforschung in der Holzwissenschaft wird die Implementierung dieser Mustererkennungsmethode als vielversprechend bewertet, schließlich weisen FVW und Holz bzw. Holzwerkstoffe starke Ähnlichkeiten bezüglich dem Zusammenhang zwischen Struktur und Funktion sowie den daher rührenden anisotropen Eigenschaften auf. Um die Methode für Holz zu validieren, wurden zunächst Miniatur-Prüfkörper aus Fichtenholz geprüft und die AE gemessen. Gleichzeitig wurden die Prüfkörper mittels Synchrotron-Strahl-basierter Mikro-Computer-

Tomographie (SRμCT) untersucht. Die Mustererkennung identifizierte zwei Klassen von AE Signalen, wobei eine Signalklasse durch eher niedrige Frequenzanteile, die zweite Signalklasse durch überwiegend höhere Frequenzanteile charakterisiert ist. Die Ergebnisse der Mustererkennung wurden durch detaillierte Auswertungen der zugehörigen SRμCT-scans ergänzt, beispielsweise durch Analysen der entstandenen Risse und Bruchflächen. Es konnte eine erste Hypothese aufgestellt werden, welche den Ursprung der zwei Signalklassen zum einen mit den eher langsamen Vorgängen der Zell-Separation und zum anderen mit den spröden Zellwandrissen erklärt. Die gleichen Untersuchungen wurden an weiteren Miniatur-Prüfkörpern durchgeführt, welche aus zwei miteinander verklebten Fichtenholzlamellen bestanden. Die Ergebnisse der Mustererkennung ähneln jenen der Vollholzproben. Eine dritte Signalklasse, die eindeutig dem Klebstoffversagen zuzuordnen wäre, wurde nicht identifiziert. Jedoch lässt der Vergleich zwischen den Bruchbildern und den leichten Abweichungen in den Hauptparametern der Schallsignalklassen vermuten, dass die vom Klebstoffversagen generierten AE Signale insbesondere in der niederfrequenteren Signalklasse abgebildet werden. Ähnliches ist für die Untersuchungen an den Sperrholzproben anzunehmen, denn auch hier wurde eine Signalklasse mit eher höheren und eine mit eher niedrigeren Frequenzanteilen identifiziert. Die Ursprünge dieser Signalklassen sind vermutlich auch hier Zellwandbrüche und Separations- bzw. Schermechanismen. Beide Versagenstypen treten während des gesamten Belastungsverlaufs, bis hin zum endgültigen Versagen des Materials auf. Für beide Defektzuwachsraten wurde, für beide AE Signalklassen, eine breite Variation der Defekt-Größen (anhand der Amplituden und Energien der auftretenden Schallemissionssignale) und damit auch eine mehrskalige Schadensentwicklung festgestellt.

Die durchgeführten Untersuchungen ergeben ein besseres Verständnis der komplexen Wechselwirkungen zwischen Größe und Funktion der verschiedenen Strukturelemente während der Schadensentwicklung in Sperrholz. Die Überwachung von Schadensentwicklung in Holzwerkstoffen mittels Kombination von AE und SRμCT sowie die Vorstellung des neuen Ansatzes zur Mustererkennung von AE Signalen liefern fortschrittliche Methoden zur experimentellen Charakterisierung, Analyse und Auswertung im Feld der Holzforschung und unterstützen die Weiterentwicklung von Test- und Überwachungsmethoden.

Content

Nomenclature

Mechanic symbols

Compliance tensor	S
Crack area	A
Deformation	u
Energy consumption associated with crack area	dU
Fracture toughness; Strain energy release rate; Shear modulus	G_c; G; G
Poisson ratio	v
Shear strain	γ
Shear stress	τ
Spring constant	k
Stiffness tensor	C
Strain	ε
Stress, fracture stress	σ, σ_f
Tensile stress parallel and normal to grain	$f_{t,p}$; $f_{t,n}$
Thickness	d
Volume portion	φ
Young's modulus, Modulus of elasticity	E; MOE

Acoustic emission parameters

Arrival time, Time of first threshold crossing	t_0
Counts of signal's threshold crossings	C
Frequency	f
Peak amplitude	A
Rise time	t_R
Signal duration	t_D
True signal energy	E

1 Introduction

1.1 Background

Over the past fifty years, society's awareness of ecological sustainability has come to the fore and is becoming more and more recognized as an integral part of everyday life. Climate change and industrial globalization have encouraged international climate and energy policies to focus on strategies of consistent and long-term direction for development (COM 2010). Considering that resource management and resource efficiency hold the key to the future of the manufacturing industry, renewable natural resources are becoming ever more prevalent in the production environment replacing conventional materials and initiating the creation of novel applications.

In this context, wood products represent a not insignificant factor, and although wood is one of the oldest building materials in the world, some recent products are also based on wood, such as the so-called "Baubuche" (www.pollmeier.com, Dworschack 2014) and Laminated Veneer Lumber (LVL). Furthermore, political, economic and technological factors, e.g. concerns about products' ecological footprint, require the design and application of new wood based products. Thus, wood products, among others plywood, LVL, glue laminated timber, cross-laminated timber (CLT) or oriented strand board (OSB) are becoming increasingly more important in the building sector, in particular with regard to the changes in fire regulations allowing multi-storey wooden buildings (Manninen 2014).

The usage of wood materials as load bearing elements, however, may entail certain risks when improperly installed. Even minor carelessness in handling the material may have serious and irreparable consequences. To avoid critical situations and to maintain safety standards, more detailed information on damage accumulation and interaction in engineered wood products is required. A detailed description of the damage process in layered wood is a challenge even today, since failure of structures results from damage accumulation due to various individual sub-macroscopic mechanisms. The complexity of damage progress in wood is hardly traceable because it involves several length scales of the wooden hierarchical structure in agreement with the growth rings at the mesoscopic scale based on the composition and arrangement of cell types and cell wall structures at the microscopic level, built up by chemical constituents (in the range of tenths of nm). In the case of the plywood, the failure behavior differs from that of solid wood, due to the additional length scales introduced by the layered structure of bonded veneers. By means of standard tests on

plywood (DIN 52376, DIN 52377, EN 310), the sub-macroscopic structure-function relation extends over a continuum, whereas complex interactions between size and properties of the microstructural units, their interfaces and the micro- and mesoscopic stress distributions leading to macroscopic failure are still yet to be gathered and largely remain to be explained. Concerning this issue, developments in experimental setup and, especially the non-destructive monitoring methods have now reached a level that bridge this gap and enable a more detailed insight into microscopic damage processes.

The method of AE is sensitive to damage mechanisms on several length scales and the development in AE monitoring and analysis benefits from the fast improvements in electronics and computing performance. During the last two decades, the testing method of AE had lost importance in the field of wood research. However, today's improved technology and data processing again offers high potential for multi-scaled material characterization and possible future monitoring of (wood) products in service. Since the AE method yields high time resolution for the determination of failure stresses and separation of damage events, it is expected to provide further details of the damage evolution on the different length scales in plywood. The additional combination of AE with optical monitoring methods entails advances in experimental characterization, analysis and evaluation, since the key challenge in AE analysis is the assignment of detected AE signals to their origins within the material.

1.2 Research objectives and motivation

The damage evolution in wood depends on a huge number of features, such as the raw density, share of early and latewood tissue, the arrangement of cellular structure due to certain wood species and the angle between fiber orientation and loading direction, among others. Based on this, the failure behavior of layered wood structures is affected by the different lay-ups constituted by the grain orientation of the layers. The adhesive and the interface layers also influence the material's mechanical behavior. The goal of this experimentally oriented thesis was the comprehensive characterization of the damage evolution in layered wood structures to yield an improved understanding of ultimate failure. This comprises two aspects of characterizing damage accumulation and failure, namely (1) damage mechanisms occurring below the macroscopic scale, i.e., on a level where they take place as individual events; and (2) their interaction and accumulation leading to macroscopic failure. (Fig. 1.1).
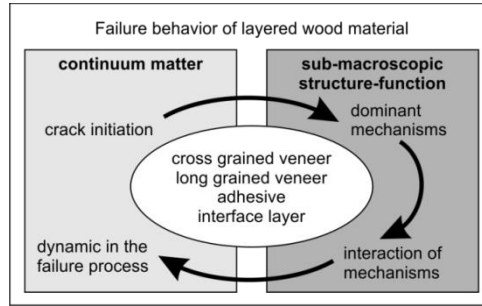
Figure 1.1 Schematic of ultimate failure of layered wood material as a result of individual microscopic mechanisms

An integrated description of failure behavior for a multi-scaled analysis demands clarification of the initial crack formation at low level stresses as well as on dominant deformations and damages and their final coalescence into mesoscopic or even macroscopic cracks. To this aim, the following key issues are focused on in the present thesis (Fig. 1.1):

- The start and the accumulation of defects at sub-macroscopic scale
- The identification and size of damage mechanisms at sub-macroscopic scale
- The changeover from microscopic mechanisms to larger scale damages
- The dynamic in damage increase in terms of defect growth rates
- The impact of the layered structures on the linear and non-linear failure behavior
- Predictions of the ultimate tensile strength by means of damage events occurring prior to failure
- The impact of intrinsic pre-damages (veneer lathe checks) on AE behavior
- The occurrence and interpretation of identified AE signal classes

Notably, the material characterization is evaluated as a function of progressive stresses to associate the material's behavior over a continuum and its structure function in microscopic or mesoscopic scale. Furthermore, decoding the origin of structural changes by means of verifying certain parameters of the detected AE is also sought. Besides the analysis of AE signal parameters in the time domain, e.g., AE amplitude, AE energy, features of the signal's frequency spectra are also focused on, particularly to identify similarities and, based on this, to assign features of the detected signals to their microscopic source mechanism. Therefore, the UPR method, which is based on features extracted from the frequency spectra, is employed. The approach for signal classification applied in the present study was originally developed for failure identification in fiber reinforced composites (Sause et al. 2012a, Sause et al. 2012b). Since these composites and wood both have distinct microstructures with anisotropic elastic properties (Fratzl et al. 2004), the

3

implementation of the UPR method for AE signal classification of failing wood seems to be straightforward and promising.

This experimental approach combines complementary non-destructive methods to perform real-time studies on failure development at microscopic and macroscopic scale constitutes a significant advance in experimental characterization of wood products or wood. The outcome of this research work will be of relevance for the design of new, more damage resistant wood-based products with better performance and improved damage resistance and durability regarding the end usage. Furthermore, the obtained findings could positively be transferred to other types of materials, e.g., fiber-reinforced polymer-matrix composites in a biomimetic approach. Micro-mechanics and modelling the mechanical behavior of wood products or other complex composite materials may profit from the detailed insight gained from this project. Moreover, especially in the field of production or in-service of the end products, (non-destructive) online monitoring methods are becoming more and more important and thus, basic research is also needed to single out suitable testing and monitoring procedures and pave the way for their application.

1.3 Structural overview

In general, studies on failure behavior of wood, specimens made of clear wood without intrinsic defects as they occur within industrially produced plywood, e.g., knots or pre-cracks, are conducted. For a first validation of damage evolution in layered wood, quasi-static tensile tests at laboratory-scale, according to DIN 52377, were performed on specimens made of clear spruce wood lamellae. The tests were monitored by acoustic emission (AE) and digital image correlation (DIC), whereby the damage initiation and accumulation of the simplified type of laminated veneer lumber and the simplified type of plywood are studied with regard to the increasing test progression. Thus, the energy content of detected AE signals reveals a correlation with strain field formation. The sizes of occurring damage events are analysed by means of AE amplitude distributions. (Chap. 6.1, Paper I)

Similar tests are performed on plywood specimens from industrial production. Due to the different lay-up of the plywood samples consisting of three, four, five or six veneers of spruce wood, differences in damage are analyzed by means of AE and DIC results as a function of the applied stress levels. Damage growth rates are determined and a first classification of AE signals is performed by means of energy content of the AE signals. (Chap. 6.2, Paper II)

The impact of pre-damages within the plywood materials is discussed in more detail in Ritschel et al. 2013 and summarized in Chap. 6.3. Thus, the AE results detected for the specimens made of clear spruce wood lamellae and for the industrially produced plywood are compared by means of cumulative AE activity and energy, as well as by the AE amplitude distributions. (Chap. 6.3)

Similarities of the AE signals detected for a certain material are assumed to be caused by the same source mechanism. An unsupervised pattern recognition approach based on the frequency spectra of the AE signals detected is employed to identify AE signal classes to provide an interpretation of related source mechanisms that occur when stressing wood materials. For a first assessment of the approach originally developed for fiber reinforced composites (Sause 2010) applicable to AE detected on stressed wood products, miniature specimens made of clear spruce wood are tested under tension. To achieve this, two different loading cases, longitudinal and radial applied tensile stresses leading to different fracture patterns of the ultimate failed specimens, are performed. (Chap. 6.4, Paper III)

Similar tests on longitudinally and radially loaded miniature specimens made of clear spruce were monitored by the AE measurement and, simultaneously, by synchrotron radiation micro computed tomography (SRμCT) to establish an improved interpretation of the AE cluster results obtained from the unsupervised pattern recognition technology. This combination is of outstanding benefit, since the SRμCT monitoring provides insight into the microscopic structure of tested specimens at the initial condition, the crack evolution at different states as well as the final fracture and, additionally, the associated crack formation and propagation in the spatial domain that results from the accumulation and interaction of single damage events detected in AE. (Chap. 6.5, Paper IV)

The adhesive layer within a bonded wood structure such as plywood also influences the material's mechanical performance and is thus expected to generate different cluster patterns in AE behavior due to lay-ups differing in the grain angles of the bonded wooden layers. Hence, further miniature specimens made of clear spruce wood bonded together with urea formaldehyde adhesive (UF) are investigated by employing the same experimental design and analyzing methods such as those used for the miniature specimens made of clear solid spruce. (Chap. 7.1)

As a reference for the laboratory scaled specimens of clear solid spruce, model layered wood without process-related pre-damages and industrially produced plywood, AE signal classification was performed using the previously tested UPR)

Table 1.1 Overview on the presented studies

Material	Model layered wood (Clear spruce lamellae bonded with UF)	Industrial plywood (Spruce veneers bonded with PRF)	Clear solid spruce	Clear solid spruce	Bonded wood (Clear solid spruce bonded with UF)	Model layered wood & industrial plywood (Columns 1 & 2)
Specimen's test section	2 cm^2	2 cm^2	1 mm^2	1 mm^2	1 mm^2	2 cm^2
Imaging method	DIC	DIC	-	SRµCT	SRµCT	DIC
Focus in AE	Damage onset & accumulation Damage intensity	Damage onset, accumulation & growth rate Prediction of ultimate failure	Signal classification based on spectra First interpretation of detected AE clusters	Improved signal classification based on spectra Calibration of crack sizes (by means of the related SRµCT scans)	Improved signal classification based on spectra	Comprehensive description of the failure development
Focus in imaging method	Elongation strain	Elongation strain Shear strain	-	Fracture zone Damage type Size of fracture area	Fracture zones Influence of the adhesive layers	Elongation strain Compression strain Shear strain
Paper	I	II	III	IV	Supplementary investigations	Supplementary investigations

approach. Therefore, only the results of the broad band AE sensors - SE 1000-H were evaluated which are likely to be comparable to the sensors used for the miniature tests. For each industrially produced plywood type, a comprehensive description of damage progression is presented including the obtained AE signal clusters, AE amplitudes and the localization of the detected AE signals, which are furthermore supplemented by selected results of the strain field formations determined by means of the DIC method. (Chap. 7.2)

References

COM 143 (2010) Report from the commission to the council, the European parliament, the European economic and social committee and the committee of the regions on the application and effectiveness of directive 2003/35/ec of the European parliament and of the council of 26 may 2003.

DIN 52376 (1978-11) Testing of plywood; determination of compression strength parallel to the surfaces.

DIN 52377 (1978-11) Testing of plywood; determination of modulus of elasticity in tension and of tensile strength.

Dworschack, M. (2014) Wachsende Windmühlen - Die Industrie entdeckt Buchenholz als Baustoff für Windkrafttürme, Hochhäuser und Parkgaragen. Werden nun mehr Laubwälder statt öder Fichtenplantagen angepflanzt? In: Der Spiegel 14:126-127.

EN 310 (1993-8) Wood-based panels: determination of modulus of elasticity in bending and of bending strength.

Fratzl, P. Burgert, I., Gupta, H.S. (2004) On the role of interface polymers for the mechanics of natural polymeric composites. Phys. Chem. Chem. Phys. 6:5575-5579.

Manninen, H (2014) Long-term outlook for engineered wood products in Europe. European Forest Institute. Technical report 91.

Ritschel, F., Zhou, Y., Niemz, P. (2013) Schallemissionsanalyse von Zugversuchen an industriell gefertigten Sperrhölzern, Zerstörungsfreie Materialprüfung: Berichtsband 2013, Deutsche Gesellschaft für Zerstörungsfreie Prüfung Jahrestagung Mai 2013, Dresden (Germany).

Sause, M.G.R. (2010) Identification of failure mechanisms in hybrid materials utilizing pattern recognition techniques applied to acoustic emission signals. Dissertation, ISBN: 978-3-86664-889-0, mbv-Verlag, Berlin , 305 pp.

Sause, M.G.R., Gribov, A., Unwin, A.R., Horn, S. (2012a) Pattern recognition approach to identify natural clusters of acoustic emission signals. Pattern Recognit. Lett. 33:17-23.

Sause, M.G.R., Müller, T., Horoschenkoff, A., Horn, S. (2012b) Quantification of failure mechanisms in mode-I loading of fiber reinforced plastics utilizing acoustic emission analysis. Compos. Sci. Technol. 72:167-174.

2 The raw material wood

2.1 Anatomy of wood

Wood reveals a complex hierarchical structure (Fig. 2.1), whereby the arrangement of cellulosic and non-cellulosic components constitute its composite character, from the macroscopic length scales down to the sub-microscopic level. At the macroscopic scale, wood is recognized as a cellular solid. The cellular composition is designed to serve the three fundamental functions of a plant, which are water transport from the roots to the leaves, the storage of biochemical substances and the plant's stability. Nature has created a number of different varieties of cell arrangements entailing the diversity of wood species (Wagenführ 2000). As a result of their early phylogenetic development, the simplest design evolved to form softwoods. The material investigated herein is the softwood spruce (*Picea abies* [L.] Karst.).

Due to the natural dimensions of the tree trunk, the cellular arrangement keeps a cylindrical symmetry, which is utilized to define the anatomical directions (Fig. 2.2a). The rotation axis runs in the longitudinal (L) direction and two further orientations are defined perpendicular to this. The radial (R) direction is normal to the symmetry axis, also passing the growth rings perpendicularly, whereas the tangential (T) axis touches the growth rings as a tangent. Based on this, three distinctive planes are determined (Fig. 2.2b). Since the plywood material consists of rotary cut veneer, the longitudinal-tangential (LT) plane is the primary focus in the following chapters. Furthermore, a wood block can be described by means of the geometric or the polar coordinate system (Fig. 2.2c).

For softwoods, more than 90% of the whole cellular structure are constituted by tracheid cells (Fig. 2.3a), whose rotation axis is oriented in the L direction. Similarly to composite tissue, the tracheids can be regarded as the reinforcing structural element embedded in the more ductile middle lamellae, which can be seen as the lignin matrix (Dinwoodie 1978).

Within the growth rings, tracheids differ in early wood cells formed at the beginning and latewood cells formed in the later section of the growth ring. For spruce wood, the early wood tracheids are characterized by relatively thin walls of 2-5μm cell wall matter enclosing a cell lumen of 15-45μm diameter. In contrast, the latewood tracheids have cell walls of 9-12μm thickness and diameters of 6-22μm. This cell composition constitutes the density profile of increasing density within a single growth ring (Lanvermann et al. 2013) in the R orientation (from early wood to

latewood). The length of spruce wood tracheids ranges between 1-5mm. Other structural elements are the wood rays, which run in the R direction. Especially in the case of spruce wood, the wood ray is uniserial (a single string of parenchyma cells one above the other). In general, the rays consist of three up to twenty parenchyma cells characterized by an averaged diameter of 10µm forming wood rays of up to 200µm in height. Spruce wood also includes resin channels, oriented longitudinally as well as radially. Since the resin channels represent less than 1% of cells, they will not be discussed further.
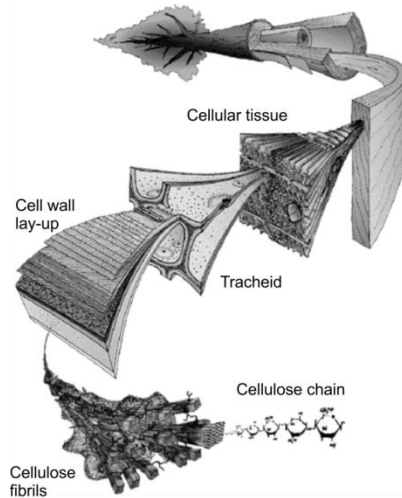
Figure 2.1 Hierarchical structure of softwood revealing its composite structure on the different length scales. Modified version of the original artwork by M. Harrington, University of Canterbury, New Zealand.
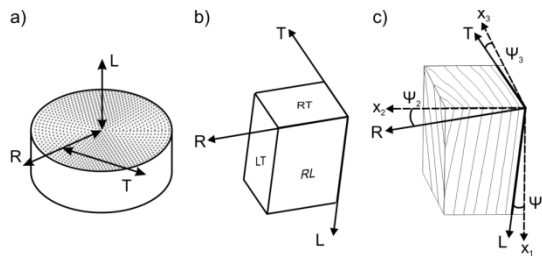
Figure 2.2 Anatomical axes and principal planes in wood. a) Longitudinal (L), radial (R) and tangential (T) direction. b) Radial section (RL), tangential section (LT) and cross section (RT). c) Geometric (x_1, x_2, x_3) and orthotropic (L, R, T) axes of a wood block, angles (Ψ_1, Ψ_2, Ψ_3) of the polar coordinate system.
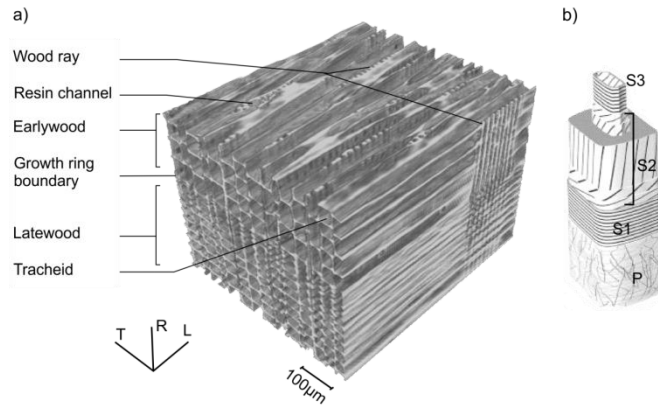
Figure 2.3 a) 3D microscopic structure of spruce wood generated using synchrotron based tomographic microscopy. b) Lay-up of tracheid cell wall: Primary (P), first secondary (S1), second secondary (S2) and third secondary (S3) cell wall; modified version of the original Brändström 2002.

The anisotropic nature of wood originates from the arrangement of tracheids oriented in the L direction and the wood rays running parallel to the R axis. In contrast, no structural elements are aligned in the T direction. Tracheids in particular show a complex ultrastructure (Fig. 2.3b) substantially contributing to the mechanical performance (Salmen and Burgert 2009). The tracheid's cell wall reveals the character of a layered composite that is built from the outer primary cell wall (P) enclosing the three-layered secondary cell wall (S1, S2 and the inboard S3) as organized in a composite laminate (Brändström 2002; Neagu et. al 2007). Each cell wall layer reveals a certain composite character due to the arrangement of the micro-fibrils embedded in a lignified matrix (Frey-Wissling 1936; Mark 1981). Thereby, the S2 layer contributes the most to the mechanical behavior of the tracheid, since it is a major bulk of the cell wall; approximately 70% (Fengel and Stoll 1973). The reinforcement of the S2 layer is adjusted in the L direction, which is induced by the orientation of the micro-fibrils nearly parallel to the tracheid axis.

2.2 Elasticity and strength

The mechanical properties, such as elasticity and strength, of a single wood species are influenced by a number of factors including fiber-load angle, loading case as well as the loading speed. As substantiated by uniaxial loading tests, wood exposed to moderate stress levels shows a linear elastic behavior and is consequently described by Hooke's Law (Eq 2.1) (Carrington 1921; Noack and Roth 1976). Thus, the correlation between stress and strain gives a measure of the stiffness C of a uniaxial loaded material, also known as the elasticity (E) or the modulus of elasticity (MOE).

$$\sigma_{kl} = C_{ijkl}\varepsilon_{ij} \qquad (2.1)$$

For the mathematical description of the wood's anisotropic character, the most common degree of anisotropy accepted is that of orthotropic material symmetry (Bodig and Jayne 1993). Therefore, idealized wood is presumed to be a continuum substance with its anatomical directions L, R and T coinciding with the symmetry axes (Hörig 1935, Hearmon 1941). Applying Hooke's law to this three-dimensional behavior, the tensorial form relates nine components of stress to nine components of strain (Eq. 2.2), where the stiffness tensor C is a fourth rank tensor comprising the elastic characteristic of the material by $3^4 = 81$ parameters.

$$\begin{bmatrix} \varepsilon_1 \\ \varepsilon_2 \\ \varepsilon_3 \\ \gamma_{12} \\ \gamma_{13} \\ \gamma_{23} \end{bmatrix} = \begin{bmatrix} S_{11} & S_{12} & S_{13} & 0 & 0 & 0 \\ S_{21} & S_{22} & S_{23} & 0 & 0 & 0 \\ S_{31} & S_{32} & S_{33} & 0 & 0 & 0 \\ 0 & 0 & 0 & S_{44} & 0 & 0 \\ 0 & 0 & 0 & 0 & S_{55} & 0 \\ 0 & 0 & 0 & 0 & 0 & S_{66} \end{bmatrix} \begin{bmatrix} \sigma_1 \\ \sigma_2 \\ \sigma \\ \tau_{12} \\ \tau_{13} \\ \tau_{23} \end{bmatrix} \qquad (2.2)$$

Since the compliance matrix S is the inverse of the stiffness matrix C, and further, considering the orthotropic character that defines the symmetry of elastic properties along three mutually perpendicular planes, the compliance matrix is given by the 12 components S_{ij}. The diagonal components S_{ij} of the compliance matrix are the inverse of the Young's modulus E_{ij} and the shear modulus G_{ij}, whereas the non-diagonal elements depend on the Poisson ratio (Tab. 2.1), which is a quotient of the strain normal to the load direction ε_i and the strain parallel to the loading direction ε_j (Eq. 2.3). By further postulating the symmetry of the non-diagonal elements, the tensor is simplified to nine independent elastic parameters (Bodig and Jayne 1993).

For the description of wood, the coordinate system L-R-T is employed for the strains ε, γ and the stresses σ, τ; consequently subscripting: L=1, R=2 and T=3. Since rotary cut veneers coincide with the LT-plane, the two-dimensional approximation of the compliance matrix is sufficient to describe the elasticity of the plywood's material component veneer (Eq. 2.4) (Bodig and Jayne 1993, pp. 347). Regarding the softwood's cellular composition, the tracheids (which constitute more than 90% of the components) run in the L direction, whereas the T direction lacks such an alignment of reinforcing cell components. It follows that wood reveals its strongest anisotropy between both the L- and T- directions, whereby, on average, the Young's modulus in the L direction is more than twenty times that in T direction (Bodig and Jayne 1993, pp. 115).

Table 2.1 Lists of the diagonal and non-diagonal components of the compliance matrix for description of wood.

Diagonal components	Non-diagonal components	
$S_{11} = E_1^{-1}$	$S_{12} = -\vartheta_{12}S_{11}$	$S_{21} = -\vartheta_{21}S_{22}$
$S_{22} = E_2^{-1}$	$S_{13} = -\vartheta_{13}S_{33}$	$S_{31} = -\vartheta_{31}S_{11}$
$S_{33} = E_3^{-1}$	$S_{23} = -\vartheta_{23}S_{33}$	$S_{32} = -\vartheta_{32}S_{22}$
$S_{44} = G_{12}^{-1}$		
$S_{55} = G_{13}^{-1}$		
$S_{66} = G_{23}^{-1}$		

$$\vartheta_{ij} = -\frac{\varepsilon_i}{\varepsilon_j} \; ; \; S_{ij} = S_{ji} \; ; \; \vartheta_{ij} \neq \vartheta_{ji} \tag{2.3}$$

$$\begin{bmatrix} \varepsilon_L \\ \varepsilon_T \\ \gamma_{LT} \end{bmatrix} = \begin{bmatrix} \frac{1}{E_L} & -\frac{v_{LT}}{E_L} & 0 \\ -\frac{v_{LT}}{E_L} & \frac{1}{E_T} & 0 \\ 0 & 0 & \frac{1}{G_{LT}} \end{bmatrix} \begin{bmatrix} \sigma_L \\ \sigma_T \\ \tau_{LT} \end{bmatrix} \tag{2.4}$$

The shear modulus in transverse RT plane is significantly lower than the shear against the L direction. For further comparison, the mechanical properties of spruce wood under tensile stress derived from several studies are listed in Tab. 2.2. Further, the ratios were determined from the data by Keunecke et al. (2007) (Eq. 2.5, Eq. 2.6).

$$E_L : E_R : E_T \approx 32 : 1.6 : 1 \tag{2.5}$$

$$G_{LR} : G_{LT} : G_{RT} \approx 11.6 : 11.1 : 1 \tag{2.6}$$

Due to the composition and arrangement of the cellular tissue, the mechanical properties of wood parallel to the grain significantly differ from that perpendicular to the grain (Gillis 1972; Gibson 2012). The characteristic stress-strain curves of tensile loading wood parallel and perpendicular to the grain demonstrate the significant differences in stiffness and strength (Fig. 2.4). Furthermore, the brittle nature of wood under tension is revealed by the significantly linear elastic region coming to a short inelastic deformation before ultimate failure.

Table 2.2 Mechanical properties of Norway spruce (Picea abies [L.] Karst.) exposed to tensile load.

Modulus of Elasticity (MPa)	E_L	14956	Požgaj et al. 1997
		12800	Keunecke et al. 2008
	E_R	625	Keunecke et al. 2008
		3088	Požgaj et al. 1997
		612.5	Welling 1987
	E_T	397	Keunecke et al. 2008
		555	Požgaj et al. 1997
		413.3	Welling 1987
Strength (MPa)	σ_L	80…90	Sell 1997
		21…90…245	Wagenführ 2000
	σ_R	3.6	Keunecke 2008
		4.8	Welling 1987
	σ_T	2.6	Keunecke 2008
		3.93	Welling 1987
	$\sigma_\perp$	1.5…2.7…4	Wagenführ 2000

Since wood is a hygroscopic material, the relation between moisture content and mechanical properties is the focus of numerous studies (Neuhaus 1983; Hering 2011; Ozyhar 2013). Comparing strength values for several wood species shows the correlation between strength and density (Gibson 2012). Analogous to the elasticity, the strength behavior of wood shows differences due to the applied fiber-load angles. Loading wood parallel to the grain yields the highest values of ultimate strength for all loading types, while R and T values are almost similar. For further comparison, the mechanical properties of spruce wood exposed to tension are listed from literature (Tab. 2.2).
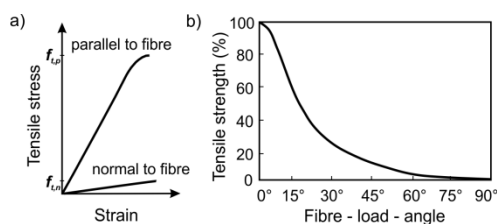

Figure 2.4 Mechanical properties of wood under tension. a) Typical stress-strain curves of wood tensile loaded parallel and perpendicular to fiber direction. b) Influence of fiber-load-angle to tensile strength (Kollmann 1951).

2.3 Fracture and failure under tension load

2.3.1 Crack growth system

Origin and appearance of fracture are multifarious, due to the microscopic properties of the material. The fracture is the consequence of crack nucleation and propagation when a material is exposed to stress. The formation or the growth of a crack creates a new surface by separation processes, respectively resolving bonding forces. Since, under tensile load, wood is a brittle material, the crack propagation is describable by the concept of linear elastic fracture mechanics (LEFM). A characteristic measure of energy available for an increment of crack extension is the strain energy release rate G, which, for wood, mainly depends on the temperature and moisture content (Debaise et al.1966).

Griffith energy balance:

$$G = \frac{dU}{dA} \qquad (2.7)$$

G Strain energy release rate; dU Energy consumption associated with created crack area; dA Change in crack area
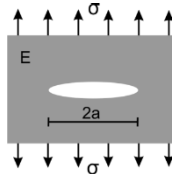
Figure 2.5 Crack growth system for a wide plate of a material with Young's modulus E and fracture toughness Gc, initially containing a crack length of 2a, is stressed in plane.

$$\sigma_f = \sqrt{\frac{EG_C}{\pi a}} \qquad (2.8)$$

σ_f Fracture stress; E Young's modulus; a Crack half-length; G_C Fracture toughness.

Equivalent to the theory of Griffith (1921), a characteristic measure of fracture is given by the energy consumption dU due to the creation of a certain crack area dA (Eq. 2.7). Thus, the internal strength of the material with Young's modulus E needs to be overcome (Fig. 2.5.). The corresponding critical energy release rate, the fracture toughness G_c (Eq. 2.8), expresses the resistance against ultimate fracture offered by the material already containing cracks (Anderson 2005). The fracture toughness G_c is a material specific property, which, in the case of brittle materials such as wood, is mainly affected by the surface energy. For an arbitrary structure, the fracture strength

decreases with increasing square root of crack size (Eq. 2.8). Fracture mechanisms in wood are of relevance when considering the failure analysis of plywood. The fracture toughness of wood is closely linked to the wood's density. By applying fracture mechanics to the wood's microscopic structure, its fracture toughness for crack propagation normal to the grain was found to be 10 times larger than for crack extension parallel to the grain. For a more comprehensive description, the reader is referred to Ashby et al. (1985).

2.3.2 Modes of crack extension

Crack extension can be caused principally by three types of loading modes (Fig. 2.6): Modes I, II and III. Mode I (opening cleavage) describes the tensile cracking by stresses opening the crack flanks. Thus, the applied tension provokes crack growth normal to the load direction. Mode II (in plane shear) is induced by shear loads arising from an opposed displacement of the crack flanks parallel to the direction of the crack propagation. In contrast, mode III (out of plane shear) summarizes all the stresses that cause a displacement of the crack flanks transversely to the crack propagation direction. For example, this mode appears when a crack is exposed to torsional stresses.
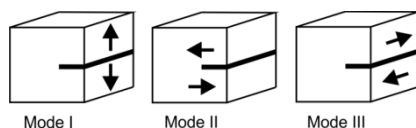
Figure 2.6 Three types of loading: Opening cleavage Mode I, In-plane shear Mode II, Out of plane shear Mode III.

Due to wood's anatomical axes, six different scenarios of crack orientations are defined. In the notation the first letter specifies the direction perpendicular to the crack, the second the direction of the crack propagation (Fig. 2.7). The lathe checks act in the TL crack system for the plywood layers loaded parallel to the grain, whereas for the cross oriented layers the TR system is applicable.

Generally, due to its natural character and depending on the tree's origin history, the wood material may already include characteristic intrinsic flaws. When exposed to low stress levels, the fracture of wood already starts by opening up and extending these intrinsic defects. The crack propagation can be characterized by means of its dynamic and lifetime, whereby the orientation of the starter crack plays an important role. Applying mode I to cracks oriented parallel to the grain (TL, RL), the crack propagates relatively slowly and unstably due to possible crack arrest when reaching the tracheid ends or passing the wood rays (Debaise et al. 1966). In contrast, when applying the mode I to a starter crack perpendicular to the grain (LR, LT), the rapid

cell wall breaking is of short cracking lifetime and rather stable character (Ashby et al. 1985).
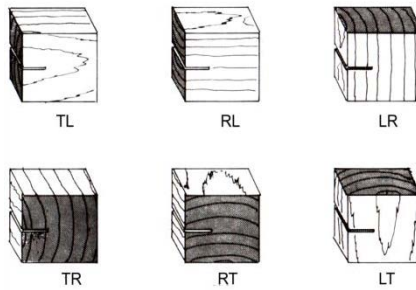
Figure 2.7 Crack systems in wood due to its three anatomic directions: Longitudinal (L), radial (R) and tangential (T).

In the following, a rough overview of typical fracture patterns and mechanisms are presented on a macroscopic as well as a microscopic scale, whereby the case of uniaxial tensile loading is of main interest due to the tests carried out on the layered wood materials and plywood products here investigated.

2.3.3 Axial tension parallel to the grain

When tensile loading a clear spruce wood specimen (with intrinsic flaws below macro-scale included, veneer lathe checks excluded), the ultimate failure is initiated by the fracture of the tracheids.
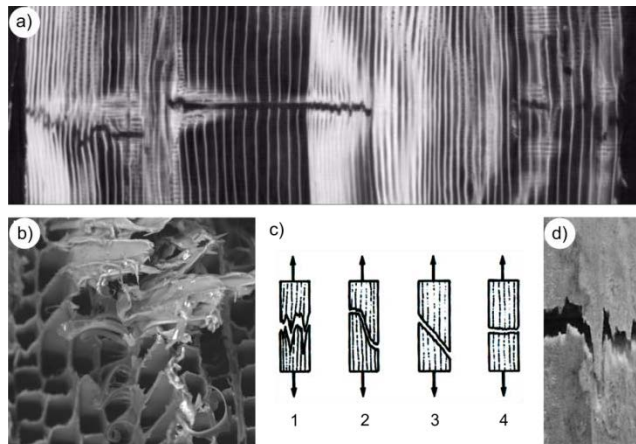
Figure 2.8 Fracture pattern of wood tensile loaded in the longitudinal direction. a) 2D tomogram shows crack propagation that pauses within the latewood zone of spruce wood. b) ESEM image of the fracture surface shows brittle failure and splintering of early wood tracheids of spruce wood. c) Macroscopic fracture pattern shows splintering. d) Failure types of wood tensile loaded: 1 splintering, 2 tension and shear, 3 shear, 4 brittle tension; Source: Bodig and Jayne (1993).

For wood and paper research, the investigation of mechanical performance of wood fibers is of great interest (Eder et al. 2008; Burgert et al. 2001); however, the outcomes are not transferable to the failure behavior of wood tissues due to the interaction of adjacent tracheids. Against crack extension in the R direction, the latewood tracheids act as a stronger barrier against breakage than the early wood tracheids which is owed to the fact that latewood tracheids consist of thicker cell walls than early wood tracheids (Fig. 2.3.a).
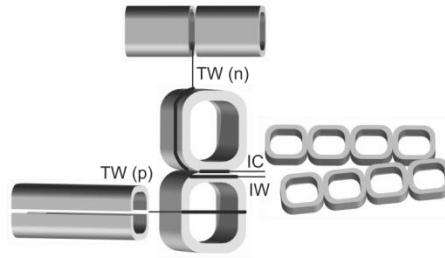
Figure 2.9 Cracking types when tensile loading wood: TW(n) Trans-Wall normal to grain, TW(p) Trans-Wall parallel to grain, IC Inter-Cellular, IW Intra-Wall. Source: Zauner 2013.

At the microscopic scale, the fracture patterns of the tracheids, as shown in Figs. 2.8a-b, can include fiber breakages with the crack plane oriented normal to the (early wood) tracheid axis (Fig. 2.9, TW(n)) as well as kinds of tear open mechanisms along the tracheid cell walls parallel to their axis (Fig. 2.9, TW(p)), which rather occur in the transition and late wood zones (Debaise et al. 1966). Moreover, it is suspected that the crack growth avoids crossing the wood rays featuring the tissue's reinforcement perpendicular to the load application (Futo 1969). As a consequence of the complexity at micro-scale, several fracture patterns at the macroscopic scale can occur: tension fracture with splintering (Figs 2.8c-1, d), combined shear and tension (Figs 2.8.c-2, c-3) or brittle failure (Fig. 2.8.c-4).

2.3.4 Axial tension normal to the grain

The mechanism of wood failure when exposed to tension perpendicular to the grain depends on the loading case and is affected by the density profile across the growth ring (Fig 2.10a). Ashby et al. 1985 found the occurring types of microscopic damage mechanisms in relation to the ratio of wood density ρ_s to cell wall density ρ_w. For wood species with the ratio ρ_s/ρ_w below 0.2, mainly the unstable cell wall fracture TW(p) was observed, whereas a larger ratio indicated both TW(p) and the intercellular (IC) or inter-wall (IW) separation mechanisms. The image from the Environmental Scanning Electron Microscopy (ESEM) in Fig 2.10b shows the fracture pattern of R loaded spruce which reveals both cell wall cracks and cell

separations. The separation of tracheids comprises crack growth within the middle lamella between adjacent cells yielding the so-called intercellular fracture IC, as well as intracellular fracture IW along the cell wall (Fig 2.9) within the cell wall lay-up (Fig. 2.3b) (Bucur 2011).
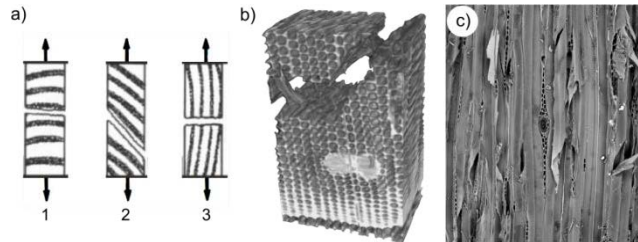

Figure 2.10 Failure behavior of wood tensile loaded perpendicular to the grain. a) Weak zone within early wood zone: 1 tension failure in early wood tracheids, 2 shearing along growth ring, 3 tension failure of wood ray; Source: Bodig and Jayne (1993). b) ESEM image of fracture zone in spruce wood tensile loaded in the radial direction shows trans-wall cracks and separation of early wood tracheids. c) Tomographic reconstruction from spruce wood tensile loaded in the radial direction reveals fiber-bridging of the early wood tracheids.

For R tensioned wood, the fracture zone is formed within the early wood bands (Fig 2.10c) revealing tension failure of tracheids (Fig 2.10a-1), whereas the wood rays had significantly contributed to the stiffness of the cellular tissue (Burgert et al. 2001; Burgert and Eckstein 2001; Reiterer et al. 2002). Tension failure is similarly observed in wood rays when loading in the T direction (Fig 2.10a-3) as it is for tensioning the cross oriented plies in plywood. Fiber-bridging is another phenomenon observed for transverse loading cases (Vasic et al. 2002; Frühmann et al. 2003; Keunecke et al. 2007; Zauner 2014) that yields a non-linear failure behavior.

References

Anderson, T.L. (2005) Fracture Mechanics. CRC press, Boca Raton, USA.

Ashby, M.F., Easterling, K.E., Harrysson, R., Maiti, S.K. (1985) The Fracture and Toughness of Woods. Proc. R. Soc. Lond. A 398:261-280.

Bodig, J., Jayne, B.A. (1993) Mechanics of wood and wood composites. Krieger, Malabar.

Brändström, J. (2002) Morphology of norway spruce tracheids with emphasis on cell wall organisation. Doctoral Thesis, Swedish university Uppsala, 39 pp.

Bucur V. (2011) Delamination in wood, wood products and wood-based composites. Springer, Netherlands.

Burgert, I., Bernasconi A., Niklas, K.J., Eckstein, D. (2001) The influence of rays on the transverse elastic anisotropy in green wood of deciduous trees. Holzforschung 55(5):449-454.

Burgert, I., Eckstein, D, (2001) The tensile strength of isolated wood rays of beech (Fagus sylvatica L.) and its significance for the biomechanics of living trees. Trees-Struct. Funct. 15(3): 168-170.

Carrington, H. (1922) Young's modulus and Poisson's ratio for spruce, Phil.Mag.VI.Ser.43:871-878.

Debaise, G.R., Porter, A.W., Pentoney, R.E., (1966) Morphology and mechanics of wood fracture. Mater. Res. Standard. 6:493-499.

Dinwoodie, J.M. (1978) Wood: Nature's cellular polymeric composite. Phys. Technol. 9:185-191.

Eder, M., Stanzl-Tschegg, S., Burgert I. (2008) The fracture behaviour of single wood fibres is governed by geometrical constraints: in situ ESEM studies on three fibre types. Wood Sci. Technol. 42:679–689

Fengel, D., Stoll, M. (1973) Über die Veränderungen des Zellquerschnitts, der Dicke der Zellwand und der Wandschichten von Fichtenholz-Tracheiden innerhalb eines Jahrringes. Holzforschung 27(1):1-7.

Frey-Wissling, A. (1936) Der Aufbau der pflanzlichen Zellwände. Protoplasma 25(1):261-300.

Frühmann, K., Burgert, I., Stanzl-Tschegg, S.E. (2003) Detection of the fracture path under tensile loads through in situ tests in an ESEM chamber. Holzforschung 57:326-332.

Futo, L.P. (1969) Qualitative and Quantitative Evaluation of the Microtensile Strength of Wood. Holz Roh. Werkst.27(5):192-201.

Gillis, P.P. (1972) Orthotropic elastic constants of wood. Wood. Sci. Technol. 6:138-156.

Gibson, L. (2012) The hierarchical structure and mechanics of plant materials. J. R. Soc. Interface 9:2749-2766.

Griffith, A.A. (1921) The phenomenon of rupture and flow in solids. Philos. T. Roy. Soc. A 221:163-198

Hearmon, R.F.S., Barkas, W.W. (1941) The effect of grain direction on the Young's moduli and rigidity moduli of beech and sitka spruce. Proc. Phys. Soc. 53:674-680.

Hering, S. (2011) Charakterisierung und Modellierung der Materialeigenschaften von Rotbuchenholz zur Simulation von Holzverklebungen. Dissertation 2011, Institute for Building Materials, ETH Zurich, 203 pp.

Hörig, H. 1935: Anwendung der Elastizitätstheorie anisotroper Körper auf Messungen an Holz. lng. Arch. 6:8-14.

Keunecke, D., Sonderegger, S., Pereteanu, K., Lüthi, T., Niemz, P. (2007) Determination of Young's and shear moduli of common yew and Norway spruce by means of ultrasonic waves. Wood Sci. Technol. 41(4): 309-327.

Keunecke, D., S. Hering, and P. Niemz, (2008) Three-dimensional elastic behaviour of common yew and Norway spruce. Wood Sci. Technol. 42(8):633-647.

Kollmann, F. (1951K) Technologie des Holzes und der Holzwerkstoffe. 2nd Ed. Springer Verlag, Berlin.

Lanvermann, C., Evans, R., Schmitt, U., Hering, S., Niemz, P. (2013) Distribution of structure and lignin within growth rings of Norway spruce. Wood Sci. Technol. 47:627–641.

Mark, R.E. (1981) Molecular and cell wall structure of wood. In: J.F. Oliver (Ed.), Adhesion in Cellulosic and Wood-Based Composites, Plenum, New York, 7–53.

Neagu, R.C., Gamstedt, E.K., Bardage, S.L., Lindström, M. (2007) Ultrastructural features affecting mechanical properties of wood fibres. Wood Mater. Scie. Eng. 1(3-4):146-170.

Neuhaus, H. (1983) Über das elastische Verhalten von Fichtenholz in Abhängigkeit von der Holzfeuchtigkeit Holz Roh. Werkst. 41(1):21-25.

Noack, D., Roth, W.v. (1976) On the theory of elasticity of the orthotropic material wood. Wood Sci. Technol. 10:97-110.

Ozyhar, T. (2013) Moisture and time-dependent orthotropic mechanical characterization of beech wood. Dissertation 2013, Institute for Building Materials ETH Zurich, 126 pp.

Požgaj, A., Chovanec, D., Kurjatko, S., Babiak, M. (1997) Wood structure and properties. (Štruktúra a vlastnosti dreva). Bratislava, Priroda, 486 pp.

Reiterer, A., Burgert, I., Sinn, G., Tschegg, S. (2002) The radial reinforcement of the wood structure and its implication on mechanical and fracture mechanical properties - A comparison between two tree species. J. Mater. Sci. 37(5):935-940.

Salmen, L., Burgert, I. (2009) Cell wall features with regard to mechanical performance. A review. Holzforschung 63:121-129.

Sell, J. (1997) Eigenschaften und Kenngrößen von Holzarten. Baufachverlag AG, Zürich.

Vasic, S., Smith, I., Landis, E.N. (2002) Finite element techniques and models for wood fracture mechanics. Wood Sci. Technol. 39:3-17.

Wagenführ, R. (2000) Holzatlas, Fachbuchverlag Leipzig.

Welling, J. (1987) Die Erfassung von Trocknungsspanunnungen während der Kammertrocknung von Schnittholz. Dissertation. Technische Universität Hamburg.

Zauner, M. (2014) In-situ synchrotron based tomographic microscopy of uniaxially loaded wood: in-situ testing device, procedures and experimental investigations. Dissertation 2014, Institute for Building Materials, ETH Zurich, 163 pp.

3 The engineered product plywood

Wood reveals a high potential for, and finds wide spread applications in, the building industry if its pronounced anisotropy can be manipulated and restrained. Designing a composite of orthotropic laminae arranged with varying grain angles of the layers leads to a reduction of the wood's anisotropic nature (Fig. 3.1, Keylwerth 1954). For instance, plywood built up of plies at 30° grain angles is rather described as an isotropic material. Thus, the elastic behavior is a superimposition of the plies' elastic properties. Among other factors, the strength, the modulus of rigidity (shear modulus G) and the dimensional change also depend on the lay-up.
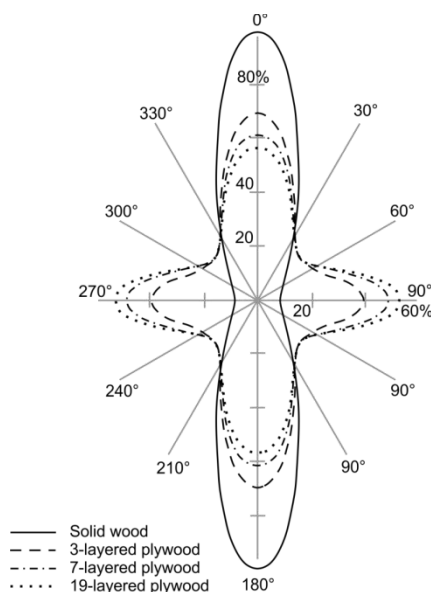
Figure 3.1 Polar diagram of Young's moduli of different plywood structures; modified version of the original Keylwerth (1951).

As an engineered product, plywood has to meet the demands of its final application. Correspondingly, EN 313-1 distinguishes plywood products by means of principal characteristics such as the durability, mechanical properties, surface appearance and surface condition. The design process of a plywood product starts from the veneer properties such as wood species, thickness and the arrangement of the plies' grain angles and, based on this, the calculation of the end product with specified properties can be performed by means of EN 14272.

3.1 History and Application

The basic principle of plywood, namely the lay-up of veneers alternating in their grain orientation, is dated back to the 18th century. Particularly, luxury items like furniture and art objects that were manufactured, for instance by David Röntgen who was one of the most famous artistic carpenters at that time, captivated with surfaces finished with veneer overlay. Thereby, the veneer was bonded on cross laminated wood stripes to reduce the wood's natural tendency toward swelling- and shrinkage-induced warping. Veneers were exclusively produced by sawing until the first veneer peeling machine was patented in 1818 (Wagenführ et al. 2011). The story of the plywood material known today started in the 19th century when the first patents for plywood were applied by John K. Mayo in 1865 in the US and Karl Witowsky in 1884, respectively, in Europe (Shi and Walker 2006). Innovative technological developments, for instance the hydraulic hot-compacting press developed by Max Harras in 1885 and the first belt dryer developed by Bernhard Hausmann in 1907, facilitated the industrial production of plywood. Leopold Lourié recognized the potential of the product and founded the first plywood production in Austria in 1903 (Kollmann 1962). Firstly, plywood was used for packaging products, but quickly spread out into new applications like in aircraft construction. Since the 1930s, plywood has been a commercial product used for packaging, in furniture and interior accessories in automobiles, boats and aircrafts, whereby also plywood molded parts and profiles constitute a special product group. Furthermore, they also comprise various interior constructions like doors and flooring and, in the building industry, exterior grade plywood is applied as formwork panels and roof structures (Perkins 1962). One of the latest developments is a laminated wood material made from rotary cut beech wood, the so-called "BauBuche" designed by Pollmeier (www.pollmeier.com, Germany). The product BauBuche allows structures with significantly slimmer dimensions, compared to softwood materials, due to its exceptionally high strength. For example, the BauBuche aspirates for application as building material of wind energy towers since, due to its more advantageous strength to weight performance, it allows higher heights (160m) than comparable constructions made of steel and concrete (Dworschack 2014).

3.2 Production

The raw material for rotary peeled veneer is a straight log, preferentially with a large diameter. First, the bark of the trunk is stripped and the trunks are cut to the length required. Afterwards, the logs are steamed in a large pit. Based on the producer's

experience and depending on the wood species and the desired color for the end product, the steaming or cooking time varies from a few hours to several days.

For rotary cutting of the veneer, the log is clamped onto the central axis and is turned on its own axis while the veneer is helically peeled from the outside as a continuous layer (Fig. 3.2). To control the vibration of the peeling knife and concurrently the thickness of the manufactured veneer, a nosebar positioned beyond the knife is pressed against the log during rotation (Baldwin 1981; Aydin et al. 2006). By doing so, the veneer's side facing the knife is exposed to bending stresses and thus, fine cracks are formed. The depth of the so called lathe checks depends on the wood species, the pre-treatment and the cutting conditions as well as the veneer thickness (Strübing 1960) and has effects on bonding quality.
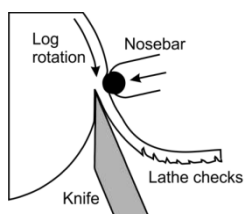
Figure 3.2 Principle of veneer cutting including a possible lathe check induction.

In general, the veneer thickness ranges from 0.1mm up to a few mm. In the following processing stage, the continuous peeled veneer is cut into sheets by means of an optical optimization clipper system before carefully being dried in a belt dryer. Afterwards, the veneer quality is proven, whereby defects are detected optically and then are repaired by inserting patches. The veneers are sorted by quality to be applied to the outermost surface layers or for building the core of the plywood.

To allow the production of panels of large dimensions, plies are produced by joining veneers with their grain orientation parallel to each other and end to end. By a roller system, both ply sides are covered with glue, combined following a certain lay-up scheme, and then hot pressed in a multiday light press. Pressing parameters depend on the requirements for the curing of the adhesive (Pizzi and Mittal 2003). Regarding the analysis of damage evolution within the plywood material, it has to be pointed out that the processing of the veneers, including the steaming of the logs, the rotary cutting and drying of the veneers, extremely stresses the wooden structure and already induces relevant pre-damages.

3.3 Plywood composition

3.3.1 Definitions

The plywood material is a panel product. The basic wood elements are rotary peeled veneers which are typically of less than 1mm up to 6mm thickness. The adjacent layers are bonded with synthetic adhesives under pressure, whereby the grain of each layer is oriented at right angle to the adjacent ones.

Definitions according to EN 313-2:

Plywood	"Wood based panel consisting of an assembly of layers glued together with the direction of the grain in adjacent layers usually at right angles."
Long grain plywood	"Plywood in which the grain of the outermost plies is parallel or nearly parallel to the long edge of the panel"
Ply	"Either one single veneer or two or more veneers joined edge to edge or end to end."
Layer	"Either one ply or two or more plies glued together with their grain direction parallel or another material."

The lay-up is symmetric about the panel's middle axis. Therefore, plywood has an odd number of layers, in which each layer may consist of one or more plies. Moreover, the grain on both outer surfaces runs in the same direction. By this symmetry, a balanced laminate panel is achieved that is less prone to swelling- and shrinkage-induced warping (Kollmann 1962). The high potential of the plywood material is offered in its load bearing performance by revealing a high level of strength to weight ratio and, at the same time, advantageous material consumption.

3.3.2 Characteristics of the adhesive

In plywood production, different types and qualities of adhesives are available for designing the optimal product regarding the final application and, especially, the related climatic conditions (EN 636). Interior plywood products are normally bonded by adhesives based on urea formaldehyde (UF), whereas phenol resorcinol formaldehyde resin (PRF) is used in construction and industrial plywood (exterior application) ensuring the materials durability and dimensional stability (Sontag and Norton 1935).

Table 3.1 Mechanical properties of UF and PRF adhesive taken from literature

	Urea formaldehyde resin (UF)	Phenol resorcinol formaldehyde resin (PRF)
Tensile strength (MPa)	60.2 ± 15.3[1]	33.8 ± 13.3[2]
Young's modulus (GPa) by tension of films	3.5 ± 9[1]	3.4 ± 8.9[2]
Young's modulus by Nanoindentation (GPa)	12[3]	7.78[4]
Shear strength (MPa)	14.86 ± 3.15[5]	14.65 ± 1.92[5]

[1] Bolton and Irle (1987); [2] Kläusler et al. (2013); [3] Stöckel et al. (2010); [4] Clauss et al. (2011a); [5] Clauss et al. (2011b)

In the here tested laminate materials both adhesives are used, the industrial plywood contains the PRF adhesive and the materials manufactured in the laboratory are glued with UF (type Placol 4507, 160g m^{-2}, 60% solid resin concentration) adhesive. The Young's moduli of pure UF and PRF adhesive films from tensile tests (Tab. 3.1) are lower than that of spruce in the L direction (Tab. 2.2) and higher compared to that of spruce in the T direction. It follows that the cross layers which are stressed in the T direction in the plywood composition are reinforced by the adherent bond lines. Similar to the wood, the bond lines based on UF or PRF behave in a brittle manner when exposed to load (Serrano and Enquist 2005; Kläusler et al. 2013).

The mechanical performance of the plywood product is influenced by the quality of the adhesive (Serrano and Enquist 2005; Wang 2012; Hass et al. 2012a). It has to be mentioned that the assessment of the glue line quality remains a persistent problem until today (Devallance et al. 2007; Hass et al. 2012b). However, an increasing share of solid resin yields a comparably higher strength of the board and an increasing share of adhesive per board thickness raises the Young's modulus of the plywood (Okuma 1976; Niemz 1993). For industrial plywood production, the adhesive mix includes approximately 2/3 solid resin and, on average, the application of the adhesive mix is approximately 200g m^{-2}, whereby both veneer sides are glued. To avoid glue stains, additives like flour are mixed in. Besides the quality of the adhesive, the impact of the wood-to-adhesive bond line composition on failure behavior is also affected by the veneer quality (Aydin 2004; Aydin et al. 2006; Demirkir et al. 2013), which is a key parameter for determining the penetration of the adhesive into the cellular wood matter (Frihart 2006; Kamke and Lee 2007; Hass 2012). Thus, reducing the veneer roughness provokes an increase in percent of wood failure (DeVallance et al. 2007;

Kläusler et al. 2014) and the minimization of depth and number of lathe checks yields comparably larger failure loads (Rohumaa et al. 2013).

3.4 Mechanical characterization of plywood

The performance of the plywood depends on the wood species and the grade of the veneer used (Norris et al. 1961) as well as on the type of adhesive. For example, the UF based adhesives are used for interior application, whereas exterior construction plywood is often produced with PRF resin (EN 313-1 1996; Kollmann 1962; Okuma 1976; Forest Products Laboratory 2010). Further, the lay-up pattern of the plies contributes to the final material's properties. The most common structure is the so-called balanced laminate (Forest Product Laboratory 1964). Balanced plywood, as investigated herein, consists of twin pairs of veneers with the same thickness, the same elastic parameters but with different grain orientation angles. The material symmetry about the plane of the center is given by using an odd number of layers, thus both outermost surface layers' grain orientations are parallel to each other. For the analogy between plywood and fiber reinforced composites, the two main categories of basic components, namely matrix-polymer and reinforcement, are constituted by the wooden layers due to their grain orientation relative to each other, while the adhesive layers' impact on the mechanical behavior is rather negligible due to its portion by volume being less than 2% (Okuma, 1967; Hearmon 1943). Correspondingly, the standard EN 14272 for calculation of plywood properties also excludes the influence of the adhesive layers.

The following paragraphs focus on the mechanical properties of plywood loaded under tension by regarding the material as symmetrically layered. This is adequate enough for the issues focused on herein, but generally constitutes a rough approximation. A more comprehensive approach is given by EN 14272 and used for designing specified plywood products, which provides a calculation method by regarding the plywood as a non-symmetrical structure due to the different quality of each ply. The elasticity of the plywood is evaluated by regarding the plies as an orthotropic continuum. In contrast, in terms of the fracture characterization, the intrinsic length scales of the wooden layers, and further, the process-related pre-damages, also need to be recognized.

3.4.1 Elasticity of plywood as continuum

When testing plywood to obtain the technical characteristic values, the material is regarded as uniform. A perfect adhesion between the veneers is assumed which yields uniform strains of the materials cross section layers. Consequently, slipping effects of

the single layers are ignored. By doing so, the continuum description is applied to the plywood meanwhile the mathematical description depends on the layers' grain orientations to each other. For instance, plywood built up of plies at 30° grain angles is rather described as an isotropic material. In contrast, since the plywood materials investigated herein are solely composed of wooden layers oriented orthogonally to each other, their elastic properties are described mathematically in terms of the orthotropic symmetry (Eq. 2.2) (Bodig and Jayne 1993; Hearmon 1943; Gerrard 1987; Keylwerth 1954). Thus, the plywood's symmetry axes coincide with the grain orientation of both outermost surface layers running parallel to each other. In total, the elasticity of the homogenous plywood material can be expressed by nine independent parameters (Fig. 3.3), since the non-diagonal terms of the compliance matrix are symmetric $S_{ij}=S_{ji}$ (Eq. 2.3).
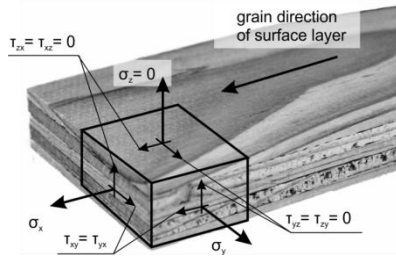
Figure 3.3 The axes of symmetry for the plywood are presented. With respect to Eq.2.2 for the description of an orthotropic continuum, the 1-, 2-, 3- directions correspond to the x-,y-,z-axes.

3.4.2 Elasticity of plywood as a component description

For characterization of the elasticity of the single layers, the plywood is regarded as a composite laminate material of fiber reinforced plies acting in the elastic range. Thus, uniaxial stresses applied to the plywood are assumed to yield uniform strains over the cross section. The adhesive primarily affects the strength and secondly the elasticity of the plywood. The deformation in the elastic range mainly depends on the plies and their grain orientation. Exemplarily, this approach of the uniform elastic deformation model is demonstrated for a plywood material consisting of three layers by three Hooke springs, whereby the two outermost layers with the grain orientation parallel to load direction are represented by the spring constant k_1 and the cross oriented (90°) middle layer is represented by the spring constant k_2 (Fig. 3.4).

Figure 3.4 Uniform elastic deformation model for the orthotropic arrangement of a three-layered plywood. The two outermost layers with the grain orientation of 0° are represented by the spring constant k_1 and the cross oriented (90°) middle layer is represented by the spring constant k_2. Source: Bodig and Jayne (1993).
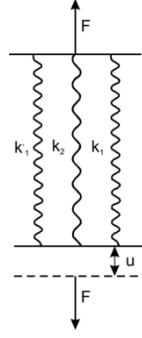
$$\varepsilon = \varepsilon_n + \varepsilon_{n+1} \qquad (3.1)$$

$$\sigma = \sum \sigma_n \qquad (3.2)$$

$$E = \sum E\sigma_n \qquad (3.3)$$

$$X_{Plywood} = \sum X_n \qquad (3.4)$$

With: $X_n = \varphi_n X_n$; X Property; φ Volume portion

Following the theory of uniform strain (Eq. 3.1), all springs with their spring rate k_i undergo the same displacement u when exposed to uniaxial stress (Fig. 3.4). Therefore, depending on the individual stiffness, different stresses are produced in each layer. Hence, the total stress σ for deformation is the sum of the stress σ_n in each spring and respectively in each layer (Eq. 3.2). Consequently, the elastic property E of the plywood is a superimposition of the plies' elasticity E_n (Eq. 3.3), whereas, the individual plies' contributions follow the law of mixtures. This rule constitutes that the contribution of each component X_n on the final product's character X is weighted by the component's proportion of volume φ (Eq. 3.4). The basic components are distinguished by the grain orientation of the veneer layers related to the direction of the load application, i.e. the reinforcing plies with their L direction, and the cross core ply with the veneer's T direction. The elastic behavior of the plywood is a superimposition of the wood's Young's moduli in the L and T directions (Eq. 3.5).

$$E_{Plywood} = \varphi_L E_L + (1 - \varphi_L)E_L \qquad \text{(Eq. 3.5)}$$

$$\varphi_N = \frac{d_n}{d_{Plywood}} \qquad \text{(Eq. 3.6)}$$

In general, for rotary cut veneer the tangential Young's modulus E_T is assumed to be only 1/35 of that for the L direction (E_L) (Bodig and Jayne 1993). This additional

reduction compared to the ratio postulated for clear wood (Eq. 2.5) takes account of the weakening pre-damages, the so called lathe checks, introduced when producing the veneers (King 1966; Plath 1974; Bodig and Jayne 1993; EN 14272). Finally, the E_L can be approximated (Fig. 3.5), while the ratio of layer thickness to plywood thickness is of main importance (Eq. 3.6); length and width are equal for all plies. The calculation of the elastic parameters as stated here is only applicable to uniaxial stress. However, when calculating the elasticity for bending or torsion, the calculations need to be transformed. Since the shear properties of a plywood panel are mainly influenced by the ply thickness, the moment of inertia and the area of moment has to be taken into account (Hearmon 1943; Norris 1962; Bodig and Jayne 1993).
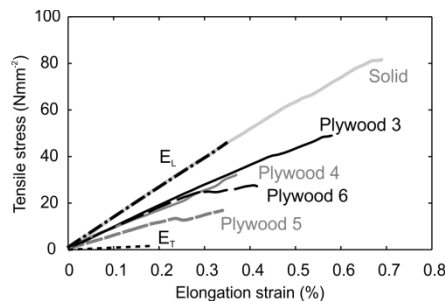
Figure 3.5 Stress-strain curves from tensile tests on solid spruce (loaded longitudinal) and plywood made of spruce. The industrial plywood products consist of 3, 4, 5 or 6 veneer layers. For comparison, the calculated Young's moduli E of veneer layers tensile loaded in the longitudinal (E_L=12GPa) and tangential (E_T=1.2GPa) directions are supplemented.

3.4.3 Strength

The tensile strength of plywood mainly depends on the grain orientation of the layers. With increasing angle between the grains of the outermost surface layers, the tensile strength significantly decreases. Furthermore, the strength decreases with increasing thickness of the plies. Also the adhesive type and its way of application, e.g. by a roller system or impregnation, influence the strength, which generally is improved with increasing portion of solid resin (King 1966; Niemz 1993). Particularly, regarding the veneer quality, the occurrence of lathe checks induced when rotary cutting the veneers is a well-known issue in plywood industry that should not be underestimated (Rohuma et al. 2013). Studies (e.g., Norris 1962, Ohya et al. 1992, Denaud et al. 2012) found this phenomenon varying with wood species and veneer thickness, but the technologic parameters of the veneer production also play an important role (Aydin et al. 2006). A minimization of lathe checks comparably improves the plywood strength (DeVallance et al. 2007; Rohumaa et al. 2013).

To predict the ultimate failure of composite materials, various strength criteria have been proposed. For laminated materials, these criteria are based on the performance of the single layers L oriented (Altenbach et al.1996). One of the most common strength criteria, namely the tensor polynomial strength theory for anisotropic materials, is well known as the Tsai-Wu-criteria (Tsai and Wu 1971). This theory states the description of failure as a macroscopic criterion containing unknown parameters that must be determined experimentally via realizable loadings. Similar to fiber reinforced composites, Hashin and Rotem (1973) and Hashin (1980, 1981) developed improved strength criteria that distinguishes between failure in the fibers and failure in the matrix while assuming transversal isotropy of unidirectional reinforced fiber composites. Its suitability for numerically investigating the failure behavior of plywood has been demonstrated by Ivanov et al. (2008).

3.4.4 Fracture and failure under tension load

To establish a comprehensive analysis of the failure behavior in plywood, numerous levels of its structural organization ranging in dimensions from 10^{-2}m to below 10^{-6}m need to be considered: Microscopic damage phenomena accumulate, as they occur in the cellular structure of wood, and the process-related pre-damages in the veneers grow further passing the layers and glue lines and, finally, resulting in the ultimate fracture of the plywood. Thereby, one of the main impacts on the damage development is given by the load angle that is applied to its wooden layers.

Due to the wood's anisotropic character, the wood layers that are tensile loaded in the T direction (cross plies) are assumed to be the first source of damage formation (Fig. 3.6). Moreover, the mechanical performance of the wooden layers is additionally reduced by the presence of lathe checks. In terms of damage initiation and formation, these pre-damages induce a further dimension affecting crack opening and growing in the range of 10^{-3}m and beyond.
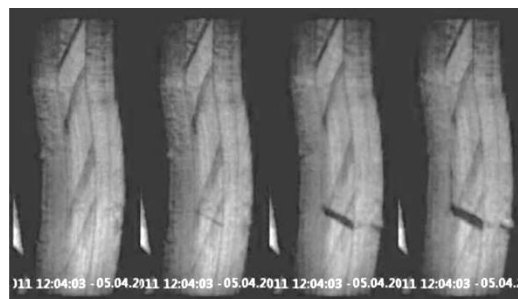

Figure 3.6 Crack evolution in tensile loaded plywood monitored by means of a high speed camera (image recording rate of 25000 images each second): Cross ply failed first.

3.4.5 Rolling shear and shear strength

The structure of plywood with the different grain orientations of the single layers induces the phenomenon of rolling shear (Fig. 3.7). Rolling shear occurs because the deformation under loading is not equal for each layer due to larger resistance of the L loaded layers compared to the cross oriented ones tensioned in the T direction in the RT plane. Since the shear strength in the RT plane is low due to the cell arrangement, hence, applying tension in the T direction results in shear forces at the boundary between the thin-walled early wood tracheids and the thick-walled latewood tracheids. Thus, deformation patterns are caused, which reveal that the wood fibers roll off across the grain, whereby the rolling shear modulus is mainly influenced by growth rings' alignment of the cross layers (Görlacher 2002).
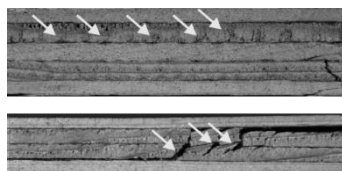

Figure 3.7 Typical fracture pattern of tensile loaded plywood made of 5 and 4 veneers. The arrows show the cracks of rolling shear in the cross plies.

While the shear modulus is rather unaffected by the plywood thickness (Ehlbeck and Collin 1985), the shear strength is mainly influenced by the number of layers to the material thickness ratio (Hearmon 1943). The shear strength of the plywood is mainly affected by the bonding quality and the size of lathe checks, whereby deep checks in the plies lead to a decrease of shear strength (Aydin et al. 2006; Rohumaa et al. 2013).

3.4.6 Failure mechanisms in the bond line

For plywood, several delamination effects are defined (ASTM D 1038), whereby most influencing issues are induced to the material while processing (veneer peeling and drying, plywood pressing) (Sinha et al. 2012). Besides the rupturing of the wooden structural elements, failure of the adhesive itself or at the interface between the adhesive and the adherent veneer will also occur. For instance, open joints between two adjacent veneers, voids and starved joints in the adhesive layers contribute to delamination and thus separation of the layers in plywood (Bucur 2011). Commonly, the definition of the bond line includes the pure adhesive part as well as the interface to the wood cells (Okuma 1976). Besides crack openings, shear and peel mechanisms may also occur in the bond line. Shear mechanisms result from forces applied parallel to the bond line, whereas peel mechanisms are caused by forces that tend to separate the parts of the bond line.

3.5 Simulation of progressive failure in plywood

The simulation of failure behavior of plywood, analogous to fiber reinforced laminate composites, constitutes a complex undertaking (Car et al. 2002; Landis et al. 2002; Ivanov et al. 2008). Modeling the damage evolution within the component wood requires approaches that consider the multi-scaled functionality of its hierarchical architecture (Vasic et al. 2002; Wittel et al. 2005; Hofstetter et al. 2008; Mishnaevsky and Quing 2008; Saavedra Flores and Friswell 2013). In the case of plywood, beside the intrinsic length scales of wood, additional length scales induced by the lay-up composition affect the damage evolution differently. Therefore, Ivanov and Sadowski (2009a) emphasized a micromechanical material approach involving a lattice network model that is based on the representative volume cell taken from the cellular structure of the veneers.
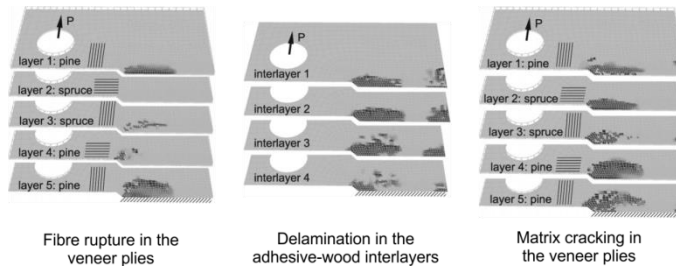
Figure 3.8 Simulation of damage mechanisms in plywood; Source: Ivanov and Sadowski (2009b).

By doing so, the numerical simulations of tensile tests on veneers with varying fiber-load-angles demonstrated that the phenomenon of fiber-bridging within the veneers, leading to a decrease in material resistance with progressive loading, was possibly more important than initially presumed. Furthermore, this approach was implemented to model the failure behavior of the plywood components during compact tension tests (Ivanov and Sadowski 2009b). Thus, the linkage between delamination, fiber rupture in the L loaded plies and matrix cracks in the cross plies was demonstrated. By this, it was shown that the impact of the adhesive might be of less importance if the adherent veneer reveals distinct weakness in the lay-up (Fig. 3.8).

References

Altenbach, H., Altenbach, J., Rikards, R. (1996) Einführung in die Mechanik der Laminat- und Sandwichtragwerke. Deutscher Verlag für Grundstoffindustrie.

ASTM D 1038 (2011) Standard Terminology Relating to Veneer and Plywood.

Aydin, I. (2004) Activation of wood surfaces for glue bonds by mechanical pre-treatment and its effects on some properties of veneer surfaces and plywood panels. Appl. Surf. Sci. 233: 268-274.

Aydin, I., Colakoglu, G., Hiziroglu, S. (2006) Surface characteristics of spruce veneers and shear strength of plywood as a function of log temperature in peeling process. Int. J. Solids Struct. 43:6140-6147.

Baldwin R.F. (1981) Plywood manufacturing practices, 2nd edn. Miller and Freeman Publication Inc., San Francisco, USA.

Bodig J., Jayne B.A. (1993) Mechanics of wood and wood composites. Krieger, Malabar.

Bolton, A.J. and Irle, M.A. (1987). Physical aspects of wood adhesive bond formation with formaldehyde based adhesives. 1. The effect of curing conditions on the physical-properties of urea formaldehyde films. Holzforschung 41(3):155-158.

Bucur V. (2011) Delamination in wood, wood products and wood-based composites. Springer, Netherlands.

Car, E., Zalamea, F., Oller, S., Miquel, J., Oñate, E. (2002) Numerical simulation of fiber reinforced composite materials - two procedures. Int. J. Solids Struct. 39:1967-1986.

Clauss, S., Gabriel, J., Karbach, A., Matner, M., Niemz, P. (2011a) Influence of the adhesive formulation on the mechanical properties and bonding performance of polyurethane prepolymers. Holzforschung 65:835-844.

Clauss, S., Joscak, M., Niemz, P. (2011b) Thermal stability of glued wood joints measured by shear tests. Eur. J. Wood Prod. 69:101.

Demirkir, C.; Ozsahin, S.; Aydin, I., Colakoglub, G. (2013) Optimization of some panel manufacturing parameters for the best bonding strength of plywood. Int. J. Adhes. Adhes. 46:14-20.

Denaud, L.E., Bléron, L., Eyma, F., Marchal, R. (2012) Wood peeling process monitoring: a comparison of signal processing methods to estimate veneer average lathe check frequency. Eur. J. Wood Prod. 70:253-261.

DeVallance, D.B., Funck, J.W., Reeb, J.E. (2007) Douglas-fir plywood gluebond quality as influenced by veneer roughness, lathe checks, and annual ring characteristics. For. Prod. J. 57(1-2):21-28.

Dworschack, M. (2014) Wachsende Windmühlen - Die Industrie entdeckt Buchenholz als Baustoff für Windkrafttürme, Hochhäuser und Parkgaragen. Werden nun mehr Laubwälder statt öder Fichtenplantagen angepflanzt? In: Der Spiegel 14:126-127.

Ehlbeck, J., Colling, F. (1985) Scherfestigkeit rechtwinklig zur Plattenebene und Schubmoduli von Bau-Furniersperrholz aus Buche. Holz Roh. Werkst.43:143-147.

EN 313-1 (1996) Plywood - Classification and terminology - Part 1: Classification.

EN 313-2 (1999) Plywood - Classification and terminology - Part 2: Terminology.

EN 636 (2012) Plywood - Specifications.

EN 14272 (2011) Plywood - Calculation method for some mechanical properties.

Frihart, C.R. 2006. Wood structure and adhesive bond strength. Characterization of the cellulosic cell wall. Ames, Iowa : Blackwell Pub., pp. 241-253.

Forest Product Laboratory (1964) Bending Strength and Stiffness of Plywood. General Technical Report FPL-RN-059, Madison, WI, U.S.

Forest Product Laboratory (2010) Wood handbook - Wood as an engineering material. General Technical Report FPL-GTR-190. Madison, WI, U.S.

Gerrard, C. (1987) The equivalent orthotropic elastic properties of plywood. Wood Sci. Technol. 21:335-348.

Görlacher, R. (2002) Ein Verfahren zur Ermittlung des Rollschubmoduls von Holz. Holz Roh. Werkst.60:317-322.

Hashin, Z. (1980) Failure criteria for unidirectional fiber composites. J. Appl. Mech. 47(2): 329-334.

Hashin, Z. (1981) Fatigue failure criteria for unidirectional fiber composites. J. Appl. Mech. 48:846-852.

Hashin, Z., Rotem, A. (1973) A Fatigue failure criterion for fiber reinforced materials. J. Compos. Mater. 7(4):448-464.

Hass, P., Wittel, F.K., Mendoza, M., Herrmann, H.J., Niemz, P. (2012a) Adhesive penetration in beech wood: experiments. Wood Sci. Technol. 46(1-3):243-25.

Hass, P., Wittel, F.K., Mendoza, M., Herrmann, H.J., Niemz, P. (2012b) Inverse determination of effective mechanical properties of adhesive bondlines. Eur. J. Wood Prod. 70:785-790.

Hass, P. (2012) Penetration behavior of adhesives into solid wood and micromechanics of the bondline. Dissertation 2012, Institute for Building Materials, ETH Zurich, 133 pp.

Hearmon, R.F.S. (1943) The significance of coupling between shear and extension in the elastic behaviour of wood and plywood. Proc. Phys. Soc. 55:67-80.

Hofstetter, K., Hellmich, Ch., Eberhardsteiner, J., Mang, H.A. (2008) Micromechanical Estimates for Elastic Limit States in Wood Materials, Revealing Nanostructural Failure Mechanisms, Mech. Adv. Mater. Struct. 15(6-7):474-484.

Ivanov, I.V., Sadowski, T., Filipiak. M., Kneć, M. (2008) Experimental and numerical investigation of plywood progressive failure in CT tests. Budownictwo i Architektura 2:79-94.

Ivanov, I.V., Sadowski, T. (2009a) Micromechanical material model of wooden veneers for numerical simulations of plywood progressive failure. Key Eng Mater 399:169-176.

Ivanov, I.V., Sadowski, T. (2009b) Numerical modelling and investigation of plywood progressive failure. Computational Materials Science 45:729-734.

Kamke, F.A. and Lee, J.N. (2007). Adhesive penetration in wood - a review. Wood Fiber Sci. 39(2):205-220.

Keylwerth, R. (1951) Die anisotrope Elastizität des Holzes und der Lagenhölzer. VDI-Verlag GmbH, Düsseldorf, DID-Forschungsheft 430.

Keylwerth, R. (1954) Errichte und erreichbare Verminderung der Anisotropie in Holzwerkstoff-Platten. Holz Roh. Werkst. 17(6):234-238.

King, E.G. (1966) A research program for establishing the strength properties of structural plywood. Material Research & Standards 6(10): 508-516.

Kläusler, O., Clauss, S., Lübke, L., Trachsel, J., Niemz, P. (2013) Influence of moisture on stress–strain behaviour of adhesives used for structural bonding of wood. Int. J. Adhes. Adhes 44: 57-65.

Kläusler, O., Hass, P., Amen, C., Schlegel, S., Niemz, P. (2014) Improvement of tensile shear strength and wood failure percentage of 1C PUR bonded wooden joints at wet stage by means of DMF priming. Eur. J. Wood Prod. 72:343–354.

Kollmann, F. (1962) Furniere, Lagenhölzer und Tischlerplatten. Springer-Verlag OHG, Berlin/Göttingen/Heidelberg.

Landis, E.N., Vasic, S., Davids, W.G., Parrod, P. (2002) Coupled experiments and simulations of microstructural damage in wood. Exp. Mech. 42(4):389-394.

Mishnaevsky, L., Quing, H. (2008) Micromechanical modelling of mechanical behaviour and strength of wood: State-of-the-art review. Comp. Mater. Sci. 44:363-370.

Niemz, P. (1993) Physik des Holzes und der Holzwerkstoffe. DRW Verlag Weinbrenner GmbH & Co. Leinfelden-Echterdingen.

Norris, C.B., Werren, F., McKinnon, P.F. (1961) The effect of veneer thickness and grain direction on the shear strength of plywood. US Forest Products Laboratory, Report No. 1801.

Norris, C. (1962) Strength of orthotropic materials subjected to combined stresses. Forest Products Laboratory - Forest Service U.S. Department of Agriculture Report 1816.

Okuma, M. (1976) Plywood properties influenced by glue line. Wood Sci. Technol. 10(1):57-68

Ohya, S., Ohta, M., Okano, T. (1992) Analysis of wood slicing mechanisms along the grain I. Mokuzai Gakkaishi 38(12), p 1089-1104.

Perkins, N.S. (1962) Plywood: Properties, Design and Construction. Douglas Fir Plywood Association.

Pizzi, A., Mittal, K.L. (2003) Handbook of adhesive technology. 2nd ed. Marcel Dekker, Inc. New York/Basel.

Plath, E. (1974) Berechnung der Dickenprofile für Sperrholz. Holz Roh. Werkst. 32:177-181.

Rohumaa, A., Hunt, C.G., Hughes, M., Frihart, C.R., Logren, J. (2013) The influence of lathe check depth and orientation on the bond quality of phenol-formaldehyde - bonded birch plywood. Holzforschung 67(7):779-786.

Saavedra Flores, E.I., Friswell, M.I. (2013) Ultrastructural mechanisms of deformation and failure in wood under tension. Int. J. Solids Struct. 50:2050–2060.

Serrano, E.; Enquist, B. (2005) Contact-free measurement and non-linear finite element analyses of strain distribution along wood adhesive bonds. Holzforschung 59(6):641-646.

Shi, S., Walker, J. (2006) Wood-based composites: plywood and veneer-based products. In: Primary Wood Processing. Springer Netherlands, pp.391-426.

Sinha, A., Nairn, J.A., Gupta, R. (2012) The effect of elevated temperature exposure on the fracture toughness of solid wood and structural wood composites. Wood Sci. Technol. 46:1127–1149

Sontag, L.A., Norton, A.J. (1935) Phenolic resin and adhesive in the plywood industry. Ind. Eng. Chem. 27(10):1114–1119.

Stöckel, F., Konnerth, J., Kantner, W., Moser, J., Gindl, W. (2010) Tensile shear strength of UF- and MUF-bonded veneer related to data of adhesives and cell walls measured by nanoindentation. Holzforschung 64:337-342.

Strübing, J. (1960) Measurement of Surface Smoothness in Veneer - Possibilities and Development. Holz Roh. Werkst. 5:181-185.

Tsai, S.W., Wu, E.M. (1971) A general theory of strength for anisotropic materials. J. Compos. Mater. 5:58-80

Vasic, S., Smith, I., Landis, E.N. (2002) Finite element techniques and models for wood fracture mechanics. Wood Sci. Technol. 39:3-17.

Wagenführ, A., Tobisch, S., Emmler, R., Buchelt, B., Schulz, T. (2011) Furnier im Innenausbau. Initiative Furnier & Natur e.V. (IFN).

Wang, L., Guan, M., Zhou, M. (2012) Influence of veneers' lathe checks on strain distribution at wood-adhesive interphase measured by electronic speckle pattern interferometry (ESPI). Proceedings of the 55th International Convention of Society of Wood Science and Technology. August 27-31, Beijing, Paper PS-67 1-8.

Wittel, F.K., Dill-Langer, G., Kröplin, B.-H. (2005) Modeling of damage evolution in soft-wood perpendicular to grain by means of a discrete element approach. Comp. Mater. Sci. 32:594-603.

4 Damage monitored by acoustic emission (AE)

4.1 Definition and principle

When materials are exposed to external stresses (mechanical, chemical, thermic, hygric or combinations), at certain stress levels short-term, locally restricted dislocation and deformation will occur (EN 1330-9). During this formation of internal structural changes, elastic energy is released in various forms, whereby one of them is acoustic emission (AE): The generation of transient elastic waves inside the material (EN 13554). Since these waves can be detected by piezoelectric sensors (AE sensors) mounted on the material's surface, information on the crack initiation and propagation processes can be obtained.
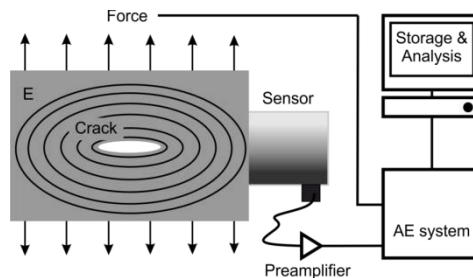
Figure 4.1 Principle of AE measurements

The stress wave received by the AE sensor is firstly converted into an electrical AE signal, then electrically amplified by a preamplifier and finally fed to an AE acquisition system (Fig. 4.1). In general, the AE system includes parallel measurement channels combining the parametric input (stress, displacement, etc.), the AE signal processing and the communication to the front-end PC. Altogether, beside information on the AE's origin, the AE measurements imply a process chain starting with the load application to the material up to the final data analysis and, thus, numerous factors influencing the end result have to be taken into account: Loading condition, density, elasticity and morphology of the material tested as well as type, position, sensitivity and response of the sensor, frequency filtering and amplification by the pre-amplifier and, finally, settings of the AE system (e.g., sampling rate, trigger, data acquisition rate).

In the field of material testing and characterization, the aim of AE measurements is to detect emission sources and, possibly, to locate and identify them. In general, the assignment of the complex AE signal waveforms to their source mechanism is difficult and thus numerous approaches have been investigated for answering this

question. For more AE basics and details on its measurement and analysis, the reader is referred to Miller et al. (2005), Grosse and Ohtsu (2008) and Sause (2010).

4.2 Advantages and challenges

The AE method provides a huge potential for extensive in-situ failure analysis of materials, since it provides information on sub-macroscopic failure phenomena as well as on the overall damage accumulation. Compared to other non-destructive testing methods (NDT) such as ultrasonic testing, in AE test procedures, the test object itself (exposed to external stress) releases the energy that will be detected. The high time resolution that the defect generation is recorded with is considered the main benefit of this method. AE signals are detected by high sampling rates (clock rate pulses of down to 100ns), and hence, large data volumes are acquired. Thus, dynamic processes regarding structural changes such as crack propagation and plastic deformation can be observed in-situ during the entire load progress without obstructing the actual experiment. Depending on specimen size, material properties, and chosen number of sensors, AE detection can cover the whole volume of the specimen. Thus, differences in AE sensitivity must be taken into account with respect to the sensor's frequency response, the position of the sensors and their distances to possible AE source location as well as the morphology of the material investigated.

In contrast to ultrasonic methods, AE monitoring of stressed materials is an irreversible procedure and an individual test is not repeatable. The same shape of specimen of a certain material does not necessarily yield similar AE activities in testing due to intrinsic differences in micro-structure and damage accumulation as well as present pre-damages. Furthermore, the most important challenge in AE analysis is to assign the features of the detected AE signals to their source mechanisms. A substantial and detailed interpretation of AE signals originating from structural failures requires additional information, e.g. by visualizing the structural changes. For the improved assessment of the detected AE characteristics, material research employs comparative studies and combinations of several measurement methods. Selected combinations, e.g., of AE and imaging methods are presented and discussed in Chap. 4.6.

4.3 Signal parameters

When the material is stressed, the signals typically recorded are discrete burst signals, i.e., transient AE which occur randomly. The first step in AE analysis is the discrimination of AE signals from the measurement's prevailing background noise.

Therefore an appropriate threshold THR in voltage amplitude is chosen (Fig. 4.2a). Consequently, only signals that overcome the threshold are detected AE signals. The time of crossing the threshold setting is defined as the AE signals' arrival time t_0. In general, the AE signals peak amplitude A_{Peak}, which occurs after the rise time t_R, is (much) larger than the background noise.
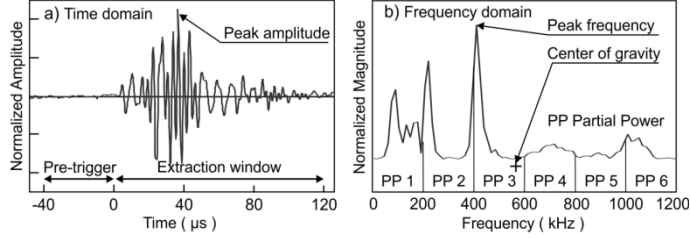

Figure 4.2 a) Schematic of AE signal parameters in the time domain: Threshold THR of signal detection, Peak amplitude A_{peak}, Risetime t_R, Counts C, Duration t_D. b) Parameters of the AE signal in frequency domain: Peak frequency PF, Center of gravity frequency CGF, Partial power PP.

When performing the AE measurement with at least two sensors, AE events can be localized along the distance between the sensors. Therefore, with respect to the acoustic propagation speed in the material, AE events are separated based on the AE detection within the feasible difference in arrival times at the sensors (Kurz et al. 2008). Usually the AE signal of a detected AE event (typically represented by more than one single AE signal) that first arrives at a sensor is employed for AE analysis.

The AE behavior of a stressed material is evaluated by first analyzing the AE activity and then the AE intensity. The AE activity is based on the number of AE events detected, following EN 1330-9, in terms of time units or external parameter units. A single AE event of large amplitude A_{Peak} and long duration time t_D produces more counts C than a smaller AE event. The duration t_D of the AE signal is a few microseconds up to a few milliseconds (Pardee and Graham 1978).

For further details on the material's failure behavior, the AE intensity is determined, often in terms of A_{Peak} or signal energy. Assuming AE monitoring of a homogeneous, isotropic material, ideally by means of linear broadband sensors, the A_{Peak} is a measure of crack size and was shown to be proportional to crack volume (Ohtsu and Ono 1986) as well as to crack surface area (Lysak 1996, Sause 2010). Thus, the energy content of a source mechanism can quantitatively be characterized by the energy of an AE signal, if the proportionality between both is given. For this case, in terms of fracture mechanics, similar loading conditions and stable crack growth are basically presupposed. Further, it has to be taken into account that this correlation can only be employed for AE signals detected within the far-field of the sensors. The

near-field behavior (widely varying amplitudes in the electrical signal) is difficult to gauge and possibly distort the AE results. However, the AE energy can be determined by integrating the absolute or the squared values of the signal's voltage curve over time (Miller et al. 2005). The latter case, also used herein (Tab. 4.1), is known as "true" energy parameter. The energy results can be directly related to physical parameters such as fracture energy or strain rate, as shown by, e.g., the analysis of carbon fiber and copper by Sause (2010).

Table 4.1 Parameters extracted from time and frequency domain of the AE signal

Feature	Abbrev.	Definition
Amplitude (mV, dB$_{AE}$)	A	Measured AE Amplitude (mV) $$dB_{AE} = 20 \log_{10} \frac{A}{1 \mu V}$$ *with 1 μV reference Voltage at sensor output*
Energy (V^{2}s)	E	$$E_i = \int_{t_0}^{t} U^2(t)dt$$
Peak frequency	PF	Frequency of maximum magnitude in spectrum
Center of gravity frequency	CGF	$$\frac{\int f \cdot \tilde{U}(f)df}{\int \tilde{U}(f)df}$$
Weighted peak frequency	WPF	$$\sqrt{f_{PF}f_{CGF}}$$
Partial Power	PP	$$\frac{\int_{f_1}^{f_2} \tilde{U}^2(f)df}{\int_{f_{start}}^{f_{end}} \tilde{U}^2(f)df}$$

These and other features extracted from the time domain of the AE signal waveform are often evaluated as cumulative or rate function of progressive time or test parameter (Brunner et al. 1995a, Brunner et al. 1995b, Nordstrom et al. 1997). Thus, damage initiation and accumulation are describable, for example in AE amplitude distribution, accumulated AE energy or energy rate. In the case of cyclic loading procedures, information on irreversible phenomena in material structure can be evaluated by two types of AE occurrence: If AE just occurs at stress levels exceeding the previous stress level, known as the Kaiser effect, structural changes formed during the previous loading cycle will not evolve further until higher stresses are applied. This is different for the Felicity effect, which describes the reappearance of AE prior

to the maximum stress level of the previous loading cycle being reached (Grosse and Ohtsu 2008).

Besides the conventional AE parameters extracted from their time domain (Fig. 4.2a), the features determined in the AE signal's frequency domain also provide information (Fig. 4.2b, Tab. 4.1). In the case of wood, the frequency of AE events is in the range of 100kHz – 2MHz (Bucur 2006). Each AE frequency spectrum contains information on the nature of the source event and on the integrity of the specimen's geometry (Stephen and Pollock 1971, Hamstad et al. 2002). However, when detecting the AE signal, depending on the source-sensor distance and sensor characteristic, the signal undergoes further distortion. Thus, for frequency based analyses, linear broadband sensors are commonly used, since their frequency response is well balanced compared to resonance sensors. Furthermore, attention needs to be paid to the acquisition settings, since the spectra significantly depend on the sampling rate of the waveform detection and on the waveform length (number of samples per wave) employed.

Analyses of the AE frequency spectra are based on the approach that similar source events are assumed to generate similarities within the spectra. A key challenge is to identify those similarities with the corresponding origin. Therefore, first, several features are extracted from the spectra, such as the peak frequency (PF), which is the frequency at the peak magnitude in the spectra, and the center of gravity frequency (CGF), which is equivalent to first moment of inertia, calculated as the sum of magnitude times frequency divided by the sum of magnitude (Tab. 4.1). Furthermore, the weighted peak frequency (WPF) is calculated from the square root of the product of PF and CGF and partial power (PP) levels can be estimated for weighting a defined frequency range (Tab. 4.1) (Sause et al. 2012a). This subdivision of the spectra facilitates the identification of meaningful frequency features yielding a reliable signal classification, since the impact of the measurement acquisition gets devalued.

4.4 Acoustic propagation

4.4.1 General basics

Once an AE event is produced, the response of the surrounding structure to the short shock is an elastic deformation. The elastic wave of this deformation propagates through the material. In an infinite solid media, different wave types can be formed, depending on particle motion relative to the direction of wave propagation. In the case of a longitudinal wave, the particles move parallel to the direction of the wave propagation, whereas a transverse wave is characterized by particle vibrations normal to the propagation direction. Assuming propagation media of linear isotropic

character, the velocity of wave propagation is significantly higher for the longitudinal than for the transverse wave. That is why the longitudinal wave is designated the Primary-wave (P-wave) and the transversal is the Secondary-wave (S-wave). Both P and S waves propagate independently of other, whereby their velocities of propagation are independent of their frequencies but influenced by density. Furthermore, the P-waves are affected by the material's modulus of elasticity (MOE) and the S-waves correlate with the shear modulus of the propagation material.

For finite propagation media, surface waves are formed by refraction of P- or S-waves into the propagation material's peripheral surface and then are guided by the specimen's geometry along the surface. The guided wave thus contains the contributions of both P- and S-wave. In case of an infinite propagation medium with only one single free surface, Rayleigh waves as a special type of guided waves occur. Another special wave type, the Lamb waves, is found for solid objects with two parallel running free surfaces such as plates, plate- or shell-like structures. Moving either symmetric or antisymmetric with respect to the midline of the plate or shell, corresponding Lamb wave modes can be distinguished. In contrast to the P- and S-waves occurring in an infinite propagation medium, the propagation velocity of Lamb waves strongly depends on frequency and wavelength, and on the ratio of wavelength and plate thickness, respectively. This wave property is known as dispersion. Except for special cases of short wavelength (Rayleigh waves) and for symmetric Lamb waves (even with very long wavelengths), the propagation velocity is almost constant. Guided waves are present in laboratory scale specimens such as those used for material characterization. The types of waves that occur are affected by the specimen's geometry.

As already outlined (see Chap. 4.3), the propagation of waves has a noticeable impact on the features of the detected AE. Thus, several effects leading to attenuation of acoustic waves within the propagation medium need to be taken into account. Since a real solid material includes inhomogeneities, either at the microscopic or macroscopic scale, for attenuation, the ratio of wavelength and size of the inhomogeneity is of relevance. Note that defects induced into the structure during load application also constitute inhomogeneities affecting the AE features. The wave propagation is less influenced when the wavelength is of a significantly larger value than the size of the intrinsic inhomogeneities. As both are in the same range, attenuation depends on frequency (Landis and Shah 1995). Hence, wave propagation suffers from reflection and dissipation processes at the structure's inner interfaces. Moreover, AE signals contain several frequency components. Thus, frequency dependent differences in

propagation velocity lead to an extended duration of the AE signal which is of constant energy content but of lower amplitudes; known as the phenomenon of dispersion. Another kind of attenuation purely depends on the distance between sensor and location of the AE source. The more distant an AE source is the less intensive (density in wave energy) is the detected AE signal.

4.4.2 Acoustic propagation in wood

In terms of acoustic propagation, wood is a dispersive material affecting distinctive attenuation due to its anisotropic character and the strong heterogeneity at several length scales (Bucur and Archer 1984). Influencing factors are the density as well as the cellular composition and arrangement which vary for each species. Also the moisture content is of importance. The most comprehensive study concerning these issues was published by Burmester (1965). By means of testing numerous wood species of certain densities, the relationship between density and acoustic propagation velocity determined is less significant (Bucur 2006, Niemz 1995). Nevertheless, for wood species of lower density (softwoods), such as spruce (*Picea excélsa* Link), higher acoustic propagation velocities were measured than for hardwoods, such as beech wood (*Fagus sylvatica* L.), which are of higher densities (Burmester 1965, Fig. 4.3).
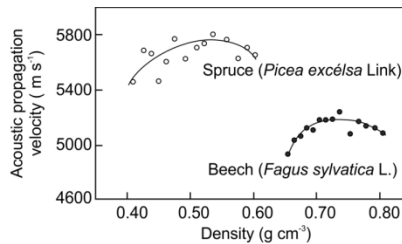

Figure 4.3 Acoustic propagation velocity of spruce and beech along the longitudinal direction versus density. Modified version presents the original data of Burmester (1965).

However, in a single wood log, for example, the acoustic propagation velocity follows the anisotropy of wood. In the L direction, the P-wave velocities are typically in the range of 4000 to 6000m/s, whereas in the R and T directions less than 50% of this velocity is reached. Due to the lack of conducting cellular elements, the lowest propagation velocity is in the T direction (Bucur 2006). With increasing frequency (100kHz to more than 1MHz), attenuation increases, whereby in the L direction, the attenuation is lower than in the R and T directions (Bucur and Böhnke 1994).

Bucur and Feeney (1992) proved that the attenuation in wood is sensitive to its anisotropic nature, since, in contrast to the wave propagation in the T direction, in the

out-of-axis propagation the L direction of wood yields the highest frequency-dependent dispersion. Regarding the structural composition, when comparing the acoustic properties of spruce and limba wood, spruce with its strictly radially oriented tracheids was found to act more complexly, similar to fiber reinforced composite materials. In contrast, the diffuse porous limba wood behaves more like a homogenous solid (Burmester 1965). Concerning the growth ring arrangement, the acoustic propagation velocity (in the L and T direction) is different in early wood and latewood, and further, lower than the velocity in solid wood, which is probably affected by dispersion caused by the specimen geometry (Bucur 2006). Burmester (1965) assumed that, besides the density and MOE of wood, the existence and length of wood cells parallel to the direction of the acoustic propagation also have a significant impact on acoustic velocity. He found a higher acoustic velocity for the comparatively longer latewood cells than for early wood cells. In the case of acoustic wave propagation in the R or T direction, a higher propagation velocity corresponds to a larger width of annual rings (Bucur and Perrin 1988).

Moreover, increased moisture content leads to reduced propagation velocity with critical impact occurring at the fiber saturation point (Sakai et al. 1990; Booker et al. 1996). Studies were carried out on the influence of the specimen's geometry, whereby a small height to width ratio of the cross section corresponded to higher propagation velocity and, less attenuation, respectively. (Bucur 2006). Furthermore, the attenuation coefficients have to be taken into account, especially when carrying out AE measurements on large wood specimens. To enable the AE detection over the whole specimen, an adequate number of sensors must be mounted and the coupling of the sensors has to be optimal. Therefore, a smooth specimen surface is advantageous which can be produced by planing or cutting with a microtome blade. Furthermore, the coupling media is also of relevance for improving sensitivity.

4.5 AE studies on wood exposed to external stress

The very first report to investigate the AE phenomena at all was also the very first to monitor the AE of failing wood: To solve problems concerning seismology, in 1933/34 Kishiouye studied the amplification and recording of AE generated when wood failed under bending stresses (Drouillard 1994). Nevertheless, it took until the 1960's for the AE method to achieve practical application in material testing of wood and wood based materials. Since then, application of the AE method as well as AE analysis has substantially progressed due to developments in technology and the associated improvements in signal processing. Though AE signals and their

parameters are a kind of measured quantity, so far, the assessment of the material behavior by means of AE is still somewhat of a qualitative nature rather than quoting specific numeric values. In general, explicit AE parameters are identified by employing comparative analyses, and of different materials, respectively.

In wood research, the material behavior when exposed to climatic or mechanical stresses is usually studied by the AE method, yielding far more details on the induced structural defects at the sub-macroscopic level. Poliszko et al. (1990) compared the results obtained from wood swelling experiments as well as those from tensile tests on wood specimens (performed at different moisture contents) with each other. Thus, the relation of the relative number of detected AE signals as a function of the degree of wood swelling and the relative wood moisture content as a function of the critical strains in wood supported the similarity in deformation and, consequently, the analogy in underlying mechanisms. The number of defects (measured in terms of number of AE signals) and the magnitudes of damages (measured in AE amplitudes or energies) were found to increase with increasing degree of inhomogeneity (Ansell 1982; Ando et al. 1992; Molinski et al. 1991). Due to the more heterogeneous arrangement of tracheids and/or vessels and the perpendicular oriented rays in the RT plane, relatively more damages occur in that plane compared to the LT plane (Molinski et al. 1991).

indicate the significant differences between the two qualities of beech wood. The high numbers of acoustic signals corresponding to opposite wood drying are caused by the creation of radial cracks (Fig. 2) and also by cell wall fractures in early wood fibres (Fig. 3).

By means of comparative drying experiments of beech tension and opposite ("normal") wood monitored by AE and Scanning electron Microscopy (beech), differences in AE behavior was linked to different damage mechanisms as a consequence of different cell structures (Cunderlink et al. 1996). Since wood drying is a key technical and economic issue in the wood industry and the AE method has emerged as a potential method for monitoring and controlling of drying processes, many studies have focused on the AE analysis of wood drying experiments (e.g., Quarles 1992, Beall et al. 2005, Rosner and Kawamoto 2010). In the course of this, the crucial question explicitly concerns the identification of AE parameters on AE classes and associated magnitude and kind of damage. Lee et al. (1996) performed a pattern recognition analysis of five features chosen from the time domain and two features chosen from the frequency domain. This approach yielded a classification of AE signals into two clusters, but since signals of both clusters occurred over the whole drying process, it was not possible to identify critical states by means of signal

types, nor was it possible to provide a control to regulate the kiln drying. Kim et al. (2005) first performed a correlation analysis (principal component analysis) to reduce multicollinearity in AE parameters and, based on the resulting classes, trained artificial neural network classifiers to identify AE signals due to surface checks or water movements. Moreover, investigation of old cultural objects made of wood demonstrated that old wood under climatic stress generates significantly more AE signals than comparable new wood (Jakiela et al. 2007 & 2008). Rosner (2012) found that irreversible drying processes were traceable by a relatively higher AE activity rate of signals with low frequencies (<175kHz) than were those for reversible mechanisms.

Studies on the elastic mechanical properties analyzed by AE are often complemented by imaging methods like post-test microscopy of fracture zones. One of the most comprehensive investigations on the mechanics of wood failure was performed by Debaise et al. (1966), who described the damage evolution of tensile stressed wood (perpendicular and longitudinal) in terms of cumulative AE density, i.e. the AE activity per stressed area. Thus, the onset of AE revealed the damage initiation in wood at a range of 5-20% of ultimate stress, which is in accordance with the observation of the swelling experiments of Poliszko et al. (1990). While the stress-strain curve of wood tensile loaded in the L direction shows a linear relationship, the damage accumulation measured cumulatively in AE signals reveals nonlinearity (Debaise et al. 1966). Further, Sato et al. (1985) demonstrated the relationship between the material's modulus of rupture and the stress level of the AE onset. The dependence of the detected AE on wood species and loading case was already determined by numerous experiments on different wood species exposed to tension, bending or compression (Debaise et al 1966; Ansell 1982; Vautrin and Harris 1987; Niemz and Lühmann 1992). Thus, spruce wood under tensile loading was found to generate a comparatively high number of AE signals (Niemz and Lühmann 1992). Since significant pre-damages in wood generate a relatively high AE activity, possibly due to friction mechanisms of pre-damaged fibers, the history of the tested wood material also needs to be taken into account (Sonderegger and Niemz 2003; Ando et al. 2006). In the case of decayed wood, brown-rotted (cellulose degradation) wood generates more AE signals than white-rotted (lignin degradation) wood (Amamura et al. 1991).

Numerous details on the sub-microscopic failure behavior of wood were obtained by analyzing the cumulative AE activity and AE rate in connection to stress application, but nevertheless, already by the 1980's the appeal for more detailed correlation

between AE features and mechanical properties arose (Ansell 1982; Vautrin and Harris 1987). Almost twenty years later, Aicher et al. (2001) and Dill-Langer et al. (2002) employed two dimensional localization algorithms to localize AE signals detected while tensile testing timber specimens made of spruce (parallel and perpendicular to the grain). By doing so, increased local accumulations of AE signals were found to be close to the failure zones of the ultimately failed specimens, and thus the potential of the AE method as a predictor of damage evolution and failure in wood was proven. Moreover, since the 1990's, features of AE signal intensity became of more interest in regard to analyzing the fracture mechanics of wood. Ando et al. (1991, 2006) proved that the AE amplitude distribution revealed different microscopic damage phenomena and thus suggested the trans-cellular cracking to generate higher AE amplitudes than cell separation mechanisms. A comparable study on the failure behavior of flax fibers was published by Romhany et al. (2003). By testing the RL-crack system of spruce wood, Aicher et al. (1992), among others, screened the amplitudes as well as the waveform and frequency spectra of the detected AE signals with the objective to decode the origin of micro-cracking phenomena, and thus proved the existence of similarities in AE features. The frequency spectra of AE signals detected while fracture testing (Mode I) different wood species revealed peak and center of gravity frequencies typically ranging below 300kHz for both soft- and hardwoods (Reiterer et al. 2000). By means of the basic fracture energy, Landis and Whittaker (2000) determined that, for eastern hemlock, one sixth of the fracture energy is released and measured in the form of AE energy from experiments on the crack propagation through wood loaded under Mode I. Ten years later, Nagy et al. (2010) even employed the AE energy release to validate their lattice model based on morphological simulations of microscopic damage evolution in wood.

Within the research field of wood-adhesive joints, adhesive joint failure has also been studied by means of AE monitoring (Suzuki and Schniewind 1987; Gozdecki and Smardzewski 2005; Smardzewski and Gozdecki 2007; Du et al. 2014). Cyclic tensile tests on welded wood joints found a critical Felicity ratio of around 0.9 (Brunner et al. 2010a; Brunner et al. 2010b). Regarding wood based products, the amount of damage measured by AE activity, has been found to be in correlation with the board density and the adhesive content, respectively for particleboards (Niemz et al. 1997). A comparative study on the internal bond of particleboard, OSB and MDF revealed almost similar damage accumulation for both particleboard and OSB, whereas MDF generates comparably slower initial rates and higher final rates of AE signals. The AE amplitude distribution of MDF follows a comparably more pronounced non-linearity, thus, the material fails in a different manner than particleboard and OSB (Beall 1985).

Besides the adhesive, wax levels affect failure of internal bonds, for example within MDF, which is also reflected in the AE behavior (Rice and Wang 2002). Ohtsuka et al. (1993) conducted shear tests of plywood specimens monitored by means of AE; the post-processed localization across the plywood thickness demonstrated that the AE signals attributed to the core layers yield larger AE amplitudes than those generated within the surface layers and glue lines. Furthermore, they observed that the locally accumulated AE signals were not in accordance with the fracture zones of the specimens. However, by means of combining AE and strain field monitoring of destructive tests on wood based materials, the 2D localization of the AE source location applied parallel to the board and load direction demonstrated consistency with the strain field formation determined from digital image correlation (DIC) (Vun and Beall 2004; Brunner et al. 2007). By carrying out these tests on MDF, particleboard, OSB and plywood, the prediction of fracture zones was found to be easier for more inhomogeneous materials like OSB and plywood (Ansell 1982; Niemz et al. 2009). Brunner et al. (2006) proved that the AE activity rate (in terms of load history), detected while tensile testing laminated wood specimens as a material dependent time-constant is analogous to damage accumulation in glass fiber reinforced polymer matrix composites. Another investigation compared the AE activity of fiber content regarding the wood fibers' pre-treatment of wood fiber reinforced polymer composites which is one of the most recent wood based products (Kocsis and Czigany 2007). Thus, less AE activity was detected when poor fiber-matrix adhesion was present. Further overviews concerning the AE technique applied to wood research are given by Cyra and Tanaka (2000), Beall (2002a), Beall (2002b) and Bucur (2006).

4.6 Combination with additional NDT methods

More details on micromechanical damage events leading to ultimate material failure will be obtained by combining the AE method with additional NDT methods. Therefore, non-contact optical methods are suited, particularly when simultaneously enabling the in-situ tracking of structural changes with the AE monitoring. One such method is optical surface deformation measurement via CCD cameras and strain mapping by means of the full-field image analysis technique which enables the determination of the contour and the displacements of a loaded test object. Planar as well as curved surfaces can be evaluated by two- or three-dimensional digital image correlation (DIC) (Chu et al. 1985; Schreier and Sutton 2002; Pan et al. 2009). For observation of deformation or crack propagation, the cross correlation algorithm of at least two images, e.g. unloaded and loaded state is employed, tracking a random high-

contrast speckle pattern that has been applied to the object surface. Choi et al. (1991) have proven its suitability for investigating the dimensional stability of wood. Using DIC, Haldar et al. (2010) demonstrated a multi-scaled mechanical characterization of wood, based on the example of Palmetto wood. Valla et al. (2011) proved the high sensitivity of the DIC method for strain field measurements of plywood by means of good discrimination between individual veneer layers.

The combination of AE and DIC is a mutually complementary approach for enabling an improved and adequate interpretation of AE results (Lyubutin and Panin 2006; Hoang et al. 2010). For instance, by simultaneous AE and DIC monitoring of uniaxial static tensile tests on specimens made of carbon–carbon composite, deformation of carbon fibers was found to be accompanied with an increase in AE activity and strain (Panina et al. 2012). Niemz et al. (2009) studied the mechanical behavior of MDF or plywood also while monitoring tensile tests with AE and DIC. Thus, an agreement between observed macroscopic fracture pattern and linear AE source location as well as corresponding surface strain field patterns confirmed the suitability of that combination for analyzing the damage evolution in wood and wood based materials.

Another promising approach is the additional implementation of tomographic monitoring, which allows spatial insights on microstructural changes (Cazaux et al. 1993). Already in 1992, Hayashi et al. (1992) announced that monitoring of stressed materials by AE and X-ray computed tomography is an applicable combination for investigating damage evolution. Two years later, Kinney et al. (1994) presented the high-brightness synchrotron X-ray tomographic microscope suitable for spatial reproduction of microscopic structures. Since then technological progress has made processing of synchrotron-based X-ray tomograms ever more time efficient, real-time studies on damage mechanisms at the sub-macroscopic scale were performed on several materials. Synchronous AE and (slow) tomographic monitoring were implemented for failure characterization of cement and mortar materials yielding an effective voxel size of $300\mu m^3$ down to $15\mu m^3$ (Chotard et al. 2003; Elaqra et al. 2007). Another study was performed by combining AE and fast continuous tomography for in-situ monitoring of tensile tests on metal, obtaining a pixel length of $1.4\mu m$ (Maire et al. 2007).

However, when studying the micro-structural changes in wood exposed to external stress, the effective resolution is fixed inevitably to the size of cell walls. For this purpose, the suitability of X-ray computed micro tomography (μXR-CT) was proven while investigating the anatomical features of beech and oak (Steppe et al. 2004). For materials built from elements with low absorption contrast, as is the case for the C N

O H elements in wood, an improved visualization is possible by phase contrast mode (Groso et al. 2006). By analyzing the cellular structure via synchrotron radiation phase contrast X-ray tomographic microscopy (SRμCT), within a sufficient observation field, a spatial resolution of approximately $1\mu m^3$ per voxel can be achieved. Based on this, micro cracks of at least 1.5μm are detectable (Trtik et al. 2007; Van den Bulcke et al. 2009). The high spatial resolution in connection with the high brilliance and, additionally, short recording times of SRμCT are advantageous conditions for in-situ monitoring of micro-mechanical failure phenomena in this context. Most suitable applications are compression or bending tests providing the quantification of deformations as well as extensive details on structural changes at several loading steps (Forsberg et al. 2008; Badel et al. 2008; Zauner 2012). Regarding the studies presented here, it has to be pointed out that recording the more spontaneous brittle failure when tensile loading wood is the key challenge in tomographic imaging.

References

Aicher, S., Grosse, C., Gappoev, M. (1992) Investigation on acoustic emissions in softwood crack initiation and growth. Otto Graf Journal 3:9-29.

Aicher, S., Höfflin, L., Dill-Langer, G. (2001) Damage evolution and acoustic emission of wood at tension perpendicular to fiber. Holz Roh Werkst. 59:104-116.

Amamura, Y., Fujii, Y., Noguchi, M., Fujisawa, K., Yukimune, K. (1991) Acoustic emission monitoring during bending test of decayed wood. Mokuzai Gakkaishi 37(11):1086-1090.

Ando K, Ohta M, Sato K, Okano, T. (1991) Fracture mechanism and acoustic emission characteristics of wood. Proc 6th Int Conf on Mechanical Behavior of Materials, Kyoto, pp 129−134.

Ando, K., Sato, K., Fushitani, M. (1992) Fracture Toughness and acoustic emission characteristics of wood II. Effects of grain angle. Mokuzai Gakkaishi 38(4):342-349.

Ando, K., Hiroshima, Y., Sugihara, M., Hirao, S., Sasaki, Y. (2006) Microscopic process of shearing fracture of old wood, examined using the acoustic emission technique. J. Wood Sci. 52:483-489.

Ansell, M.P. (1982) Acoustic emission from softwoods in tension. Wood Sci. Technol. 16:35-58.

Badel, E., Delisee C., Lux, J. (2008) 3D structural characterization, deformation measurements and assessment of low-density wood fibreboard under compression: The use of X-ray microtomography. Compos. Sci. Technol. 68:1654–1663.

Beall, F.C. (1985) Relationship of acoustic emission to internal bond strength of wood-based composite panel materials. J Acoust Emis 4(1):19-29.

Beall, F.C. (2002a) Acoustic emission and acousto-ultrasonics. In: Pellerin, R.F., Ross, R.J. (Eds.) Nondestructive evaluation of wood. Publ 7250. Forest Products Society, Madison, Wisconsin, pp 37−48.

Beall, F. C. (2002b) Overview of the use of ultrasonic technologies in research on wood properties. J. Wood Sci. Technol. 36(3):197-212.

Beall, F. C., Breiner, T.A., Wang, J. (2005) Closed-loop control of lumber drying based on acoustic emission peak amplitude. Forest Prod. J. 55(12):167-174.

Booker R.E., Froneberg J., Collins F. (1996) Variation of sound velocity and dynamic Young's modulus with moisture content in the three principal directions. In: Proc.10th international symposium on non-destructive testing of wood, Lausanne, Switzerland pp. 279-295.

Brunner, A.J., Nordstrom, R., Flüeler, P (1995a) Two-Parameter Description of the AE Rate Behaviour of Glass-Fiber Reinforced Epoxy and Polyester Under Static Tensile Loading. Proceedings Fifth International Symposium on Acoustic Emission from Composite Materials (AECM-5), American Society for Nondestructive Testing ASNT, (ISBN 1-57117-012-X), 101-110.

Brunner A.J., Nordstrom, R., Flüeler, P. (1995b) A Study of Acoustic Emission-Rate Behavior in Glass Fiber-Reinforced Plastics. J Acoust Emis 13(3-4):67-77.

Brunner, A.J., Howald, M.T., Niemz, P. (2006) Acoustic emission rate behavior of laminated wood specimens under tensile loading. J Acoust Emis 24:104-110.

Brunner, A.; Niemz, P.; Walter, O. (2007) Damage accumulation and failure of different types of wood-panels under tensile loading. Proc. 22. Technical Conference of the American Society for Composites (ASC).

Brunner, A.J., Tannert, Th., Vallée, T. (2010a) AE Monitoring of Tensile Tests on Welded Wood-Joints, Proceedings 29th European Conference on Acoustic Emission, European Working Group on Acoustic Emission, EWGAE, Paper No. 4, 7 pp.

Brunner, A.J., Tannert, Th., Vallée, T. (2010b) AE Waveform Analysis of Acoustic Emission Monitoring of Tensile Tests on Welded Wood-Joints, J Acoust Emis 28:59-67.

Bucur, V. (2006) Acoustics of Wood. 2nd edn. Springer, Heidelberg.

Bucur, V., Archer, R.R. (1984) Elastic constants for wood by an ultrasonic method. Wood Sci. Technol. 18:255-265.

Bucur, V., Böhnke, I. (1994) Factors affecting ultrasonic measurements in solid wood. Ultrasonics 32(5):385-390.

Bucur, V., Feeney, F. (1992) Attenuation of ultrasound in solid wood. Ultrasonics 30(2):76-81.

Bucur, V., Perrin, J.P. (1988) Ultrasonic waves−wood structure interaction. Proc. Inst. Acoustics. Edinburgh 10(2):199−206.

Burmester, A. (1965) Relationship between Sound Velocity and the Morphological, Physical and Mechanical Properties of Wood. (German) Holz Roh. Werkst. 23(6):227−236.

Cazaux, J., Erre, D., Mouze, D., Patat, J.M., Rondot, S., Sasov, A., Trebbia, P., Zolfaghari, A. (1993) Recent developements in X-ray projection microscopy and X-ray microtomography applied to material science. J. Phys. IV France 03:C7-2099-C7-2104.

Choi, D., Thorpe, J.L., Hanna, R.B. (1991) Image-analysis to measure strain in wood and paper. Wood Sci. Technol. 25(4):251-262.

Chotard, T.J., Smith, A., Boncoeur, M.P., Fargeot, D., Gault, C. (2003) Characterisation of early stage calcium aluminate cement hydration by combination of non-destructive techniques: acoustic emission and X-ray tomography. J. Eur. Ceram. Soc. 23(13):2211–2223.

Chu, T.C., Ranson, W.F., Sutton, M.A., Peters, W.H. (1985) Applications of Digital.Image-Correlation Techniques to Experimental Mechanics. Exp. Mech. 25, 232.

Cunderlik, I., Molinski, W., Raczkowski, J. (1996) The monitoring of drying cracks in the tension and opposite wood by acoustic emission and scanning electron microscopy methods. Holzforschung 50(3):258-262.

Cyra, G., Tanaka, C. (2000) The effects of wood-fiber directions on acoustic emission in routing. Wood Sci. Technol. 34:237-252.

Debaise, G.R., Porter, A.W., Pentoney, R.E., (1966) Morphology and mechanics of wood fracture. Mater. Res. Standard. 6:493–499.

Dill-Langer, G., Ringger, T., Höfflin, L., Aicher, S. (2002) Location of acoustic emission sources in timber loaded parallel to grain. Proc. 13th Int. Symp. on Nondestructive Testing of Wood, Berkeley, pp:179−186.

Drouillard, T.F. (1994) Acoustic emission - the first half century. Progress in Acoustic Emission VII, Sapporo, Japan: The Japanese Society for NDI.

Du, Y., Zhang, J., Shi, S. (2014) Acoustic emission of bolt-bearing testing on structural composite lumbers. Wood Fiber Sci. 46(1):118-126.

Elaqra, H., Godin, N., Peix, G., R'Mili, R., Fantozzi, G. (2007) Damage evolution analysis in mortar, during compressive loading using acoustic emission and X-ray tomography: Effects of the sand/cement ratio. Cement Concrete Res. 37:703−713.

EN 1330-9 (2009) Non-destructive testing - Terminology - Part 9: Terms used in acoustic emission testing.

EN 13554 (2011) Non-destructive testing - Acoustic emission testing - General principles.

Forsberg, F., Mooser, R., Arnold, M., Hack, E., Wyss, P. (2008) 3D micro-scale deformations of wood in bending: synchrotron radiation muCT data analyzed with digital volume correlation. J. Struct. Biol. 164:255-262.

Gozdecki, C., Smardzewski, J. (2005) Detection of failure of adhesively bonded joints using the acoustic emission method. Holzforschung 59:219-229.

Groso, A., Abela, R., Stampanoni, M. (2006) Implementation of a fast method for high resolution phase contrast tomography. Opt. Express 14:8103-8110.

Grosse, C.U., Ohtsu, M. (2008) Acoustic emission testing. Springer-Verlag Berlin Heidelberg.

Haldar, S., Gheewala, N., Grande-Allen, K.J., Sutton, M.A., Bruck, H.A. (2011) Multi-scale mechanical characterization of Palmetto wood using digital image correlation to develop a template for biologically-inspired polymer composites. Exp. Mech. 51:575-589.

Hamstad, M.A., Gallagher, A.O., Gary, J.A (2002) Wavelet Transform Applied To Acoustic Emission Signals: Part 1: Source Identification, J Acoust Emis 20:39-61.

Hayashi, K.; Nagata, Y.; Yamaji, H.; Ishida, T. (1992) Investigation of fracture processes in composites using X-ray computed tomography and acoustic emission method. Proc. 13th World Conference on Non-Destructive Testing, Sad Paulo, Brazil. 2:755-759.

Hoang, T.D., Herbelot, C., Imad, A. (2010) Rupture and damage mechanism analysis of a bolted assembly using coupling techniques between A.E. and D.I.C. Eng. Struct. 32: 2793-2803

Jakiela, S., Bratasz, L., Kozlowski, R. (2007) Acoustic emission for tracing the evolution of damage in wooden objects. Stud.Conserv. 52:1-9.

Jakiela, S., Bratasz, L., Kozlowski, R. (2008) Acoustic emission for tracing fracture intensity in lime wood due to climatic variations. Wood Sci. Technol. 42:269-279 .

Kim, K.B., Kang, H.Y., Yoon, D.J., Choi, M.Y. (2005) Pattern classification of acoustic emission signals during wood drying by principal component analysis and artificial neural network. Key Eng. Mat. 297-300:1962-1967.

Kinney, J.H., Haupt, D.L., Nichols, M.C., Breunig, T.M., Marshall, G.W.Jr., Marshall, S.J. (1994) The X-ray tomographie microscope: three-dimensional perspectives of evolving microstructures. Nucl. Instr. Meth. Phys. Res. A 347:480-486.

Kurz, H., Köppel, S., Linzer, L., Schechinger, B., Grosse, C., Source location, In: Acoustic Emission Testing in Engineering - Basics and Applications (Eds. Grosse, C., Ohtsu, M.), Heidelberg: Springer Publ. 2008, pp.101-147.

Landis, E. N., Shah, S. P. (1995) Frequency-dependent stress wave attenuation in cement-based materials. J. Eng. Mech. 121(6):737-743.

Landis, E.N., Whittaker, D.B. (2000) Acoustic emission and the fracture energy of wood in condition monitoring of materials and structures. Ansari, F. (Ed.), ASCE, Reston, VA, 302:21-29.

Lee, S.-H., Quarles, S.L., Schniewind, A.P. (1996) Wood fracture, acoustic emission and the drying process. Part 1. Acoustic emission associated with fracture. Wood Sci. Technol. 30:283-29.

Lysak, M. V. (1996) Development of the theory of acoustic emission by propagating cracks in terms of fracture mechanics. Eng. Fract. Mech. 55(3):443-452.

Lyubutin, P.S. and Panin, S.V. (2006) Measuring Deformations at the Mesolevel by Analyzing Optical Images of the Surfaces of Loaded Solids, Prikl. Mekh. Tekh. Fiz., 47(6):158–164.

Maire, E., Carmona, V., Courbon, J., Ludwig, W. (2007) Fast X-ray tomography and acoustic emission study of damage in metals during continuous tensile tests. Acta Mater. 55(20):6806-6815.

Miller, R.K., Hill, E.v.K., Moore, P.O. (2005) Nondestructive Testing Handbook, Vol. 6 Acoustic Emission Testing, American Society for Nondestructive Testing ASNT, Columbus, USA, Chaps. 1-5.

Molinski, W., Raczkowski, J., Poliszko, S. (1991) Mechanism of acoustic emission in wood soaked in water. Holzforschung 45(1):13-17.

Nagy, E., Landis, E.N., Davids, W.G. (2010) Acoustic emission measurements and lattice simulations of microfracture in spruce. Holzforschung 64(4): 455-461.

Niemz, P., Lühmann, A. (1992) Application of the acoustic emission analysis to evaluate the fracture behavior of wood and derived timber products. Holz Roh. Werkst. 50:191-194.

Niemz, P. (1995) Schallausbreitungsgeschwindigkeit einiger chilenischer Holzarten. Holz Roh. Werkst. 53:100.

Niemz, P., Kucera, L.J., Pridöhl, E., Poblete, H. (1997) Influence of board density and solid resin content on the acoustic emission of particleboards. Holz Roh. Werkst. 55(2-4):149-152.

Niemz, P., Brunner, A.J., Walter, O. (2009) Investigation of the mechanism of failure behaviour of wood based materials using acoustic emission analysis and image processing. Wood Res. 54(2):49-62.

Nordstrom, R., Brunner, A.J., Bohse, J. (1997) Sammlung von SE-Daten - Anregung für einen SE-Aktivitäts-Atlas. In: Statusberichte zur Entwicklung und Anwendung der Schallemissionsanalyse (11. Kolloquium Schallemission), Deutsche Gesellschaft für Zerstörungsfreie Prüfung DGZfP, Berichtsband 58: 171-178.

Ohtsu, M., Ono, K. (1986) The generalized theory and source representation of acoustic emission. Journal of Acoustic Emission 5:124-133.

Ohtsuka, H., Okumura, S., Noguchi, M. (1993) Acoustic emissions from plywood in shear by tension loading. Mokuzai Gakkaishi 39(7):795-800.

Pan, B., Qian, K., Xie, H., Asundi, A. (2009) Two-dimensional digital image correlation for in-plane displacement and strain measurement: a review. Meas. Sci. Technol. 20: 062001, 17 pp.

Panina, S.V., Burkova, M.V., Byakova, A.V., Lyubutina, P.S., Khizhnyakc, S.A. (2012) Staging of a localized deformation during tension of specimens of a carbon–carbon composite material with holes of different diameters according to acoustic-emission, surface-deformation mapping, and strain-gauging data. Russian Journal of Nondestructive Testing, 48(10): 598-608.

Pardee, W.J., Graham, L.J. (1978) Frequency analysis of two types of simulated acoustic emissions. J. Acoust. Soc. Am. 63(3):793-799.

Poliszko, S., Molinski, W., Raczkowski, J. (1990) Acoustic emission of wood during swelling in water. J Acoust Emis 10(3/4):107-111.

Quarles, S.L. (1992) Acoustic emission associated with oak during drying. Wood Fiber Sci. 24(1):2-12 .

Reiterer, A., Stanzl-Tschegg, S.E., Tschegg, E.K. (2000) Mode I fracture and acoustic emission of softwood and hardwood. Wood Sci. Technol. 34:417-430.

Rice, R.W., Wang, C. (2002) Assessing the effect of swelling pressures in particleboard and MDF using acoustic emission technology. Wood Fiber Sci. 34(4):577-580.

Romhány, G., Karger-Kocsis, J., Czigány, T. (2003) Tensile fracture and failure behavior of thermoplastic starch with unidirectional and cross-ply flax fiber reinforcements. Macromol. Mater. Eng. 288:699-707.

Rosner, S., Kawamoto, S. (2010) Acoustic emission activity of spruce sapwood becomes weaker after each dehydration-rewetting cycle. J Acoust Emis 28:76-83.

Rosner, S. (2012) Waveform features of acoustic emission provide information about reversible and irreversible processes during spruce sapwood drying. Bioresources 7(1):1253-1263.

Sakai, H., Minamisawa, A., takagi, K. (1990) Effect of moisture content on ultrasonic velocity and attenuation in woods. Ultrasonics 28:382-385.

Sato, K., Okano, T., Asano, I., Fushitani, M. (1985) Application of AE to mechanical testing wood. Proc. 2nd Int. Conf. AE, Lake Tahoe, pp. 240-243.

Sause, M.G.R. (2010) Identification of failure mechanisms in hybrid materials utilizing pattern recognition techniques applied to acoustic emission signals. Dissertation, ISBN: 978-3-86664-889-0, mbv-Verlag, Berlin , 305 pp.

Sause, M.G.R., Gribov, A., Unwin, A.R., Horn, S. (2012a) Pattern recognition approach to identify natural clusters of acoustic emission signals. Pattern Recognit. Lett. 33:17-23.

Sause, M.G.R., Müller, T., Horoschenkoff, A., Horn, S. (2012b) Quantification of failure mechanisms in mode-I loading of fiber reinforced plastics utilizing acoustic emission analysis. Compos. Sci. Technol. 72:167-174.

Schreier, H. W., Sutton, M.A.. (2002) Systematic errors in digital image correlation due to under-matched subset shape functions. Exp. Mech. 42: 303-310.

Smardzewski, J., Gozdecki, C. (2007) Decohesion of glue bonds in wood connections. Holzforschung 61:291-293.

Sonderegger, W., Niemz, P. (2003) Acoustic emission studies on bending specimens made from wind thrown spruce wood (Picea abies Karst.). 14. Kolloquium Schallemission, pp.111-118.

Stephen, R.W.B., Pollock, A.A. (1971) Waveform and frequency spectra of acoustic emissions. J. Acoust. Soc. Am. 50 (3):904-910.

Steppe, K., Cnudde, V., Girard, C., Lemeur, R., Cnudde, J.-P., Jacobs, P. (2004) Use of X-ray computed microtomography for non-invasive determination of wood anatomical characteristics. J. Struct. Biol. 148:11-21.

Suzuki, M., Schniewind, A.P. (1987) Relationship between fracture toughness and acoustic emission during cleavage failure in adhesive joints. Wood Sci. Technol. 21:121-130.

Trtik, P., Dual, J., Keunecke, D., Mannes, D., Niemz, P., Stähli, P., Kaestner, A., Groso, A., Stampanoni, M. (2007) 3D imaging of microstructure of spruce wood. J. Struct. Biol. 159:46-55.

Valla, A., Konnerth, J., Keunecke, D., Niemz, P., Müller, U., Gindl, W. (2011) Comparison of two optical methods for contactless, full field and highly sensitive in-plane deformation measurements using the example of plywood. Wood Sci. Technol. 45(4):755-765.

Van den Bulcke, J., Boone, M., Van Acker, J., Stevens, M., Van Hoorebeke, L. (2009c). X-ray tomography as a tool for detailed anatomical analysis Ann. For. Sci. 66(5): 508, 12pp.

Vautrin, A., Harris, B. (1987) Acoustic emission characterization of flexural loading damage in wood. J. Mater. Sci. 22:3707-3717.

Vun, R. Y., Beall, F.C. (2004) Monitoring creep-rupture in oriented strand board using acoustic emission: Effects of moisture content. Holzforschung 58:387-399.

Zauner, M., Keunecke, D., Stampanoni, M., Niemz, P. (2012) Synchrotron-based tomographic microscopy (SbTM) of wood: Development of a testing device and observation of plastic deformation of uniaxially compressed Norway spruce samples. Holzforschung 66:973-979.

5 Overview of materials and methods

5.1 The materials investigated

In the first test series, layered wood composites manufactured from clear spruce wood lamellae (density of $510 \pm 53 \text{kg m}^{-3}$) were tested. The number of veneer layers was reduced to three layers. Two different types of specimen were produced: the type consisting of three unidirectional oriented lamellae (UD) and the cross-plywood (CP). In order to prevent lathe checks (typical pre-damages in rotary cut veneers), the lamellae were planed. For the bonding, UF based adhesive was used.
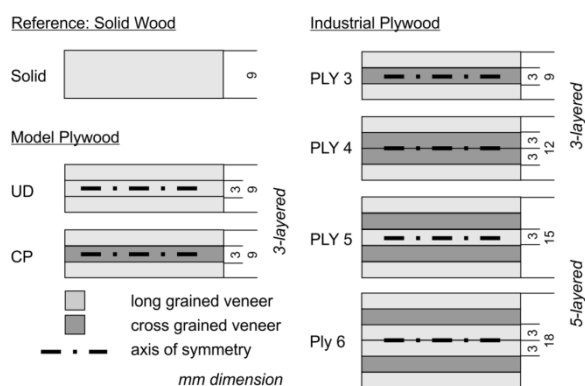

Figure 5.1 Cross-sections of all materials investigated: Reference specimens made from clear spruce wood. Model plywood materials manufactured from clear spruce wood planks planed down to 3mm thickness (UD = three layers oriented unidirectional, CP = cross ply in the center). Reference specimens made from clear spruce wood. Industrially produced plywood materials (PLY) with different lay-up made of 3-, 4-, 5,-6 spruce veneers (3mm thick) with process-related lathe checks.

Table 5.1 Overview of the plywood materials investigated

	Layered wood based without checks	Industrial plywood (including lathe checks)
Wood component :	Spruce wood	Spruce wood
Veneer thickness :	3mm	3mm
Adhesive :	Urea formaldehyde	Phenolic resin
Designation of the material type, grain orientation of the wood layers, Thickness of the core layer :	Solid, [0°], 9mm	PLY 3, [0° 90° 0°], 3mm
	UD, [0° 0° 0°], 3mm	PLY 4, [0° 90° 0°], 6mm
	CP, [0° 90° 0°], 3mm	PLY 5, [0° 90° 0° 90° 0°], 3mm
		PLY 6, [0° 90° 0° 90° 0°], 6mm

Table 5.2 Overview on the mechanical performance of the tested specimens and materials based on spruce wood under normal climatic conditions

Type of specimen	Experimental setup	Layer grain orientation to load direction	N	Density (kg/m³)	MC (%)	Cross section (mm²)	Cross-head speed (mm/min)	Test duration (s)	Strength (MPa)	E_{yy} strain (%)	MOE (GPa)	No. of load steps
Solid	Fig. 5.3a	[0°]	5	445 ± 18	9	176±1	2.5	204 ± 17	89 ± 8	0.79 ± 0.08	13 ± 0.2	1
UD	Fig. 5.3a	[0° 0° 0°]	5	566 ± 39	9	167±3	2.5	134 ± 48	75 ± 12	0.40 ± 0.06	21 ± 2	1
CP	Fig. 5.3a	[0° 90° 0°]	5	500 ± 27	9	176±0.73	2.5	159 ± 43	68 ± 8	0.68 ± 0.10	11 ± 3	1
Solid	Fig. 5.3b	[0°]	8	400 ± 11	8.6	156±0.77	2.5	151 ± 15	87 ± 9	0.69 ± 0.1	14 ± 1	1
PLY 3	Fig. 5.3b	[0° 90° 0°]	8	508 ± 16	7.2	157±1.3	2.5	107 ± 13	51 ± 6	0.67 ± 0.2	10 ± 0.1	1
PLY 4	Fig. 5.3b	[0° 90° 90° 0°]	8	469 ± 21	7.2	209±2.6	2.5	85 ± 14	33 ± 6	0.42 ± 0.08	9 ± 1.8	1
PLY 5	Fig. 5.3b	[0° 90° 0° 90° 0°]	8	420 ± 7	7.1	272±3.0	2.5	67 ± 8	18 ± 3	0.34 ± 0.07	9 ± 1.8	1
PLY 6	Fig. 5.3b	[0° 90° 0° 0° 90° 0°]	8	436 ± 12	7.2	330±5.6	2.5	154 ± 44	31 ± 4	0.42 ± 0.09	9 ± 2	1
L	Fig. 5.3c	[0°]	7	280±11	8.3	1.17± 0.23	0.6	1080±360	54±11			1
L	Fig. 5.3d	[0°]	1	349	8.3	1.2	0.6	6420	62			4
R	Fig. 5.3c	[90°]	7	337±6	7.8	4.08± 0.19	0.3	3240±360	8±1			1
R	Fig. 5.3d	[90°]	1	342	8.5	4.15	0.3	5400	6.34			2
LL	Fig. 5.3d	[0° 0°]	1	452	9.1	1.0176	0.6	2910	44			3
TL	Fig. 5.3d	[90° 0°]	1	478	-	1.51	0.3	2900	30			3
TT	Fig. 5.3d	[90° 90°]	1	450	7.9	2.6 ± 0.04	0.3	3360	2.68			3

N … Number of tested specimens, MC … Moisture content, MOE … Modulus of elasticity, UD … unidirectional, CP … crossply, LL = bonded specimen of 2 wooden layers oriented longitudinal, TL =bonded specimen of 1 longitudinal and 1 tangential loaded wooden layer, TT = bonded specimen of two wood layers loaded in the tangential direction

The industrially produced plywood investigated was made from 3mm thick spruce wood veneers (approximately 460kg m^{-3}, manufacturer information); originally produced for exterior application in construction by using the PRF based adhesive. Different lay-up structures, all symmetric, were tested: The typical and well-known three- and five-layered plywood products as well as plywood made of four veneers and plywood containing six veneers. A rough overview of all plywood materials investigated is given in Fig. 5.1 and Tab. 5.1. For reference, solid spruce wood was also tested.
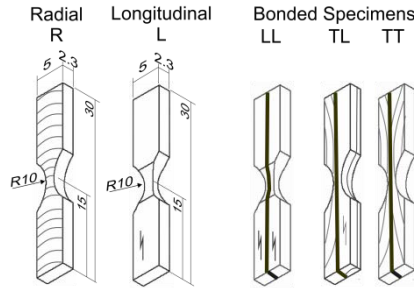
Figure 5.2 Miniature specimens investigated under tension. Solid specimens of clear spruce wood: a) radial (R) and b) longitudinal (L) specimens. Bonded wood specimens: c) two bonded lamellae longitudinally oriented (LL), d) two bonded lamellae tangentially oriented and e) one longitudinal and one tangential lamella bonded to each other. Dimension in mm.

Experiments at microscopic scale were performed on miniature specimens made of clear spruce wood (approximately 330kg m^{-3}). Tensile tests were carried out for two loading cases: longitudinally (L) and radially (R) stressed. Furthermore, some miniature specimens of two spruce wood lamellae bonded with each other were tested (Fig. 5.2). Analogous to the layered wood composites UD and CP, the miniature specimens were also bonded with UF adhesive. An overview on the testing conditions and the mechanical performance of all tested materials and specimens is given in Tab. 5.2.

5.2 The experimental setups

For a first validation of damage evolution in the layered wood composites UD and CP, quasi-static tensile tests at laboratory-scale, according to DIN 52377, were monitored by AE and DIC (Fig 5.3a). Similar tests were performed on plywood specimens from industrial production (Fig. 5.3b). Further, the AE was monitored for miniature specimens made of clear spruce wood tested under tension (Fig. 5.3c). Similar tests were monitored by the AE measurement and, simultaneously, by SRµCT (Fig. 5.3d).
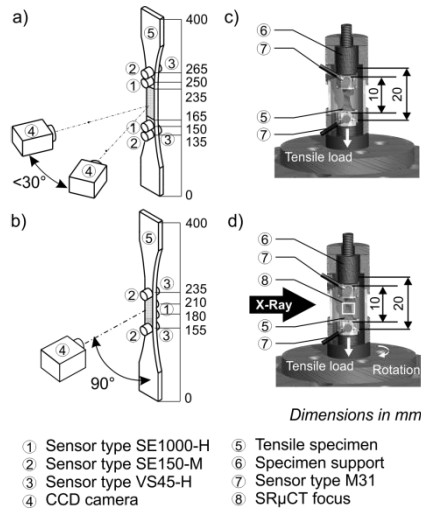
Figure 5.3 Overview of the experimental setups used in the investigations. a) Standard tensile tests on laboratory scale specimens made of layered wood materials UD and CP. b) Standard tensile tests on laboratory scale specimens made of industrially produced plywood materials. c) Tensile tests on miniature specimens made of clear spruce wood. d) Tensile tests on miniature specimens made of clear spruce wood and made of two spruce lamellae glued together.
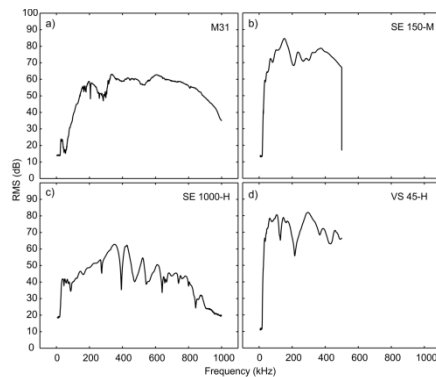

Figure 5.4 Response curves measured of a) the miniature sensor type M31, b) the resonant sensor type SE 150-M, c) the broad band sensor type SE 1000-H and d) the multipurpose sensor type VS 45-H. These measurements were performed by using the VST (by means the Vallen Sensor Tester, Vallen GmbH, Germany).

The AE systems used in the studies performed here is digital AMSY6 equipment (Vallen GmbH, Germany) with ASIP-2 channels, which convert the AE signal into a digital data stream. Fig. 5.4 presents the average response curves of the sensor types used in these investigations: the miniature sensor type M31, the resonant sensor type SE 150-M, the broad band sensor type SE 1000-H and the multipurpose sensor type VS 45-H. Due to the strong acoustic attenuation of wood, sensors need to be placed relatively close to the defect

generating zone of the specimen. Hence, detection within the near-field and respective effects on measurements could not be excluded. For the frequency based pattern recognition performed herein, it can be assumed that the rather resonant characters of the AE sensors are negligible for signal classification (see Chap. 4.3).

5.3 Acoustic properties of the investigated materials

In preparation of the studies presented here, the attenuation of surface waves was tested for solid spruce wood and industrial plywood made of spruce veneers. Therefore, pencil break tests were performed (Fig. 5.5). Blanks of 20cm x 200cm were cut from the same plywood boards used for specimen preparation. Boundary effects and reflections cannot be excluded. The strongest attenuation coefficients were determined for three-layered plywood (layer thickness of 3mm), especially for a distance of pencil break to sensor below 40cm (Fig. 5.6., Tab. 5.2). The maximum attenuation value of plywood is about $1dB_{AE}$ cm^{-1}, which is in good agreement with other studies on wood (Bucur 2006; Landis 2008). In comparison to the plywood, the solid spruce reveals better acoustical properties.
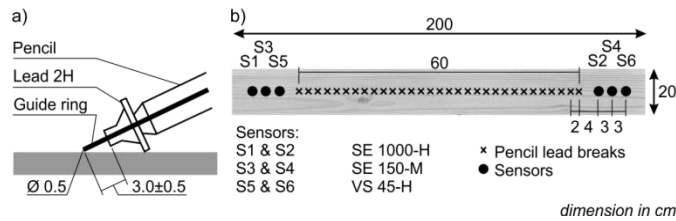

Figure 5.5 a) Principle of the pencil lead break (Hsu-Nielsen source). b) Coordinates of the attenuation tests.

Table 5.2 Attenuation coefficients for spruce wood and several plywood structures (PLY3-6) determined for three sensor types by means of pencil lead breaks (Hsu-Nielsen source). The coefficients are presented for two different detection zones; compare Figs. 5.5.-5.6.

	Attenuation coefficient (dB_{AE} cm^{-1})					
Sensor type:	SE 150-M		SE 1000-H		VS 45-H	
Distance (cm):	10-40	41-70	10-40	41-70	10-40	41-70
Solid spruce	0.41	0.62	0.39	0.34	0.17	0.09
PLY 3	1.01	1.00	0.99	0.19	0.36	0.32
PLY 4	0.67	0.48*	0.50	0.39	0.48*	0.24
PLY 5	0.78	0.73	0.59*	0.23	0.44	0.59*
PLY 6	0.72	0.72	0.71	0.36	0.38	0.39

... attenuation coefficient determined for distance of 10cm to 70cm

Moreover, it has to be pointed out that the specimen geometries of all experiments are plate-like structures (see Chap. 4.4.1). Thus, it is assumed that the AE waves are lamb waves.

Depending on source type and position within the specimen's geometry, possibly symmetric and antisymmetric waves are generated (Vergeynst et al. 2014).
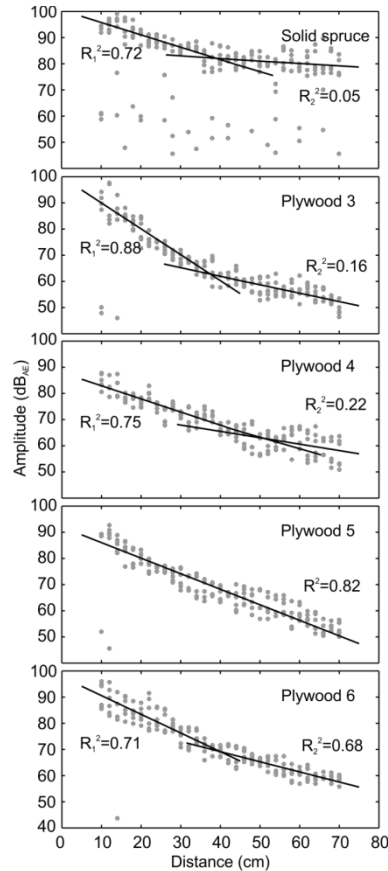

Figure 5.6 Attenuation in solid spruce and in plywood made up of 3, 4, 5 and 6 layers. Amplitudes of the performed pencil lead breaks (Hsu-Nielsen source) detected by the multi-purpose AE sensor VS45-H are plotted vs. the distance to the sensor.

References

Bucur, V. (2006) Acoustics of Wood. 2nd edn. Springer, Heidelberg.

DIN 52377 (1987) Prüfung von Sperrholz. Bestimmung des Zug-Elastizitätsmoduls und der Zugfestigkeit.

Landis, E.N. (2008) Acoustic emission in wood. In: Acoustic Emission Testing, Eds. Grosse, C.U., Ohtsu, M., Springer Verlag, Heidelberg. pp. 311-322.

Vergeynst, L.L., Sause, M.G.R., Ritschel, F., Brunner, A.J., Niemz, P., Steppe, K. (2014) Finite element modelling used to support wood failure identification based on acoustic emission signals. Proc. COST-Timber Bridges Conference, Biel/Bienne, Switzerland. pp. 141-146.

6 Main investigations

6.1 Paper I

Nondestructive evaluation of damage accumulation in tensile test specimens made from solid wood and layered wood materials

Franziska Ritschel [a,*], Andreas J. Brunner [b], Peter Niemz [a]

[a] Institute of Building Materials, Swiss Federal Institute of Technology, Zürich, Schafmattstrasse 6, CH-8093 Zürich, Switzerland

[b] Laboratory for Mechanical Systems Engineering, Swiss Federal Laboratories for Materials Science and Technology, Überlandstrasse 129, CH-8600 Dübendorf, Switzerland

Abstract

As a first step towards developing a test methodology for characterization of microscopic damage mechanisms in wood-based materials, quasi-static tensile tests were performed on simplified laboratory-scale specimens of laminated veneer lumber (LVL) or plywood and compared with solid wood. The tests were monitored by acoustic emission (AE) and digital image correlation (DIC). Evaluation of the AE and DIC data indicated distinct differences between the specimen types with respect to the time sequence of damage growth resulting in macroscopic failure. Sufficient time resolution in data recording is crucial for the interpretation of the mechanical behavior and the damage accumulation.

Keywords

Wood materials; Load tests; Damage mechanisms; Nondestructive testing; Acoustic volume methods; Optical surface methods

Introduction

Wood is an anisotropic material that is organized in a complex hierarchical structure. Parallel to the growth direction of wood, the cellulose fibers, embedded in a matrix of hemicelluloses and lignin, provide the high longitudinal strength [1]. This can be seen as analogous to fiber-reinforced polymer-matrix (FRP) composite materials. Hence, plywood and laminated veneer lumber (LVL) are composed of several layers of adhesively bonded

veneer. The fiber orientation of the individual layers of LVL and plywood has a significant impact on their mechanical properties. Layered wood-based materials show many analogies to FRP laminates, specifically, orthotropic mechanical properties and similarities in acoustic emission (AE) behavior under tensile loads [2].

Knowledge of the mechanical behavior and of the damage evolution of engineered wood-based materials is limited, especially at the microscopic scale. The present contribution deals with an approach to analyze the micromechanical damage phenomena in layered wood materials under tensile load. It focuses on the mechanisms occurring below the macroscopic scale and their interaction and accumulation leading to localized damage and, finally, to macroscopic failure. As a first step, tensile tests are performed at macroscopic laboratory scale in combination with the simultaneous monitoring of acoustic emission (AE) and digital image correlation (DIC).

Previous studies have shown the applicability of AE in studies of damage accumulation in wood (e.g., [2-4]). Further tests have explored the feasibility of combining different nondestructive testing methods for this purpose [5]. Many wood products show a good correlation between AE and DIC results in tensile tests [6].

Experimental Design

Materials and specimens

For this investigation, flawless spruce wood (*Picea abies* L. H. Karst.) was chosen, because, in comparison to hardwoods, it releases higher numbers of AE [7]. In industry, laminated veneer wood is produced from rotary-cut veneer. This investigation focuses on the two-layered materials; plywood and laminated veneer lumber (LVL). Plywood usually consists of an odd number of veneers, where the fiber orientation of adjacent veneers is directed at right angles. In contrast, the structure of LVL consists of almost no, or only a few, cross layers.

For the initial investigations presented here, the structure of plywood and LVL was simplified. The industrial production of peeled continuous veneer causes cracks oriented in the fiber direction. This type of pre-damage does not occur in specimens manufactured in the laboratory, since the spruce layers used for the wood materials were planed down from wooden planks. Analogous to the orientation of the growth rings within the rotary-cut veneer, the laminates were prepared with horizontal annual growth rings in the cross-section. To limit the complexity, the number of veneer layers was reduced to only three layers. In total, three types of sample structures were manufactured. For the laminated wood

type plywood samples, the middle layer was oriented perpendicular to the two surface layers [0°; 90°; 0°], hence the material type consisting of one cross ply in the middle is called "CP". The LVL like structured samples differ in that all three layers are oriented unidirectional [0°; 0°; 0°], accordingly they are called "UD". For comparison of AE results, samples of solid wood (SW) with a thickness of 9mm were also prepared. For the later discussion of the three materials, one representative sample of each was chosen.

Table 6.1 Physical properties of solid spruce wood (SW), laminated wood type LVL (UD) and laminated wood type plywood (CP)

Material	Orientation of the layers	n	Raw density (kg/m^3)	MC (%)	MOE (GPa)	Tensile strength (MPa)	Tensile strain (%)
SOLID	[0°]	5	445±18	9	13±0.2	89±8	0.79±0.08
UD	[0°,0°,0°]	5	566±39	9	21±2	75±12	0.40±0.06
CP	[0°,90°,0°]	5	500±27	9	11±3	68±8	0.68±0.10

n… Number of tests; MC … Moisture content; MOE … Modulus of rupture

The density of the solid spruce used to produce the different materials is about $510 \pm 53 \text{kg m}^{-3}$, thus its distribution is in the range of the wood's natural variability. There are differences in the density of the material types (Tab. 6.1). The reason for this is, firstly, the selection of the wooden lamellae for each material type. In regard to this, the challenge of manufacturing the samples is the required dimension of the clear wood lamellas due to the possible dimension of the natural grown trunk. On the other hand, the processing of the layered materials has another major impact on the material's density. The lamellae for the layered wood specimens have a thickness of 3mm. For bonding the lamellae, urea formaldehyde (in total 130g m^{-2} applied on both sides) was used as adhesive. The cold pressing was performed at a pressure of 1.8N mm^{-2} for 8h.

Specimens, according to DIN 52377 [8], were cut from the material types for the tensile tests. From each sample type five specimens were tested. Since this German standard is for tensile tests on plywood, the specimen geometry was not favored for use on solid wood samples. However, for purposes of comparison, this geometry slightly modified was also used for the solid wood samples. To avoid failure of the specimens near the clamped end (spruce wood is a very soft wood material), the clamping areas of the specimens were reinforced with semicircular pieces of hardwood (Fig. 6.1).

Experimental Setup

Investigations on AE of wood materials under various load types have shown that wood under tensile load releases high numbers of AE [9]. On this account, macroscopic tensile tests were performed (laboratory scale, in adaption to DIN 52377 [8]) with in-situ monitoring of AE and of surface deformation by DIC (Fig. 6.1).
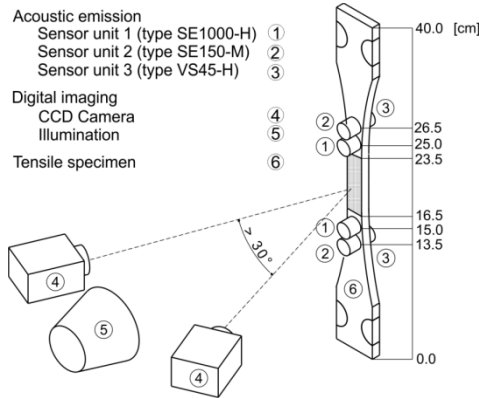

Figure 6.1 Experimental setup including specimen with coordinates of area of interest and sensor positions.

These quasi-static tensile tests were performed on an universal test machine (Zwick Roell 100) with a load cell calibrated in the load range of 100kN. The specimens were clamped mechanically with wedge grips. In all tests, load was applied under displacement control with a constant cross-head speed of 2.5mm min^{-1} until the specimen failed (defined by a load drop of -5kN ms^{-1}). The SW and the UD specimens were tensile loaded in the fiber direction. When testing the CP, the fiber-load-angle on both surface layers was 0°. Consequently, its middle layer was loaded perpendicular to fiber orientation. The machine load signals were recorded synchronously with the AE and DIC data with a time resolution of about 250ms.

The AE monitoring is a volumetric measurement method performed with digital AE equipment (AMSY6, Vallen Systeme GmbH, Germany) with a sampling rate of 10MHz. Three different types of piezoelectric sensors were used to ensure the AE detection within a broad range of frequencies: Two flat response displacement sensors (type SE1000-H, sensor unit 1), sensitive to AE from 300kHz to 1MHz, provide data for further waveform analysis. Two additional 150kHz resonant sensors (type SE150-M, sensor unit 2) allow comparison with previous tests on a wide range of materials [6]. To cover the lower frequency range, two multipurpose sensors (type VS45-H, sensor unit 3) were applied. These six sensors were

coupled to the surface of the specimens with silicone-free vacuum grease and fixed with metallic spring clamps. To avoid any influence on the synchronous image recording, all sensors were placed outside the area of interest in which the failure of the specimen was expected (Fig. 6.1). The frequency range of the preamplifiers (AEP3, gain of 34dB into 50Ω, Vallen Systeme GmbH, Germany) was limited between 30kHz to 960kHz. The rearm time was set to 3.2ms. Since the sensors detect interfering signals of various high amplitudes due to their sensitivity and are influenced by their position relative to the sample's fixture, different threshold settings were selected. Hence, the lowest threshold was $33dB_{AE}$ whereas the highest was $43dB_{AE}$, depending on the signal noise level. The conventional AE signal parameter set [10] was recorded during the test.

Before the tensile tests, simulated AE signals (i.e., Hsu-Nielsen sources [11]) were applied on the surface of the specimens to determine the average signal speed and the signal attenuation in each specimen. The determined average sound speeds of about $4100m\ s^{-1}$ to $5200m\ s^{-1}$ agree fairly well with literature values [12]. For CP, the acoustic wave speed transverse to the fiber direction is significantly lower than that in fiber direction. Hence, CP yields the lowest average value of about $4100m\ s^{-1}$.

Depending on specimen type and material composition, preliminary tests yielded different attenuation curves. Generally, it is difficult to clearly distinguish near- and far-field ranges in these curves. For all material types, a large scatter in attenuation behavior was observed for signals applied with a distance to the sensor of up to 30cm. In the tensile tests, AE is detected only at small source-sensor distances of less than 30cm. Due to the specimen dimension and the small distance between the sensors, a quantitative determination of the longitudinal attenuation characteristics of the specimens is difficult. Consistent with the preliminary tests on the specimens, an average attenuation of about $-1dB_{AE}\ cm^{-1}$ was determined for all materials.

Attenuation and average sound velocity depend on the anatomical features of the wood, e.g. fiber load angle and alignment of growth rings. In the longitudinal direction, wood fibers (tracheids) transmit elastic waves well. In comparison, the significantly lower share of ray cells is sufficient for transmitting acoustic waves in the R direction. The highest attenuation and the lowest wave speed occur in the tangential direction due to the absence of continuous structural elements [12], [13].

The DIC system is a non-contact optical method to determine surface displacements [14], [15]. The displacements and strains are computed by the cross-correlation of two images, one in a loaded and the other in the unloaded state, respectively. To enable the system to

evaluate displacement fields, a high contrast random pattern is applied on the surface of the specimens. The three-dimensional DIC equipment includes two synchronized CCD-cameras (maximum resolution of 2048x2048 pixels). This allows for the correlation of surface displacements in the three-dimensional domain. The displacements on the wide side of the specimens were monitored. During the trials the cameras of the DIC system took images at a frequency of 2Hz. The processed images had a resolution of 0.21×0.01mm pixel^{-1}. Deformation and elongation growth were analyzed with respect to the load direction.

Results and Discussion

Mechanical properties of the materials

The mechanical properties of wood and wood-based materials depend on a variety of structural features, e.g. the raw density and moisture content, fiber load angle and alignment of the growth rings, but also the history of the wood. Furthermore, wood is an anisotropic material. Consequently, with increasing fiber load angle, strength decreases.

The SW samples yield tensile strengths of 89 ± 8MPa and ultimate strains of $0.79\pm0.08\%$ (Tab. 6.1). The UD and the CP material tolerate less stress due to disruption of the naturally grown structure of wood by cutting. The UD specimens show average tensile strengths of about 75 ± 12MPa and ultimate strains of $0.40\pm0.06\%$. In contrast, as expected, the orientation of the middle layer of CP results in a reduced tensile strength of about 68 ± 8MPa, but at higher failure strain ($0.68\pm0.10\%$) compared to the UD samples. This can be traced back to the strength of wood transverse (R) to fiber orientation that is approximately $1/30$ of tensile strength parallel to fiber direction [16].
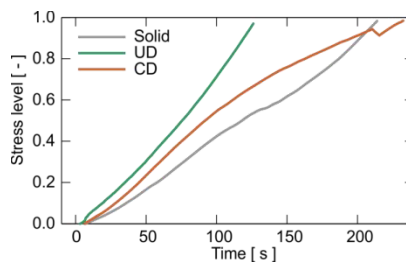

Figure 6.2 Stress levels of the selected specimen types: Solid spruce specimen, UD specimen of LVL type and CP specimen of plywood type.

For comparison purposes, the stress level of the representative specimens of SW, UD and CP is normalized by maximum load (Fig. 6.2). In the range of 10% to 30% stress level, all three specimens behave approximately linear. The test duration for the SW as well as for the CP specimen was in the same range. Changes in the plastic range are clearly visible. The

UD sample fails in a more brittle manner, it tolerates more stress per unit time and, compared to the SW and the CP sample, fails after half the test time of SW and CP.

AE activity and intensity

Damage growth in materials releases elastic energy, among others, in the form of AE. Tensile loading of the specimens showed no evidence of identifiable damage at stress levels less than 50%, but AE is already detected at very early stages of applied stress. AE signals, therefore, indicate mechanisms acting at the sub-macroscopic scale.

Table 6.2 Acoustic emission activity of solid spruce wood (SW), laminated wood type LVL (UD) and laminated wood type plywood (CP)

		Average number of cumulative AE signals per sensor unit		
		Sensor unit 1 SE 1000-H	Sensor unit 2 SE 150-M	Sensor unit 3 VS 45-H
Solid	n = 5	1001 ± 518	25857 ± 7092	51884 ± 7517
UD	n = 5	897 ± 478	6024 ± 2492	11659 ± 7051
CP	n = 5	8815 ± 2518	30182 ± 9891	47792 ± 16450

n… Number of tests;

As a first step in the AE analysis, AE activity and intensity are evaluated. AE activity is based on the number of detected single signals. AE intensity, i.e. looking at measures for the magnitude of the AE signals, provides information on the amount of energy released. The analysis takes into account all events recorded until maximum load was reached, thus also the beginning of macroscopic failure.

The AE activity of the three sensor units (Tab. 6.2) shows trends for the different specimens as follows: SW generates AE activity similar to that of CP. The AE activity of UD is comparatively lower. This correlates with the ultimate strain values (Tab. 6.1). Since AE activity also depends on test duration, it has to be considered that test duration for UD is less than for SW and CP. During testing, the first AE signals occurred at very low stress levels for all three materials (Figs. 6.3a, 6.4a, 6.5a). Of course, the start of AE activity depends on the threshold setting and on the attenuation in the material. Presumably, AE activity (and hence microscopic events) starts even earlier than detected with the specific threshold settings selected here. On evaluating the AE activity from the start of the test until the stress level of 40% is achieved, for the representative sample of UD the lowest average AE activity was detected (sensor unit 2), whereas SW and CP generated more than twice as

much. With increasing stress level, the AE activity of the UD (Fig. 6.4.a) and CP specimens (Fig. 6.5a) propagates roughly exponentially.

Furthermore, by analyzing the exponential increase of AE activity via a bi-linear approach, the location of the intersection of both straight lines can be interpreted as a "knee-point", indicating the onset of significant damage accumulation [17]. For UD and CP, this point of intersection is found at a stress level of approximately 30% to 50% of maximum load. In contrast to UD and CP, the AE activity of SW (Fig. 6.3a) increases in a roughly linear manner with test duration. This indicates a fairly constant damage evolution with time with distributed damage accumulation rather than early localization of significant damage.
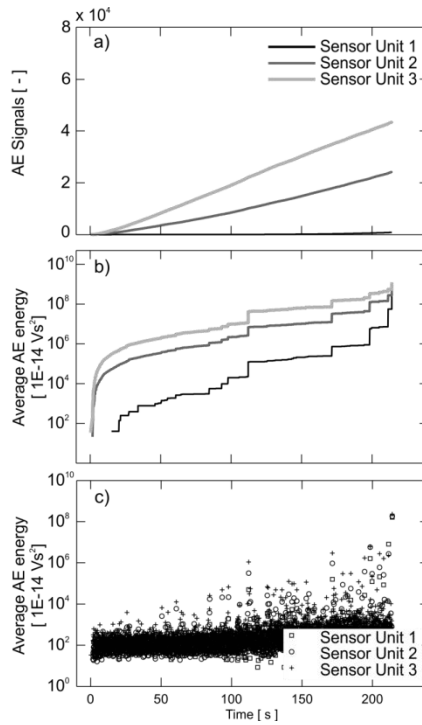
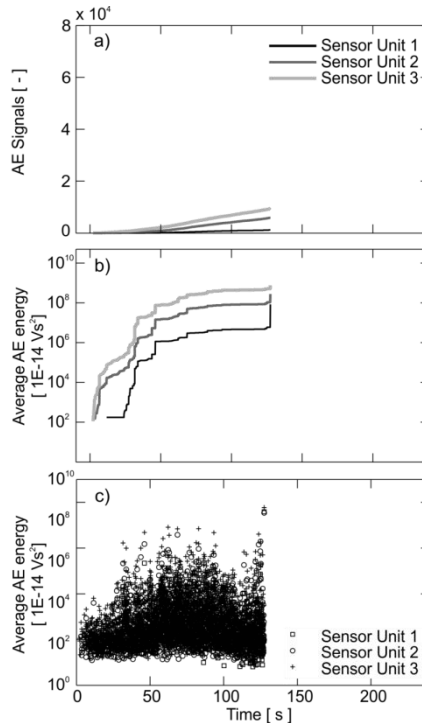
Figure 6.3 Acoustic emission of selected solid wood specimen (SW): a) AE activity, expressed in cumulative number of signals vs. test duration; b) AE intensity, expressed as cumulative AE signal energy; c) Average acoustic emission energy per event (time differential of 0.05 s) depending on the progress of the test.

Contrary to the AE activity (Figs. 6.3a, 6.4a, 6.5a), the cumulative AE intensity shows distinct, step-wise increases in AE energy that seem to occur stochastically (Figs. 6.3b, 6.4b, 6.5b), but at different times into the test for the different materials. Furthermore, the AE intensity is also expressed in terms of the average energy per event, depending on the

progress of the test duration (Figs. 6.3c, 6.4c, 6.5c). For the differential analysis, a time interval of 0.05s was chosen.

In the case of SW, step-wise increases of cumulative AE energy do not occur prior to 50% of ultimate stress (Fig. 6.3b). As soon as SW is stressed, diffuse micro cracks begin to form. With increasing load, microscopic damage phenomena accumulate and lead to the formation of flaws throughout the wooden structure of the entire specimen. Mesoscopic damage and stress distribution then yield the stepwise increase in AE energy. Although cracks pass through the cell walls in early wood, the fibers are mainly pulled apart in latewood [18] generating AE events of high energy values. Correspondingly, close to failure, average AE energy values per event (Fig. 6.3c) of more than 1E06 (in units 1E-14 V^2s) are recorded. This is consistent with the splintered fracture pattern of wood loaded parallel to the fibers (Fig. 6.8a).
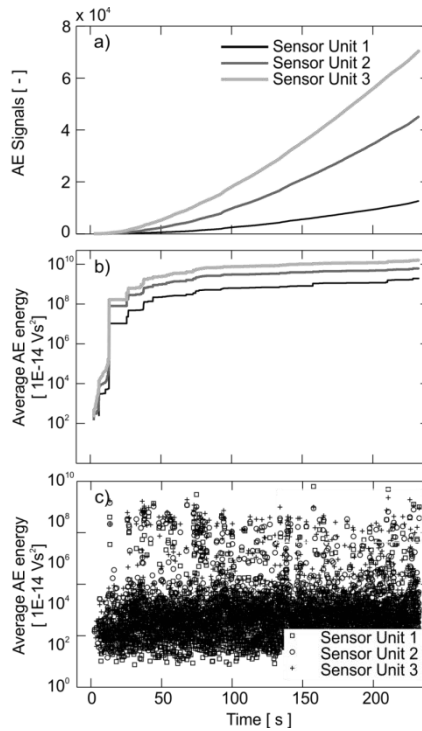

Figure 6.4 Acoustic emission of selected specimen of laminated wood type LVL (UD): a) AE activity, expressed in cumulative number of signals vs. test duration; b) AE intensity, expressed as cumulative AE signal energy; c) Average acoustic emission energy per event (time differential of 0.05 s) depending on the progress of the test.

For the tested UD sample, the cumulative AE energy (Fig. 6.4b) shows stepwise increases at lower stress levels than SW. This is substantiated by the structure function relation of its lay-

up. The Young's Modulus of UF adhesive is approximately in the same range as that of spruce wood. Since the wood cells at the interface with the adhesive are penetrated and filled by UF, these interface layers show a significantly higher modulus [19] and this results in local stiffening of the UD specimens. However, it is likely that intrinsic micro cracks exist in the UF adhesive layer already prior to load application [20]. Upon loading, damage accumulates in the wood lamellae and the adhesive layer yielding early stepwise increases in AE energy [21]. In addition to this, the AE onset in UD (Fig 6.4c) shows more variation in average energy per event than SW (Fig 6.3c). To form global flaws within the entire specimen, the crack path is forced to change to larger scales faster because of the more rigid material composition.

Figure 6.5 Acoustic emission of selected specimen of laminated wood type plywood (CP): a) AE activity, expressed in cumulative number of signals vs. test duration; b) AE intensity, expressed as cumulative AE signal energy; c) Average acoustic emission energy per event (time differential of 0.05 s) depending on the progress of the test.

For the CP, the cumulative AE energy graphs rapidly increase to comparatively high levels of E08 (in units 1E-14 V^2 s) shortly after the test was initiated (Fig. 6.5b). The average AE energy per event also yields high values (Fig. 6.5c) throughout the whole test duration for CP. This is different from SW and UD, where a limit of E07 (in units 1E-14 V^2 s) of average

AE signal energy is only exceeded at fracture. All in all, the high AE intensity in the CP is combined with high AE activity. The observed AE intensity is consistent with significant damage in the cross layer, even at low applied stress levels due to the low strength perpendicular to the fiber direction. At the interface between the layers oriented parallel and normal with respect to the loading direction, shear mechanisms (typically rolling shear [22]), delamination [23] and inter-cellular damage (matrix cracks) [24] occur. Macroscopic failure then evolves from this combined mesoscopic damage, yielding a roughly exponential increase in AE activity up to fracture (Fig. 6.5a).
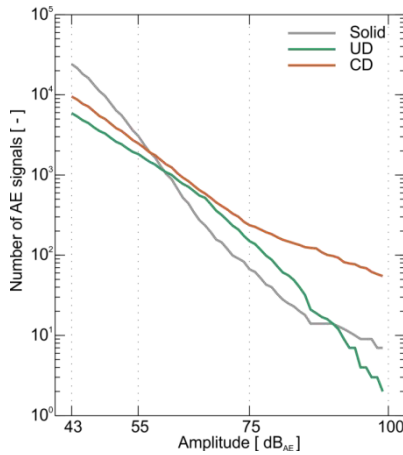
Figure 6.6 Peak amplitude distribution of AE signals detected by the sensor type SE150-M (sensor unit 2) for the three selected samples of solid spruce wood (SW), laminated wood type LVL (UD) and laminated wood type plywood (CP).

Following an approach originally developed in geophysics [25], the AE intensity data (detected by sensor unit 2) are plotted as amplitude distribution, i.e., number of AE signals as a function of the peak AE signal amplitude (Fig. 6.6). Therefore, the range of amplitudes is limited by the threshold setting ($43dB_{AE}$) and the maximum dynamic range of the AE equipment ($100dB_{AE}$). The amplitude distribution of the three representative specimens roughly follows a decreasing linear trend with increasing amplitudes. The absolute value of the slope of these curves is defined by the b-value. Independent of the absolute number of signals recorded, a high b-value, i.e., a steep slope, indicates a higher relative share of AE signals with low amplitudes in the data set. Empirically, the relative shares of low, medium and high amplitude AE signals can be correlated with respective amounts of microscopic, mesoscopic and macroscopic damage that occurred during testing.
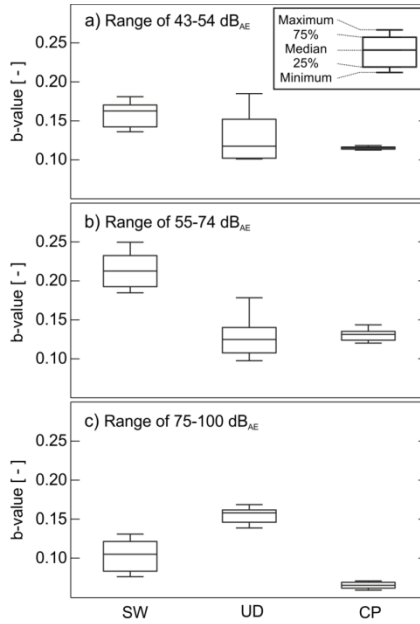
Figure 6.7 b-values of solid spruce wood (SW), laminated wood type LVL (UD) and laminated wood type plywood (CP) at different amplitude ranges: a) 43-54dB$_{AE}$, b) 55-74dB$_{AE}$, c) 75-100dB$_{AE}$. The evaluation focuses on the peak amplitude distribution of AE signals detected by the sensor type SE150-M (sensor unit 2) and is based upon five datasets for each sample type.

In the analysis presented here, the b-value is calculated and averaged for three amplitude ranges (43-55dB$_{AE}$, 55-75dB$_{AE}$, 75-100dB$_{AE}$) for each specimen (Fig. 6.7). Average b-values and their standard deviation are distinctly different for the different materials in the three amplitude ranges. The relatively high b-value (b=0.21±0.02) for SW in the range of 55dB$_{AE}$ to 74dB$_{AE}$ (Fig. 6.7b) compared to those of UD (0.13±0.03) and CP (0.13±0.01) implies a higher number of damages mechanisms acting at the microscopic scale [26]. For the CP, there clearly is a higher relative share of large amplitude AE signals and hence a higher relative number of damage mechanisms yielding a larger scale AE energy emission. The b-values for UD are similar to those of CP in the lower two amplitude ranges, but clearly higher for the highest amplitude range (75-100dB$_{AE}$).

The differences between the three specimen types shown by the amplitude distribution and b-value analysis reflect the morphology and lay-up of SW, UD and CP. For SW, damage mechanisms act over the entire volume of the specimens resulting first in distributed local micro-damage. With increasing load and continued accumulation of microscopic damage, micro-cracks start to coalesce into mesoscopic and, later, into macroscopic cracks that finally lead to macroscopic failure. The inherent variability in the properties of solid wood

result in a roughly similar standard deviation for the SW b-values in the three amplitude ranges.

For CP type specimens, the b-values are low in all three amplitude ranges, and the standard deviations are significantly lower than for the other specimen types. The corresponding relatively high share of larger amplitude AE signals is consistent with the occurrence of greater damage (also indicated by the high average AE energy per event, see Fig. 6.5c) throughout the test.

The morphology of CP with a fiber orientation of the center layer normal to the loading direction, and hence lower strength in that layer, already induces significant damage in the cross ply in the early stages of tensile loading. With increasing load and significant damage in the center layer, damage mechanisms then start acting in the outer layers and the adhesive with progressive damage until macroscopic failure. This damage sequence seems to be very reproducible as shown by the very low standard deviation of the average b-values. Intrinsic variability of wood (and maybe adhesive) properties only plays a minor role at best.

UD specimens show low b-values and large standard deviations in the lower amplitude ranges of the distribution (Fig. 6.7a, b), but also the highest b-value of all specimen types, however with low standard deviation, for the highest amplitude range (Fig. 6.7c). This can be explained by the lay-up interplay, all layers of fibers oriented parallel to the loading direction and adhesive layers, as well as the effect of the inherent variability of wood properties. Compared with SW the damage is limited in size to some extent by the three-layer morphology and results in the lowest relative share of large amplitude AE signals (75-100dB$_{AE}$).

The different behavior observed among the three specimen types (SW, UD, CP) by AE activity and intensity analysis shows that AE is well suited for investigating and discriminating damage accumulation from a variety of microscopic damage events in wood materials. Furthermore, it provides a basis for a consistent sequence of damage progression (from microscopic, mesoscopic to macroscopic) under quasi-static tensile loads. Specifically, the complex interaction between morphology (lay-up and microscopic wood structure) and inherent variability of wood properties is clearly reflected in the AE data.

Strain field distribution by DIC

The development of strain fields corroborates the interpretation of the AE data and the related damage progress for the different materials. For all three sample types, the start of the load application induces diffuse singular strain fields that appear on the entire specimen

surface within the observed area. The diffuse points of small deformation indicate micro mechanisms at the surface of the specimens (within the wooden structure). With further test progress, strain formation differs for SW, UD and CP.

For SW, with increasing load (>50% of the ultimate stress) these initial diffuse flaws extend further (Fig. 6.8a). Subsequently, at stress levels of more than 70%, localized regions of higher strains than their surrounding area, appear and clearly reoccur. This is the state from which damage accumulation and interaction take the path of least resistance leading to ultimate failure.
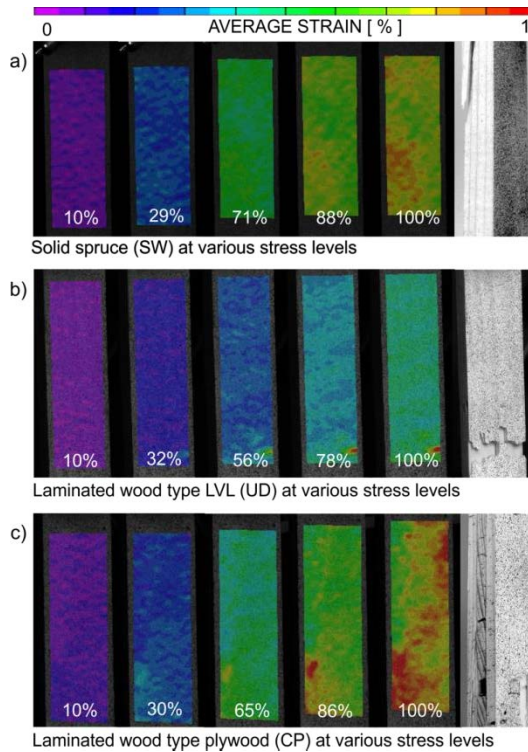
Figure 6.8 Sequences of the progress of strain distribution until failure for the selected specimen a) solid spruce wood (SW), b) laminated wood type LVL (UD) and c) laminated wood type plywood (CP) at different stress levels (%). The ultimate failure is located between 20-26cm of the specimen's longitudinal axis.

In the case of UD, the occurrence of diffuse strain fields (Fig. 6.8b) is followed by the rapid development of a more balanced strain field with increasing load. This process is repeated several times up to a load range of about 70%. The reappearance of the diffuse strain points mostly relates to the step wise increases in the cumulative AE energy. Bearing in mind the limited observation area on only one surface layer of the UD specimens, appearance and

disappearance result from the damage accumulation and the interaction in the three single wooden layers and the adhesive. Shortly before failure, localized dominating deformation patterns reappear, surrounded by simultaneously shifting strain fields and changing strain points. Fortunately, for the UD specimen presented here (Fig. 6.8b), the weakest point leading to ultimate failure is on the observed surface layer. Already at 30% of failure load, this region of damage accumulation is indicated by the strain field distribution. In this case the interaction of the lay-up becomes slightly less clear, but is still perceptible. However, by means of the strain field distributions, a prediction of the failure location was intrinsically not possible for the SW as well as for the UD samples.

While the diffuse pattern of strain formation of the CP specimens persists (Fig. 6.8c), at about 30% of failure load, regions of higher strain start to form and become localized. This deformation development at low stress is evidence of damage perpendicular to the load axis in the center layer of the specimen. Further, with increasing stress (more than 50%), these localized regions of higher strain values remain, whereas the surrounding diffuse strain pattern extends and develops more coherent areas. This is an indicator of the increasing importance of the surface layers stressed parallel to the fibers for damage progress. A prediction of failure location for the CP material is hence possible by the strain field distribution.

Comparison of the AE and DIC analysis

AE and DIC yield complementary information, mainly due to their characteristic as volumetric (AE) and surface method (DIC). Furthermore, AE is more sensitive than DIC to microscopic mechanisms and events. DIC, on the other hand, yields information on the (surface) location of significant strain concentrations.

The analysis presented and discussed so far clearly shows that both layered wood materials, UD and CP, differ significantly in their damage behavior and failure from SW. This is evident from, for example, the amplitude distributions (Fig. 6.6) and the b-values (Fig. 6.7). However, there is also clear evidence for different damage accumulation between UD and CP. In the early stages of tensile loading, CP yields on average clearly higher AE energies per event than SW and UD. Typically for CP, more than 80% of the total cumulative energy (including that emitted during macroscopic failure) is recorded during the first 40% of applied stress. High energy bursts are clearly more frequent in CP than in SW and UD material (Figs. 6.3c, 6.4c, 6.5c). Looking at the DIC (Fig. 6.8) data from the late stage of the tensile test, DIC shows clear evidence for different strain distributions between UD and CP.

Combining this information, it can be concluded that number and magnitude of microscopic events from AE differ between UD and CP, starting already at low stress levels. However, a precise prediction of failure location was not possible (neither by DIC nor AE monitoring). The DIC analysis of CP material shows evidence of significant damage much earlier than SW. The strain distribution indicates the localized area of damage accumulation with high strains several seconds before macroscopic failure.

Conclusion and outlook

The combination of acoustic emission (AE) and digital image correlation (DIC) data from tensile tests on three different types of wood materials clearly indicate different patterns of damage initiation and accumulation leading to macroscopic failure. The specimen types were solid wood (SW), a simplified type of laminated veneer lumber (UD) and an analogous simplified type of plywood (CP).

Compared with SW, damage initiation and accumulation in UD and CP under quasi-static tensile loads is affected by the layered structure and the adhesive bonds, as well as by the relative fiber orientation in the layers. CP yields significant early damage on the mesoscopic, and maybe even macroscopic scale in the center cross-ply. In UD, significant damage starts later than in CP, but earlier than in SW. This is mainly shown by AE intensity, i.e., average AE signal energy per event and the cumulative AE energy curves as a function of time. Analysis of AE signal amplitude distributions (again a measure of AE intensity and related to the damage size) in terms of the so-called b-value indicated that the layered morphology of the UD and CP specimens yielded a larger share of higher amplitude signals compared with SW. This correlates with localized damage on the mesoscopic and maybe even macroscopic scale, occurring relatively early at stress levels below 50% in the layered specimens, which then evolve into macroscopic fracture. The findings for SW are consistent with a fairly continuous damage evolution in which microscopic damage mechanisms acting throughout the volume of the specimens coalesce into mesoscopic and finally macroscopic damage, ultimately leading to fracture.

As an outlook, it can be noted that the tensile tests on simplified specimen types presented in this paper would be complemented by tests on plywood specimens from industrial production in the near future. This is expected to yield information on the effects of damage present in the specimens from the industrial veneer cutting and manufacturing process. The damage mechanisms will be further investigated by combining AE with microscopic techniques on smaller specimens. The insights gained from these investigations may, in the future, also prove beneficial for improving fiber-reinforced polymer (FRP) matrix laminates

and making them more damage resistant by transferring morphological features from wood to FRP in a biomimetic approach.

Acknowledgement

References

[1] Wiedenhoeft A. Structure and Function of Wood. In: Ross RJ. Wood HandBook: Wood as an Engineering Material. Madison: Forest Products Laboratory, 2010.

[2] Ansell MP. Acoustic Emission from Softwood in Tension. Wood Science Technology 1982; 16: 35-58.

[3] Debaise GR, Porter AW, Pentoney RE. Morphology and Mechanics of Wood Fracture. Materials Research and Standards 1966; 6: 493-499.

[4] Dill-Langer G, Ringger T, Höfflin L, Aicher S. Location of Acoustic Emission Sources in Timber Loaded Parallel to Grain. In: Spectroscopic Techniques, Proceedings of the 13th International Symposium on Nondestructive Testing of Wood, Berkeley, 2002.

[5] Niemz P, Brunner AJ, Walter O. Investigation of the Mechanisms of Failure Behavior of Wood-based Materials Using Acoustic Emission and Image Processing. Wood Research 2009; 54(2): 49-62.

[6] Brunner AJ, Niemz P, Walter O. Damage Accumulation and Failure of Different Types of Wood-panels under Tensile Loading. In: Proceedings of American Society for Composites 22nd Annual Technical Conference, Seattle, 2007. CP-ROM Paper No. 13.

[7] Reiterer A, Stanzl-Tschegg SE, Tschegg EK. Mode I Fracture and Acoustic Emission of Softwood and Hardwood. Wood Science and Technology 2000; 34: 417-430

[8] DIN 52377. Prüfung von Sperrholz. Bestimmung des Zug-Elastizitätsmoduls und der Zugfestigkeit. Berlin: Deutsches Institut für Normung e.V. , 1978.

[9] Niemz P, Lühmann A. Application of the Acoustic Emission Analysis to Evaluate the Fracture Behavior of Wood and Derived Timber Products. Holz als Roh- und Werkstoff 1992; 50(5): 191-194.

[10] Shiotani T. Parameter Analysis. In: Grosse CU, Ohtsu M. Acoustic Emission Testing. Berlin Heidelberg: Springer-Verlag, 2008.

[11] Moore PO. Nondestructive Testing HandBook: Acoustic Emission Testing, 3rd ed., Vol. 6. USA: American Society for Non-destructive Testing, 2005.

[12] Bucur V. Acoustics of Wood. Berlin: Springer, 2006.

[13] Keunecke D, Sonderegger W, Pereteanu K, Lüthi T, Niemz P. Determination of Young's and Shear Moduli of Common Yew and Norway spruce by Means of Ultrasonic Waves. Wood Science and Technology 2007; 41(4): 309-327.

[14] Luo PF, Chao YJ, Sutton MA, Peters WH. Accurate Measurement of Three-dimensional Deformations in Deformable and Rigid Bodies Using Computer Vision. Experimental Mechanics 1993; 33(2): 123-132.

[15] Lord JD, Roebuck B, Morrell R, Lube T. Aspects of strength and strain measurement in miniaturised testing for engineering metals and ceramics. Material Science Technology 2010; 26: 127-148.

[16] Niemz P, Caduff D. Research into determination of the Poisson ratio of spruce wood (Original in German). European Journal of Wood and Wood Products 2008; 66(1): 1-4.

[17] Mitchell JR. Standard Test to Quantify the Knee in the AE versus Load Curve as a Material Parameter for Composites. In: Proceedings 3rd International Symposium on Acoustic Emission from Composite Materials (AEMC-3), Paris, July 1989. p. 207-219.

[18] Aicher S, Dill-Langer G. Monitoring and Localization of Damage Evolution in Wood. In: Busse G, Kröplin B-H, Wittel FK. Damage and its Evolution in Fiber Composite Materials: Simulation and Non-Destructive Evaluation. Stuttgart: ISD Verlag, 2006. p. 263-281.

[19] Stöckel F, Konnerth J, Kantner W, Moser J, Gindl W. Tensile shear strength of UF- and MUF-bonded veneer related to data of adhesives and cell walls measured by nanoindentation. International Journal of the Biology, Chemistry, Physics and Technology of Wood 2012; 66(6): 337–342

[20] Hass P, Wittel FK, Mendoza M, Herrmann HJ, Niemz P. Adhesive penetration in beech wood: experiments. Wood Science and Technology 2012; 46: 243-256.

[21] Gozdecki C, Smardzewski J. Detection of failures of adhesively bonded joints using the acoustic emission method. International Journal of the Biology, Chemistry, Physics and Technology of Wood 2005; 59: 219-229.

[22] Dahl KB, Malo KA. Nonlinear shear properties of spruce softwood: experimental results. Wood Science and Technology 2009; 43: 539-558.

[23] Bucur V. Delamination in Wood, Wood Products and Wood-Based Composites. Springer, 2011.

[24] Bodig J, Jayne BA. Mechanics of Wood and Wood Composites. Malabar: Krieger, 1993. p. 4-31.

[25] Rao MVMS, Prasanna Lakshimi KJ. Anlaysis of b-value and improved b-value of acoustic emissions accompanying rock fracture. Current Science 2005; 89: 1577-1582.

[26] Enescu B, Ito K. Spatial analysis of frequency-magnitude distribution and decay rate of aftershock activity of the 2000 Western Tottori earthquake. Earth Planets Space 2002; 54: 847-859.

6.2 Paper II

Acoustic emission analysis of industrial plywood materials exposed to destructive tensile load

Franziska Ritschel [(1)], Yang Zhou [(2)], Andreas J. Brunner [(3)], Thomas Fillbrandt [(2)], Peter Niemz [(1)]

[(1)] Institute of Building Materials, Swiss Federal Institute of Technology, Zürich, Schafmattstrasse 6, CH-8093 Zürich, Switzerland

[(2)] Chair of Forest Utilization, University of Freiburg, Freiburg i.Br., Werthmannstraße 6, DE-79085 Freiburg i.Br., Germany

[(3)] Laboratory for Mechanical Systems Engineering, Empa, Swiss Federal Laboratories for Materials Science and Technology, Überlandstrasse 129, CH-8600 Dübendorf, Switzerland

Abstract

Several plywood materials made from spruce wood and, for comparison, solid spruce wood were investigated focusing on the sub-macroscopic damage evolution during tensile loading of the specimens. The destructive tests were simultaneously monitored by the acoustic emission (AE) method and strain field deformation measurement using digital image correlation (DIC). The bilinear interpretation of exponential defect growth identified the start of significant nonlinear behavior at 70 % of ultimate strength for all plywood materials. However, already the preceding and more stable damage evolution at lower stress levels has indicated a variation in intensity of the source mechanisms evaluated by AE energy of the detected events. Additional information on the formation of strain field concentration, which correlates with discrete accumulation in AE events and increased spreading in the distribution of AE energy, reveals the complexity of pre-damage due to the variation in cracks' magnitude and timescales involved. The correlation between ultimate tensile strength and damage accumulation below 70 % of ultimate strength is determined, as well as the influence of layered structures on damage size shown by the percentage distribution of AE energy.

Introduction

Characterization of damage evolution in wood is a challenge even today. Numerous failure mechanisms have already been extensively documented, especially from various structural elements and load cases. However, since several length scales are involved, such as those introduced by the chemical constituents, cell wall structures, the composition and arrangement of cell types at the microscopic level and also the annual rings at the mesoscopic scale, the complexity of damage progress in wood is hardly traceable (Kollmann 1961; Smith et al. 2003).

Moreover, in the case of wood-based products, such as those studied in the present contribution, the investigated plywood materials, with their layered structure of bonded veneers, induce additional mechanisms at the mesoscopic and macroscopic dimensions. This entails having to analyze the layered material as a continuum matter, while concurrently focusing on its sub-macroscopic structure-function relation (Ivanov and Sadowski 2009). Therefore, one of the most suitable methods is acoustic emission (AE) analysis, because of its sensitivity to elastic waves that have been caused by structural changes at several length scales. Thus, the measurement of AE facilitates multi-scale information on damage progress covering almost the whole specimen volume (Scruby 1987; Beall 2002; Grosse and Ohtsu 2008).

Studies on wood failure using the AE method have already substantiated its nonlinear progress. Furthermore, crack initiation and accumulation, due to load application, have been analyzed for several wood species with respect to the fiber orientation (Debaise et al. 1966; Ansell 1982; Reiterer et al. 2000; Aicher et al. 2001; Ando et al. 2006; Bucur 2006) as well as for several wood-based products (Dunlop 1980; Vun et al. 2005; Brunner et al. 2006; Niemz et al. 2009). Since it is well known that tension loading of wood generates a high degree of AE (Niemz and Lühmann 1992), the present destructive investigations on plywood were performed by tensile loading applied parallel to the grain orientation of the face veneers. However, since the most crucial issue concentrates on the interpretation of AE parameters, additional measurements, such as optical methods, are needed. For that reason, the AE measurement is combined with the digital image correlation (DIC) monitor on one of the face veneers. This method provides additional information on the materials' behavior by evaluation of the strain field formation (Valla et al. 2010), also revealing indirect information about the underlying plies. In conclusion, the monitoring of tensile tests simultaneously by AE and DIC yields a detailed description of damage evolution due to the

layering up of several plywood materials and, by means of a comparison with solid wood, further information is derived.

The present study focuses on the characterization of damage progress of plywood materials during tensile load by taking a closer look at the following issues:

- The onset and the accumulation of defects at microscopic scale.
- The changeover from microscopic mechanisms to pre-damage events at larger scale leading to ultimate failure.
- The dynamic in damage increase in terms of defect growth rates.
- The impact of the layered structures (regarding grain orientation of the veneers) on the linear and non-linear failure behavior.
- The link between the occurrence of damage events prior to failure and the ultimate tensile strength.

Therefore, the AE activity is analyzed as a function of progressive strain and applied stress level. Furthermore, the individual damage events and mechanisms at several length scales and their interaction are focused on in more detailed by AE energy and complementary DIC analysis.

Material

The present investigation was carried out on several commercial plywood materials with differently layered structures. The basic constituents are the same: industrially produced rotary-cut veneers of spruce glued together with phenol resin (water boiled proofed). Altogether, 3-layered and 5-layered plywood materials (EN 14272 2011) consisting of three to six veneer plies (designated as plywood types 3-6), each of 3 mm thickness, were tested (Fig. 6.9). Plywood type 3 consists of three layers, whereas the grain of the core ply is oriented perpendicular to the surface layers. The basic layer structure of plywood type 4 is similar to that of plywood type 3, but its core contains an additional cross grained ply (DIN EN 313-2 1999) (Fig. 6.9). Analogous to the plywood type 3, the structure of plywood type 5 includes an odd number of veneers. Its core layer is oriented long grained, embedded in adjoined cross-plies. Plywood type 6 contains a double core of long grained plies compared to plywood type 5. In accordance with EN 14272 (2011), plywood type 3 and type 4 are regarded as 3-layered plywood materials, whereas plywood types 5 and 6 are defined as 5-layered plywood material (Fig. 6.9).
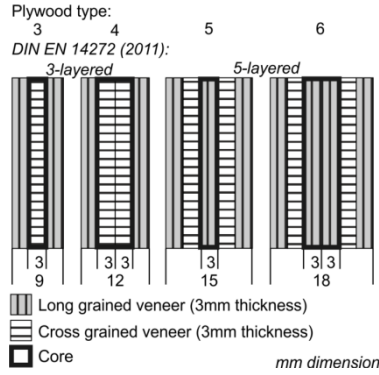
Figure 6.9 Layered structures of investigated plywood materials differentiated by their core lay-up
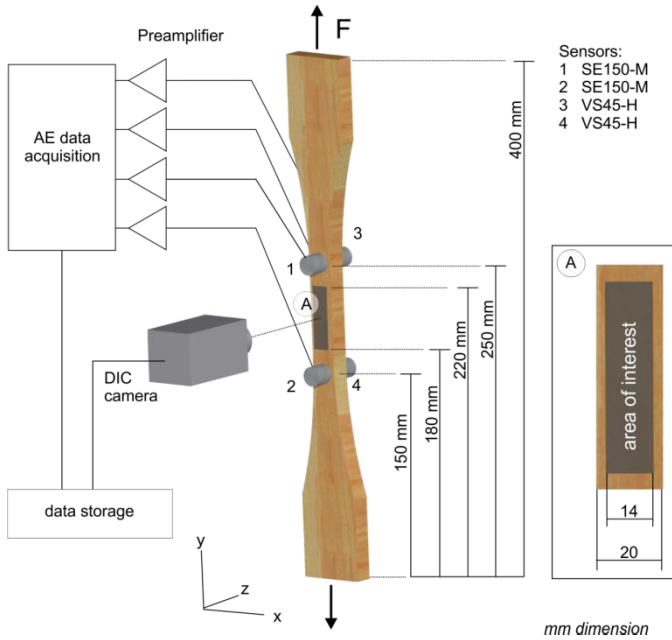

Figure 6.10 Schematic of the experimental setup

The specimens (Fig. 6.10) were prepared in accordance with the German standard DIN 52377 (1978) for tensile tests on plywood. Tensile load is applied parallel to the grain orientation of the face layer. Moreover, specimens of the same geometry (with a thickness of 9 mm) were made of flawless solid spruce wood (*Picea abies* L.) for purposes of comparison. Overall, eight samples of each material type were tested, which is considered a minimum sample number regarding the natural variation in wood. Nevertheless, eight samples facilitate ranking the materials properties and obtaining sufficient information on

damage evolution for each sample (Fig. 6.11a). However, it has to be taken into account that the plywood materials are not of the same stock as the solid wood material.
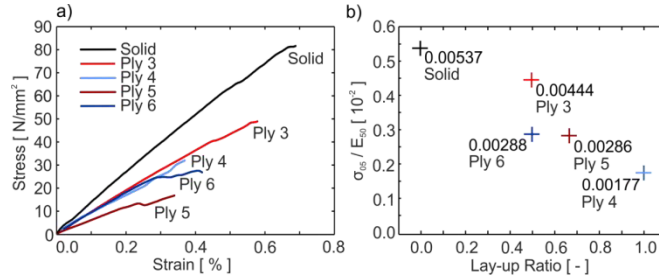
Figure 6.11 a) Average stress-strain graphs of the investigated specimens made of several plywood materials and of the solid spruce wood specimens. b) Relation between the lay-up ratio (share of the cross grained layers to share of the long grained layers) and the low ratio of stress (5%-quantile) to Young's Modulus (50%-quantile) of the tested material samples.

Table 6.3 Characterization of the investigated material samples.

	N	Structure Lay-up ratio [-]	T [mm]	Raw density [kg/m³]	MC [%]	MOE [GPa]	Tensiles trength [MPa]	Ultimate Elongat. Strain [%]
Ply 3	3	I – I 0.5	9	500 (3)	7.2	9.6 (14)	51 (11)	0.58** (17)
Ply 4	4	I – – I 1	12	464 (4)	7.2	9.0 (25)	29 (28)	0.37 (30)
Ply 5	5	I – I – I 0.67	15	419 (1)	7.1	5.6 (34)	18 (19)	0.34 (32)
Ply 6	6	I – I I – I 0.5	18	435 (3)	7.2	8.0 (40)	30 (10)	0.42 (23)
Solid	1	I 0	9	400 (3)	8.6	13.5 (10)	87 (11)	0.69 (16)

N...Number of wooden layers; T...Original thickness before planing down by 0.5 mm per surface, each veneer of 3 mm thickness; MC ... Moisture content; MOE ... Modulus of elasticity.

*Mean Value (Variation Coefficient [%]), no. of Samples n=8, ** n=7*

Due to the materials' varying origin and history, there are differences in their densities (Tab. 6.3). Hence, the correlation of increasing strength with increased raw density applies to plywood, but the solid wood has to be regarded separately. Just for validation, it can be noted that the mechanical properties (Tab. 6.3) of the tested solid wood specimens correspond to those reported by several references (e.g., Wagenführ 2000).

Since the selection of the commercial plywood panels was made arbitrarily, more precise information on processed raw material cannot be provided. Therefore, a validation of the

material samples is given by the ratio of the tensile strength (5%-quantile) to the Young's Modulus (50%-quantile) estimated from the tensile tests. Thereby, the material samples are characterized by the lower ratio of the material's ultimate strength and elastic behavior. Obviously, the correlation between this ratio and the lay-up ratio (defined as the number of cross grained plies divided by the number of long grained plies) shows the influence of the cross grained plies in relation to the material's total thickness (Fig. 6.11b).

Regarding the final tensile strength parallel to the board orientation (long grain), the cross grained plies of course have no significant impact on this characteristic property value of the plywood product (EN 14272 2011). Since the present investigation focuses on preceding multi-scaled damage evolution, the ratio of the weak cross-grained plies within the cross section of the specimens is not negligible and thus is taken into account by the layup ratio divergent from the calculation of the thickness to layer ratio proposed by Plath (1974). The quality of the un-planed plywood panels, only defined by the grade of the face veneers, is assigned to class III/III (DIN 68705-2 2003) due to present open defects such as knots and lathe checks. The plywood specimens as well as the solid wood specimens were planed down by 0.5mm each to create smoother surfaces, in order to improve the coupling of AE sensors to the specimens.

Methods

For quasi static tensile tests, the specimens were fixed in the universal test machine (type Zwick Roell, load cell calibrated to 100 kN) with mechanically self-tensioning clamping grips. Stress was applied under displacement control with a constant crosshead speed of 2.5mm/min until the specimen failed (defined by a load drop of at least -5kN/ms).

The AE measurements were performed with digital AE equipment (type AMSY-6, Vallen Systeme GmbH, Germany) using a sampling rate of 5MHz. The rearm time was set to 1ms, and the recording of the AE signals was performed with a resolution of 4096 samples per set including 200 pre-trigger samples. In each case, two multipurpose sensors of type VS45-H were used, characterized by a relatively flat response displacement in the range of low frequencies between 20kHz up to 200kHz, and two 150kHz resonant sensors of type SE150-M, which are sensitive in the range of 150kHz to 450kHz (Fig. 6.10). The sensors were coupled to the planed surfaces of the specimens with silicone-free vacuum grease and fixed with metallic spring clamps. Prior to acquisition, the AE signals were amplified by an AEP3 preamplifier (AEP3, gain of 34dB into 50Ω, Vallen Systeme GmbH, Germany) and were limited by a (digital) band-pass filter of 30kHz to 960kHz. The threshold was set to the minimum noise-free level 43dB$_{AE}$. Noise signals from the grips were excluded by means of

two additional guard sensors coupled to both specimen clamps on the testing machine. The AE analysis includes only AE signals (first hit of AE event) recorded prior to the macroscopic failure.

Deformation measurement was performed by the non-contact optical method of two-dimensional DIC. Therefore, during the tensile tests, the area of interest on one wide side of each specimen (Fig. 6.10 detail A) was monitored with a CCD camera (maximum resolution of 2048x2048 pixels). The images were taken at a frequency of 2Hz. Specimens were illuminated by means of a diffuse white-light source. However, to enable full field strain and displacement field measurements, a high contrast random pattern was applied to the surface of the specimens by air-brushing. Displacements, strains and shear were post-processed by the cross-correlation of a subset in the undeformed image mapped to the corresponding subset in a deformed image. The processed images have a resolution of 0.12±0.01mm/pixel. The evaluation focuses predominantly on the strain field formation with respect to the load direction (e_{yy}). Additionally, shear (e_{xy}) was also considered. Both nondestructive methods, AE and DIC measurements, were synchronized by the load signal output of the testing machine.

Results and discussion

Mechanical properties and fracture patterns

First, the several tested (layered) wood materials are regarded as a homogeneous material. Therefore, their mechanical behavior at the macroscopic scale is determined by the stress-strain curves (Fig. 6.11a). Until shortly before failure, the plywood materials type 3-5 consisting of three, four or five veneers behave in a quasi-brittle manner, just like the solid spruce wood specimens. In contrast, the plywood type 6 shows a distinct plastic deformation at large stresses.

The Young's Moduli of the plywood types 3, 4 and 6 are of similar level at 8-10GPa (Tab. 6.3), whereas the plywood type 5 has the lowest Young's Modulus of <6GPa. Obviously, the highest stiffness is determined for the solid specimens with an averaged Young's Modulus higher than 13GPa (Tab. 6.3). The variation coefficient of the Young's Modulus, which increases with every additional layer in the plywood structure, points to the more complex elastic behavior of the multilayered structures. Certainly, layered structures of more plies degrade the ultimate strength of the final plywood product (Kufner 1966). Accordingly, of all the tested plywood types, type 3 shows the highest strength of approximately 50MPa, and ultimate strains of almost 0.6% (Tab. 6.3). However, in contrast

to the elastic behavior of plywood, the ultimate strength linked to fracture formation at the macroscopic scale correlates with the lay-up ratio of the number of cross grained plies to that of long grained plies within the plywood's structure. For plywood types 3 and 6, which contain one half long grained plies as cross grained plies (lay-up ratio of 0.50), the variation coefficients of ultimate strengths and strains are lower than that of plywood type 4 (layup ratio of 1.00) and type 5 (layup ratio of 0.67). Thus, the increasing share of cross-plies within the layup section provokes variation in failure behavior.

Since the layered structures are exposed to complex loads and hence, in addition to elongation, shear behavior is also involved (Keylwerth 1954; Norris et al. 1961). However, the averaged results of shear strain of the face veneers are not evident, since the shear strain of the rotary peeled veneers is mainly influenced by the defined growth ring edges on the longitudinal-tangential plane.
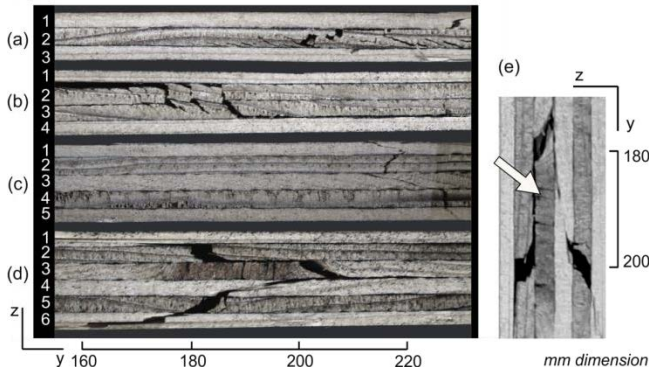
Figure 6.12 Exemplary fracture patterns of plywood type a) 3, b) 4, c) 5 and d) 6 that has been exposed to tension. e) Knot in the core layer of plywood type 6 specimen (indicated by arrow).

In all tested plywood samples, several types of damage occur that are characteristic for plywood (Fig. 6.12). The final fracture of the plywood specimens passes through several layers, irrespective of their grain orientation, but it does seem to depend on a number of structural features, such as grain orientation among others, and intrinsic flaws or the grade of adhesive layers (Vassiliou 1996). The degraded glue lines and especially the damaged interfaces of the bonded plies lead to delamination and separation of the adjacent veneers. This was preceded by crack propagation in the cross-grained veneers, formed by shearing the wood structure normal to the grain orientation (Görlacher 2002), where the alignment of growth rings as well as the grain orientation of the enclosing layers plays a role. Hence, cracks opened in the longitudinal-radial (LR) plane and cavities of various sizes were

created in the R plane. Also the fractured layers with longitudinal grain orientation show shear failures due to the position of the interface of early and latewood.

The damage development of plywood types 3 and 4 are dominated by cracks within their cross plies, entailing flaws within the associated bond line interfaces, which are mainly caused by rolling shear. Compared to the damage in plywood type 3 (Fig. 6.12a veneer 2), the crack lengths in the cross-grained layers of plywood type 4 are longer due to its double cross-grained core (Fig. 6.12b veneers 3 and 4). The most stressed layer in plywood type 5 is its long grained core layer (Fig. 6.12.c veneer 3). Hence, rolling shear within the cross layers (Fig. 6.12c veneers 2 and 4) occurred mainly close to the inner bond lines. The fracture of the presented specimen continues by shear and tension failure of the core ply (Fig. 6.12c veneer 3). The presented specimen of plywood type 6 (Fig. 6.12d) shows the most complex failure path, where all damage mechanisms described above occurred, but of even larger size. Compared with plywood type 5, the double long grained core of plywood type 6 is stiffer. Besides, one core layer (Fig. 6.12d veneer 3) includes an additional flaw in the form of a knot (Fig. 6.12e), inducing the surrounding crack path formation.

Acoustic emission activity and knee point evaluation

Since macroscopic failure is preceded by crack initiation and accumulation at the microscopic and mesoscopic scale, analyzing the results from AE measurements gives additional information about the damage evolution within the tested plywood structures. For this reason, the AE analysis is limited to AE events preceding the macroscopic failure and ending with an AE signal linked to the highest stress value of the tensile test.

To quantify the damage, the AE activity is summarized by the cumulative numbers of detected AE events. In comparison to the tested plywood samples, the solid wood specimens generated the highest number of AE events (Tab. 6.4). Specimens of the plywood type 6 solely showed an AE activity of approximately the same amount. For plywood type 3, even though its specimens have the same physical dimension as the solid wood specimens, only half the AE activity of that for solid wood was measured. Besides the fact that glued wooden structures generally generate a lower number of AE events than solid wood (Gozdecki and Smardzewski 2005), the intrinsic pre-damage due to industrial production of plywood is also of relevance. In particular, lathe checks have already led to a prior release of the material's elastic energy during veneer processing. The AE activity monitored by the two different sensor types (Tab. 6.4) is almost the same (Harris and Dunegan 1974).

Table 6.4 Acoustic Emission activity and energy of the investigated materials.

	AE Cumulative Activity [a]		AE Cumulative Energy *	
	SE150-M	VS45-H	SE150-M	VS45-H
Ply 3	6.2 ± 2.8	7.0 ± 2.7	1.5 (62)	2.6 (57)
Ply 4	5.2 ± 3.8	3.7 ± 2.2	1.2 (60)	1.0 (67)
Ply 5	4.0 ± 2.2	4.5 ± 2.6	0.7 (72)	1.2 (86)
Ply 6	11.1 ± 4.7	13.9 ± 5.7	2.2 (61)	3.0 (48)
Solid	14.6 ± 3.5	16.3 ± 8.5	0.8 (70)	0.8 (86)

Mean value (variation coefficient %), n = 8; no. of samples
[a] *AE signals of ultimate specimen failure excluded*

An overview on damage initiation and accumulation during the load application is given by the cumulative AE activity plotted versus strain (Fig. 6.13a-b). Thus, the AE activities of the plywood samples are presented normalized to the cumulative AE activity of solid wood. The cumulative AE activity of solid wood roughly follows a linear curve, but with a lower slope closer to failure strain (Fig. 6.13a). The normalized curves of the plywood samples increase exponentially. Comparing the diagrams that present the AE activities measured by SE 150-M (Fig. 6.13a) and VS 45-H (Fig. 6.13b), the curves are almost similar. Furthermore, the normalized cumulative AE activity is set in relation to the stress level defined by the progressive load normalized to the ultimate tensile strength (Fig. 6.13c-d). Hereby, the curves of plywood types 3 and 4 overlap at stress levels below 50%. This similarity in normalized AE implies an almost similar damage accumulation at the microscopic scale for both plywood types. At higher stress levels, plywood type 4 shows a slower increase in AE activity than plywood type 3. The number of detected AE signals is probably reduced by the path length between the originating source and the sensor location (Aicher et al. 2001), and thus induced reflection and attenuation of the AE signals (Bucur and Feeney 1992).

Since cumulative AE of the plywood materials behave exponentially as a function of time or load, it can be seen by interpreting these curves using the bi-linear approach (Fig. 6.14) that the intersection of both straight lines leads to the so called knee-point strain value (Kuznetsova et al. 2013). These knee-point values are interpreted to identify the switch from dominating microscopic mechanisms to significant damage onset at a larger scale. For all plywood samples, the knee-point strains were determined from the AE activity progress independently for each sensor type (Tab. 6.5). In accordance with the almost similar AE

activity curves detected by the two sensor types (Fig. 6.13a-b), the estimated strain values and the related stress levels at the knee-points are comparable (Tab. 6.5).
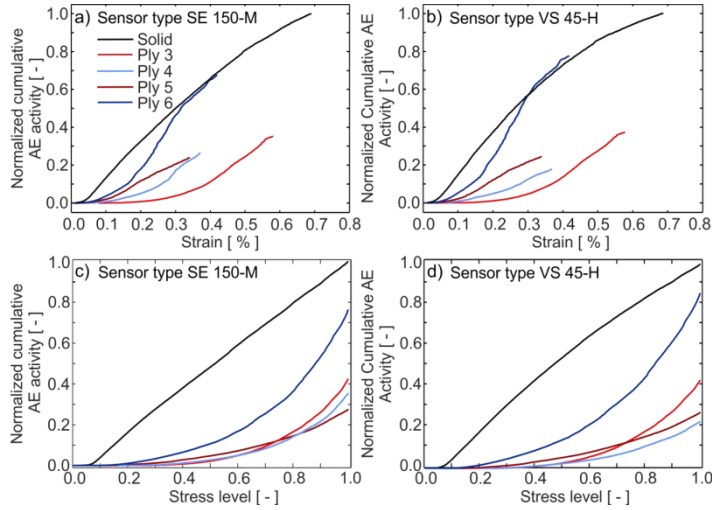

Figure 6.13 Normalized cumulative Acoustic Emission activity of solid spruce and plywood materials in unit of elongation strain measured by sensors of type a) SE 150-M and b) VS 45-H. Normalized cumulative Acoustic Emission activity of solid spruce and plywood materials versus level of ultimate stress measured by sensors of type c) SE 150-M sensor and d) VS 45-H. All curves are averaged from 8 specimens of each material.
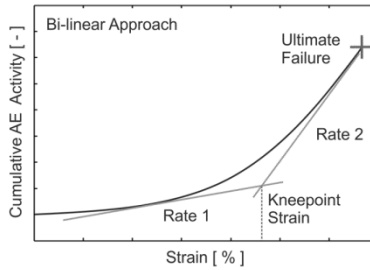
Figure 6.14. Principle of bi-linear approach to analyze cumulative Acoustic Emission activity

Obtained data reveal the onset of significant damage in plywood type 3 at strain values of about 0.4%. If plywood consists of more than three layers, regardless of their fiber orientation, damage growth on a larger magnitude starts earlier, specifically at strain values of approximately 0.2% (Tab. 6.5). The larger range of elastic behavior of plywood type 3 might be affected by the adhesive and the interface layer, respectively. While the core ply is of the same size as each face ply, the two stiff wood-adhesive interfaces play a more important role than they do in plywood with a higher number of core layers, and respectively with a greater thickness of the core layer (Okuma 1976). However, for all tested

plywood materials the stress levels associated with the knee-point values are almost equal (70±5%). Entailing a low variation of 4% in the determination of the knee-point stress levels in the case of plywood types 3 and 4, the additional cross grained core layer in plywood type 4 induces an earlier acceleration in AE activity growth at 68% of ultimate stress, whereas the knee-point for plywood type 3 was determined at 74 % stress level. Moreover, the knee-point in AE activity predicts the start of viscoelastic behavior (Vun et al. 2005), the significant non-linear behavior of plywood type 6 observed in the stress-strain curve above 20MPa (Fig. 6.11.a) correlates with the identified knee-point at 75% stress level (Tab. 6.5).

Extending the bi-linear approach, the slopes of both straight lines indirectly indicate two rates of flaw growth (however, as a function of strain rather than time) derived from the AE activity rates (Fig. 6.14). The first AE activity rate characterizes the initial damage accumulation mainly at the microscopic scale, whereas the second AE activity rate, determined from the stress levels of ca. 70% until the ultimate failure, characterizes the damage increments leading to structural changes at the lay-up's mesoscopic and macroscopic scales. Here, the AE activity rates are defined by the number of detected AE events per 0.01% of the progressive strain (Tab. 6.5).

Table 6.5 Longitudinal strain and stress level at knee point in Acoustic Emission activity and rates in Acoustic Emission activity of several plywood materials and solid spruce.

	Elongation strain at knee point		Stress level at knee point	1st AE Rate (Initiation)		2nd AE Rate (Initiation)	
	SE150-M	VS45-H		VS45-H	SE150-M	SE150-M	VS45-H
Ply 3	0.41 (19)	0.39 (17)	74 (4)	39 (45)	53 (38)	258 (24)	291 (29)
Ply 4	0.23 (33)	0.22 (30)	68 (4)	59 (52)	52 (48)	281 (63)	227 (46)
Ply 5	0.20 (28)	0.19 (32)	67 (8)	79 (45)	75 (64)	248 (46)	283 (46)
Ply 6	0.23 (29)	0.22 (27)	75 (21)	132 (17)	191 (30)	531 (49)	694 (53)
Solid				225 (29)	236 (27)	-	-

Mean value (variation coefficient), n = 8; no. of samples, s; no. of detected AE signals
[b] % of ultimate stress; [b] % elongation strain

Among all tested plywood materials the initial (first) AE activity rate rises with almost every additional ply, irrespective of the grain orientation of the attached veneer (Tab. 6.5). Even bearing in mind the high coefficients of variation, this is still consistent since every additional ply implemented in the material structure offers additional wood matter. Accordingly, additional adhesive joints are being stressed and damaged simultaneously.

Hence, flaw development is accelerated. Analogous to the Young's Modulus indicating the material behavior at low stress levels within its linear elastic range, the first AE activity rate characterizes the consequences of damage initiation and accumulation within the structural elements of the tested plywood samples at the microscopic scale.
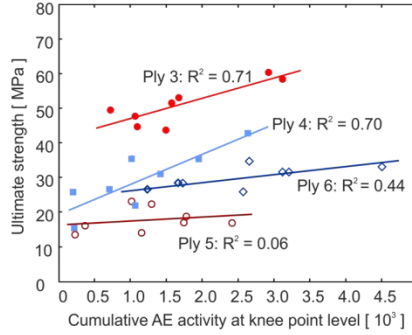

Figure 6.15 Correlation between the ultimate strength of plywood materials and their cumulative number of detected Acoustic Emission events due to development of initial damages

Furthermore, continuing the progressive damage evolution of plywood types 3, 4 and 5 from stress levels >70%, the second AE activity rate of about 200-300 AE events per 0.01% strain is more than twice that at low stress levels. Hence, even though crack paths switch to larger scales due to the layered structure, the flaw growth rate of the plywood types 3, 4 and 5 at high stress levels (second AE activity rate) is almost similar to the increase of defects in solid wood. This is due to the increased stress applied to the long grained plies behaving almost similar to the solid wood specimens (Ansell 1982). However, in accordance with its mechanical behavior (Fig. 6.11a), the second AE activity rate of plywood type 6 is clearly different. In accordance with its distinct plastic deformation on the macroscopic scale, damage growth increases to more than 500 AE events per 0.01% strain. This is more than double of the second AE activity rate compared to plywood type 5, which contains only one long grained veneer in the core layer. This is not in contradiction with the distinct plastic deformation already mentioned above, because these structural changes at greater scale are accompanied by an increased number of damages of smaller size.

In conclusion, the damage accumulation within the initial state of destruction below the knee-point is found to be in correlation with the ultimate strength of plywood (Fig. 6.15). The exception of plywood type 5 is discussed below in more detail.

Acoustic emission intensity and strain field formation

Besides the AE activity summarizing the number of occurring damage events, the AE energy (Eq. 6.1) of the detected events specifies the intensity of the caused damage. All in all, the destructive tension tests of the plywood materials release a total AE energy yielding almost double that of failing solid wood (Tab. 6.4), even though plywood samples generate a lower number of AE events. Again, the only exception is plywood type 5, which released more or less the same AE energy as the solid spruce wood. First, for a better understanding of the damage processes, the cumulative curves of the AE energies averaged for each material sample are expressed as a function of the applied stress level (Fig. 6.16). The cumulative AE energy is expressed relative to the absolute AE energy output of each tested material type, and consequently, at stress levels of 100%, all curves continue by a normalized cumulative AE energy of 100%.

$$E_i = \int_{t_0}^{t} U^2(t)\,dt \qquad\qquad (6.1)$$

E_i AE Energy [V^2s]; U Magnitude of AE signal; t_0 Arrival time of AE signal;
$(t - t_0)$ Duration of AE signal.
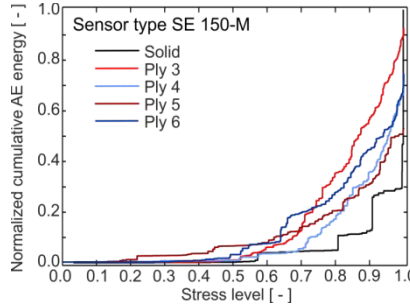
Figure 6.16 Acoustic Emission energy (detected by sensor type SE 150-M) due to stress level of several plywood materials and of solid spruce.

While the AE activity curve of solid wood increases linearly with increasing stress levels (Fig. 6.13c), its cumulative AE energy follows an almost exponential increase path (Fig. 6.16) and hence indicates the nonlinearity in damage evolution (Nagy et al. 2010). In the case of plywood materials, the exponential increase in normalized cumulative AE activity (Fig. 6.13c) is accompanied by an almost exponential increase in normalized cumulative AE energy (Fig. 6.16). At the identified knee-point levels (approximately at a stress level of 70%), each of the plywood materials released <30% of their total AE energy, whereas the solid wood released <10% at the same stress level (70%). By the time the

plywood materials had approached close to 100% of the stress level, they had already set free >50 % of their total AE energies (Fig. 6.16). In particular, plywood type 3, until shortly before its total fracture, had already released 90% of its total AE energy, whereas the solid wood generated <50% of its total AE energy release at comparable stress level.
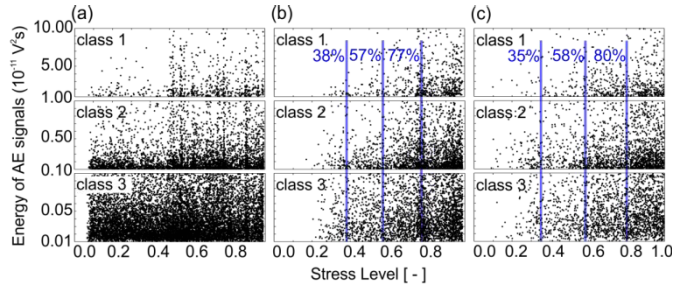

Figure 6.17 Acoustic Emission energies of the signals against stress level, exemplary presented for one specimen made from a) solid spruce wood, b) plywood type 4 and c) plywood type 5. The subplots present the Acoustic Emission energies of three different limitations: 1-10 x10^{-11}V^{2}s (1), 0.11-1.0 x10^{-11} V^{2}s (2), 0.01-0.10 x10^{-11} V^{2}s (3).

Since the AE energy of the detected AE events can be used as a measure of damage magnitude (Harris and Bell 1977), the AE signals are classified with respect to their energy content (Fig. 6.17). This evaluation is performed for AE events detected by the sensor type SE150-M. Thus, for investigated materials, the number of signals of each class, relative to the absolute number of AE signals, revealed three main classes; class 1 includes signals with AE energies of 1-10 x10^{-11} V^{2}s, class 2 contains the signals of 0.11-1.0 x10^{-11} V^{2}s, and class 3 those of 0.01-0.10 x10^{-11} V^{2}s. Moreover, for selected specimens, the AE energies of the single AE events are plotted versus applied stress level (Fig. 6.17a-c). Since the AE energies are within a range of less than 10^{-12} up to 10^{-8} V^{2}s, the plots only present the three main AE energy classes already described above.

For solid wood, only 2% of the detected AE signals were due to AE energy class 1. The distribution of AE events within the energy range of class 1 of 10^{-11}-10^{-10}V^{2}s increased with increasing stresses (Fig. 6.17a class 1). Especially at stresses above 50%, there are several discrete stress levels identified by accumulations of AE events ranging from 10^{-11}-10^{-10}V^{2}s. At these discrete stress levels, AE events of approximately 10^{-10}V^{2}s are accompanied by a huge number of AE events of lower energy content. The AE energy has been found to be a measure of the damage size, thus the increased distribution of AE energies indicates the variation of damage due to increased stress application (Qi et al. 2010). Hence, it is concluded that, at those discrete stress levels yielding a high variation in AE energy in all three energy classes, complex pre-damages are formed. These high variations in AE energy are also consistently represented throughout the plots of AE energy class 2 (Fig. 6.17a class

2) and class 3 (Fig. 6.17a class 3). Substantially, about 23% of the detected AE signals for solid wood are counted among AE energy class 2 and 73% belong to class 3. This fact might correlate with the presence of two main source mechanisms, as already found by Ando (Ando et al. 2006). However, the limitation of the evaluation due to stress levels <70% of ultimate strength does not completely exclude damages above the microscopic structure. While 73% of AE signals due to class 3 originated from microscopic damages with very high probability, the events of energy class 2 might be caused by possible pre-damage at a higher scale (Fig. 6.17a). Altogether, the AE energy release characterizing the damage evolution in solid wood under tension is dominated by a large amount of microscopic damage events generating AE energy contents of $<10^{-12}V^2$s.

In the case of plywood samples, another percentage distribution in AE energy per event is obtained, which is similar for all plywood types. This correlates with the fact that the failure progress of plywood is dominated not only by microscopic damage mechanisms, but also by flaw growth at the mesoscopic scale due to the layered structure. Hence, more than 10% of the detected AE events are assigned to AE energy class 1, whereas with increasing stress level, AE energies of approximately 10^{-10} V^2s occur more frequently (Fig. 6.17b-c class 1). These 10% are due to energy class 1 of significantly high energy values, which lead to significant increases in the cumulative AE energy curves of single specimens. This is interpreted as an instable flaw growth that shows the effect of damage evolution due to the crack size range induced by the layered structure. Furthermore, the plywood materials also release a higher share (35-37%) of signals in AE energy class 2. Within the energy range of class 2, plywood (Fig. 6.17b-c class 2) and solid wood (Fig. 6.17a class 2) clearly show an accumulation of AE energies beyond $0.3\times10^{-11}V^2$s. Moreover, the more balanced AE energy distribution of events assigned to energy class 3 (Fig. 6.17b-c class 3), and additionally, the minor share of 40-50% of AE events of class 3, might result from the less microscopic damage initiation within the wooden structure. The growth of intrinsic lathe checks is of larger magnitude and, hence, expected to yield AE events of energy class 1 or 2. Also, matrix cracking is presumed to yield AE energy class 1 and 2. Possibly, fiber breakages within the long grained plies are also reflected in AE energy class 1 and even by AE energy values $>10^{-10}V^2$s, whereas debonding is likely to appear in the lower range of AE energy class 3 (Haselbach and Lauke 2003, if wood materials and polymer-composites are assumed to behave analogously).

To sum up, the multiple AE energy classes occurring during plywood tensile loading, which altogether show an increasing energy trend of AE events (Fig. 6.17b-c), result from the cracks progressing through an additional length scale introduced by the layered structure of

the plywood. The linear elastic behavior of tensile stressed plywood is mainly dominated by the lower strength of the cross-grained plies. This is verified by the correlation of the ratio of cross-grained plies to the share of events of AE energies above $10^{-12}V^2s$ (energy class 1, 2 or even above). Thus, with the increasing ratio of cross grained plies, the share of AE events induce cracks a somewhat larger than micro-cracks (Fig. 6.18). Above the linear elastic behavior of tensile stressed plywood, until the initiation state runs out, the damage accumulation is less dependent on the lay-up ratio (Fig. 6.18). For all plywood materials there is an almost similar share of AE events inducing cracks larger than micro-cracks at an AE energy $>10^{-12}$ V^2s.
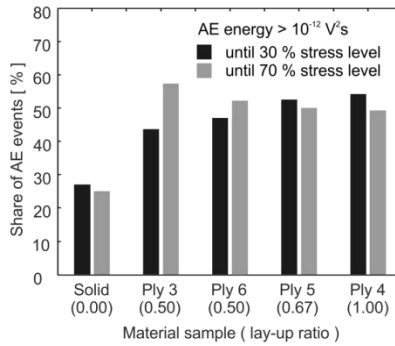
Figure 6.18 Influence of lay-up ratio on the share of Acoustic Emission events with respect to the Acoustic Emission energy of $>10-12$ V^2s evaluated until the stress level of 30 % (linear range) and 70%

Finally, more detailed insight in damage evolution is obtained exemplarily for plywood type 4 and type 5 by correlating the AE energy results (Fig. 6.17b-c) and the strain field development monitored by the DIC method (Figs. 6.19-6.20). Therefore, sequences of the elongation strain (e_{yy}) and the shear strain (e_{xy}) formation at discrete stress levels as a percentage of the ultimate strength are presented for the selected plywood specimens.

Hence, for the plywood specimen type 4, a first formation of local concentrations in higher elongation strains of approximately 0.3% shows the pattern of the specimen's weak region (Fig. 6.19c1) at 38 % of ultimate strength. By further increasing the stress level, a more homogeneous elongation strain formation at 57% stress level develops (Fig. 6.19c2).
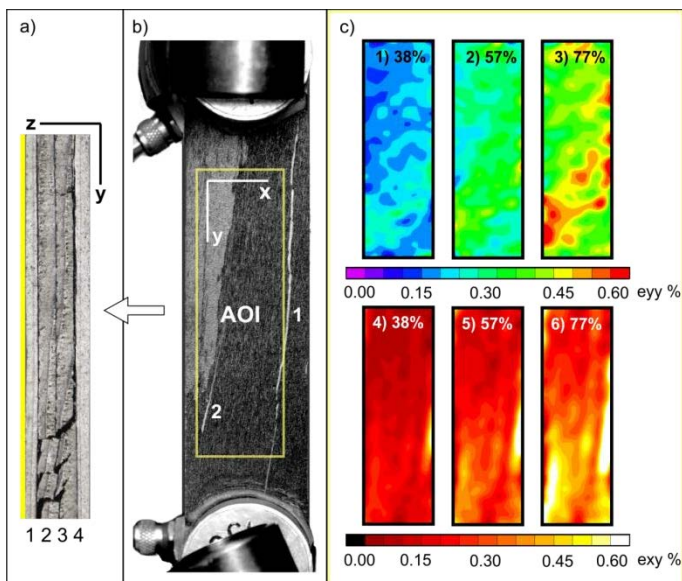
Figure 6.19 Visualization of deformation of a selected specimen made of plywood type 4 detailing a) the fracture pattern through the layered structure, b) area of interest monitored by Digital image Correlation including the cracks 1 and 2, c) progress of strain and shear at several levels of stress (% of ultimate strength).

Finally, the pattern of weakness does not reoccur until a stress level of 77% is reached (Fig. 6.19c3). In contrast, for plywood type 3, the reoccurring patterns of high strain concentrations already start at about 30% of ultimate strength and remain until failure (Ritschel et al. 2013). These differences in elongation strain field can be explained by the different importance of the interface of adhesive and wood close to the face veneers. Plywood type 4 consists of a double cross grained layer with an adhesive in-between. This adhesive interface reinforces the cross-grained core layer normal to the load direction, due to the penetration of the adhesive into the intrinsic flaws of both core plies (Okuma 1976). Thus, the core layer dominates the damage evolution. Consequently, both interfaces close to the face veneers are of less relevance. Concurrently, a shear strain of more than 0.1% is distributed over the entire surface at stress levels below 30% and further yields first local shear strain concentrations at 38% stress level, which steadily increases until the specimen fails (Fig. 6.19c4-6). Hence, at 38% of ultimate strength, the ultimate elongation strain of the brittle phenol resin glue line between the core and the face veneer is mainly overcome (Serrano 2004; Serrano and Enquist 2005) and shear dominates the failure behavior. The fracture (Fig. 6.19a) of the specimen plywood type 4 clearly shows the presence of rolling shear, just like the other plywood types.

However, it must also be mentioned here, that the presented specimen is an exception among all specimens of plywood type 4, because it forms significant shear strain due to the arrangement of the cut annual rings enclosing the dominant weakness point. Excluding the shear strain of the specimen, the averaged shear strain of plywood type 4 registers 0.10% (80% coefficient in variation). Nevertheless, this specimen works well for interpretation of AE results, because the original DIC monitoring photographs enable tracing the initial crack opening of the first macroscopic crack (Fig. 6.19b, crack 1) caused by the significant pattern in elongation strain and shear strain at a stress level of 77% observed in the face veneer. This pre-failure in the long grained face ply is also reflected in the AE energy plots of all three AE energy classes, revealing a large distribution of AE energy per event close to the discrete stress level of 77% (Fig. 6.17b). Further, a similar pattern in AE energy occurs at a stress level of approximately 95% (Fig. 6.17b), which is generated by the formation of the second crack. Finally, the ultimate failure of the specimen brought the first crack to its final size shown in Fig. 6.19b (crack 2).

For plywood type 5, the most stressed ply is the long grained veneer in the core. Strains detected by DIC are affected essentially by details of surface deformation only. However, the surface deformation is also affected by the deformation of the underlying layers. Thus, inhomogeneous patterns of small strains are not replaced by significant concentrations in elongation strain until 80% stress level (Fig. 6.20c1-3). The formation of shear strain concentrations shows a similar trend (Fig. 6.20c4-6). The AE measurements, especially the plots of the AE energy per event (Fig. 6.17c), do not indicate the complex pre-damages. Significant accumulation of AE events at discrete stress levels is absent. Nevertheless, the fracture of the selected specimen shows complex damage through all five plies (Fig. 6.20a), and implies a very brittle failure behavior of the specimen. It also has to be taken into account that the sensitivity of the sensors is reduced due to the layered structure: number of veneers, and presence of adhesive interfaces as well as the increase of the specimen's thickness. However, the AE onset yields a wide spread of AE energy per event within all three classes. Hence, damage initiation and accumulation also includes multiple mechanisms distributed over several length scales due to the intrinsic lathe checks within the veneers and the layup.

All in all, the high variation of AE energies indicates damage mechanisms of several length scales. For plywood types 4, 5 and 6 shear mechanisms dominate the damage progress below the knee-point level (Tab. 6.5). However, above the knee-point of 70% of ultimate strength, and the correlated strain values above 0.2%, the long grained face plies play the more important role.
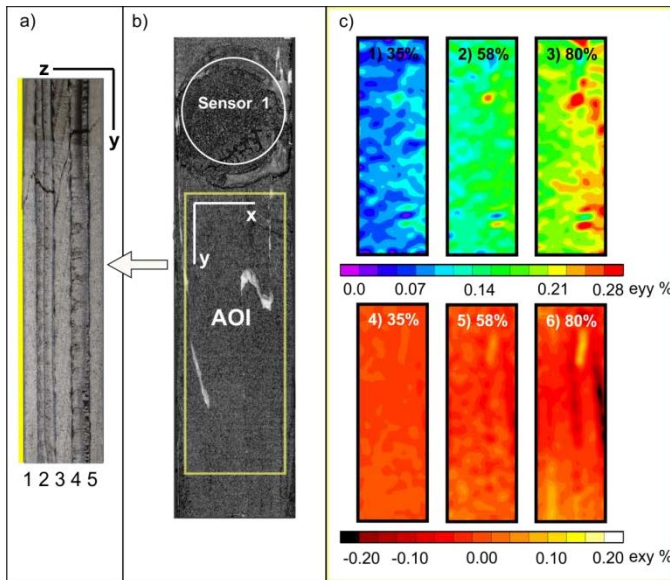
Figure 6.20 Visualization of deformation of a selected specimen made of plywood type 5 detailing a) the fracture pattern through the layered structure, b) area of interest monitored by Digital image Correlation, c) progress of strain and shear at several levels of stress (% of ultimate strength).

Summary and Conclusion

Multi-scaled damage initiation and accumulation from tensile loading was investigated for plywood samples consisting of three, four, five or six veneers of spruce wood. Additionally, specimens of solid spruce wood were tested for comparison purposes. The destructive tests were performed under tension parallel to the board direction at a constant displacement rate synchronously monitored by AE and DIC. Due to the different layup of the plywood samples, differences in damage progression are reflected in the detailed analyzes of AE and DIC results.

- Damage accumulation of plywood is characterized by an exponential increase, expressed in the exponential curve of the cumulative number of AE events with progressive test duration.
- The amount of damage that occurred, measured in numbers of detected AE events, is approximately the same size for plywood types 3, 4 and 5. Significantly more damage is observed for the plywood type 6. This is in compliance with the plastic deformation already observed at the macroscopic scale in the stress strain graph.
- Two growth rates (number of AE events per 0.01% elongation strain) are identified in the damage evolution: The initial state of damage growth is represented by the 1st rate, while the 2nd rate specifies the increase of damage progress leading to ultimate failure.

- With increasing number of veneers, the 1st rate also increased. Thus, the initial flaw development is accelerated, because each additional veneer implemented in the material structure offers additional matter (of wood and adhesive joints) that is stressed and damaged simultaneously.
- For all plywood samples the 2nd rate of damage increase leading to ultimate failure is nearly quadruple the amount of the initial rate. This is attributed to the fact that microscopic and mesoscopic damage mechanisms act through the veneers and bond lines, and coalesce into mesoscopic and macroscopic scale due to lay-up, finally leading to ultimate failure.
- The state of initial damage accumulation ends at approximately 70% stress of ultimate strength, whereas shear mechanisms dominated the damage progress below the knee-point level (see Fig. 6.14) and the long grained face plies play the more important role above the knee-point level.
- The initial AE is affected by the degradation of the natural wooden structure of the veneers by pre-damages (e.g. lathe checks) induced while processing the plywood.
- Within the range of initial damage accumulation (less than 70 % of ultimate stress), less than 30% of absolute AE energy is released by all plywood materials. However, multi-scaled damage mechanisms are already included. This is indicated by a high variability in AE energy content of events that covers almost six decades from $0.001\text{-}100\text{x}10^{-11}\text{V}^2\text{s}$.

All in all, the suitability of combining AE measurement and the optical method of DIC has been substantiated. Furthermore, the high time resolution in AE analysis enables more detailed investigations of complex damage mechanisms allowing further verification of parameters encoding the origin of structural changes.

Acknowledgement

References

Aicher, S., Höfflin, L., Dill-Langer, G. (2001) Damage evolution and acoustic emission of wood at tension perpendicular to fiber. Eur J Wood Wood Prod 59:104-116.

Ando, K., Hirashima, Y., Sugihara, M., Hirao, S., Sasaki, Y. (2006) Microscopic processes of shearing fracture of old wood, examined using the acoustic emission technique. J Wood Sci 52:483–489.

Ansell, M.P. (1982) Acoustic emission from softwood in tension. Wood Sci Technol 16(1):35–57.

Beall, F.C. (2002) Overview of the use of ultrasonic technologies in research on wood properties, Wood Sci Technol 36(3):197-212.

Bucur, V., Feeney, F. (1992) Attenuation of ultrasound in solid wood. Ultrasonics 30(2):76-81

Bucur, V. (2006) Acoustics of wood. Springer, Berlin, pp 221-235.

Brunner, A.J., Howald, M.T., Niemz, P. (2006) Acoustic emission rate behavior of laminated wood specimens under tensile loading. J Acoust Emis 24:104-110.

Debaise, G.R., Porter, A.W., Pentoney, R.E. (1966) Morphology and mechanics of wood fracture. Mater Res Stand 6:493–9.

Dunlop, J.I. (1980) Testing of particle board by acoustic techniques. Wood Sci Technol 14(1):69-78.

Görlacher, R. (2002) Determination of the rolling shear modulus of wood (original in German) Eur J Wood Wood Prod 60(5):317–322.

Gozdecki, C., Smardzewski, J. (2005) Detection of failures of adhesively bonded joints using the acoustic emission method. Holzforschung 5(2):219-229.

Grosse, C., Ohtsu, M. (Eds.) (2008) Acoustic emission testing in engineering - Basics and applications. Springer publ., Heidelberg.

Harris, D.O., Dunegan, H.L. (1974) Continuous monitoring of fatigue-crack growth by Acoustic-Emission techniques. Exp Mech 14(2):71-81.

Harris, D.O., Bell, R.L. (1977) The measurement and significance of energy in Acoustic Emission. Exp Mech 17(9):347-353.

Ivanov, I.V., Sadowski, T. (2009) Micromechanical material model of wooden veneers for numerical simulations of plywood progressive failure. Key Eng Mater 399:169-176.

Haselbach, W., Lauke, B. (2003) Acoustic Emission of debonding between fibre and matrix to evaluate local adhesion. Composi Sci Technol 63:2155-2162.

Keylwerth, R. (1954) Actual and Possible Reduction of Anisotropy in Composite Wood Boards (original in German) Eur J Wood Wood Prod 17(6):234-238.

Kollmann, F. (1961) Rheology and structural strength of wood (original in German) Eur J Wood Wood Prod 19(3):73-80.

Kufner, M. (1966) Permissible stresses in veneer board. (original in German) Eur J Wood Wood Prod 24(11):537-539.

Kuznetsova, R., Ergun, H., Liaw, B. (2013) Acoustic Emission of failure in fiber-metal laminates. In Büyüköztürk, O. et al. (eds.), Nondestructive Testing of Materials and Structures, RILEM Bookseries 6.

Nagy, E., Landis, E.N., Davids, W.G. (2010) Acoustic emission measurements and lattice simulations of microfracture events in spruce. Holzforschung 64(4):455–461.

Niemz, P., Lühmann, A. (1992) Application of the acoustic emission analysis to evaluate the fracture behavior of wood and derived timber products. Eur J Wood Wood Prod 50(5):191–194.

Niemz, P., Brunner, A.J., Walter, O. (2009) Investigation of the mechanism of failure behavior of wood based materials using Acoustic Emission analysis and image processing. Wood Res 54:49-62.

Norris, C.B., Werren, F., McKinnon, P.F. (1961) The effect of veneer thickness and grain direction on the shear strength of plywood. US Forest Products Laboratory, Report No. 1801.

Okuma, M. (1976) Plywood properties influenced by the glue line. Wood Sci Technol 10:57-68.

Plath, E. (1974) Calculation of the thickness / layer ratio of plywood. (original in German) Eur J Wood Wood Prod 32:177-181.

Qi, G., Wayne, S.F., Penrose, O., Lewis, G., Hochstein, J.I., Mann, K.A. (2010) Probabilistic characteristics of random damage events and their quantification in acrylic bone cement. J Mater Sci Mater Med 21(11): 2915-2922.

Reiterer, A., Stanzl-Tschegg, S.E., Tschegg, E.K. (2000) Mode I fracture and acoustic emission of softwood and hardwood. Wood Sci Technol 34:417-30.

Ritschel, F., Brunner, A.J., Niemz, P. (2013) Nondestructive evaluation of damage accumulation in tensile test specimens made from solid wood and layered wood materials. Compos Struct 95:44-52.

Scruby, C.B. (1987) An introduction to acoustic emission. J. Phys. E: Sci. Instrum. 20.

Serrano, E. (2004) A numerical study of the shear-strength-predicting capabilities of the test specimens for wood-adhesive bonds. Int J Adhes Adhes 24(1): 23-35.

Serrano, E., Enquist, B. (2005) Contact-free measurement and non-linear finite element analyses of strain distribution along wood adhesive bonds. Holzforschung 59(6): 641-646.

Smith, I., Landis, E., Gong, M. (2003) Fracture and Fatigue in Wood. John Wiley & Sons Ltd.

Valla, A., Konnerth, J., Keunecke, D., Niemz, P., Müller, U., Gindl, W. (2010) Comparison of two optical methods for contactless, full field and highly sensitve in-plane deformation measurements using the example of plywood. Wood Sci Technol 45:755-765.

Vassiliou, V. (1996) Bending strength of thin 3-ply poplar plywood in relation to core veneer joints. Eur J Wood Wood Prod 54(5): 360-366.

Vun, R.Y., deHoop, C., Beall, F.C. (2005) Monitoring critical defects of creep rupture in oriented strandboard using acoustic emission: incorporation of EN300 standard. Wood Sci Technol 39(3): 199-214.

Wagenführ, R. (2000) Holzatlas. (original in German) Fachbuchverlag Leipzig, pp 177-178.

DIN EN 313-2 (1999) Sperrholz - Klassifizierung und Terminologie - Teil 2: Terminologie (original in German).

DIN EN 14272 (2011) Sperrholz - Rechenverfahren für einige mechanische Eigenschaften (original in German).

DIN 52377 (1978) Prüfung von Sperrholz; Bestimmung des Zug-Elastizitätsmoduls und der Zugfestigkeit (original in German).

DIN 68705-2 (2003) Sperrholz - Teil 2: Stab- und Stäbchensperrholz für allgemeine Zwecke. (original in German).

6.3 Comparison of model layered wood & industrial plywood

Further results of model layered wood materials (UD and CP; 5 specimens for each) manufactured in the laboratory without inducing numerous pre-damages compared with the (pre-damaged) plywood industrially produced (plywood type 3-6; 8 specimens for each) are presented. Also the results of solid spruce specimens from the 1st (5 specimens) and the 2nd (8 specimens) test series are shown. Firstly, the AE behavior of CP and industrial plywood materials is presented by focusing on the AE activity and AE intensity over the duration of the test. The AE amplitude distributions for all materials are discussed in the second part.

6.3.1 Cumulative number and energies of AE signals

In order to compare the AE behavior of the tested plywood types, which were manufactured in the laboratory with less pre-damages (CP) and industrially produced (plywood type 3-6), the results of one single test of each material type are presented. In Fig. 6.21., the stress curves, the cumulative number and energy of the AE signals located by the sensors of type SE 150-M are plotted against test duration for each specimen type.
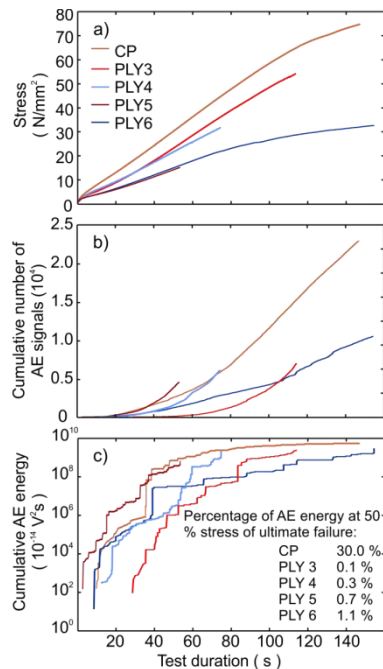
Figure 6.21 Failure behavior of five different types of plywood specimens characterized by their a) stress curves, b) cumulative number and c) cumulative AE energy of AE signals detected and located by means of two SE 150-M sensors. Results are based on one single specimen selected from each material type.

Regarding the stress curves, the industrial plywood types 3-5 follow linear elasticity, whereas the CP specimen made of clear spruce lamellae reveals plastic deformation at higher stresses (Fig. 6.21a). The stress behavior of plywood type 6 also started in the linear elastic range, but the relationship becomes rather nonlinear already before 50% of test duration until ultimate failure.

The total number of AE signals detected for the four industrial plywood specimens is low compared to the CP specimen. Particularly, the plywood type 3 consists of lay-up, which is almost similar to that of the CP specimens, shows significant differences in AE behavior. Though, the CP was glued with UF adhesive and, contrarily the plywood types were produced using PRF, these differences cannot solely be attributed to the adhesive performances, particular with regards to their almost similar MOE (Tab. 3.1). Hence, it is concluded that the larger amount of pre-damage induced when processing the industrial plywood leads to relatively lower AE activity. Moreover, the linear stress curves of the plywood types 3-5 correlate with an exponential increase in defect growth based on AE activity (Fig. 6.21b).

In contrast, elastic and plastic parts in stress behavior, as observed for the CP and the plywood type 6, generate bi-linear defect growths. For all specimens, CP as well as plywood type 3-6, the AE energy release is of almost similar range; between 10^{-6} V^{2}s and 10^{-4} V^{2}s (Fig. 6.21c). However, the CP generates the highest absolute value of cumulative AE energy. At 50% ultimate stress, CP released about 30% of its absolute AE energy, whereas the AE energy output of the industrial plywood yields only approximately 1% (Fig. 6.21c). The lower AE energies produced by the industrial plywood are also explained by the energy released earlier due to process-related pre-damages.

6.3.2 Amplitude distributions

An assessment of AE intensity is presented by means of the amplitude distribution. The amplitude distributions presented here are the averages of all first hits of AE signals detected from each specimen from each material type (Fig. 6.22). For comparison purposes, the relative number of AE signals (scaled logarithmically) is plotted against the peak AE signal amplitude (scaled in dB$_{AE}$). The range of amplitudes is limited by the minimum value of 43dB$_{AE}$ (related to the threshold setting) and the maximum dynamic range of the AE equipment (100dB$_{AE}$). For completeness, the distributions are presented for each material type and for each sensor type and thus, reveal roughly similar slopes (b-value, see Chap. 6.1) by the sensor types for a certain material type (Fig. 6.22). Since the subsequent studies are mainly based on the SE 1000-H sensors (Chap. 6.), the corresponding amplitude

distributions (Fig. 6.22e-f) are discussed in more detail. The reference specimens made of spruce wood are analyzed separately for the first (Chap. 6.1) and the second (Chap. 6.2) test series. Though, the properties of both spruce wood materials are very similar (Tab. 6.6), a significant deviation between both slopes (Fig. 6.22e, gray and black curves) is observed.

Table 6.6 Overview of the mechanical properties of the laboratory scale reference specimens made of clear spruce tested during the 1st (Chap. 6.1) and 2nd (Chap. 6.2) tensile test series:

	n	MC (%)	Raw density (kg m^{-3})	Tensile strength* (GPa)	MOE* (MPa)	Tests presented ir
1st series	5	9.0	445±18	89±8	13±0.2	Chap. 6.1
2nd series	8	8.6	400±11	87±9	14±1.0	Chap. 6.2

*n… Number of tests; MC…Moisture content; MOE…Modulus of elasticity; * Longitudinal direction*
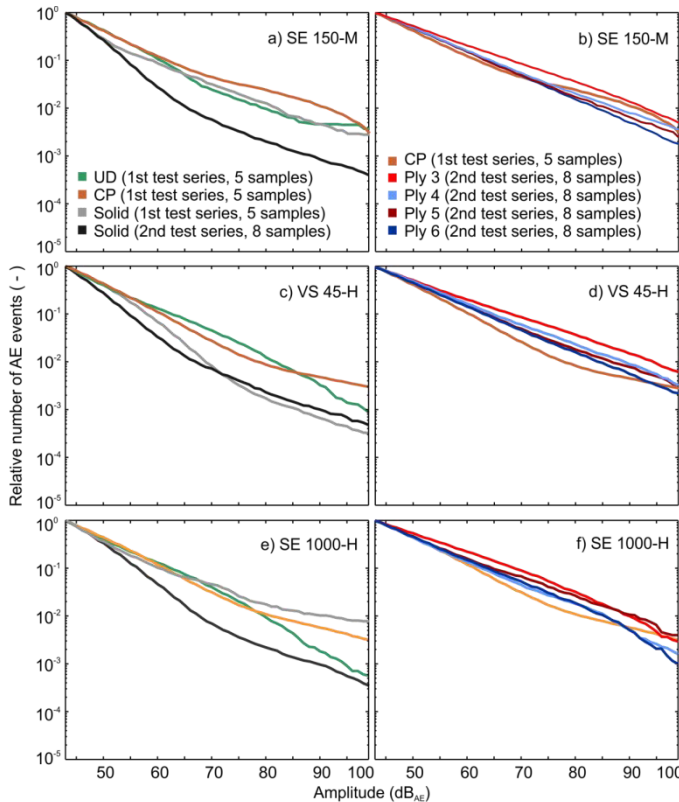
Figure 6.22 Amplitude distributions of the investigated layered wood and plywood materials and solid spruce (compare Fig. 3.3): a-b) Relative cumulative numbers of AE signals detected by the sensor type SE 150-M, c-d) VS 45-H and e-f) SE 1000-H plotted against AE amplitudes. Distributions are the averages over all specimens of the specific material types tested.

The distribution of the 2nd tests series reveals a higher b-value than that of the 1st series. In addition to the natural variability of wood, the different sensor positions also contribute to this difference, since the data evaluated are based on located events (VISUALAE Location Calculation, Vallen System GmbH). In the 2nd series the SE 1000-H sensors were only 30mm apart (in the 1st series: 100mm apart) and closely located to the reduced tests section of the dog bone specimens. Hence, in the 2nd series, the SE 1000-H sensors may have been more sensitive to AE signals of low amplitude.

The CP yields a relative large share of amplitudes not higher than the reference solid wood of the 1st series (Fig. 6.22e), which could be affected by the 100mm sensor distance and the attenuation effects $(0.1dB_{AE}\ mm^{-1})$ coupled with that. However, the situation is different when detecting AE with the SE 150-M (Fig. 6.22a) and the VS 45-H sensors (Fig. 6.22c). As already stated in Chap. 5.1, the b-value for UD is similar to those of CP in the lower two amplitude ranges, but clearly higher for the highest amplitude range between 75 to 100 dB_{AE} (Fig. 6.22e).

A comparison of the amplitude distributions of CP and industrial plywood types 3-6 shows significant differences for all three sensor types (Figs. 6.22b, d, f). The industrial plywood materials show rather an almost linear decrease in amplitude distributions, whereas the curvature of CP is more similar to that of solid spruce. For the plywood type 3 in particular, with its layup being very similar to CP (3 wooden layers of 3 mm thickness each with a center cross ply), but with intrinsic pre-damages such as lathe checks, a significantly lower b-value is observed meaning a lower share of signals with low amplitudes than for CP (Fig. 6.22f). Thus it is assumed that the damage initiation and accumulation in industrial plywood generates damage events of larger magnitude than in clear solid wood and the model layered materials. Furthermore, compared to the CP generating amounts of AE events from the beginning of AE onset at tension stresses of 1-2GPa, for the industrial plywood type 3, the AE onset, also in the range of 1-2GPa, is characterized by few separate AE events that occur with progressing test duration followed by more significant occurrences of AE events at stresses clearly above 2GPa. Based on this, it is concluded that most damage events at the microscopic scale were already eliminated while processing the industrial plywood.

6.4 Paper III

Damage evolution in wood – Pattern recognition based on acoustic emission frequency spectra

Franziska Baensch[1] / Markus G.R. Sause[2] / Andreas J. Brunner[3] / Peter Niemz[1]

[1]ETH Zurich – Institute for Building Materials, CH-8093 Zürich, Switzerland

[2]University of Augsburg – Institute for Physics, Experimental Physics II, D-86135 Augsburg, Germany

[3]Swiss Federal Laboratories for Materials Science and Technology – Laboratory for Mechanical Systems Engineering, CH-8600 Dübendorf, Switzerland

Corresponding author: Franziska Baensch, ETH Zurich – Institute for Building Materials, CH-8093 Zürich, Switzerland, Email: fritschel@ethz.ch

Abstract

Tensile tests on miniature spruce specimens have been performed by means of acoustic emission (AE) analysis. Stress was applied perpendicular (radial direction) and parallel to the grain. Nine features were selected from the AE frequency spectra. The signals were classified by means of an unsupervised pattern recognition approach, and natural classes of AE signals were identified based on the selected features. The algorithm calculates the numerically best partition based on subset combinations of the features provided for the analysis and leads to the most significant partition including the respective feature combination and the most probable number of clusters. For both specimen types investigated, the pattern recognition technique indicates two AE signal clusters. Cluster A comprises AE signals with a relatively high share of low-frequency components, and the opposite is true for cluster B. It is hypothesized that the signature of rapid and slow crack growths might be the origin for this cluster formation.

Keywords

Introduction

Research results are not yet available concerning tracking back the evolution of a wood fracture zone to its origin. Such research should determine the temporal-spatial occurrence of damage mechanisms and their interactions at different length scales, i.e., in the cell wall at the microscale and in the tissue at the mesoscale and macroscale. However, damage mechanisms have been frequently studied (Ashby et al. 1985; Frühmann et al. 2003), and failure scenarios have also been investigated in model analyses (Hofstetter et al. 2008; Saavedra Flores and Friswell 2013). The synchronous monitoring of multiscaled damage evolution, as a result of load exposure, is difficult because of the limited observable length scales. The acoustic emission (AE) method facilitates the detection of damage events at the microscopic and macroscopic scale. Additionally, the high time resolution in the range of μs allows detailed monitoring of the damage evolution. Nevertheless, the most challenging task is to assign features of the detected AE signals to their sources. A multitude of approaches focuses on this issue. The conventional AE analysis investigates the parameters of the AE signals in the time domain (Fig. 6.23a) by means of AE signal amplitudes (Debaise et al. 1966; Ansell 1982; Ando et al. 1992a; Cunderlik et al. 1996; Lee et al. 1996; Aicher et al. 2001; Kim et al. 2005; Rosner 2012). Other studies focused on the AE frequency features (frequency domain, see Fig. 6.23b) (Ogino et al. 1986; Tyree and Sperry 1989; Reiterer et al. 2000; Jakiela et al. 2008).

The present contribution introduces an approach based on frequency spectra of the detected AE events followed by pattern recognition. To the best of the authors' knowledge, this approach to AE analysis of wood materials is unprecedented. The AE frequency spectra contain the main characteristics of the signal's origin (Stephens and Pollock 1971), and thus, similar source mechanisms are assumed to generate similar AE frequency features near the source location. The propagation of AE through the material is accompanied by reflection processes, which induce intrinsic similarities to the AE signal. To classify the AE signals properly, these similarities have to be identified and weighted for their significance. Therefore, the method of unsupervised pattern recognition (UPR) is a useful tool. It is a purely mathematical approach to obtain dataset partitions by means of multivariate data analysis. The approach for signal classification applied in the present study was originally developed for failure identification in hybrid materials (Sause et al. 2012a). Its applicability is well established in the field of failure mechanism studies of fiber-reinforced composites (Sause et al. 2012b). Because these composites and wood have distinct microstructures with anisotropic elastic properties (Fratzl et al. 2004), the implementation of the UPR method for AE signal classification of failing wood seems to be straightforward and promising.
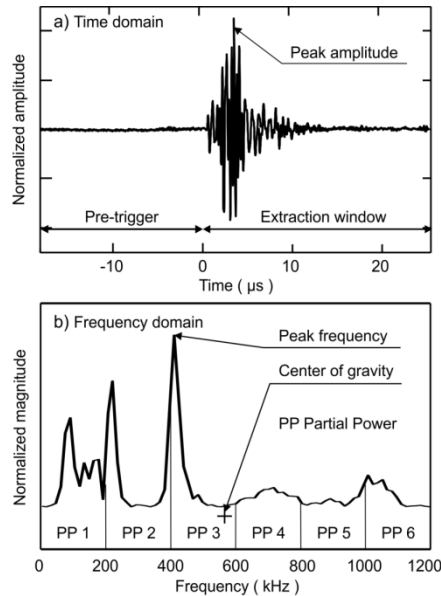
Figure 6.23 Parameters of AE signals in a) time domain and b) frequency domain. a) A pretrigger of 18 μs was chosen, the frequency spectra were calculated from the first 25.6 μs of the detected signal (extraction window). b) The unsupervised pattern recognition was performed by using nine frequency features: PF, CGF (Eq. 6.2), WPF (Eq. 6.3), and PP1–6 (Eq. 6.4).

Materials and experimental design

The specimens were cut from clear spruce wood [Picea abies (L.) Karst.] grown in the canton of Grisons (Switzerland) at altitudes above 1000m (age approximately 250 years). The mechanical properties of that wood stock, which is characterized by a low average raw density of approximately 340kg m^{-3}, have already been described by Sonderegger et al. (2008).

Table 6.7 Characterization of the investigated radial (R) and longitudinal (L) spruce wood specimens (mean ± StdD)

Type	n	Density	MC	Cross section	Growth ring width	Traverse velocity	Test duration	Tensile strength
		(kg/m^3)	(%)	(mm^2)	(mm)	(mm/s)	(s)	(MPa)
R	7	337±6	8.5	4.1±0.2	1.49±0.10	0.005	54±6	8±1
L	7	280±11	8.3	1.2±0.2	-	0.010	18±6	54±11

n… Number of specimens, MC … Moisture content

The tests presented here were carried out on miniature specimens to allow the implementation of the testing setup into a synchrotron computed microtomography

(SRµCT) beam line for further investigations. Two sets of specimens were manufactured regarding the applied fiber-load angle (Fig. 6.24a, b). The specimens prepared for load application in the radial (R) direction will be denoted as R specimens, and those prepared for load application parallel to the grain will consequently be denoted as longitudinal (L) specimens.

The first step in sample preparation was cutting blanks of dimension $30 \times 5.7 \times 2.3 mm^3$ (length×width×thickness), whereby the most important step was the preparation of a plane cut of one specimen surface by a microtome blade. The created surface has the sufficient quality for coupling the piezoelectric AE sensors. Failure in the R specimens is expected mainly within the earlywood (EW) (Müller et al. 2003). Thus, L specimens were selected for comparability also from EW, resulting in the low density of 280kg m^{-3} (Tab. 6.7). To ensure crack initiation between both AE sensors, the specimen's geometry is tapered. The R specimens have only a two-sided taper of approximately 4 mm^2 test cross-section, whereby approximately five to six growth rings are within the tapered volume. In contrast, the L specimens are taper shaped at all four sides, yielding a test cross-section down to 1 mm^2. The specimens were transferred into the specimen supports made of aluminum with a single component polyurethane adhesive, which enabled an interlocking mount of the specimens in the testing device by a connection thread (Fig. 6.24c).
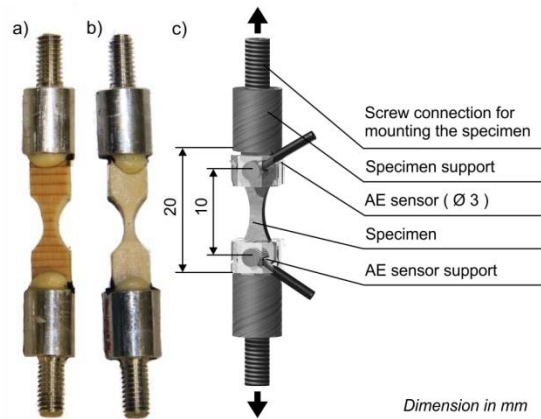
Figure 6.24 Design of a) the radial specimens and b) the longitudinal specimens glued into the specimen holders. c) Experimental setup.

Tensile tests were performed with a loading device for miniature specimens (Zauner et al. 2012) with a load cell of 1kN, which was designed to be implemented at the synchrotron beam line. The load application was performed under displacement control. Tests were continued up to the ultimate failure of the specimen. The R specimens were loaded with a

cross-head speed of 0.005mm s^{-1}, whereas the L specimens were tested at 0.01mm s^{-1} to prevent possible creeping in the adhesive within the specimen supports. In total, seven specimens of each type were tested. Despite their low densities (Tab. 6.7) and taking into account the size effect yielding heightened strengths due to the tiny test cross-sections, the tensile strengths of the specimens are in good agreement with values determined by Wagenführ (2000). The high standard deviation of the strength measured for the L specimens might be due to different density profiles within the growth rings located in the cross-sections (Lanvermann et al. 2013).

The AE monitoring was performed with a digital AE equipment (AMSY-6, Vallen Systeme GmbH, Icking, Germany). Two miniature piezoelectric sensors [type M31 (Fuji Ceramics Corp., Shizuoka, Japan)] with a coupling area of 3mm in diameter were mounted single sided on the surface of the specimen (Fig. 6.24c). The even mounting of the AE sensors' piezoelectric bearing face was facilitated by precisely machined sensor supports. Silicone-free vacuum grease was used as couplant (Pöllath J.P. Labortechnik, Bamberg, Germany) between sensor and specimen surface. The M31 AE sensors are sensitive to a frequency range of 300kHz–800kHz, in which the sensor response is almost constant (±3dB; see Fig. 6.25). Below 300kHz, the sensor response steeply decreases by approximately -30dB. Because the sensors are positioned quite close to the specimen's failure zone, far field attenuation effects are assumed to be negligible (approximately 0.25dB cm^{-1}; Bucur and Böhnke 1994), but higher attenuation in the near field zone around the source cannot be excluded. However, regarding the different cell compositions of both specimen types (L specimens of EW tracheids, R specimens containing growth rings), the AE detection of the R specimens might be affected by a higher damping due to the differences in density within the growth rings (growth ring width of approximately 1.5mm; Tab. 6.7). The frequency range of the preamplifiers (AEP3, gain of 34dB into 50Ω; AMSY-6, Vallen Systeme GmbH, Icking, Germany) was limited between 30kHz and 960kHz. The detection of the AE waveforms was performed with a sampling rate of 10MHz, yielding a signal duration of 409.6μs including an 18μs-pretrigger. The threshold was set to 32.1dB$_{AE}$ (≈0.04mV). The chosen rearm time of 1ms is based on empirical values.

The AE measurement performed with two sensors enables the localization of AE events. However, tracking the source position is not considered in this investigation, but exclusively AE events localized between both sensors (max. 10mm distance) are selected for AE analysis. The acoustic propagation velocity through spruce wood is ca. 6000m s^{-1} in the L direction and ca. 2200m s^{-1} in the R direction (Sonderegger et al. 2008), and based on this, the AE events can be separated by means of AE detection by both sensors (Kurz et al. 2008)

within the maximum possible difference in arrival times (≤10μs). The waveforms from the first signal of each AE event provide the basis for all analyses presented here. Hence, in the following, these first signals of the AE event are denoted as AE signals. The number of detected AE signals during one single tensile test is quite low (on average 16 AE events for each test). To ensure a suitable statistical database for pattern recognition processing, the extracted AE feature datasets of all seven tests are analyzed simultaneously for each specimen type.
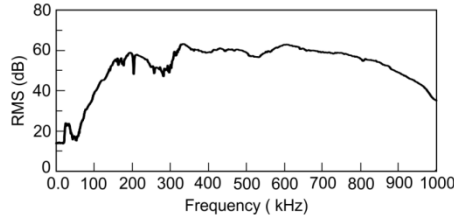
Figure 6.25 Average frequency response curve of the miniature AE sensors.

Method of UPR: The UPR technique was applied for evaluation of AE signal features extracted from the frequency domain. To this purpose, the AE signal frequency spectra were calculated via Fourier transformation (Hamming window function, 256 samples) applied to the first 256 samples of the AE signal in the time domain (0-25.6μs) excluding the 18-μs pretrigger (Fig. 6.24a). The limitation in the time domain was set with regard to the rise time of the AE events ranging from <1μs up to 10μs to ensure the proper selection of signal features only from the first part of the signal burst. Because the lifetime of an AE source event is in the range of some ns to a few μs (Pardee and Graham 1978), the most significant effects of the source mechanism are expected at the beginning of the signal's arrival at the sensor. The propagation of AE through the material structure is accompanied by reflection processes causing intrinsic similarities in the AE signals. Especially in tiny specimen sizes, as investigated here, these self-similarities must be considered in AE frequency analysis.

The input features for the cluster algorithm are selected exclusively from the AE signal's frequency spectra. Besides the peak frequency (PF) (Fig. 6.24b) and center of gravity frequency (CGF) (Eq. 6.2), the weighted PF (WPF) (Eq. 6.3) is also introduced as an AE feature. The WPF combines the PF and the CGF for an improved representation of the AE signal frequency spectra. Additionally, the total frequency range is divided into six different partial power levels (PP) (Eq. 6.4, Fig. 6.24b). To yield comparable frequency spectra, these features were normalized by their maximum magnitude for eliminating the influence of different source excitation energies. Altogether, these nine frequency features are chosen as input parameters for the pattern recognition approach.

| Center of gravity frequency | $$f_{CGF} = \frac{\int f \cdot \tilde{U}(f) df}{\int \tilde{U}(f) df}$$ | (6.2) |

| Weighted peak frequency | $$\sqrt{f_{PF} \cdot f_{CGF}}$$ | (6.3) |

| Partial power | $$\frac{\int_{f_1}^{f_2} \tilde{U}^2(f) df}{\int_{f_{start}}^{f_{end}} \tilde{U}^2(f) df}$$ | (6.4) |

The UPR algorithm used in the current study tries to find the best possible partition by investigating subset combinations of the features given. Partitions are compared based on cluster validity measures, and the optimum partition that includes the respective feature combination and the number of clusters is returned. The details of this algorithm have been described by Günter and Bunke (2003) and Sause et al. (2012a).

In the present study, all possible subset feature combinations are evaluated, ranging from the predefined minimum number of four features to the maximum nine previously defined features. Thus, in total, 382 possible feature sets are investigated. Another limitation of the algorithm is related to the expected number of signal clusters. Generally, the expected number of clusters should be within the range of the number of actual physical damage phenomena or mechanisms and possibly additional noise sources. The discrimination of different emission phenomena is difficult, although intrinsic damage phenomena are provoked by the applied fiber-load angles because of the complex hierarchical structure of wood and the spectral sensitivity of the AE sensors. Hence, the cluster algorithm is applied to seek for 2, 3, …, 10 possible clusters, which yields 3438 partitions to investigate in total.

The Euclidean distance is the basis for the distance measurement of the dataset inputs. Based on this metric, as cluster validity indices, the Davies-Bouldin index R (Davies and Bouldin 1979), the Tou index τ (Tou 1979), the Rousseeuw's silhouette value S (Rousseeuw 1987), and Gamma statistic σ (Calinski and Harabasz 1974) are calculated to obtain a measure for the cluster separation. A voting scheme combining the rankings of these individual indices yields the partition with the optimal performance based on points, whereby the best possible performance is rated by a maximum of 100 points (Sause et al. 2012a).

Results and discussion

The UPR technique was performed separately for the R and L specimen types. In both cases, one feature combination (rated with 100 points) was found to be the numerically best separation of the AE signals into two clusters (Tab. 6.8). For the R specimens, the obtained feature combination consists of the PF, the CGF, and the WPF as well as PP4. For the L specimens, the feature combination also comprises the PF, CGF, and the WPF, but it is based on PP2 instead. For comparison of the pattern recognition result, the PP4 and the WPF were chosen to present the cluster results of both specimen types (Fig. 6.26) as the significance of the clusters is reflected most clearly by their WPFs.
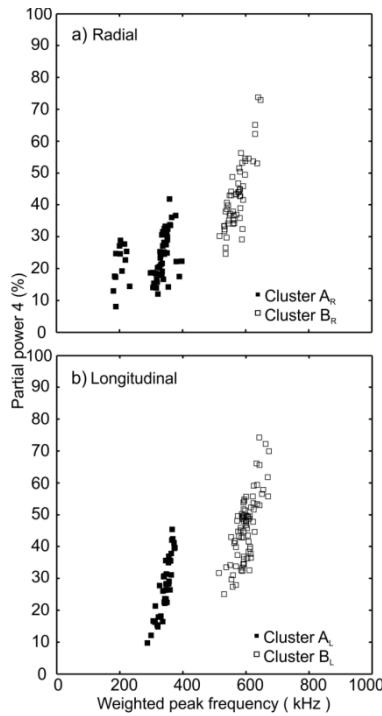
Figure 6.26 The clustering of the AE signals yields the two clusters A and B. Partial power 4 range of 600-800 kHz) versus weighted peak frequency are presented for AE signals detected during tensile testing of the spruce specimens in the a) radial and b) longitudinal directions.

For both specimen types, the signals of cluster A_R (R tests) and A_L (L tests) contain WPFs below 500kHz, while those of cluster B_R and B_L contain WPFs above 500kHz. Furthermore, signals of the B clusters show a larger share of high-frequency content (compared to the A clusters) due to an average PP4 of approximately 40% (Tab. 6.9). Hence, the clusters can

roughly be differentiated into signals with a relatively high share of low-frequency (A clusters) and high-frequency (B clusters) contents, respectively.

For the R tests, 60 signals are assigned to cluster A_R and 55 signals to cluster B_R (Tab. 6.9), which is more or less a ratio of 1:1. Within the damage history (Fig. 6.27), the brittle failure behavior of the R specimens is reflected, as the AE starts just shortly before the ultimate failure (above 70% of maximum load). Furthermore, a clear trend in AE onset is not observable, as the cluster A_R matches with the AE onset in 3 of 7 cases. During load progression, the AE amplitudes of both clusters increase, mainly ranging from 40 dB_{AE} up to 80 dB_{AE}. Near and during the ultimate failure of the R specimens, the maximum AE amplitudes reach values above 80dB_{AE} in both clusters A_R (Fig. 6.27a) and B_R (Fig. 6.27b). Hence, for tensile loading in the R direction, both clusters and their origin mechanisms are assumed to have a rather equal standing in damage evolution.

Table 6.8 Results of clustering of the radial (R) and longitudinal (L) specimens

Type	n	No. C	Points*	FC	R	τ	S	σ
R	7	2	100	28	0.6246	3.0205	0.6325	299
L	7	2	100	10	0. 5605	3. 4826	0.6734	350

Maximal possible points: 100; n…Number of test; No. C…Number of cluster; FC…Feature Combination; R…Davies–Bouldin-index; τ…Tou-index, S…Rousseeuw's Silhouette value; σ… Calinski and Harabasz index.

Feature Combination No. 10: peak frequency, weighted peak frequency, center of gravity frequency, partial power 2 (200-400kHz).

Feature Combination No. 28: peak frequency, weighted peak frequency, center of gravity frequency, partial power 4 (600-800kHz)

Table 6.9 Cluster characteristics

C	N	PF (kHz)	CGF (kHz)	WPF (kHz)	PP 1 (%)	PP 2 (%)	PP 3 (%)	PP 4 (%)	PP 5 (%)	PP 6 (%)
A_R	60	278 (85/376)	399 (286/491)	332 (181/399)	23±10	35±8	16±5	23±7	3±2	0±0
B_R	55	671 (583/723)	495 (412/616)	572 (518/648)	15±7	22±6	16±5	43±11	4±2	0±0
A_L	42	276 (269/290)	439 (300/500)	346 (286/374)	17±8	40±8	11±4	27±9	5±2	1±0
B_L	80	687 (593/737)	524 (383/650)	595 (514/674)	12±6	23±7	12±5	46±10	7±3	1±0

C…Cluster; N…Number of signals; PF…Peak frequency; CGF…Center of gravity frequency; WPF…Weighted peak frequency; PP… Partial power
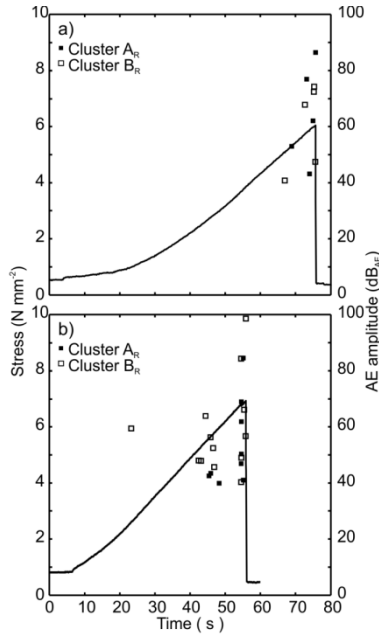
median (min / max); PP: mean ± StdD

Figure 6.27 Stress and AE signal amplitudes versus test duration of two specimens tensile loaded in the radial direction, distinction between both clusters A_R and B_R is included.

Furthermore, in the frequency domain, both clusters reveal broadband spectra with three distinct peaks at approximately 100kHz, 280kHz, and 670kHz (Fig. 6.28c, d). Consistently, the plot of PP4 vs. WPF (Fig. 6.26a) indicates a possible separation of cluster A_R (with low-frequency components) into AE signals with a WPF close to 200kHz and AE signals close to 330kHz. The available miniature sensor is limited to frequencies between 300kHz and 800kHz (Fig. 6.25), and therefore, a low significance in difference of the low-frequency components (compared to that of the high-frequency domain) might be caused by this limitation. Additional research is needed to clarify the role of several parameters (e.g., material properties and specimen geometry) influencing these frequency peaks. However, the cluster A_R is characterized mainly by low-frequency components below 600kHz, which is also reflected in PP1–PP3 containing ca. 75% of the signals' frequency content (Tab. 6.9). The signals of cluster B_R contain more high-frequency components. The normalized average magnitude at the PF of 670kHz is not significantly larger than the comparable peak in cluster A_R (Fig. 6.28c, d). The more significant difference, compared to the cluster A_R, is found in the lower normalized average magnitude at 280kHz. This implies a lower relative share of low-frequency content, which thus results in a relative increase in PP4. To sum up the R tests, both clusters A_R and B_R are essentially differentiated by their relative share of low-frequency content. The normalized average AE signals of clusters A_R and B_R in the

time domain are clearly different (Fig. 6.28a, b). In comparison to the average waveform of cluster A_R, that of cluster B_R is more similar to a characteristic burst signal with fast oscillations vs. time.
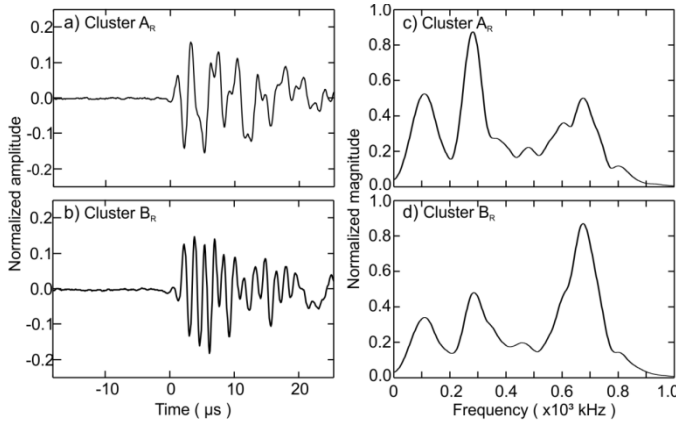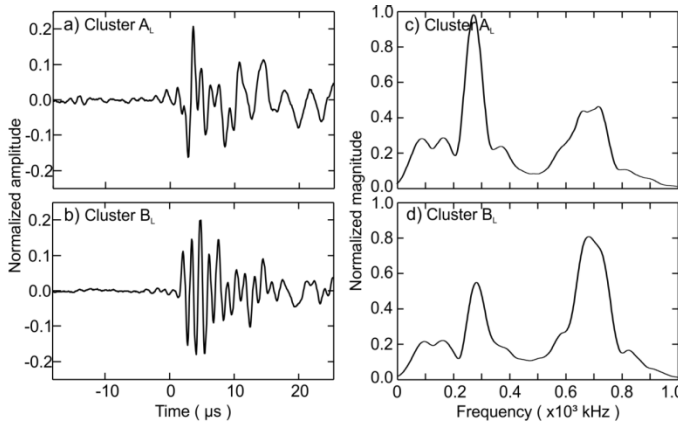

Figure 6.28 Averaged normalized AE signals of cluster A_R (a, b) and cluster B_R (c, d) detected during tensile testing of the spruce specimens in the radial direction. AE signals are presented in time domain (a, c) and frequency domain (b, d).

The ratio of signals attributed to clusters A_L and B_L differs when tensile load is applied in the L direction (42:80), which is different to the R load results (60:55). Moreover, in contrast to the linear behavior of the R specimens (Fig. 6.27), the stress curves while loading parallel to the grain show premature, transient load drops (Fig. 6.29), which are also accompanied by AE signals for both A_L and B_L. The deviations in the stress curves reveal predamages, probably of truncated tracheids on the tapered edges. Analogously to the R tests, the AE onset was generated either by cluster A_L (Fig. 6.29a) or by cluster B_L (Fig. 6.29b). With progressive load application, there is a consistent and corresponding increase in the AE amplitude values (40-80 dB_{AE}) in both signal clusters. Moreover, cluster B_L solely generates the maximum AE amplitudes during the ultimate failures, and thus, cluster B possibly indicates the L specimens' total destruction. Contrary to the R specimens, the generated maximum AE amplitudes generated here generally remain below the 80dB_{AE} (Ando et al. 1992b).

Comparing the normalized average waveform of both clusters in the time domain, the signals of cluster A_L start with a short term of fast oscillations (0-10µs) and level off in slower oscillations (Fig. 6.30a). The average signal of cluster B_L (Fig. 6.30b) shows a burst signal similar to that of cluster B_R. Both clusters reveal broadband spectra, but only two distinctive peaks at approximately 280kHz and 690kHz (Fig. 6.30c, d). Cluster A_L is

characterized mainly by low-frequency components, which are most notably reflected in the contribution of PP2 with approximately 40% of the signals' frequency content (Tab. 6.9). In contrast, the relative share of high-frequency components in cluster B_L is reflected in PP4–PP6, which yields about 54% of the frequency content beyond 600 kHz. Compared to cluster A_L, the magnitude of the peak at 690 kHz in cluster B_L shows a significant increase (Fig. 6.30c, d). This leads to the pronounced differences in PP2 and PP4 between both clusters. Consequently, in contrast to clusters A_R and B_R, clusters A_L and B_L are differentiated by their relative share of high-frequency content.
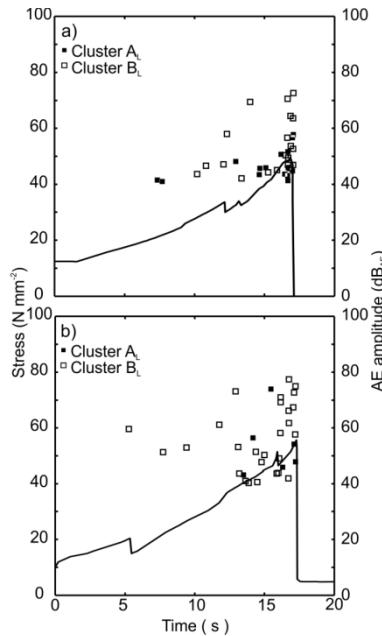
Figure 6.29 Stress and AE signal amplitudes versus test duration of two specimens tensile loaded in the longitudinal direction, distinction between both clusters A_L and B_L is included.

Clusters A and B are almost of similar nature for the R and the L tested specimens (Fig. 6.26), as indicated by the averaged WPF of approximately 340kHz (cluster A_R and A_L) and 580kHz (cluster B_R and B_L), respectively. Thus, it is assumed that the source mechanisms are similar in both specimen types. The peaks at approximately 670–690kHz, observed in all clusters (Fig. 6.28c, d, Fig. 6.30c, d), might be caused by longitudinal waves propagating parallel to tracheid axes and thus correspond to the frequency response of the structural vibration (600kHz up to 700kHz) (Bucur 2006). Tyree and Sperry (1989) suggested that cellulose induces the high-frequency components. At microscopic scale, the transcellular fracture yields rapid crack growths (Debaise et al. 1966). With respect to the

characteristic WPFs of the AE clusters, it is worth considering that the signature of such rapid crack growths might well be reflected within both B clusters, especially with regard to the ultimate failure of all seven L specimens generating the maximum amplitudes seen solely in cluster B_L (Fig. 6.29).

Figure 6.30 Averaged normalized AE signals of cluster A_L (a, b) and cluster B_L (c, d) detected during tensile testing of the spruce specimens in the longitudinal direction. AE signals are presented in time domain (a, c) and frequency domain (b, d).

For interpreting the low-frequency A clusters (Fig. 6.26), the 1:1 ratio of the AE signals observed in clusters A_R and B_R for R tests gives a first hint. Following Ashby et al. (1985) a ratio of the material density (Tab. 6.7) to the cell wall density (1500kg m^{-3}) above 0.2 indicates the phenomena of cell wall cracks as well as cell separation, which also applies to the tested material. Thus, since the B clusters are assigned to rapid cell wall cracks, the formation of the A clusters could tentatively be attributed to slow cell separation phenomena.

Since the AE amplitude values for both signal clusters increase more or less alike, the attributed damage mechanisms are not restricted to certain amplitude values as expected by Ando et al. (1992a) or Romhány et al. (2003). Instead, this might reflect the complexity in failure behavior due to the cellular composition resulting from the strong interaction between both cellulose fibrils and the lignin matrix.

Conclusions

This preliminary study introduces a new approach of UPR to identify clusters of AE signals detected on wood under tensile stress. For each loading case, tensile loading spruce specimens in the R and L directions, the two clusters A and B of AE signals were detected: AE signals of cluster A are characterized by WPFs of approximately 340kHz, whereby those

of cluster B yield WPFs of approximately 580kHz. A first working hypothesis assumes the A clusters to indicate slow crack growth such as cell separation mechanisms, whereas the B clusters are attributed to transcellular cracks. To provide a substantial evidence of the cluster's origin, subsequent experiments combining this setup with synchronous SRµCT monitoring are continued in another study.

Acknowledgement

References

Aicher, S., Höfflin, L., Dill-Langer, G. (2001) Damage evolution and acoustic emission of wood at tension perpendicular to fiber. Holz Roh Werkst. 59:104–116.

Ando, K., Ohta, M., Sato, K., Okano, T. (1992a) Mechanical Behavior of Materials – VI. Fracture Mechanism and Acoustic Emission Characteristics of Wood. Pergamon Press Ltd., Oxford, 1992. pp. d129–d134.

Ando, K., Sato, K., Fushitani, M. (1992b) Fracture-toughness and acoustic-emission characteristics of wood. 2. Effects of grain angle. Mokuzai Gakkaishi 38:342–349.

Ansell, M.P. (1982) Acoustic emission from softwoods in tension. Wood Sci. Technol. 16:35–57.

Ashby, M.F., Easterling, K.E., Harrysson, R., Maiti, S.K. (1985) The fracture and toughness of woods. Proc. R. Soc. Lond. A 261–280.

Bucur, V. (2006) 4.3 System measurment. In: Acoustics of Wood. Eds. T.E. Timell and R. Wimmer. Springer, Berlin. pp. 71–81.

Bucur, V., Böhnke, I. (1994) Factors affecting ultrasonic measurements in solid wood. Ultrasonics 32:385–390.

Calinski, R., Harabasz, J. (1974) A dendrite method for cluster analysis. Commun. Stat. 3:1–27.

Cunderlik, I., Molinski, W., Raczkowski, J. (1996) The monitoring of drying cracks in the tension and opposite wood by acoustic emission and scanning electron microscopy methods. Holzforschung 50:258–262.

Davies, D.L., Bouldin, D.W. (1979) A cluster separation measure. IEEE Trans. Pattern Anal. Mach. Intell. 1:224–227.

Debaise, G.R., Porter, A.W., Pentoney, R.E. (1966) Morphology and mechanics of wood fracture. Mater. Res. Standard. 6:493–499.

Fratzl, P., Burgert, I., Gupta, H.S. (2004) On the role of interface polymers for the mechanics of natural polymeric composites. Phys. Chem. Chem. Phys. 6:5575–5579.

Frühmann, K., Burgert, I., Stanzl-Tschegg, S. (2003) Detection of fracture path under tensile loads through in situ tests in an ESEM chamber. Holzforschung 57:326–332.

Günter, S., Bunke, H. (2003) Validation indices for graph clustering. Pattern Recognit. Lett. 24:1107–1113.

Hofstetter, K., Hellmich, Ch., Eberhardsteiner, J., Mang, H.A. (2008) Mechanics of advanced materials and structures. Mech. Adv. Mater. Struct. 15:474–484.

Jakiela, S., Bratasz, L., Kozlowski, R. (2008) Acoustic emission for tracing fracture intensity in lime wood due to climatic variations. Wood Sci. Technol. 42:269–279.

Kim, K.B., Kang, H.Y., Yoon, D.J., Choi M.Y. (2005) Pattern classification of acoustic emission signals during wood drying by principal component analysis and artificial neural network. Key Eng. Mater. 297–300:1962–1967.

Kurz, H., Köppel, S., Linzer, L., Schechinger, B., Grosse, C., Source location, In: Acoustic Emission Testing in Engineering - Basics and Applications (Eds. Grosse, C., Ohtsu, M.), Heidelberg: Springer Publ. 2008, pp.101-147.

Lanvermann, C., Evans, R., Schmitt, U., Hering, S., Niemz, P. (2013) Distribution of structure and lignin within growth rings of Norway spruce. Wood Sci. Technol. 47:627–641.

Lee, S.-H., Quarles, S.L., Schniewind, A.P. (1996) Wood fracture, acoustic emission, and drying process. Part 2. Acoustic emission pattern recognition analysis. Wood Sci. Technol. 30:283–292.

Müller, U., Gindl, W., Teischinger, A. (2003) Effects of cell wall anatomy on the plastic and elastic behaviour of different wood species loaded perpendicular to grain. IAWA J. 24:117–128.

Ogino, S., Kaino, K., Suzuki, M. (1986) Prediction of lumber checking during drying by means of acoustic emission technique. J Acoust Emis 5:61–65.

Pardee, W.J., Graham, L.J. (1978) Frequency analysis of two types of simulated acoustic emissions. J. Acoust. Soc. Am. 63:793–799.

Reiterer, A., Stanzl-Tschegg, S.E., Tschegg, E.K. (2000) Mode I fracture and acoustic emission of softwood and hardwood. Wood Sci. Technol. 34:417–430.

Romhány, G., Karger-Kocsis, J., Czigany, T. (2003) Tensile fracture and failure behavior of technical flax fibers. J. Appl. Polym. Sci. 90:3638–3645.

Rosner, S. (2012) Waveform features of acoustic emission provide information about reversible and irreversible processes during spruce sapwood drying. BioResources 7:1253–1263.

Rousseeuw, P.J. (1987) Silhouettes: a graphical aid to the interpretation and validation of cluster analysis. J. Comput. Appl. Math. 20:53–65.

Saavedra Flores, E.I., Friswell, M.I. (2013) Ultrastructural mechanisms of deformation and failure in wood under tension. Int. J. Solids Struct. 50:2050–2060.

Sause, M.G.R., Gribov, A., Unwin, A.R., Horn, S. (2012a) Pattern recognition approach to identify natural clusters of acoustic emission signals. Pattern Recognit. Lett. 33:17–23.

Sause, M.G.R., Müller, T., Horoschenkoff, A., Horn, S. (2012b) Quantification of failure mechanisms in mode-I loading of fiber reinforced plastics utilizing acoustic emission analysis. Compos. Sci. Technol. 72:167–174.

Sonderegger, W., Alter, P., Niemz, P. (2008) Investigations on selected properties of tonal wood of spruce from Grisons. Holz Roh Werkst. 66:345–354.

Stephens, R.W.B., Pollock, A.A. (1971) Waveforms and frequency spectra of acoustic emission. J. Acoust. Soc. Am. 50:904–910.

Tou, J.T. (1979) DYNOC – a dynamic optimal cluster-seeking technique. Int. J. Comput. Inform. Sci. 8:41–547.

Tyree, M.T., Sperry, J.S. (1989) Characterization and propagation of acoustic emission signals in woody plants: towards an improved acoustic emission counter. Plant Cell Environ. 12:371–382.

Wagenführ, R. Holzatlas. Fachbuchverlag, Leipzig, 2000. pp. 177–178.

Zauner, M., Keunecke, D., Mokso, R., Stampanoni, M., Niemz, P. (2012) Synchrotron-based tomographic microscopy (SbTM) of wood: development of a testing device and observation of plastic deformation of uniaxially compressed Norway spruce samples. Holzforschung 66:973–979.

6.5 Paper IV

Damage evolution in wood: synchrotron radiation micro-computed tomography (SRµCT) as a complementary tool for interpreting acoustic emission (AE) behavior

Franziska Baensch[1], Michaela Zauner[1], Sergio J. Sanabria[1], Markus G.R. Sause[2], Bernd R. Pinzer[3,5], Andreas J. Brunner[4], Marco Stampanoni[3] and Peter Niemz[1]

[1]ETH Zurich – Institute for Building Materials, CH-8093 Zürich, Switzerland

[2]University of Augsburg – Institute for Physics, Experimental Physics II, D-86135 Augsburg, Germany

[3]Swiss Light Source, Paul Scherrer Institut, CH-5232 Villigen, Switzerland

[4]Swiss Federal Laboratories for Materials Science and Technology – Laboratory for Mechanical Systems Engineering, CH-8600 Dübendorf, Switzerland

Corresponding author: Franziska Baensch, ETH Zurich – Institute for Building Materials, CH-8093 Zürich, Switzerland, Email: fbaensch@hnee.de

Abstract

Tensile tests of miniature spruce wood specimens have been performed to investigate the damage evolution in wood at the microscopic scale. For this purpose, the samples were stepwise tensile loaded in the longitudinal (L) and radial (R) directions and the damage evolution was monitored in real-time by acoustic emission (AE) and synchrotron radiation micro-computed tomography (SRµCT). This combination is of outstanding benefit as SRµCT monitoring provides an insight on the crack evolution and the final fracture at microscopic scale, whereas AE permits the detection of the associated accumulation and interaction of single damage events on all length scales with high time resolution. A significant drawback of the AE testing of wood has been overcome by means of calibrating the AE amplitudes with the underlying crack length development. Thus, a setup-dependent and wood species-dependent calibration value was estimated, which associates $1\mu m^2$ crack area with generating of 0.0038mV in the detected AE amplitude. Furthermore, for both L

and R specimens, AE signals were classified into two clusters by using a frequency-based approach of unsupervised pattern recognition. The shares of AE signals of both clusters correlate with the ratio of the relative crack area of the interwall and transwall cracks gained from the fractographic analysis of SRµCT scans.

Keywords

Introduction

The observation of the complex hierarchical interdependency of damage phenomena within the wooden structure is a key challenge (Frühmann et al. 2003; Saavedra Flores and Friswell 2013). For an improved understanding of the failure behavior, the acoustic emission (AE) measurement is a useful tool that enables a multiscale analysis of the damage progress with respect to load history in the whole specimen's volume. An additional advantage of the AE method is the high time resolution during the recording of defect generation. However, the interpretation of AE data is difficult concerning the signal's origin. In a previous study (Baensch et al. 2015) a new unsupervised pattern recognition (UPR) technique based on AE frequency features was adopted for wood. This algorithm, which had already been established for composite materials (Sause et al. 2012a, b), seeks for the numerically best partition of selected frequency features to identify the natural classes of AE signals.

A substantial and detailed interpretation of these AE clusters requires additional information. For this purpose, in situ X-ray tomography is suitable, as it allows a comprehensive 3D observation of microstructures (Cazaux et al. 1993; Stampanoni et al. 2006). Further, the feasibility of real-time studies on submacroscopic damage mechanisms by combining synchronous AE and tomographic monitoring has already been proven for several materials (Chotard et al. 2003; Elaqra et al. 2007), whereby an effective pixel length down to 15µm was reached. Another study was performed on metals yielding a spatial resolution of even $1.4µm^3$ (Maire et al. 2007). For the investigation of the anatomical features of the wooden microstructure, the suitability of micro-computed tomography proves to be satisfactory, because a spatial resolution down to $1µm^3$ is feasible (Steppe et al. 2004; Trtik et al. 2007; Van den Bulcke et al. 2009). The microstructure of wood under different moisture loads has also been investigated by synchrotron radiation micro-computed tomography (SRµCT) (Derome et al. 2011). Moreover, for a miniature wood specimen under bending load, Forsberg et al. (2008) showed the potential of the SRµCT method to

evaluate the deformation at microscale by means of digital volume correlation. In the present study, tensile tests of miniature spruce wood specimens will be performed to investigate the damage evolution in wood at the microscopic scale, which should be simultaneously monitored by AE and SRµCT. The expectation is that the SRµCT results will provide complementary evidence for interpreting AE signal clusters already presented in a previous study by Baensch et al. 2015.

Materials and Method

The investigations were carried out on approximately 250-year-old clear spruce wood (*Picea abies* (L.) Karst.) grown at 1000 m altitude in the canton of Grisons (Switzerland). The specimens were taken from the same wood stock whose mechanical properties were already described by Sonderegger et al. (2008) and Baensch et al. 2015.
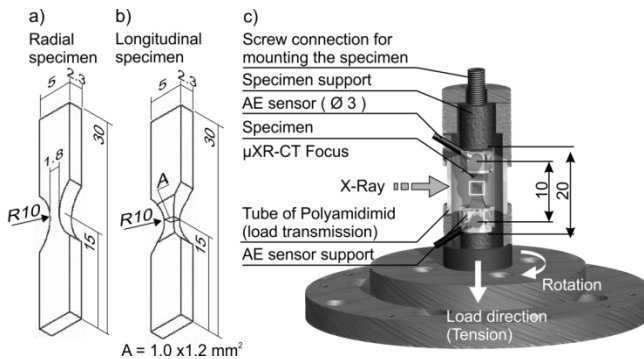
Figure 6.31 Specimen geometries and experimental design.

Two specimens differing in fiber-load-angle were in focus. The radial (R) specimen was loaded in the R direction, and the longitudinal (L) specimen was loaded parallel to the grain (Fig. 6.31a, b), whereby an L specimen was selected that only contained earlywood within the tested cross-section. The specimens were manufactured from blanks with dimensions of $30 \times 5.7 \times 2.3 mm^3$ (length×width×thickness). To ensure a defined crack initiation within the volume of interest (VOI), which can be monitored by both AE and SRµCT (Fig. 6.31c), the specimens were tapered. The L specimen was taper shaped at all four sides, yielding a test cross-section of $1 mm^2$ (Fig. 6.31b), whereas the R specimen had only a two-sided taper of approximately $4 mm^2$ test cross-section (Fig. 6.31a), which could not be reduced further due to the fragile structure. The specimen geometry is in accordance with that tested by Baensch et al. 2015.

The SRµCT trials were carried out at the TOMCAT beam line, a synchrotron beamline at the Paul Scherrer Institute in Villigen, Switzerland (Stampanoni et al. 2007). The tensile tests were performed with a loading device (load cell of 1kN) for miniature specimens designed for implementation at the synchrotron beam line (Zauner et al. 2012). The R specimen was loaded with a cross-head speed of 0.005mm s^{-1} and the L specimen was loaded with 0.01mm s^{-1} (Tab. 6.10). For load transmission, a plug system of three tubes was put over the specimen and fixed by a thread washer at the upper end (Fig. 6.31c). This three-pieced plug system was needed to facilitate the mounting of AE sensors. The center tube was made of polyamideimide (PAI 4203, Fa. Quadrant EPP Deutschland GmbH, Sinsheim, Germany). The duroplast PAI (165 MPa compression strength) was suitable for the SRµCT monitoring of load tests on wood specimens because of its low absorption of the radiation.

Table 6.10 Characterization of the investigated spruce wood specimens

Specimen	Density kg m^{-3}	Moisture content %	Cross section mm^2	Speed of traverse mm sec^{-1}	Load steps -
L	349	8.3	1.20	0.010	5
R	342	7.8	4.15	0.005	2

Specimen	Test duration min	Strength MPa	SRµCT resolution µm px^{-1}	Thickness of cell wall µm px^{-1}	Acoustic velocity* m s^{-1}
L	107	54.3	0.65	5.2±1.5	6000
R	89	6.3	1.62	8.1±1.1	2200

Sonderegger et al. 2008

To enhance the contrast of the X-ray images, a propagation based phase-contrast reconstruction algorithm was applied (Paganin et al. 2002). The details on the SRµCT monitoring parameters are presented in Tab. 6.11. The resolution was changed for both specimen types, allowing a field of view large enough to monitor the total VOI of the taper shape. Thus, for the L specimen, a digital resolution of 0.65µm px^{-1} could be realized, whereas, in the case of the R specimen, a lower digital resolution of 1.62µm px^{-1} was reached. AE monitoring was performed with a digital AE equipment (AMSY-6, Vallen Systeme GmbH, Icking, Germany). Two miniature piezoelectric sensors (type M31, Fuji Ceramics Corp. Shizuoka, Japan) with a coupling area of 3 mm diameter were mounted single sided on the surface of the specimen (Fig. 6.31c). The sensor coupling was achieved by silicone-free vacuum grease (Poellath J.P. Labortechnik, Bamberg, Germany). AE sensors were sensitive to the frequency range of 300-800kHz. The frequency range of the

preamplifiers (AEP3, gain of 34dB into 50Ω, Vallen Systeme GmbH, Icking, Germany) was limited to the range from 30 to 960kHz. Moreover, guard sensors (SE 150-M, Dunegan Engineering Co., Inc. Midland, USA) were mounted onto the testing device and on the mounting table at the beam line.

Table 6.11 Acquisition settings for SRµCT monitoring

Energy of radiation	20 keV
Mode	Phase contrast
Scintigram size recorded by CCD camera	2048 px x 2048 px
Rotation	180° in 0.12° steps
Projections	1501
Dark field projections	32
White field projections	150
Recording time of one scan	6 minutes
Monitoring the longitudinal specimen objective UPLAPO10x	
Field of view, digital resolution	1.43 x 1.43mm^2, 0.65µm px^{-1}
Monitoring the radial specimen with the objective UPLAPO4x	
Field of view, digital resolution	3.58 x 3.58mm^2, 1.62µm px^{-1}

For AE analysis, only the first signal of an AE event detected by both sensors (maximum distance of 10 mm) was evaluated by means of 1D localization (Kurz et al. 2008). AE signals were windowed with a Hamming window function (Tab. 6.12), and the selected frequency features were extracted from the frequency spectra. For the UPR algorithm, nine features in total (Tab. 6.13) were chosen as input, namely, the peak frequency (PF), the center of gravity frequency (CGF), weighted peak frequency (WPF), and six partial power (PP) levels (Sause et al. 2012a).

Before each test, the specimens were preloaded to < 20% of the ultimate stress and an initial SRµCT of the intact structure was recorded. The tensile tests were performed stepwise by stopping the traverse at predetermined positions, which were preliminarily defined with respect to the predicted AE occurrence. Specifically, in pre-tests (Baensch et al. 2015), the AE onset was evaluated by means of the applied traverse displacement. Before and after each load step, the quality of the AE sensor coupling was checked by autocalibration (in the course of which, each sensor served subsequently as an emitter and a sensor). When the displacement ceased, the load immediately decreased, indicating the relaxation processes of the wood.

Table 6.12 Acquisition of AE waveform detection and settings of frequency spectra calculation

Threshold setting	32.1 dB$_{AE}$ ($\approx$ 0.04 mV)
Rearm time	1 ms
Sampling rate	10 MHz
Signal duration	409.6 µs, 18 µs pre-trigger included
Signal evaluation	First signal of AE event based on 1D-localization
Fourier Transformation of waveform	
Extraction window in time domain:	First 256 samples of the waveform
	0 µs - 25.6 µs (18 µs pre-trigger excluded)
Window function:	Hamming window of 256 samples
Frequency spectra	0-1200 kHz

Table 6.13 AE frequency features used to perform the unsupervised pattern recognition

Feature	Abbrev.	Definition	
Amplitude (mV)	A	Measured AE Amplitude (mV)	
Peak frequency	PF	Frequency of maximum magnitude in frequency spectrum	
Center of gravity frequency	CGF	$\dfrac{\int f \cdot \tilde{U}(f)df}{\int \tilde{U}(f)df}$	
Weighted peak frequency	WPF	$\sqrt{f_{PF} \cdot f_{CGF}}$	
Partial Power	PP	$\dfrac{\int\limits_{f_1}^{f_2} \tilde{U}^2(f)df}{\int\limits_{f_{start}}^{f_{end}} \tilde{U}^2(f)df}$	PP1: 0 - 200 kHz PP2: 200 - 400 kHz PP3: 400 - 600 kHz PP4: 600 - 800 kHz PP5: 800 - 1000 kHz PP6: 1000 - 1200 kHz

To minimize the risk of recording artifacts (structural movement) within the tomograms due to relaxation, an idle time of 1–2 min was allowed before starting the SRµCT scan, which was also monitored by AE. However, performing the SRµCT scan might have a destructive impact on the tiny, wooden test cross-section due to relaxation processes during the time the

traverse is arrested. For this reason, only selected SRμCT scans were performed. Thus, the tests imply a sequence of test stages comprising one or more loading steps, which are completed by one SRμCT scan. The tests were continued up to the ultimate failure of the specimens. AE and SRμCT data were synchronized by the load signal output of the testing device.

Results

UPR

For each specimen, the UPR technique yielded the numerically best separation of the detected AE into two clusters (Fig. 6.32). These clusters (Fig. 6.32, black circles) are in good agreement with those from the pre-investigation (without SRμCT) by Baensch et al. (2015) (Fig. 6.32, gray squares); thus, the validity of the tests is proven. One cluster (A) comprises AE events of a relatively high share of low-frequency components, expressed by an average WPF of approximately 350kHz. In contrast, the other cluster (B) contains AE events of a relatively high share of high-frequency components, which is characterized by an average WPF of approximately 575kHz. A first working hypothesis to explain this AE behavior assumed that the A clusters indicated slow crack growths (e.g., cell separation mechanisms), whereas the B clusters signified brittle crack growths due to cell wall cracks (Baensch et al. 2015).
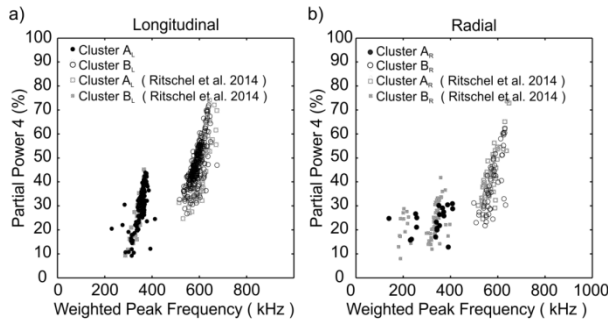
Figure 6.32 The clustering of the AE signals yields the two clusters A and B. Partial power 4 versus weighted peak frequency (Table 6.13) are presented for AE signals detected during tensile tests on spruce specimens loaded in the a) longitudinal and b) radial direction. The reproducibility of the clusters is demonstrated by comparing the seven pre-trial results in the laboratory (gray squares) with the specimens tested at the SRμCT beamline (black circles).

L specimen

During four test stages (I–IV), a total of eight load steps were applied to the L specimen until its ultimate failure (Fig. 6.33). AE and SRμCT monitoring gained complete data sets

for the test stages I to III (Fig. 6.33a–c), whereas an SRμCT scan of the fractured specimen after the last test stage IV (Fig. 6.33d) yielded insufficient quality for reconstruction on account of the artifacts that distorted the tomograms due to the movement of the specimens. The cuboid in Fig. 6.34a represents the volume ($650{\times}650{\times}650\mu m^3$) including all damages detected by SRμCT until the test stage III. In total, the observed cracks affected approximately 140 tracheids, which is equivalent to 10% of the tracheids within the entire VOI of the specimen.
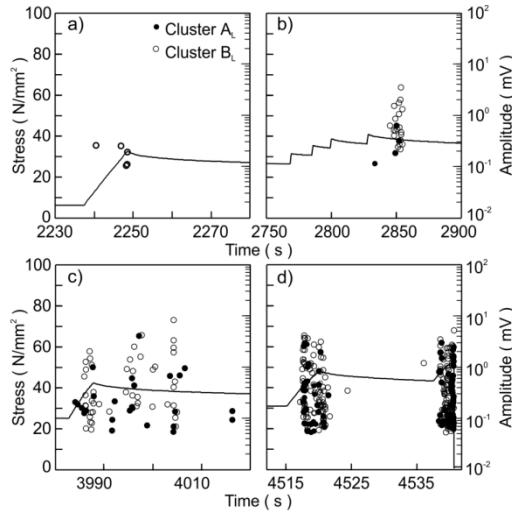
Figure 6.33. Tensile test on the longitudinal specimen: a) test stage I, b) test stage II, c) test stage III and d) test stage IV with the ultimate failure (load step 8). Stress and AE signal amplitude vs. test duration. The two AE signal clusters A_L and B_L are separated in plots.

During the first load step (Fig. 6.33a), only AE events of cluster B_L were generated. However, in light of the pre-investigations consistent with the current results (Baernsch et al. 2015), the cluster type matching the AE onset is rather random. In the test stage II (Fig. 6.33b), the traverse was displaced four times to yield a sufficient stress application for AE generation. Because no AE was detected during the first three steps, a SRμCT scan was not performed. However, AE was detected during relaxation after the fourth traverse displacement in the test stage II, whereby cluster B_L already yielded AE amplitudes more than 3mV (Tab. 6.14). During the test stage III (sixth load step) and the subsequent relaxation (Fig. 6.33c), cluster B_L yielded the maximum AE amplitude of 8.4mV for the whole test, whereas cluster A_L only generated AE amplitudes < 4.1mV (Tab. 6.14). During the last two load steps in the test stage IV (Fig. 6.33d; Tab. 6.14, steps 7 and 8), the intention to increase the load application until the ultimate failure of the L specimen was achieved. For this reason, a SRμCT scan was omitted after the seventh load step. For both load steps 7

and 8, the generated AE showed a high number of signals in both clusters with a wide range of AE amplitudes.

Table 6.14 AE Parameters of the loading steps for the longitudinal and radial specimen

Specimen	Test stage	Load step	N (-)	Minimum AE amplitude Cluster A / B (mV)	Maximum AE amplitude Cluster A / B (mV)	Cumulative AE amplitude Cluster A / B (mV)
L	I	1	0 / 5	- / 0.10	- / 0.26	- / 0.92
	II	2-5	5 / 19	0.12 / 0.22	0.64 / 3.56	1.60 / 17.41
	III	6	25 / 46	0.05 / 0.06	4.09 / 8.37	11.00 / 42.57
	IV	7	35 / 88	0.07 / 0.05	2.99 / 4.19	22.25 / 67.14
		8	58 / 96	0.07 / 0.05	3.06 / 4.19	27.59 / 66.48
R		1	3 / 7	0.06 / 0.09	4.44 / 15.40	4.57 / 20.41
		2	17 / 41	0.04 / 0.04	52.27 / 35.86	156.03 / 102.86

N...Number of AE events of the clusters A / B
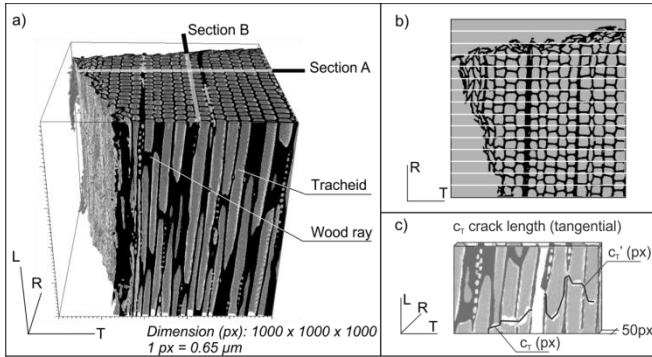
Figure 6.34 a) Initial state of the longitudinal tested specimen. This cubic section includes the state of crack after the load steps 1-3. Dimension: 650 x 650 x 650 μm^3. Resolution of the reconstruction: 1 Pixel (px) = 0.65 μm. The sections A and B are shown in detail in Figure 5. b) For the crack length measurements, the cube is cut into 15 sections of 50 px thickness in the radial direction. c) Crack length c_T is measured along the cell walls in the LT plane for each of these 15 sections. Analogously, the crack length (c_R) is determined. Based on both measurements, the average crack length $\bar{c}$ is estimated.

Although no cracks were observed after the first load step (I), the reconstructions after reloading the specimen (II) revealed significant damages (Fig. 6.35). As the crack is only visible in the surrounding cell wall, 3D volume subsets visualize the cell walls rather than single slice images. Thus, with respect to the average tracheid dimensions in the radial-tangential (RT) plane, the selected volume (Fig. 6.34a) was cut along the R direction into 15 sections of 50px thickness (32.5μm) corresponding to the white lines marked in the RT

plane in Figure 6.34b. Additionally, this subdivision into 15 sections was repeated along the tangential (T) direction. The diameter of one tracheid (27±3.7μm) is smaller than the section's thickness (32.5μm); therefore, the focus was only on one boundary containing cell walls of the two connected tracheids within the sections.

1 - Wood ray   2 - Tracheid end 3 - Tracheids 4 - Truncated cell wall of tracheid
a - Crack tip   b - Trans-wall crack   c - Trans- & Inter-wall crack

Dimension (L T R): 650 μm x 650μm x 33μm
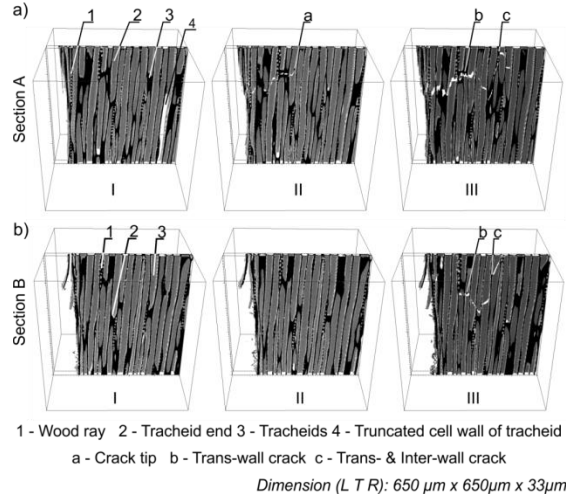
Figure 6.35 Crack growths through the microscopic structure of the longitudinal stressed specimen. The cube represents the part of the specimen involving the whole crack evolution detected after load steps 2 and 3. a) In section A the crack growth is tracked in the LT-plane. b) In section B the crack growth is tracked in the LR-plane. The dimensions of sections A and B are 650 x 650 x 32.5 μm^3.

For sections A and B (Fig. 6.34a), the initial state and the states of the crack after test stages II and III are presented in Fig. 6.35. After the test stage II, the LT plane in section A already shows cracks crossing the tracheid cell wall boundaries (Fig. 6.35a), which indicates transwall cracks as well as cracks within the middle lamella. The identified crack tip (Fig. 6.35a, detail a) propagated further in the test stage III with larger and stepped displacements (Fig. 6.35a, detail c) in the L direction. Moreover, the crack path avoids passing through the wood rays. The LR plane in section B (Fig. 6.35b) shows no damage in test stage II, whereas the crack path in stage III (Fig. 6.35b, details b and c) also switches its propagation along the L direction. Hence, it seems that interwall cracks are of more relevance during the test stage III than in the earlier stage. This additionally coincides with the ratio of the signal numbers attributed to clusters A_L and B_L, changing from 5:19 after the test stage II to 25:46 after the stage III (Tab. 6.14).

The crack at three different stages (I–III) was recorded by both AE and SRμCT, and a calibration between the results of both methods was attempted. For this purpose, the AE amplitude was taken as a measure of damage magnitude. This approach is probably closest

131

to the amplitude of the elastic wave that is proportional to the newly formed crack area (Radon and Pollock 1972; Lysak 1996; Sause 2010). Thus, the crack area (square micrometer of cell wall matter) and the corresponding cumulative AE amplitudes after each test stage II and III were compared (Tab. 6.15).

Table 6.15 Correlation between crack growth $\bar{c}$ and cumulative AE amplitudes A for the longitudinal specimen

State*	c_R	c_T	$\bar{c}$	$\bar{S}$	$\sum A$	Correlation
	px	px	px	µm^2	mV	%
I	0	0	0	0	0.92	} = 30
II	1470	2088	1780	6016	19.02	
III	5095	6472	5783	19547	73.50	= 100

State of the tested specimen at the test stage

The crack length in both states was measured within the 15 SRµCT sections along the R direction as well as along the T direction (Fig. 6.34c). The crack length is measured within the tracheid cell wall volume containing both cell walls of two adjacent tracheids. The average crack length c was estimated from the measured crack length, once in the R direction c_R and a second time in the T direction c_T (Fig. 6.34c) for the stages II and III (Tab. 6.15). For the L specimen, the averaged double cell wall thickness c_{cw} is of 5.2µm (Tab. 6.10). Hence, the averaged crack area $\bar{S}$ (Tab. 6.15) is calculated based on the averaged crack length c and on the double cell wall thickness t_{cw} (Eq. 6.5).

$$\bar{S} = 0.65 \frac{\text{µm}}{\text{px}} \times \bar{c}(\text{px}) \times t_{CW}(\text{µm}) \qquad (6.5)$$

The crack size in the ultimate failed state is unknown; thus, the crack area after the test stage III (19547µm^2) is defined as 100% (Tab. 6.15, III). The corresponding AE amplitude of 73.5mV cumulated for stages I to III is equally defined as 100%. With respect to the crack size at the test stage III, the crack area measured after the test stage II is 30% (Tab. 6.15). Although no damages were found within the sample reconstruction of the SRµCT scan after the test stage I (possibly due to relaxation and crack closing processes), the AE detected there indicates initial pre-damages of the later crack. As a result, the AE amplitudes of the test stages I and II are summed up, also yielding 30% of the total cumulative AE amplitude. By this, the cumulative AE amplitude is found to behave proportionally to the area of the crack (Lysak 1996). Based on this, a scale factor b was approximated by the ratio of the cumulative amplitude A (73.5mV) to the averaged crack area S (19547µm^2) at the test stage III (Eq. 6.6)

$$b = \frac{\sum A}{\sum \bar{S}} = 0.0038 \ \frac{mV}{\mu m^2} \tag{6.6}$$

However, the amplitude of AE events is setup dependent; therefore, SRµCT is required to calibrate the coefficient b for crack size measurements. For the tests presented here, a crack area of $1\mu m^2$ is associated to approximately 0.0038mV in the detected AE amplitude (Eq. 6.6). This correlation allows an estimation of the length scale of the damage events detected in AE. Consequently, the threshold setting of 0.04mV might enable detecting damage events that are too small for observation within the tomograms. The correlating crack area of approximately $10.5\mu m^2$ (whereas the averaged double cell wall thickness is 5.2µm) implies a crack length of 2µm, which falls beyond the effective resolution of the SRµCT measurements. The same applies for the maximum AE amplitude measured during the first load step (Tab. 6.15, I). During the ultimate failure, the maximum AE amplitude of 8.4mV was generated in cluster B_L (Tab. 6.14), whereby the resulting crack length $\bar{c}$ of approximately 424µm consistently correlates with half the edge length of the specimen's test cross-sections (Tab. 6.10).

Nevertheless, the correlation value of 0.0038mV μm^{-2} has to be treated with caution, as it assumes homogeneous material properties. Thus, a differentiation of the cracking components is lacking, although their Young's modulus has a main impact on the measured AE amplitude (Scruby 1985). For instance, the Young's modulus of lignin in the middle lamellae (3GPa; Cousin 1978) is smaller by a factor of about 10 than that of the cell wall (25GPa; Eder et al. 2009), and this is the reason why cracks in the middle lamellae of $1\mu m^2$ should yield AE amplitudes lower than 0.0038mV. A direct and unambiguous correlation is not feasible between the cumulative AE amplitudes generated by each cluster and the attributed crack types because the crack's origin cell wall layers are difficult to track within the SRµCT reconstructions.

R specimen

The R specimen was tested in two test stages. During the first load step (Fig. 6.36a), 10 AE events were recorded, which already revealed a significant range of AE signal amplitudes (0.06–15.4mV; Tab. 6.14). However, no structural changes and damages were observed within the corresponding SRµCT scan. The second loading reached the maximum stress of 6.7MPa, whereas the ultimate failure of the R specimen occurred during the subsequent relaxation process, a few seconds after the traverse had been stopped (Fig. 6.36b). During the ultimate failure, AE events of both A_R and B_R clusters yielded amplitudes above 10mV (Tab. 6.14). The damage analysis is supported only by the SRµCT scan of the failed state;

thus, the whole fracture surface was analyzed (i.e., particularly the broken specimen's bottom half). The obtained results are exemplarily presented by means of the selected detail C (Fig. 6.37). Detail C has dimensions of $650 \times 650 \times 650 \mu m^3$ and thus represents 10% of the total fracture zone, which is located within the earlywood zone, clearly identifiable by comparing the initial state (Fig. 6.38a) and the failed state (Fig. 6.38b). A fractographic analysis of the fracture zone differentiates between transwall cracks and the peeling of the tracheids by interwall cracks within the middle lamellae or possibly by intrawall cracks within the primary cell wall (cell separation phenomena). The procedure from this analysis performed for the whole fracture zone is demonstrated by detail C in Fig. 6.39a.
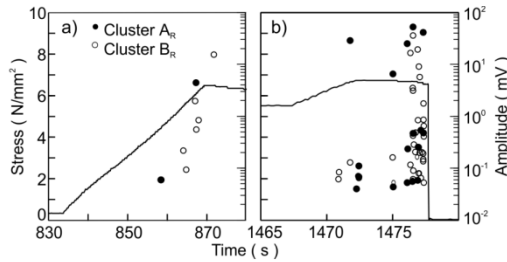
Figure 6.36 Tensile test of the radial specimen: a) load step 1 and b) load step 2 including the ultimate failure. Stress and AE signal amplitude vs. test duration. The two AE signal clusters A_R and B_R are distinguished.

To provide a quantitative assessment of the contribution ratio of both fracture types, the fracture surface was subdivided into units. Each of these units is limited in size to one tracheid in the T direction and $80\mu m$ (50px) in the L direction; see the definition in Fig. 6.39a. A projection map of the damaged surface in the LT plane was obtained, which indicates the relative positions of tracheids and wood rays and further distinguishes the units characterized by transwall cracks or cell separation (Fig. 6.39a). Approximately 70% of the total fracture surface shows cell wall cracks. Overall, 100 wood rays and 50 tracheids are affected, and each of the tracheids shows both damage types.

This observation is in agreement with the study by Ashby et al. (1985), who predicted the occurrence of both cell wall cracks and cell separation phenomena for a ratio of the raw density to the cell wall density ($1500kg\ m^{-3}$) beyond 0.2, as is the case for the spruce wood tested here. The impact of the wood rays' mechanical performance on the crack formation through the walls of the adjacent tracheids becomes obvious, because all parts of those tracheids that completely enclose one wood ray show a similar damage type (Fig. 6.39a).
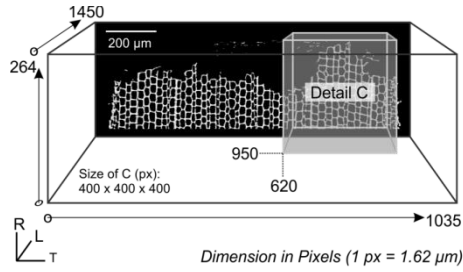
Figure 6.37 The dimension of the fracture zone of the spruce wood specimen tensile loaded in the radial direction is represented by the rectangular box. The back side of the cube shows the fracture path through the RT-plane. Exemplarily, the results are presented for selected detail C. Position and dimension $(650 \times 650 \times 650 \mu m^3)$ are represented by the smaller gray cube. Resolution of the reconstruction from SRμCT monitoring: 1 Pixel (px) = 1.62μm.
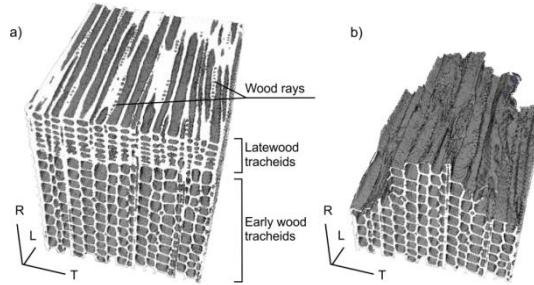
Figure 6.38 Spruce wood specimen tensile stressed in the radial direction. Detail C (650 x 650 x 650 μm^3) at initial state a) and at failed state b).

For an improved visualization of this linkage in the fracture formation (Fig. 6.39b), the intact wood rays were segmented from the reconstruction of the initial state (black) and finally were superimposed onto the reconstruction of the failed state (gray). For the section in Fig. 6.39b, the failure within the earlywood implies three wood rays a to c. The failure in the vicinity of both wood rays a and b occurred close to the latewood zone, and they are assumed to have induced strong reinforcing effects on the adjacent earlywood tissue. In contrast, the weak point of the wood ray c was located deeper inside the earlywood zone. The failure of that wood ray induced a pullout mechanism, yielding a complex tensile shear fracture of the adjacent tracheids in the first row and even in the second row Fig. 6.39b, tracheids 9 and 10). The mechanical performance of wood rays and their position relative to each other affect the magnitude of the damage events (Reiterer et al. 2002) and, therefore, influence the AE amplitude during loading the tissue in R direction.
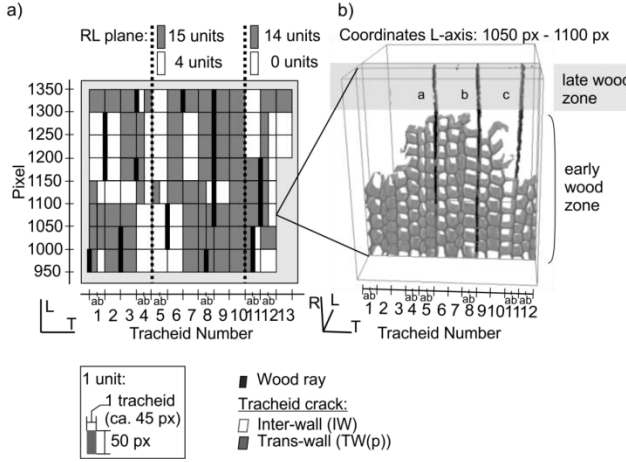
Figure 6.39 Fractographic analysis a) Fracture surface of detail C presented as a 2D projection pattern (LT plane). For the fractographic analysis, the surface is divided into units. In the longitudinal direction, the length of one unit is 50 px (~80 μm), in the tangential direction the size of one unit is due to one tracheid. Cell wall cracks and cell separation are differentiated in the TL plane. In the RL-plane the complex shear fractures include 29 units of cell wall cracks and 4 units of cell separation. b) Section of the fracture zone from the detail C (L-axis: 1050-1100 px). For visualization of the wood rays' influence on damage development, the intact wood rays segmented at the initial state (dark colored) are superimposed on the reconstruction of the ultimate failure (gray colored). For orientation, the late wood zone is highlighted. Wood rays a and b failed close to the late wood zone. The weak point of wood ray c, located deeper within the early wood zone, led to tensile shear failure in the RL-plane.

The scale factor b (Eq. 6.6) was applied to AE signals detected during the first load application of the R specimen, for which a maximum AE amplitude of 15mV ($\approx$3950μm^2) was monitored, whereas the damage was not detected in the SRμCT scans. Taking into account the double cell wall thickness of 8μm (Tab. 6.10), the correlated averaged crack length c (Eq. 6.6) of approximately 490μm ($\approx$305px; resolution of 1.62μm px^{-1}) is physically possible, particularly because this AE event of cluster B$_R$ is assumed to be cell wall damage. If the crack would not have affected the cell wall of two adjacent tracheids and would occur only within the cell wall of one single tracheid, it would not be detectable. within the SRμCT scan. Another explanation could be the possibility that the crack closes during the relaxation process before the SRμCT scan is performed. The ultimate failure generated maximum AE amplitudes of 36mV in cluster B$_R$ (Tab. 6.14), correlating with an averaged crack length $\bar{c}$ of approximately 1180μm, which is more or less half the edge length of the specimen's test cross-section (Fig. 6.31a; Tab. 6.10).

Moreover, a correlation between fiber breakage and the number of detected AE events can be assumed, which is also usually the case in composite materials (Harris et al. 1972). Based on this, the ratio of the relative crack area of the cell wall crack (67%) and cell separation

136

(33%) estimated from SRμCT also might be reflected by the relative number of detected AE events due to cluster B_R (70%) and cluster A_R (30%) (Tab. 6.14).

Conclusion

Tensile tests on miniature spruce specimens, R and L loaded under tension, were monitored by AE and simultaneously by SRμCT. This combination is very useful because the SRμCT monitoring provides insight on the microscopic structure of tested specimens under initial, crack evolution, and final fracture development. AE is a supplementary data source, which makes possible to detect the associated crack formation and propagation in the spatial domain, which results from the accumulation and interaction of single damage events.

The 3D SRμCT monitoring yields the following main observations at the microscopic level: the crack path usually avoids crossing wood rays, which are the weak points within the wood structure when loading in the L direction. For tensile loading in the R direction, the main impact of the reinforcing wood rays on the fracture pattern shows similar damage types observed for those tracheids that completely enclose one wood ray. Each single tracheid within the fracture zone shows both transwall and interwall cracks.

An approximate correlation between the crack size from SRμCT scan and the crack formation detected by AE was obtained: a crack area of $1\mu m^2$ was associated to approximately 0.0038mV in the detected setup-dependent and wood species-dependent AE amplitude. Depending on the threshold setting of 0.04mV, the AE method turned out to be sensitive to minimum defect sizes of $10.5\mu m^2$, which scales with the tracheid cell wall's thickness.

Two clusters were determined by means of the frequency based UPR approach. This supports the previously outlined hypothesis that the low-frequency cluster A is assignable to interwall cracks and the high-frequency cluster B to cell wall cracks in the tracheids. For the L specimen, the increasing share of AE events due to the cluster A_L seems to correlate with more pronounced crack propagation switching parallel to the grain. For the R specimen, the shares of AE events of both clusters A_R and B_R (30%/70%) correlate with the ratio of the relative crack area of the cell wall crack (67%) and cell separation (33%) estimated from the fractographic analysis.

Further insights may be obtained by performing a 3D morphological analysis of SRμCT scans for the evaluation of the deformation at the individual cell scale for the different load states as well as by simulating the AE waves' origin from the damage process and their propagation in the wood materials.

References

Ashby, M. F., Easterling, K. E., Harrysson R., Maiti, S.K. (1985) The fracture and toughness of woods. Proc. R. Soc. Lond. A:261-280.

Baensch, F., Sause, M.G.R., Brunner, A. J., Niemz, P. (2015) Damage Evolution in Wood - Pattern Recognition based on Acoustic Emission Frequency Spectra. Holzforschung (Online 01/2015), DOI: 10.1515/hf-2014-0072, *(Chap. 5.4. in this Thesis)*.

Cazaux, J., Erre, D., Mouze, D., Patat, J.M., Rondot, S., Sasov, A., Trebbia, P., Zolfaghari, A. (1993) Recent developments in X-ray projection microscopy and X-ray microtomography applied to materials science. J. Phys. III. 3:2099-2105.

Chotard, T.J., Smith, A., Bonceur, M. P. Fargeot, D., Gault, C. (2003) Characterisation of early stage calcium aluminate cement hydration by combination of non-destructive techniques: acoustic emission and X-ray tomography. J. Eur. Ceram. Soc. 23(13):2211-2223.

Cousin, W. J. (1978) Young's modulus of hemicellulose as related to moisture content. Wood Sci. Technol. 12(3):161-167.

Derome, D., Griffa, M., Koebel, M., Carmeliet, J. (2011) Hysteretic swelling of wood at cellular scale probed by phase-contrast X-ray tomography. J. Struct. Biol. 173(1):180-190.

Eder, M., Jungnikl, K., Burgert, I. (2009) A close-up view of wood structure and properties across a growth ring of Norway spruce (Picea abies [L] Karst.). Trees-Struct. Funct. 23(1):79-84.

Elaqra, H., Godin, N., Peix, G., R'Mili, M. R., Fantozzi, G. (2007) Damage evolution analysis in mortar, during compressive loading using acoustic emission and X-ray tomography: Effects of the sand/cement ratio. Cem. Concr. Res. 37(5):703-713.

Frühmann, K., Burgert, I., Stanzl-Tschegg, S.E. (2003) Detection of the fracture path under tensile loads through in situ tests in an ESEM chamber. Holzforschung 57(3):326-332.

Forsberg, F., Mooser, R., Arnold, M., Hack, E., Wyss, P. (2008) 3D micro-scale deformations of wood in bending: synchrotron radiation μCT data analyzed with digital volume correlation. J. Struct. Biol. 164(3):255-262.

Harris, D. O., Tetelman, A. S., Darwish, F. A. (1972) Detection of fiber cracking by acoustic emission. ASTM STP 505:238-249.

Kurz, J. H., Köppel, S., Linzer, L., Schechinger, B., Grosse, C. (2008) Source localization. In: Acoustic emission testing in engineering - basics and applications, Eds. Grosse, C., Ohtsu, M. Springer-Verlag, Heidelberg. pp108-109.

Lysak, M. V. (1996) Development of the theory of acoustic emission by propagating cracks in terms of fracture mechanics. Eng. Fract. Mech. 55(3):443-452.

Maire, E., Carmona, V., Courbon, J., Ludwig, W., (2007) Fast X-ray tomography and acoustic emission study of damage in metals during continuous tensile tests. Acta Mater. 55(20):6806-6815.

Paganin, D., Mayo, S. C., Gureyev, T. E., Miller, P. R., Wilkins, S. W. (2002) Simultaneous phase and amplitude extraction from a single defocused image of a homogeneous object.. J. Microsc. 206(1):33-40.

Radon, J. C., Pollock, A. A. (1972) Acoustic emission and energy transfer during crack propagation. Eng. Fract. Mech. 4: 295-310.

Reiterer, A., Burgert, I., Sinn, G. Tschegg, S. (2002) The radial reinforcement of the wood structure and its implication on mechanical and fracture mechanical properties - A comparison between two tree species. J. Mater. Sci. 37(5):935-940.

Saavedra Flores, E.I., Friswell, M.I. (2013) Ultrastructural mechanisms of deformation and failure in wood under tension. Int. J. Solids Structures. 50:2050-2060.

Sause, M. G. R. (2010) Identification of failure mechanisms in hybrid materials utilizing pattern recognition techniques applied to acoustic emission signals. Dissertation, ISBN: 978-3-86664-889-0, mbv-Verlag, Berlin, 305 pg.

Sause, M.G.R., Gribov, A., Unwin, A.R., Horn, S. (2012a) Pattern recognition approach to identify natural clusters of acoustic emission signals. Pattern Recognit. Lett. 33:17-23.

Sause, M.G.R., Müller, T., Horoschenkoff, A., Horn, S. (2012b) Quantification of failure mechanisms in mode-I loading of fiber reinforced plastics utilizing acoustic emission analysis. Compos. Sci. Technol. 72:167-174.

Scruby, C.B. (1985) Quantitative acoustic emission technique. Nondestr. Test. 8:158 – 159.

Sonderegger, W., Alter, P., Niemz, P. (2008) Investigations on selected properties of tonal wood of spruce from Grisons. Holz Roh Werkst. 66(5):345-354.

Stampanoni, M., Groso, A., Isenegger, A., Mikuljan, G., Chen, Q., Bertrand, A., Henein, S., Betemps, R., Frommherz, U., Böhler, P., Meister, D., Lange, M., Abela, R. (2006) Trends in synchrotron-based tomographic imaging: the SLS experience. Proc. of SPIE 6318:M1-M14.

Stampanoni, M., Groso, A., Isenegger, A., Mikuljan, G., Chen, Q., Meister, D., Lange, M., Betemps, R., Henein, S., Abela, R. (2007) TOMCAT: a beamline for tomographic microscopy and coherent radiology experiments. Synchroton Radiat. Instrum., 879, pp. 848–851.

Steppe, K., Cnudde, V., Girard, C., Lemeur, R., Cnudde, J.-P., Jacobs, P. (2004) Use of X-ray computed microtomography for non-invasive determination of wood anatomical characteristics. J. Struct. Biol. 148(1):11-21.

Trtik, P., Dual, J., Keunecke, D., Mannes, D., Niemz, P., Stähli, P., Kaestner, A., Groso, A., Stampanoni, M. (2007) 3D imaging of microstructure of spruce wood. J. Struct. Biol. 159(1):46-55.

Van den Bulcke, J., Boone, M., Van Acker, J., Stevens, M., Van Hoorebeke, L. (2009) X-ray tomography as a tool for detailed anatomical analysis. Ann. For. Sci. 66(5):508-520.

Zauner, M., Keunecke, D., Mokso, R., Stampanoni, M., Niemz, P. (2012) Synchrotron-based tomographic microscopy (SbTM) of wood: development of a testing device and observation of plastic deformation of uniaxially compressed Norway spruce specimens. Holzforschung 66(8):973-979.

7 Supplementary investigation

7.1 Pattern recognition on miniature specimens made of glued spruce wood

7.1.1 Materials

The investigation was carried out on bonded wood specimens of miniature size made of clear spruce wood (*Picea abies* (L.) Karst.). Contrary to the industrial plywoods glued by phenolic formaldehyde resorcinol (PRF), urea formaldehyde adhesive (UF) was used (Tab. 3.1) for gluing the wood lamellae of the laboratory scale specimens made of model layered wood as well as of the miniature specimens presented in the following. Three different specimen types were tested; whereby the geometry of these miniature specimens is similar to that of the miniature specimens made of solid spruce wood (Chaps. 6.4, 6.5). Each specimen type consists of two wooden layers which are glued together by one single adhesive layer. In all three cases the adhesive layer is oriented parallel to the load direction (shear stresses). The specimen types differ in fiber-load-angle of the wooden layers: The "LL" specimen (Fig. 7.1a) consists of two wooden layers oriented with tracheid axes parallel to load direction (longitudinal); The "TL" type (Fig.7.1b) consists of one longitudinally and one tangentially loaded wooden layer; The "TT" specimen (Fig. 7.1c) consists of two wooden layers loaded in the tangential direction. For each type, the results are presented by means of selected single specimens.

Table 7.1 Characterization of the bonded spruce wood specimens investigated

Sample	Raw density	MC	Cross section	Speed of traverse	Tensile strength	Load steps	Test duration
	$kg\ m^{-3}$	%	mm^2	$mm\ sec^{-1}$	MPa	-	min
LL	471	9.1	1.01	0.010	44	3	60
TL	478	-	1.51	0.010	30	3	49
TT	450	7.9	2.60	0.005	2.68	3	56

MC...Moisture content

The LL specimen was designed to investigate the damage evolution located close to the adhesive layers in the plywood type 6 with two center veneers oriented in the L direction which is also similar to the adhesive-wood connections in LVL materials (all plies run parallel to each other; loaded in the longitudinal direction).
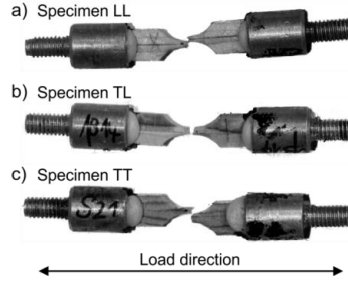
Figure 7.1 Photographs of the bonded miniature specimens tested under tension. a) The LL specimen of two longitudinal oriented wooden layers, b) TL specimen of one longitudinal and one tangential oriented wooden layer and c) TT specimen of two tangentially oriented wooden layers bonded with urea formaldehyde adhesive (UF). Compare also Fig. 5.2.

The TL specimen was developed in accordance to two adjacent plies oriented perpendicular to each other, as is the case for three- (CP, plywood type 3-4) and five-layered (plywood type 5) plywood. Since the impact of wooden layers loaded in L direction was assessed to be significant in the miniature specimens, the TT specimen was designed to focus on the failure behavior of adhesive-wood interfaces loaded in the T direction. This design is also in accordance with the linkage of two cross oriented center veneers in the plywood type 4. In this case, since the wooden tissue lacks structural reinforcing elements when loaded in the T direction, the reinforcing, load bearing structure is the adhesive layer.

The specimens were manufactured from blanks with dimensions of 30 x 5.7 x 2.3mm^3 (length x width x thickness). To ensure a defined crack initiation within the volume of interest that can be monitored by both AE and SRµCT, the specimens were tapered at all four sides yielding a test cross section of 1-2.6mm^2 (Tab. 7.1). For a detailed description of the specimen preparation, see Zauner 2014.

7.1.2 Experimental setup and AE data processing

The experiments (Fig.5.2.d) were performed analogously to those presented in Chap. 6.5. The trials were carried out at the TOMCAT beamline at the PSI Villingen. The tensile tests were performed with a loading device (load cell of 1 kN). The TT specimen was loaded with a cross-head speed of 0.005mm s^{-1}, and the LL and TL specimens with 0.01mm s^{-1}. In tomographic monitoring, a digital resolution of 1.62µm px^{-1} was realized. The AE monitoring was performed with digital AE equipment (AMSY-6, Vallen Systeme GmbH, Icking, Germany); using two miniature piezoelectric sensors (type M31, Fuji Ceramics Corp. Shizuoka, Japan). For AE analysis, only the first signal of an AE event detected by both sensors (maximum distance of 10 mm) was evaluated by means of 1D localization. The AE signals were windowed with a Hamming window function, and selected frequency

features were extracted from the frequency spectra as input parameters to the UPR technique.

7.1.3 Results and Discussion

For each specimen the unsupervised pattern recognition technique yielded the numerically best separation of the detected AE signals into two clusters (Tab. 7.2). The four main features to identify similarities between the different waveforms are the peak frequency (PF), center of gravity frequency (CGF) and weighted peak frequency (WPF) and the partial power 2 (PP2) instead of partial power 4 (PP4) as conducted for the tested solid wood specimens (Chap. 6.4). However, for comparison purpose, the results are presented with the same set of features as for the latter; PP4 plotted against WPF (Fig. 7.2). For later comparison between the results of both miniature and laboratory scaled specimens, another plot presents the PP2 against WPF (Fig. 7.3).

Table 7.2: Results of clustering of the radial (R) and longitudinal (L) specimens

Sample	NC	Points*	FC	R	τ	S	σ
LL	2	89	7	0.521	3.190	0.674	84
TL	2	100	7	0.557	3.256	0.669	290
TT	2	100	7	0.643	3.070	0.594	676

Maximal possible points: 100;

n…Number of test; No. C…Number of cluster; FC…Feature Combination; R…Davies–Bouldin-index; τ…Tou-index, S…Rousseeuw's Silhouette value; σ… Calinski and Harabasz index.

Feature Combination No. 7: peak frequency (PF), weighted peak frequency (WPF), center of gravity frequency (CGF), partial power 2 (200-400kHz) (PP2).

Essentially, two clusters with WPFs of around 300kHz (A clusters) and 570kHz (B clusters) were sought out by the UPR technique. The B clusters, compared with the A clusters, yield a higher contribution from PP2. The former ranges from about 10% to about 80% for all specimen types, the latter from about 0% to 40%. These signal classification results are very similar to those derived from testing solid spruce wood (L and R specimens). In the case of the L and R specimens, the two clusters have tentatively been attributed to inter-wall cracks (cluster A) and to cell wall cracks in the tracheids (cluster B).

However, the identification of two clusters with comparable WPF ranges and similar amounts of PP4 raises the question of how the layered structure of the bonded miniature specimens with different layup (LL, TL, TT) affects damage behavior compared with solid wood. The plots of PP4 vs. WPF (Fig. 7.2), clearly reveal that the A cluster forms different patterns of distribution due to different lay-up systems. For the LL and the LT specimen, the pattern of both clusters A and B (Fig. 7.2a-b) are comparable to that for the R specimens

(Fig. 6.32b). Equivalent to the R specimens, the A cluster indicates a possible separation into AE signals with a WPF close to 180kHz and AE signals close to 330kHz, though the AE signals with WPFs ranging from 0-400kHz are found to be only associated with the single A cluster. In the case of the TT specimen, the A cluster could be subdivided into three clusters, since a possible third cluster occurs at 240kHz (Fig. 7.2c). However, these different distribution patterns of the A clusters might be generated by possible different underlying microscopic damage mechanisms due to the lay-up systems loaded.
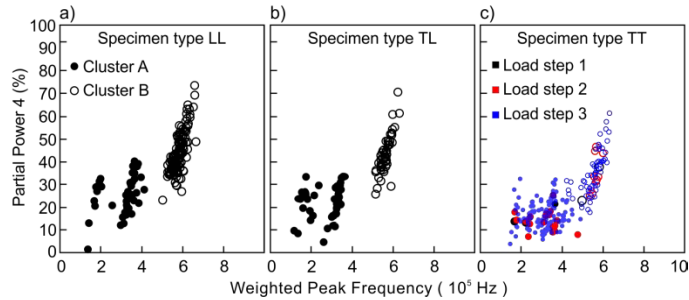
Figure 7.2 Cluster formed by pattern recognition of acoustic emission signals (detected by two miniature sensor M31) for the bonded wood specimen types a) LL, b) TL and c) TT are shown; full circles belong to cluster A, open circles to cluster B. (c) Load steps 1 (black), 2 (red) and 3 inclusive ultimate failure (blue) distinguished for specimen TT. The frequency feature partial power PP4 (600-800kHz) is plotted against the weighted peak frequency WPF.
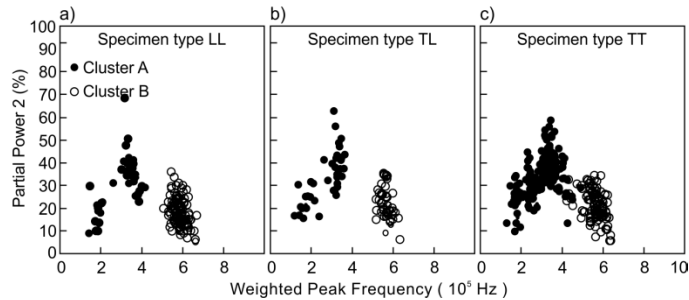
Figure 7.3 Cluster formed by pattern recognition of acoustic emission signals (detected by two miniature sensors type M31) for the bonded wood specimen types a) LL, b) TL and c) TT are shown; full circles belong to cluster A, open circles to cluster B. For comparison with Figs. 7.10 & 7.11 the frequency feature partial power PP2 (200-400kHz) is plotted against the weighted peak frequency WPF.
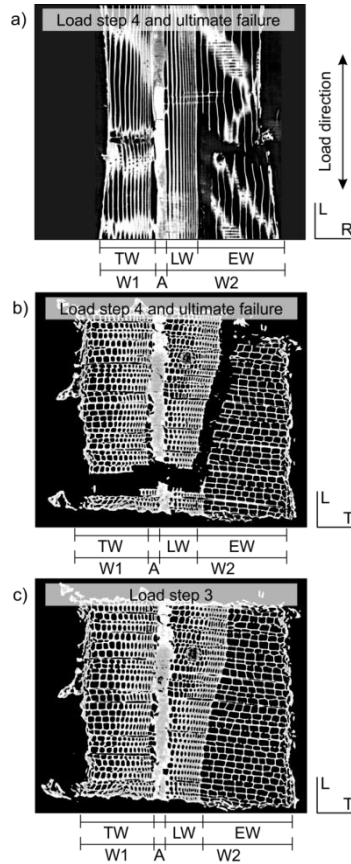
Figure 7.4 Fracture pattern of the bonded LL specimen with the view a) parallel and b) perpendicular to load after load step 4. c) The microscopic structure after the previous loading step 3. The position within the specimen is the same in b) and c). Wood layer W1 and W2 bonded together with urea formaldehyde adhesive (A). Early wood (EW), transition wood (TW) and latewood (LW) tissue are distinguished.

The appropriate explanation is supported by the results from the SRμCT scans recorded between the loading steps. The LL specimen (Fig. 7.4), especially the scan taken after the ultimate failure of the specimen (Fig. 7.4a, b), shows a crack path mainly running along the growth ring boundary (T direction) and along the grain (R direction), whereby passing the glue line seems to have no impact on the crack path propagation (Fig. 7.4: View of the specimen's test cross section, load direction in the L direction, perpendicular to R and T). Furthermore, numerous single tracheids fiber bridges were observed (Fig. 7.5). Since UF adhesive provides mechanical properties that are in the same range as that of spruce when stressed in the L direction, significant weakening or reinforcing effects by the adhesive might be excluded. Instead, the line of least resistance mainly progressed within the two longitudinal loaded wood layers (the load bearing elements in the LL lay-up). The same

conclusion was derived by means of Environmental Scanning Electron Microscopy (ESEM) images of the fractured cross section, as the complex fracture pattern was formed within both wood layers, whereas the adhesive reveals a smooth fracture surface (Fig. 7.6a).
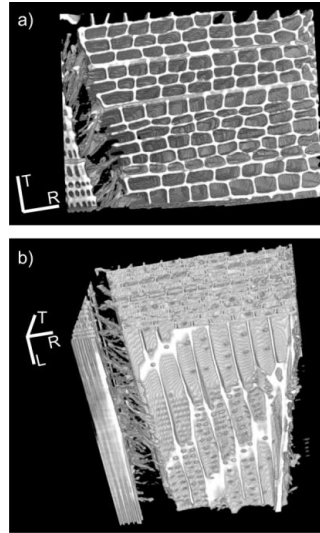
Figure 7.5 Section of fracture pattern in bonded miniature specimen LL. Fiber bridging at the growth ring border in the a) RT and b) LR plane.
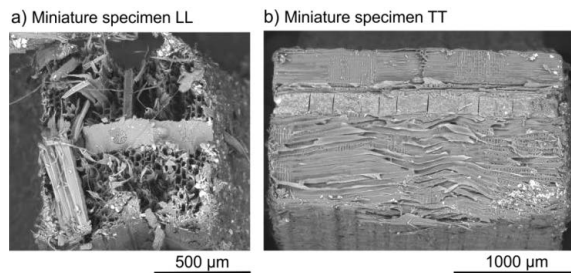
Figure 7.6 Fracture surface at the cross section of the tensile loaded miniature specimens LL (a) and TT (b) taken by ESEM.

However, it has to be pointed out, that the bonded miniature specimens tested herein, do not provoke the typical tension shear failure, since wood and adhesive layers are loaded equally as described by Hooke springs connected parallel and exposed to pure tension load (Fig. 3.4). In the case of the TT specimen, the fracture surface of the adhesive looks the same and the wood parts reveal a smooth fracture surface (Fig. 7.6b). However, the complexity of its failure behavior is more visible after observation of the tomographic scans taken after each applied load step. In the Fig. 7.7.a, a section of the specimen after the second loading is presented whereby the reconstruction was cut through the glue line to

show one half of the specimen with adjacent adhesive. Within the UF adhesive layer, small crack lines induced during hardening are observed (Hass et al. 2012).
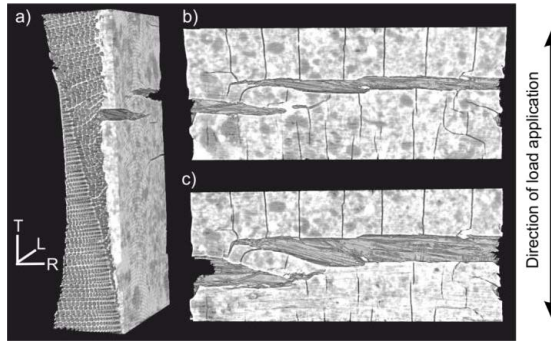
Figure 7.7 a) Crack evolution within the adhesive layer (urea formaldehyde) of the miniature TT specimen is presented by a section of the half specimen. The cut passes the reconstruction through the adhesive layer. Frontal view to the crack opening within the adhesive layer after a) the 2nd and c) the 3rd loading.
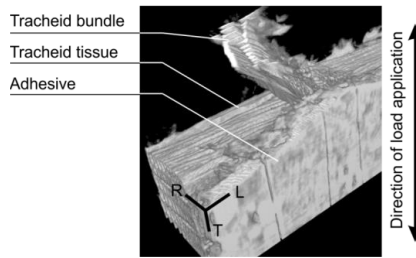
Figure 7.8 Section of fracture pattern in bonded miniature specimen TT. Tracheid bundle separated by fiber bridging mechanisms close to the adhesive layer (urea formaldehyde).

It seems that crack initiation is located in the adhesive layer and crack lines propagate further parallel to the load direction. After the second loading, significant cracks in the adhesive layer are observed running perpendicular to the load direction (Fig. 7.7b), whereby the crack opening also results in displacements within the bordering tracheid tissue (Fig. 7.7a). The tracheids are lifted along the T axis, parallel to the direction of load and crack opening. Cell separation mechanisms and cell wall cracks occur along the RL plane (Fig. 7.6b). The comparison of these crack openings after the second and third loading steps gives an insight into the relevance of the adhesive within this layup structure of the TT specimen when exposed to tensile load (Fig. 7.7b-c). Another detail selected from the ultimate fracture surface detected immediately after failure shows a tracheid bundle bridge, which was pulled out very close to the glue line (Fig. 7.8).

The PP4 vs. WPF plot distinguishes the AE signals with regard to their occurrence due to the three loading steps applied to the TT specimen (Fig. 7.2c; first, second, third step =

black, red, blue colored). This reflects the mechanisms of the starting crack (second loading) and of further crack openings (third loading and ultimate failure) as well as the increased consequences for the surrounding tissue in the cluster pattern. However, regarding the three loading steps, no significant trend of occurring cluster positions on the WPF axis is determined. After the first loading step (black colored), few signals of the cluster A already cover the WPFs of 180kHz to 380kHz (Fig. 7.2c). During the third loading step and the ultimate failure, some AE signals of both cluster A and B show an increased contribution of PP4 (meaning a higher share of high frequency components). However, to verify this tendency, more tests are needed.

The analysis of the TL specimen was not continued, since, unfortunately, the quality of the SRμCT scans is unsuitable. Also the investigation by means of ESEM has proven unsatisfactory due to the couplant for sensor coupling covering the fracture surfaces of the specimen (Fig. A.1).

7.1.4 Conclusion

Similar to the miniature tests on solid spruce wood, the acoustic emission signal classification by an unsupervised pattern recognition approach yields two signal clusters for tensile tests to failure for the bonded miniature specimens for the same levels of partial powers. The clusters essentially differ with respect to higher shares of low and high frequency components. It is assumed that AE signals generated by damage mechanisms of the adhesive layer might be covered by the A cluster as discussed for the LL and TT specimens. The impact of the adhesive layer on the damage evolution of the TT specimen was proven by the reconstructions of the SRμCT scans, whereas the failure behavior of the LL specimen was mainly dominated by the wooden layers with the tracheid axes oriented parallel to the load direction. This different outcome of the rather brittle UF adhesive is a result of the different grain orientations of the adhered wooden layers. Compared to the UF adhesive (Tab. 3.1), the longitudinally loaded layers have stronger load bearing capabilities, whereas the tangential loaded wood layers reveal greater weakness. The cluster results plotted as PP4 against WPF prove these observations, since the cluster patterns of the TL specimen shows a more individual pattern compared to the solid spruce tested in L and R direction (Fig. 6.32) than the LL specimen. It is assumed that AE signals generated by crack mechanisms of the adhesive are among the signals of the low frequency cluster. This tentative conclusion, however, will have to be verified by further investigations, possibly by performing similar tests using other combinations of adhesives and wood species with greater difference in mechanical performance and with a larger number of specimens.

7.2 Pattern recognition on laboratory scaled specimens made of layered wood

7.2.1 Materials and experimental setups

For pattern recognition analysis, the datasets of the investigated layered spruce wood manufactured in the laboratory (Chap. 6.1) and those of the tested industrial plywood materials (Chap. 6.2) were used. For reference, the analysis was also performed for solid spruce wood specimens of 9 mm thickness. The overview on the different materials is given in Fig 5.1 and Tab. 5.1. The specimen shape was adapted from DIN 52377. The quasi-static tensile tests were carried out on a universal test machine (Zwick Roell 100, load cell 100kN) with a constant cross head speed of 2.5mm min^{-1} (Fig 5.3a, b; Tab. 5.2).

The AE measurement was performed with commercial equipment (type AMSY-6, Vallen Systeme GmbH, Icking, Germany) using three types of sensors (two each of types SE 150-M, VS 45-H and SE1000-H from Dunegan Engineering Corp.). In the following chapters, supplementary evaluations for all three sensor types are presented. Further, the UPR technique was performed only for the SE-1000H sensors. Their frequency response fits best with that of the miniature sensors (type M31 from Fuji Ceramics Corp.) used in the experiments on miniature specimens (Chaps. 6.4, 6.5, 7.1). The sensor positions differ for the model layered wood (UD and CP) from those monitoring the industrial plywood (plywood type 3, 4, 5, 6) and the reference solid wood (SOLID). When testing the UD and CP specimens, the SE 1000-H sensors were mounted about 100mm apart (Fig. 5.3a), whilst monitoring the tests on industrial plywood and solid spruce, the SE 1000-H sensors were mounted 30mm apart (Fig. 5.3b). This was necessary to ensure good detection quality also for the plywood type 6 with its large thickness of 18mm. In both cases, both SE 1000-H sensors are mounted on the same side of the specimen, as close as possible to the area of interest which was also monitored by a DIC system. The following supplementary AE analyses are based on the first signals of the AE events detected and localized by both sensors of each sensor type. In the following, these AE event signals are denoted as the AE signals.

7.2.2 Data processing for cluster analysis

The detection of the AE waveforms was performed with a sampling rate of 5MHz yielding signal duration of 819.2μs including 38μs pre-trigger (Fig. 6.9), which is different from the miniature tests (10MHz sampling rate, 409.6 μs signal duration, see Chap. 6.4). The threshold settings for the SE 1000-H sensors range from 0.04 mV up to 0.06mV (Tab. 6.3).
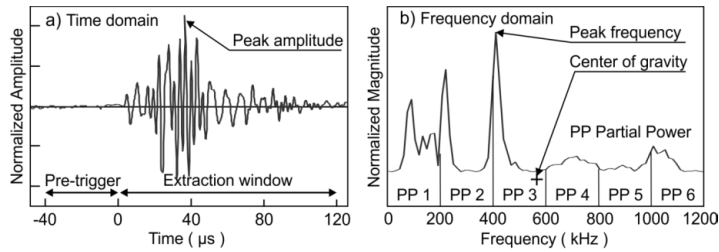
Figure 7.9 Parameters of AE signals in time and frequency domains. a) A pre-trigger of 38μs is chosen, the frequency spectra were calculated from the first 120μs of the detected signal (extraction window). b) The unsupervised pattern recognition was performed by using nine frequency features: peak frequency (PF), center of gravity frequency (CGF), weighted peak frequency (WPF) and partial powers (PP).

Table 7.3 Acquisition of AE waveform detection and frequency spectra calculation settings.

SE 1000-H sensor threshold settings when testing the material …	UD:	35.5 dB$_{AE}$ ($\approx$ 0.06 mV)
	CP:	33.2 dB$_{AE}$ ($\approx$ 0.05 mV)
	plywood type3-6:	35.1 dB$_{AE}$ ($\approx$ 0.06 mV)
	Solid:	35.1 dB$_{AE}$ ($\approx$ 0.06 mV)
Rearm time	1 ms	
Sampling rate	5 MHz	
Signal duration	819.2 μs, 38 μs pre-trigger included	
Signal evaluation	First signal of AE event based on 1D-localization	
Fourier Transformation of waveform		
Extraction window in time domain:	First 600 samples of the waveform	
	0 μs - 120 μs (38 μs pre-trigger excluded)	
Window function:	Hamming window of 600 samples	
Frequency spectra	0-1200 kHz	

The AE signals frequency spectra were calculated via Fourier transformation applied to the first 600 samples of the AE signal in the time domain (0μs-120μs) excluding 38μs pre-trigger (Fig. 7.9a). Therefore, the AE signals were windowed with a Hamming window function (600 samples) (Tab. 7.3). The input features for the cluster algorithm are selected exclusively from the AE signal's frequency spectra (Fig. 7.9b). According to the analysis of the miniature tests (Chaps. 6.3 and 6.4), beside the WPF, additional eight features in total (Fig. 7.9b) were chosen as input for the UPR algorithm, the PF, the CGF and six PP levels. To yield comparable frequency spectra, these features were normalized by their maximum

magnitude to eliminate the influence of different source excitation energies. To ensure a suitable statistical database for UPR processing, the extracted AE feature datasets from all tests (five tests for each CP and UD, eight tests for plywood type 3-6 and solid spruce) are analyzed simultaneously.

7.2.3 Results and Discussion

Cluster results

For all material types, the UPR technique yielded the numerically best separation of the detected AE into two clusters (Figs. 7.10-7.11; Tab. 7.4.). Thus, the highest ratings were estimated for the solid spruce, the UD and plywood type 6 specimens. Furthermore, by excluding the UD material with its outstanding lay-up structure, it can be observed that the performance of the partitions (best possible performance is rated by a maximum of 100 points) decreases as the layers that form the plywood structure decrease in number. The best partition of 89 points was rated for the plywood type 6, whereas the rating for type 3 only yielded 73 points. However, these ratings imply that the occurrence of two clusters is generally still expressive enough, since they are above 60 points (Sause et al. 2012).
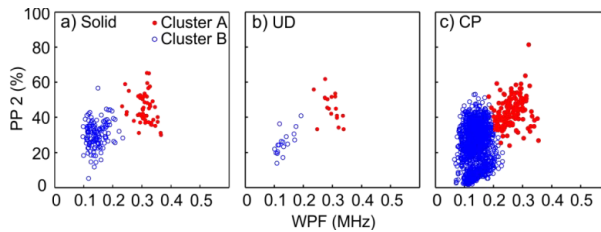
Figure 7.10 Cluster from pattern recognition of acoustic emission signals for a) solid spruce and the model layered wood specimens b) with all layers aligned unidirectional (UD) with the tensile load and c) with the center cross ply (CP) normal to the tensile load. Only signals from the first hit sensor type SE 1000-H are shown: full/red circles indicate cluster A, open/ blue circles indicate AE emitted by cluster B.

For all materials except the plywood type 3, the obtained feature combination consists of the PF, WP, PP1 and PP2. For the plywood type 3, the feature combination also comprises the PF, WPF, the CGF and the PP3 (Tab. 7.4). For the purpose of comparing the cluster results of all tested material types, the PP2 and the WPF were chosen (Figs. 7.10-7.11) as the significance of the clusters is reflected most clearly by their WPFs.

Consistent with the investigation on the miniature specimens, the A clusters comprise AE events of a relatively high share of low frequency components, expressed by an average WPF of around 130kHz. The B clusters contain AE events of a relatively high share of high frequency components, which is characterized by an average WPF of approximately

300kHz. Furthermore, the A clusters yield a higher contribution from PP2 compared with the B clusters. For the A clusters, the PP2 ranges from about 0% to about 60%, whereas the B clusters are characterized by PP2 ranging between 20% to 70%. The cluster pattern of CP (Fig. 7.10c) compares well with the clusters from the industrial plywood (Fig. 7.11).
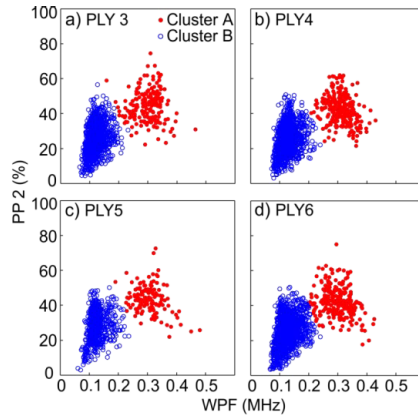

Figure 7.11 Cluster from pattern recognition of acoustic emission signals for the industrial plywood specimen types designed with a) 3 layers, b) 4 layers, c) 5 layers and d) 6 layers. Only signals from the first hit sensor type SE 1000-H are shown: full/red circles belong to cluster A, open/blue circles belong to cluster B.

Table 7.4 Results of clustering of solid spruce, model layered wood and plywood specimens

Material	n	No. of AE signals	No. C	Points*	FC	R	τ	S	σ
SOLID	8	180	2	99	13	0.699	2.676	0.580	295
U D	5	36	2	100	13	0.511	3.744	0.659	130
C P	5	1765	2	75	13	0.638	3.057	0.591	1268
PLY 3	8	1434	2	73	5	0.829	2.221	0.568	564
PLY 4	8	1522	2	89	13	0.581	3.380	0.640	2551
PLY 5	8	804	2	89	13	0.626	3.193	0.622	1197
PLY 6	8	1693	2	98	13	0.629	3.129	0.614	2305

Maximal possible points: 100; n...Number of tests; No. C ... Number of clusters; FC Feature Combination; R Davies–Bouldin-index; τ Tou-index, S Rousseeuw's Silhouette value; σ Calinski and Harabasz index.

Feature Combination No. 5: peak frequency (PF), weighted peak frequency (WPF), center of gravity frequency (CGF), partial power 3 (200-400kHz) (PP3).

Feature Combination No. 13: peak frequency (PF), weighted peak frequency (WPF), partial power 1 (0-200 kHz) (PP1), partial power 2 (200-400 kHz) (PP2).
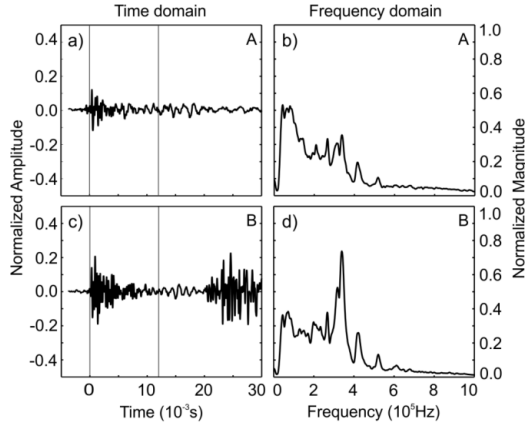
Figure 7.12 Averaged normalized AE signals of cluster A (a-b) and B (c-d) detected during tensile testing of solid spruce in the longitudinal direction. Characteristics are presented in time (a, c) and frequency (b, d) domains.
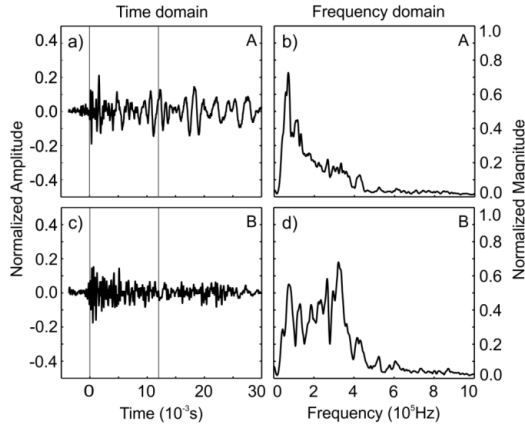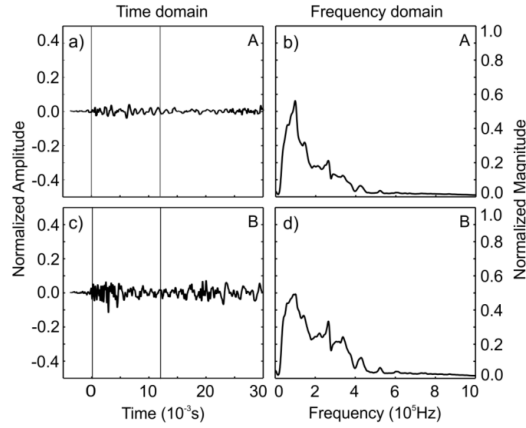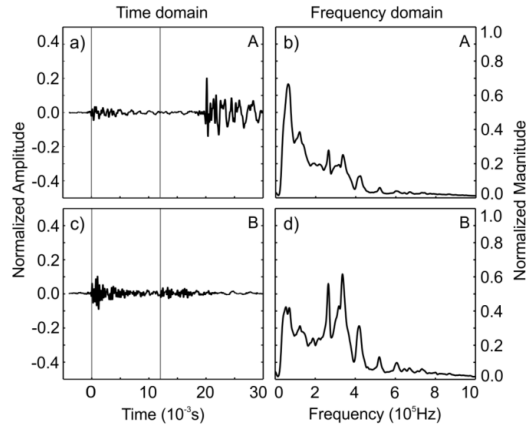

Figure 7.13 Averaged normalized AE signals of cluster A (a-b) and B (c-d) detected during tensile testing of the model layered wood with three layers aligned unidirectional (UD). Characteristics are presented in time (a, c) and frequency (b, d) domains.

For the solid spruce specimens, the normalized average AE signals of both A and B clusters in the time domain are typical burst signals for all tested materials (Fig. 7.12), whereas the normalized average AE signals of clusters A and B in the time domain are clearly different for the plywood materials (Figs. 7.13-7.15). For the industrial plywood, the average waveform of cluster A compared to that of cluster B is less similar to a characteristic burst signal and shows rather slow oscillations vs. time (Fig. 7.15). The same is also true for the UD and CP (Figs. 7.13-7.14). The averaged signal of the B cluster for solid spruce (Fig. 7.12c) as well as that of the A cluster for plywood type 5 (Fig. 7.15a) reveal possible reflections after 200μs, which are not taken into account since the extraction window in the

time domain is limited between 0μs-120μs (vertical lines in the time domains in Figs. 7.12-7.15a, c).

Figure 7.14 Averaged normalized AE signals of cluster A (a-b) and B (c-d) detected during tensile testing of the model layered wood with one center cross ply (CP). Characteristics are presented in time (a, c) and frequency (b, d) domains.

Figure 7.15 Averaged normalized AE signals of cluster A (a-b) and B (c-d) detected during tensile testing of plywood type 5. Characteristics presented in the time (a, c) and the frequency (b, d) domains are very similar to the other industrial plywood types 3, 4 and 6.

In the frequency domain, both clusters reveal broadband spectra, for all tested materials. Thus, the main peaks are located at approximately 70kHz and 330kHz (Figs. 7.12b, c & Figs. 7.15b, c). Generally, the spectra of solid spruce and the UD are almost similar. CP is rather comparable to plywood types 3-6. This makes sense, since the spectra of the plywood types are affected by their layup structure including cross-plies which is not the case for solid spruce and UD. However, despite the varying layered structure of the industrial

plywood types, their spectra reveal very strong similarities, possibly indicating the damage mechanisms that either occurred in the parallel or cross oriented plies. However, the identification of two clusters with comparable WPF ranges and similar amounts of PP2 raises the question whether the underlying microscopic damage mechanisms are the same in all types of specimens; plywood as well as solid spruce and UD.

Table 7.5 Cluster characteristics

Material	No. layers	Cluster	N*	PF (kHz)	CGF (kHz)	WPF (kHz)	PP 1 (%)	PP 2 (%)	PP 3 (%)
SOLID	1	A	124	78±35	288±60	144±28	47±11	30±8	10±4
		B	56	319±44	303±36	310±28	34±7	45±8	12±4
UD	3**	A	18	77±24	242±50	135±26	58±10	26±7	7±3
		B	18	292±42	305±35	297±27	33±5	46±8	11±3
CP	3	A	1618	92±30	213±52	137±27	66±15	21±13	5±3
		B	147	270±58	260±36	263±35	42±7	44±8	8±4
plywood type 3	3	A	1245	67±22	238±56	123±24	57±13	26±8	8±4
		B	189	304±62	302±43	301±44	33±9	45±9	11±6
plywood type 4	4	A	1254	71±24	243±57	129±26	57±12	26±8	8±4
		B	268	313±54	310±43	310±38	33±8	43±8	14±6
plywood type 5	5	A	661	74±27	234±53	129±27	57±12	28±9	8±4
		B	143	315±55	303±50	307±44	34±9	44±8	13±6
plywood type 6	6	A	1428	74±29	231±61	127±29	59±14	25±9	7±4
		B	265	287±61	310±47	296±44	33±8	43±8	13±6

*Number of signals; mean±SD; ** grain of all three layers is oriented parallel to each other*

The number of AE signals detected and located in solid spruce and UD is significantly lower than for the plywood materials (Tab. 7.5). CP generated a few hundred signals more than plywood type 3 (both of which have the same layup structure, but CP is almost without pre-damages). Among the industrial plywood, type 5 generated an extremely low number of AE signals, almost half that of CP and plywood type 3, 4 and 6. For the latter, most AE signals were evaluated. The percentage of signals assigned to the A cluster is beyond 80% for all industrial plywood materials, yielding almost 90%, in the case of plywood type 3 and CP. In contrast, for the solid spruce, the A cluster represents only 70% of all detected signals. This ratio of cluster A to B is the opposite to the cluster results of the miniature L-specimens

(Chap. 6.4, A:B = 42:80). Presumably, for the L-specimens, the size effect led to the different shares of damage mechanisms assigned to the clusters.
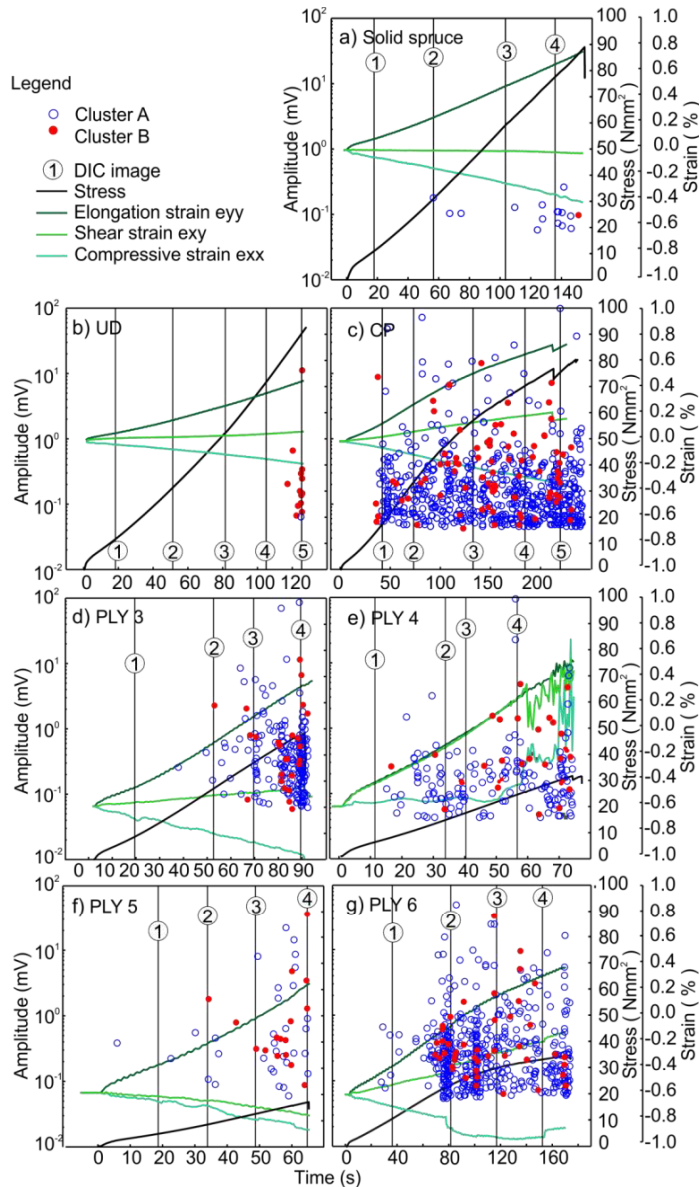

Figure 7.16 AE signal amplitudes from cluster A and B (detected by the sensor type SE 1000-H) for selected specimens as a function of time, stress and strain (DIC measurement): a) Solid spruce, model layered wood with b) three layers aligned unidirectional (UD) and with c) the center cross ply (CP), industrial plywood types d) 3, e) 4, f) 5 and g) 6.

However, within its damage history, the solid spruce also shows similarity to the miniature specimens, since the cluster B matches in seven of eight tests with the ultimate failure, and further, in five of those seven cases, the B cluster yielded the maximum AE amplitudes during ultimate failure (Fig. 7.16a). Thus, and in accordance to the miniature L-specimens, the cluster B is assumed to indicate the L specimens' macroscopic failure. No similar trends were observed for the CP and industrial plywood specimens. The occurrence of clusters during loading of plywood seems rather random (Figs. 7.16c-g). This is also the case for solid spruce and UD specimens, when comparing more than one specimen of each material type. The early occurrence of A clusters in the case of the solid spruce specimen (Fig. 7.16a) was not observed in all cases. The same holds for the large number of B cluster signals detected for the UD (Fig. 7.16b), especially regarding the fifty-fifty signal ratio between cluster A and cluster B determined over all tested UD specimens (Tab. 7.5). The very late AE onset was observed in all five UD specimens, but only with the detection by the SE 1000-H sensors (Fig. A.2-A.3). This could be due to the sensibility of the SE 1000-H sensors, which is lower than for the SE 150-M and the VS 45-H sensors (Fig. A.2).

Generally, for all specimens, the first AE events occurred as soon as 1/4 to 1/3 of the maximum load was reached (Fig. 7.16). For all types of plywood, in both clusters A and B, the AE event amplitude values seem to appear randomly rather than restricted to a certain limit in amplitude or stress level. Thus, the AE amplitude histories of CP, plywood type 4 and 5 show large scatter in AE amplitude values and occurrence in time, and thus, almost no linkage between the appearance of clusters A and B was found. In contrast, in the case of plywood type 3 (Fig. 7.16d), at 70s of test duration, close to the DIC image 3, few AE signals of cluster B are accompanied by numerous signals of cluster A. The same is observed for the plywood type 6 (Fig. 7.16g) at 80s test duration, close to the DIC image 2. This is possibly explainable by a certain defect generation within the load bearing outer plies oriented longitudinally, respectively, causing damages in the intermediate cross plies. However, by means of AE parameters (amplitude, energy, etc.) as well as focusing on the appearance of clusters with respect to load history, a clear identification of the clusters' origin is not possible.

Localization in AE and DIC

The following analysis combines the results from DIC and the AE detection by means of all three sensor types, and takes into consideration the identified clusters by the detection of the sensor types SE 1000-H. Therefore, the results of a single test of each specimen type are presented and discussed in the following. The selected specimens are the same as presented

in Fig. 7.16. To gain an overview, photos of the fractured specimens are shown, including the Y-coordinates to allow locating the cracks. The results of AE measurements present the Y-location of the located AE events detected by the SE 1000-H (distinguishing the clusters A and B), as well as by both sensor types VS 45-H and SE150-M. The results of the AE analysis as well as the stress and strain history are plotted against time. Strain curves of elongation strain (eyy), compression strain (exx) and shear strain (exy) were measured by the DIC method. Furthermore, the numbers 1 to 4 mark certain points in time when those DIC images were taken. The results of DIC analyses of these four images are presented in another figure. By doing this, comprehensive descriptions of the failure behavior of solid wood and all industrial plywood types are provided. For the UD and CP the results presented in Chap. 6.2 were supplemented by the AE location, but not further discussed herein. These results are provided in Figs. A.2-3.

The damage evolution in the tensile loaded solid spruce specimen (Fig. 7.17) developed a complex fracture pattern. The specimen's broad side monitored by DIC shows splintering tension between 14 and 15 cm on the Y axis, the back side shows brittle fracture that is located between 22 and 23 cm (Fig. 7.17.c). Unfortunately, both macroscopic cracks are positioned outside the area of interest (AOI) monitored by DIC. Both narrow sides of the specimen reveal the crack path running along the growth ring boundary oriented parallel to the load direction. This part of the fracture passes the AOI, but leaves no significant traces in the eyy strain fields (Fig. 7.17.d). Within recording image 4 taken at 137s, very close to the AE that signalizes the subsequent ultimate failure (Fig. 7.17a, b), the compression strain field exx formed a large area of increased strain values between 19 and 21cm (Fig. 7.17d) which is linked to the inner shear crack along the growth rings (Fig. 7.17c). It is plausible that the locations of the AE events detected by SE 1000-H (Fig. 7.17a) are also due to that part of the fracture. The amount of AE detected by the SE 150-M is less, but the VS 45-H sensors show massive AE, especially located between 14 and 17 cm which fits well with the lower fracture part (Fig. 7.17a, b). With respect to its frequency sensitivity to low frequency components (<100 kHz), possibly, shear or friction mechanisms are detected which are assumed to generate low frequencies. In accordance to this, the SE 1000-H also detected low frequency signals of cluster A in the lower part of the AOI.

The plywood type 3 specimen after ultimate failure (Fig. 7.18a-d) reveals no significant fracture path, but the broad sides are covered by numerous cracks running parallel to the load direction (Fig. 7.18c). These cracks are lathe checks which opened further with progressive stress. This kind of crack was observed for all industrial plywood materials tested. Furthermore, within the cross ply (at the narrow sides of the specimen), cracks occur

that are caused by rolling shear. This kind of crack was observed more pronounced for the specimen of plywood type 4 (Fig. 7.19c). These cracks are oriented perpendicular to the load direction. The VS 45-H detected numerous AE signals in the upper part of the plywood type 3 (Fig. 7.18b), but fracture patterns as well as DIC results reveal no corresponding characteristic changes close to that location (Figs. 7.18c-d). Also the DIC results related to the recorded image 3 at 70s of test progress give no hint to changes in damage evolution which would have otherwise helped to explain the accumulation of cluster A signals at 70s. The strain patterns do however comply with those taken at recording point 2. The stress curve also shows no deviations (Fig. 7.18a, b).

However, it might be the case that the origin of the cluster A accumulation at 70s test duration is mainly located within the center ply or the adhesive layer, which are only indirectly monitored by the DIC due to its influence on the strain formation at outer surface ply. A similar observation is made for the specimen of plywood type 4 between the 20th and 30th s of test progression. Here, also an accumulation of signals assigned to the A cluster appears between 18 and 20cm. Regarding the strain field formation in *exx*, compared to the 1st recorded image, the 2nd one reveals a region of increased strain values (also between 18 and 20 cm) (Fig. 7.19d). Within the *eyy* strain field, no locally restricted region of increased values is formed. The photographs of the fractured plywood type 4 specimen show rolling shear below 18 cm, but it seems that the stress field continued within the adhesive layer between the cross ply and the surface ply on the left (Fig. 7.19a). However, the sensors VS 45-H as well as the SE 150-M detected only minimal amounts of AE (Fig. 7.19b).

The fracture pattern of plywood type 5 (Fig. 7.20a-d) contains a brittle failure at the surface's veneer, fully monitored by DIC (Fig. 7.20c). Furthermore, besides the rolling shear cracks within the cross ply, the left cross ply includes the crack path running along the adhesive layer at the border to the center ply (L-oriented). However, indications such as locally increased strain values were not determined (Fig. 7.20d). Some AE signals of cluster B are located at 19 cm (Fig. 7.20.a) close to the brittle crack of the surface veneer (Fig. 7.20c). Generally, cluster B is accompanied by AE signals of cluster A.

As already discussed in Chap. 6.2, the plywood type 6 specimen formed very complex fracture patterns over the layup structure. The high AE activity measured for plywood type 6 yields a complex location pattern for all three sensor types (Fig. 7.21a, b). Shortly before 80 seconds into the test's progress, all three sensors detected massive amount of AE signals. Thus, AE events of cluster A predominantly appeared (Fig. 7.21a). The related image 2 recorded by the DIC system reveals a local increase in *exx*, and significant changes in *exy*

positioned in the upper part of the AOI (Fig. 7.21d). The fracture path at the narrow sides of the specimen (Fig. 7.21c) provides further information on crack development. In Fig. 7.21c, the weak point within the right cross layer can be seen. The crack could be continued within one or both L-oriented center layers or within the adhesive layer. Thus, both cracks within the cross ply oriented perpendicular to the load direction and adhesive failure could possibly be correlated to low frequency AE events, especially considering that the AE accumulation was also clearly detected by the low frequency sensitive VS 45-H sensors (Fig. 7.21b).

For all plywood types tested, the bulk of AE events assigned to cluster A seems to correlate with significant formations of locally restricted regions of increased or decreased shear (*exy*) and compression (*exx*) strain. One exception was found for plywood type 5, since it yields the same ratio of 80% for AE events of cluster A as determined for the other industrial plywood types, but in contrast, the DIC results show a rather uniform strain field development in elongation, shear and compression strain. This might be due to stress compensation within the L oriented centre layer not significantly affecting strain field formation at the surface layer. Here, the major disadvantage of the DIC measurement as surface monitoring method emerges and needs to be taken into account. The same could be assumed for DIC measurements of plywood type 6, but here, the two reinforcing center layer (L oriented) cause larger differences in central surface layer stresses. These stresses are reduced by means of rolling shear within the cross plies, which is also reflected in strain field formation at the outer surface.

7.2.4 Conclusion

For the laboratory scaled specimens of clear solid spruce, model layered wood (UD, CP) and industrially produced plywood (plywood types 3-6), the AE signal classification by an unsupervised pattern recognition approach yields two signal clusters. The clusters essentially differ with respect to higher shares of low (cluster A) or high (cluster B) frequency components. This confirms the evaluation of the miniature tests on solid spruce and bonded wood specimens. That the miniature specimens yield higher WPF for the clusters than laboratory scale might be due to specimen size and signal attenuation. Furthermore, the different sensor types also appear to have influenced the AE waveform characteristics.

However, compared to solid spruce, for the plywood materials, no separate, third signal cluster was detected that can be attributed to the adhesive layers. Besides, by applying the UPR technique to tensile tests of bonded miniature specimens with different grain orientation of the wooden layers, monitored by AE and SRµCT, two clusters, which are also
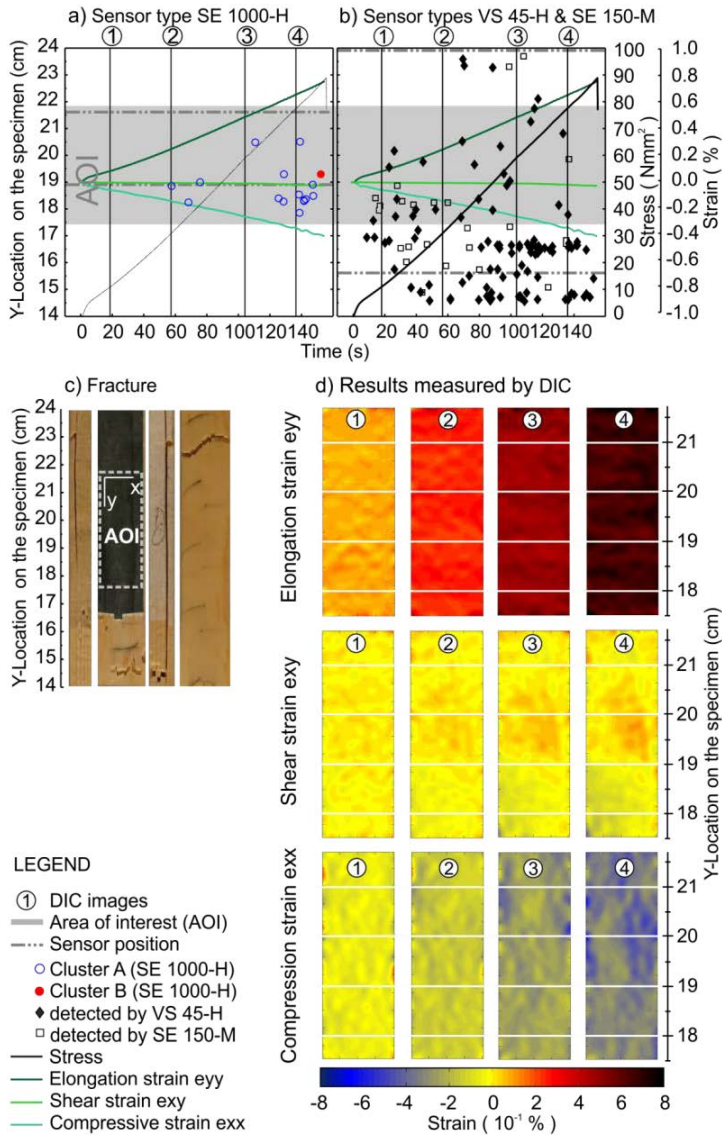
Figure 7.17 Failure behavior of a selected spruce wood specimen by means of AE detected and located by a) the sensors SE 1000-H including the clusters A (unfilled/blue) and B (filled/red), and by b) the sensors VS 45-H (filled/black diamond) and SE 150-M (unfilled/ black square). c) The macroscopic crack path close to the area of interest (AOI) monitored by DIC is shown by photographs of all four sides of the specimen. d) Selected results 1-4 determined by DIC show the strain field formation at different points of progress throughout the test.
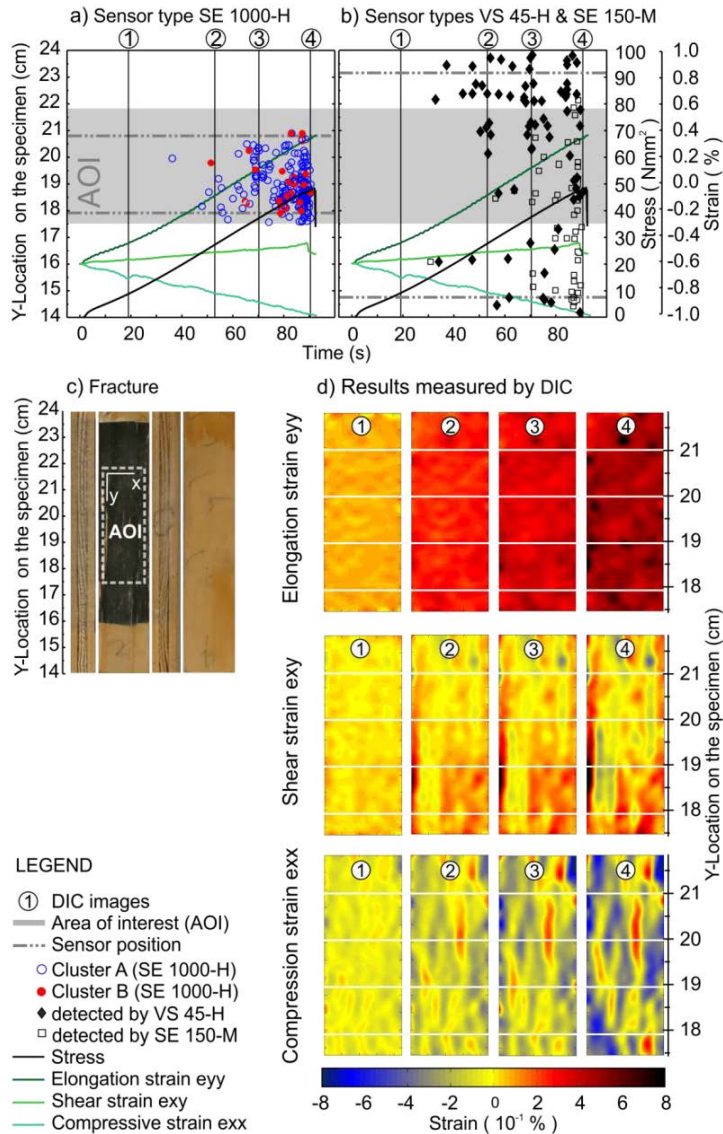
Figure 7.18 Failure behaviour of a selected plywood specimen consisting of three veneer layers (plywood type 3) by means of AE detected and located by a) the sensors SE 1000-H including the clusters A (unfilled/blue) and B (filled/red), and by b) the sensors VS 45-H (filled/black diamond) and SE 150-M (unfilled/ black square). c) The macroscopic crack path close to the area of interest (AOI) monitored by DIC is shown by photographs of all four sides of the specimen. d) Selected results 1-4 determined by DIC show the strain field formation at different points of progress throughout the test.
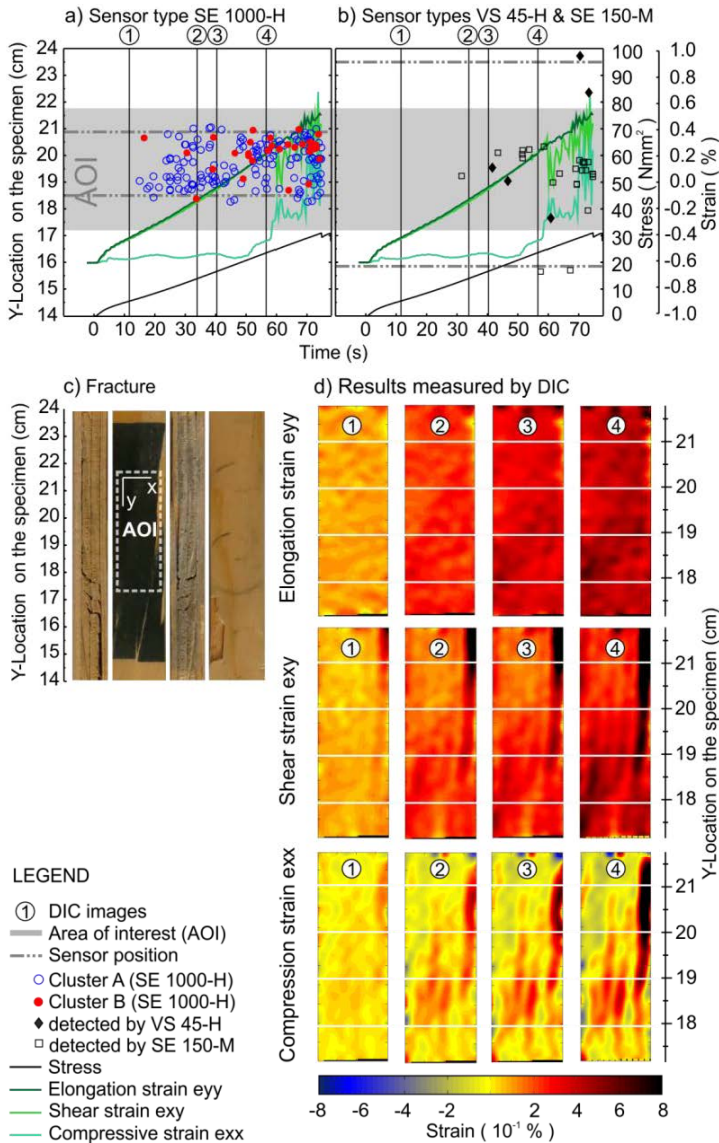
Figure 7.19 Failure behavior of a selected plywood specimen consisting of four veneer layers (plywood type 4) by means of AE detected and located by a) the sensors SE 1000-H including the clusters A (unfilled/blue) and B (filled/red), and by b) the sensors VS 45-H (filled/black diamond) and SE 150-M (unfilled/ black square). c) The macroscopic crack path close to the area of interest (AOI) monitored by DIC is shown by photographs of all four sides of the specimen. d) Selected results 1-4 determined by DIC show the strain field formation at different points of progress throughout the test.
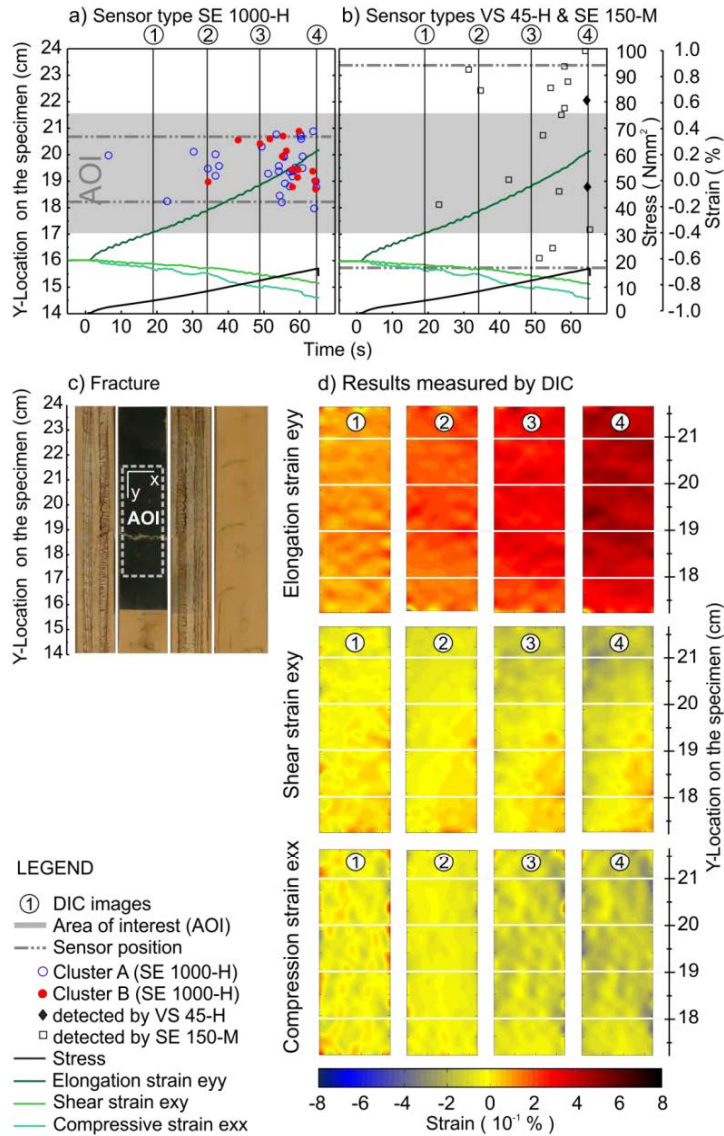
Figure 7.20 Failure behaviour of a selected plywood specimen consisting of five veneer layers (plywood type 5) by means of AE detected and located by a) the sensors SE 1000-H including the clusters A (unfilled/blue) and B (filled/red), and by b) the sensors VS 45-H (filled/black diamond) and SE 150-M (unfilled/ black square). c) The macroscopic crack path close to the area of interest (AOI) monitored by DIC is shown by photographs of all four sides of the specimen. d) Selected results 1-4 determined by DIC show the strain field formation at different points of progress throughout the test.
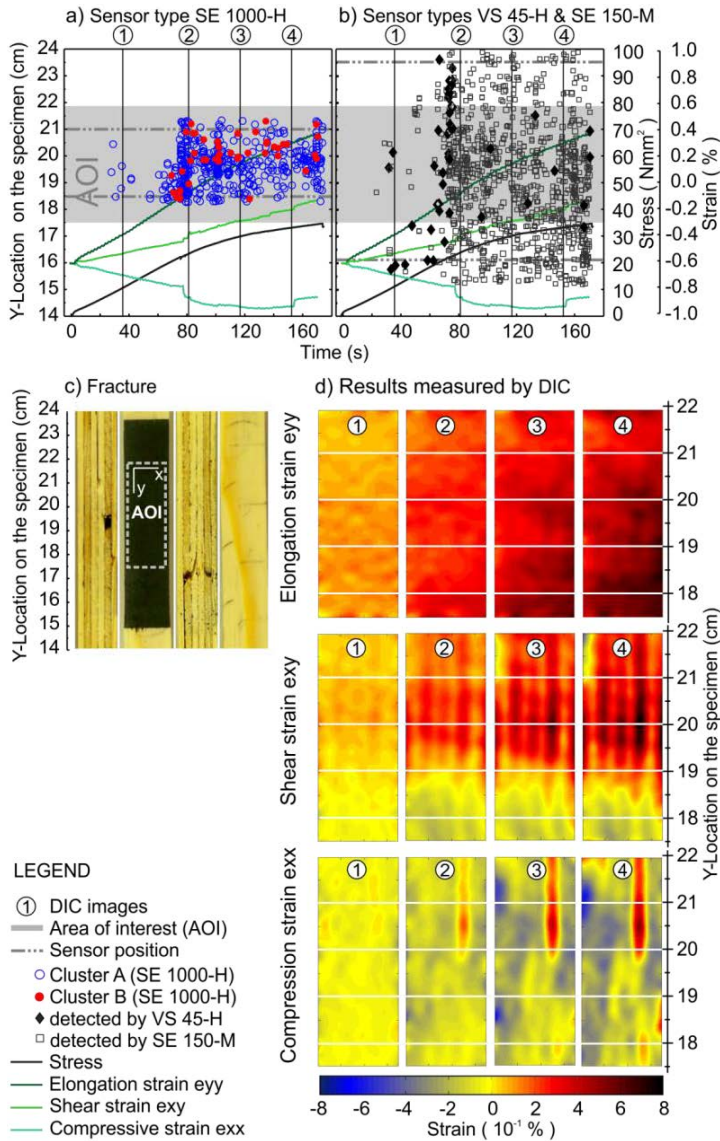
Figure 7.21 Failure behaviour of a selected plywood specimen consisting of six veneer layers (plywood type 6) by means of AE detected and located by a) the sensors SE 1000-H including the clusters A (unfilled/blue) and B (filled/red), and by b) the sensors VS 45-H (filled/black diamond) and SE 150-M (unfilled/ black square). c) The macroscopic crack path close to the area of interest (AOI) monitored by DIC is shown by photographs of all four sides of the specimen. d) Selected results 1-4 determined by DIC show the strain field formation at different points of progress throughout the test.

distinguishable into signals of higher shares of low or high frequency components, were also determined. However, for the different layered structures of the bonded miniature specimens (regarding the fiber-load angles of the wooden layers), the SRμCT scans revealed significant differences concerning the impact of the adhesive layer on the damage history, which seem to be also reflected by the cluster pattern with respect to the low frequency cluster. It was speculated, that AE signals generated by crack mechanisms of the adhesive are among the signals of the low frequency cluster. The same may be true for the laboratory scaled specimens made of model layered wood and industrial plywood. The macroscopic mechanical properties of the different specimen types as well as the fracture pattern are clearly different. Though no cluster can clearly be assigned solely to damage events within the adhesive layers, it is indisputable that the adhesive layers are damaged. Thus, the question remains whether the feature extraction needs to be improved for the applied UPR technique or the damage types need to be reinterpreted to also be applicable to failure within the adhesive, for example, crack openings parallel or perpendicular to load direction.

Larger sized damages, as in the laboratory scaled plywood specimens, yield AE signals representing microscopic mechanisms acting locally. For the plywood materials, almost 80% of detected AE are of low frequency components. Thus, the bulk of AE events assigned to the low frequency cluster A seem to correlate with significant formations of locally restricted regions of increased or decreased shear (exy) and compression (exx) strain. Based on this, AE signals of cluster A are tentatively assumed to be linked to mechanisms within the cross oriented layers. Regarding the laboratory scaled specimens made of solid spruce, the ultimate failure generating B clusters in seven of eight cases is in agreement with observations from the longitudinally tested miniature specimens. It is hence speculated that the same microscopic cell separation mechanisms and trans-cellular cracks, as identified in X-ray micro-tomography images of miniature specimens, also produce the AE signals during damage accumulation in plywood materials under tensile load.

References

Hass, P., Wittel, F.K., Mendoza, M., Herrmann, H.J., Niemz, P. (2012) Adhesive penetration in beech wood: experiments. Wood Sci. Technol. 46(1-3):243-25.

Sause, M.G.R., Gribov, A., Unwin, A. R., Horn, S. (2012) Pattern recognition approach to identify natural clusters of acoustic emission signals. Pattern Recogn. Lett. 33(1): 17-23.

Zauner, M. (2014) In-situ synchrotron based tomographic microscopy of uniaxially loaded wood: in-situ testing device, procedures and procedures and experimental investigations. Dissertation 2014, Institute for Building Materials, ETH Zurich, 163 pp.

8 Synthesis

8.1 Main findings

8.1.1 Solid spruce wood

The brittle failure behavior of solid spruce wood, as revealed by its stress-strain behavior, correlates with a roughly linear increase in defect growth measured by means of cumulative AE signals with test duration. A damage growth rate of about 200 defects was determined per 0.01% elongation strain (Paper II). Thus, the majority of defects are of relatively small magnitude as determined by means of amplitude distribution. Microscopic defects act throughout the whole specimen's volume, as proven by the initial diffuse flaws observed in AE source location as well as in strain field formations that, beyond 50% up to 70% of ultimate strength, coalesce into damages at larger, mesoscopic or even macroscopic scale. Hence, the damage progress in solid wood starts with a continuous damage accumulation of microscopic damage mechanisms acting throughout the volume of the specimen and is continued by a final coalescence of damages into mesoscopic and macroscopic cracks shortly before the ultimate failure (Paper I).

The cumulative AE energy follows an almost exponential increase, and hence indicates the nonlinearity in damage evolution. Over the whole test duration, AE signals of higher and lower AE energy content occur, indicating different magnitudes of damages. However, about 73% of the detected AE signals are characterized by relatively low AE energies of less than $10^{-12} V^2 s$ (Paper II).

The unsupervised pattern recognition (UPR) technique applied to AE detected when tensile loading the laboratory scaled specimens according to DIN 52377 (Chap. 7) as well as to the miniature specimens with a test cross section of 1-4mm^2 (Paper III) yields two signal clusters. These clusters essentially differ with respect to higher shares of low and high frequency components. The distinct average low and high frequency components for the two clusters, however, seem to depend on specimen size. Miniature specimens of solid spruce and bonded spruce layers yield somewhat higher weighted peak frequency (WPF) for the clusters than laboratory scale specimens. By means of the Synchrotron radiation micro computer tomographic (SRμCT) images recorded while testing the miniature specimens, the low frequency cluster is tentatively assigned to slow crack growth phenomena such as cell separation mechanisms, whereas the high frequency cluster is attributed to trans-cellular cracks (Paper IV).

Regarding the laboratory scale specimens, damages of larger size yield many AE representing microscopic mechanisms acting locally. It is hence speculated that similar microscopic mechanisms are the origin of the two clusters determined for the laboratory scale specimens. It has to be taken into account that the miniature sensor type M31 is significantly less sensitive to frequencies below 100kHz. The AE measurement of laboratory scale specimens performed by means of the sensor type SE 45-H with its sensitivity at frequencies below 100kHz proved the presence of AE signals characterized by low frequencies. Hence, it can be reasoned that these low frequency signals also occur as a result of the damage in the miniature specimens but were less likely to be detected due to the sensitivity of the used sensor type M31. This could lead to a preferential recording of signals with specific frequency content and hence have an effect on the frequency range of the clusters from pattern recognition as well as on the number of signals in each cluster. For both miniature and laboratory scale specimens, the generated AE showed a high number of signals in both clusters with progressive loading, and hence, it can be concluded that a certain kind of damage mechanism is not restricted to damage initiation or a certain stress level range. However, while tensile loading solid wood in the longitudinal direction, trans-cellular cracks (attributed to high frequency clusters) often match the ultimate failure of the specimen. Based on AE signals detected during tensile loading miniature specimens of solid spruce and on the related SRμCT scans, a calibration between AE amplitudes and underlying crack length development was performed (0.0038mV μm^{-2}). For AE studies on wood materials, such a calibration was realized for the very first time. However, the calibration value is not generally applicable to AE signals generated in wood, since the AE measurement strongly depends on the experimental setup also given that, for example, the AE amplitudes are significantly influenced by the wood species, the propagation distance of the signals through the material and the sensor position and response (Paper III; Paper IV; Chap. 7).

8.1.2 Layered wood material

Tensile tests on miniature specimens made of bonded wood (UF adhesive) demonstrated the different impact of the adhesive layer depending on the grain orientation of the joint wood layers. While the failure of the LL specimen made of two longitudinally oriented wooden layers was mainly the result of the damage evolution within the wooden tissues, the adhesive played a more important role in the case of the TT specimens with its two tangentially oriented wooden layers. This was proven by the fracture progress detected in the SRμCT scans of the tested specimens. The corresponding cluster patterns of AE signals yielded two clusters, characterized by either low or high frequency contents, similar to the

miniature specimens made of solid wood, which are also attributed to the same source mechanisms. However, small differences within the low frequency cluster are observed for the TT specimen whose failure was dominated by the failure of the adhesive layer. Thus, it is hypothesized that possibly AE signals generated by adhesive cracks are among those low frequency signals, cannot be resolved as a separate cluster (Chap. 7).

The brittle failure behavior of industrial plywood materials (phenol resorcinol formaldehyde adhesive), as revealed in the stress-strain behavior of plywood types 3-5, associates with a roughly exponential increase in defect growth measured by means of cumulative AE signals with test duration (Paper II). For the plywood types 3-5, more or less the same number of defects was measured regardless of the different numbers of layers. The stress-strain behavior of the plywood type 6 shows a distinct plastic deformation prior to ultimate failure that is, besides the longer test duration, the reason for the significantly larger number of defects (double the defect number for plywood types 3-5) (Paper II). In comparison to the model layered wood CP (UF adhesive), which was manufactured in laboratory without inducing pre-damages such as veneer lathe checks, the industrially produced plywood materials generated less damage events (AE events). Additionally, in regard to the relating amplitude distributions, the model layered wood CP reveals a relatively higher share of microscopic damages (expressed in a higher b-value at amplitudes below $70dB_{AE}$) than the industrial plywood materials (Chap. 6.3).

Employing the bi-linear approach to the exponential increase in damage growth, two growth rates were estimated for the plywood materials indicating the occurrence of initial cracks (1st rate) and the damage accumulation through the whole specimen finally leading to ultimate failure (2nd rate) (Paper II). The initial rate of damage growth increases with increasing number of layers, whereby only about 30% of AE energy, which also gives a relative measure of fracture energy, was released. At 70% of ultimate stress, the 2nd rate of damage growth commenced, which is almost quadruple the 1st rate. The 2nd rate implies defect increase caused by relatively larger sized damages including numerous microscopic and mesoscopic scaled mechanisms. The presence of two defect growth rates, which is affected by the layered structure of plywood materials, is a main difference in damage evolution compared with that in solid wood (Papers I; II). Thus, at the beginning, the continuous damage accumulation is restricted to the single layers, which was further found to be in correlation with the ultimate strength: A larger number of defects occurring during the 1st defect growth rate predicted a higher tensile strength of the material. A comparable correlation could not be proven for the tests of solid spruce. The 2nd rate of defect growth indicates the path of lowest resistance through all layers (Paper II).

Moreover, the technique of unsupervised pattern recognition was applied to the AE detected when tensile loading the laboratory scaled specimens made of model layered wood (CP, UD) and industrial plywood (plywood types 3-6) (Chap. 7). Two clusters were identified, which differ with respect to higher shares of either low or high frequency components, similar to the cluster results of the laboratory scaled specimens made of solid spruce. A third cluster exclusively attributed to the failure in the adhesive layers was not identified. Regarding the results of the bonded miniature specimens, based on the combination of SRµCT images and related pattern recognition of the AE, it is assumed that AE signals generated by crack mechanisms of the adhesive might be among the signals of the low frequency cluster. This may also be true for the laboratory scaled specimens made of model layered wood and industrial plywood. The coincidental occurrence of both AE signal clusters at the beginning of load application until the ultimate failure of the specimen shows that different kinds of damage mechanisms (attributed to the AE clusters) occur during both growth rates (Chap. 7). Furthermore, the broad range in AE energy of the detected AE events over the whole test duration proves that multi-scaled damages are generated during both growth rates (Paper II).

8.2 Hypotheses and open questions

The complexity in failure behavior of wood and layered wood materials such as plywood was demonstrated by the results obtained through monitoring the sub-macroscopic damage evolution. Therefore, tensile tests were carried out on solid spruce, model layered wood made of clear spruce wood lamellae bonded together with UF adhesive and plywood materials industrially produced including process-related pre-damages (lathe checks). These destructive tests were simultaneously monitored by means of AE and the strain field measurements (DIC), which allow studying the sub-macroscopic damage evolution within the materials. Supplementary, tensile tests of miniature scaled specimens made of solid spruce and bonded (UF) spruce layers were monitored by combining the AE and SRµCT methods. On average, the miniature specimens are sized more or less a 20th of the size of the standard specimens according to DIN 52377 (1987).

Via application of the method of UPR to the AE results, similarities of the detected AE signals are identified that are assumed to give indications of their source mechanisms. For all tested materials, whether for the miniature specimens or for the laboratory scaled ones (DIN 52377 1987), two clusters of AE signals were determined. One cluster is characterized by low frequency AE signals and the other by dominating high frequency components.

Based on the correlations of the results by means of AE and SRμCT obtained from the miniature tests, a first hypothesis assigns the low frequency clusters to cell separation mechanisms, whereas the high frequency clusters might be the consequence of brittle trans-wall cracks. One specific characteristic in the cluster pattern was shown for the tested radial miniature specimens made of solid spruce: the low frequency cluster could be divided into further two clusters. A similar observation was made for the miniature specimens made of two spruce wood layers loaded tangentially which were bonded together with UF: In this case, the low frequency cluster could be subdivided into three clusters. Since the impact of the adhesive layer on the failure behaviour of this specimen was proven by the SRμCT scans, it is assumed that mechanisms due to the adhesive might also be included in the low frequency cluster.

For the laboratory scaled specimens of model layered wood and industrial plywood, the two clusters identified by the pattern recognition technique contain somewhat lower frequency components than those detected for the miniature specimens. This is consistent since high frequencies undergo stronger attenuation with increasing distance between source location and sensor position. Due to the wood morphology, the clusters are assigned to the same mechanisms for the larger specimens as for the miniature specimens. The analysis of the AE cluster results and strain field formations (DIC) versus test progression led to the consideration that the low frequency cluster is linked to mechanisms within the cross oriented layers or is possibly dominated by shear mechanisms.

For all tested materials and specimen sizes, their macroscopic mechanical properties as well as their meso- and macro-scale fracture pattern reveal clear differences. Regarding the occurrence of both clusters with progressive tensile load, their distributions in time and in their ranges in amplitudes do not indicate significant differences.

To sum up, the complex microstructure of wood yields complex crack paths and damage patterns involving different mechanisms acting simultaneously throughout the duration of the test. However, only two clusters of AE signals were determined for different material types and specimen geometries, thus opening up new questions to be answered. Additional investigations are needed to validate the interpretation of the clusters obtained by unsupervised pattern recognition; the following main issues should be focused on further:

I.   Is there further evidence for the assignment of the low frequency cluster to cell separation/shear mechanisms and the high frequency cluster to be generated by trans-wall cracks, or is another possible interpretation of the similarities in the frequency spectra more valid (e.g. vibration or resonance

phenomena due to the cellular wood morphology and/or specimen geometry)?

II. Could one or both clusters possibly contain different mechanisms? This is based on the possible separation of the low frequency cluster of the radially tested miniature specimens or the bonded miniature specimens. Even for the laboratory scaled specimens of model layered wood (UD and CP), the position and pattern of the low frequency clusters might indicate more than one single kind of damage mechanism.

III. Is the impact of damage within the adhesive layers detectable by means of AE measurement?

The datasets generated during this research work, either by means of AE, DIC or SRμCT, are very extensive and demanding with respect to extracting information, and hence, potential for further analysis remains. In the following section, beside proposals for further investigations, also further analysis to be done on those existing databases will be noted.

8.3 Potential for future research

The experiments detecting the microscopic damage in miniature specimens by combining the AE method with the in-situ SRμCT monitoring (TOMCAT beam line at the PSI) yielded datasets at different load states of the specimens. An ongoing analysis of the reconstruction from the SRμCT monitoring will focus on describing structural deformations at microscopic scale. From these results, a dedicated segmentation and geometric parameterization of specific wood cells is currently being performed (Fig. 8.1) and, based on a 3D morphological approach, the volumetric strain fields at different load states are analyzed (Fig. 8.2) and discussed with regard to the final fracture path (Sanabria et al. 2015).
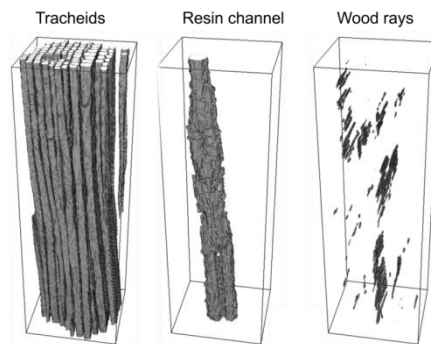
Figure 8.1 Segmentation of a) wood tracheids, b) resin canal and c) wood rays from SRμCT dataset.

a) Category of cells
- identified tracheid
- excluded tracheid
- identified wood rays
- edge cells

b) Cell indices

c) Deformation
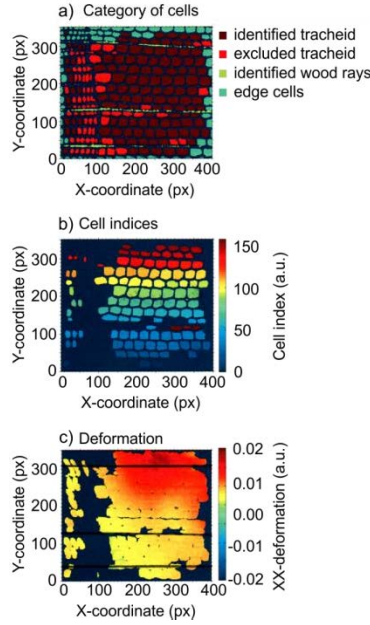
Figure 8.2 Provisional results of the 3D morphological analysis of SRµCT scans developed and provided by Sergio J. Sanabria. a) Cells are categorized into cells located at the edge of the volume of interest (VOI), wood rays and tracheids identified and implemented for analysis. Tracheids that are not sufficiently identified for analysis are excluded (light red). b) Tracheid cells identified in each loading state (dark-red) are registered by an individual cell index. c) The XX-deformation (parallel to load direction) of the cellular structure at the loaded state is given in arbitrary units (a.u.).

Thus, the developed 3D morphological approach allows the determination of the deformation based on the individual cells (Fig. 8.2a, b) identified at each monitored load state which differs from the approach by Forsberg et al. 2010 who performed DVC by means of correlating selected subsets without an identification of the individual cells. Therefore, a relatively large sub-volume (correlation windows) of 32^3 voxels with 16 pixel separation between consecutive sub-volumes was used. The improved 3D morphological approach of DVC by Sanabria et al. 2015 enables tracking the deformation of the individual cells and, based on this, yields higher resolution of deformation (Fig. 8.2c).

Moreover, since these trials yielded structural information of more than six different specimens on their initial state and after ultimate failure, a statistical investigation focusing on the dimensions of cells that have been involved in fracture could reveal parameters of the weakness points within a tissue. Therefore, the fracture zone needs to be identified within the undamaged initial state of the specimen and then, it has to be evaluated first to determine that no pre-damage was locally induced while processing the specimens. A reference section could be chosen from an undamaged region of the specimen. When counting the cells within

these sections and measuring their dimension, the frequency of morphological cell features, for example calculated in ratios of cell wall thickness to cell diameter of the tracheids and height and length of wood rays could be estimated. Complementary to this, the evaluation of distances between different types of cells (position of the tracheid with regard to the surrounding wood rays) would be worthwhile allowing for an insight on the performance of the tissue structure. Additionally, these databases might also be helpful for future modeling work of multi-scale wood failure.

Regarding the analysis of the tested miniature specimens made of bonded wood, improved image processing of the SRμCT scans could reveal further insight into the failure behavior of the adhesive as well as of the adhesive-wood interface. Furthermore, employing a calibration of AE amplitudes detected and crack area measured within these specimens could possibly help to identify AE signals generated by a failing adhesive. Complementary to this, the AE energy could be correlated with crack volume if values can be reliably determined.

Moreover, although not yet realized because it is not easily applicable to the 3D morphology of wood tissue, the segmentation of cracks for 3D visualization would be worthwhile. Indeed, the demonstration of fracture paths by means of destructed wood hinders overviewing its real extent. Furthermore, this could be the link between FEM simulations of AE signal sources (Fig. 8.3) and AE clusters from experimental tests, since crack extension in 3D could be measured and set in relation with AE amplitude or energy values as a measure for crack area and volume, and, additionally, it could be compared with simulations of crack opening directions.

The insights on submicroscopic damages in wood materials yielded in the here presented research work are mainly based on newly identified parameters of AE. Though, first interpretations were done, some uncertainties raised questions as outlined in the previous section. Therefore, two different approaches are suggested in the following that are anticipated to yield further insight.

Finite element simulation of signal sources, signal propagation and signal recording is expected to provide crucial information for reliably assessing signals from the different microscopic damage mechanisms. Therefore, Sause (2010) developed a comprehensive approach that takes into account the elastic properties of microscopic crack tips to model prototype mechanisms (dipole vs. multi pole sources) as observed in fiber reinforced composites. Furthermore, AE signal propagation within the specimen is modeled including the formation of guided waves. Beside the properties of the source mechanisms generating

the AE such as source excitation time, source energy and source position, the impact of the specimen geometry and propagation medium on the AE frequency spectra are also investigated. Based on the frequency features of the AE events, damage mechanisms can be studied. A preliminary analysis was already performed for the tensile tests on the miniature specimens made of solid spruce and this demonstrated that the excitation time of the AE source mechanism (different speeds of crack opening) significantly changed the frequency content of the AE signal (Vergeynst et al. 2014) (Fig. 8.3). Hence, the herein presented interpretation of both obtained clusters is supported. However, a further comprehensive investigation on combinations of excitation time, source location and crack opening direction might yield more reliable evidence. Moreover, studying the impact of the specimen geometry on location of the frequency peaks in the spectra, e.g. by changing the specimen thickness and the depth of the taper shapes will yield a better understanding of the influencing parameters' relevance. Further investigations could provide more solid proof by implementing a detailed sensor model. Possibly, questions concerning the cluster results obtained from damaging the bonded miniature specimens or the laboratory scaled plywood specimens (20 times larger than miniature tests) could also be implemented in the simulations.
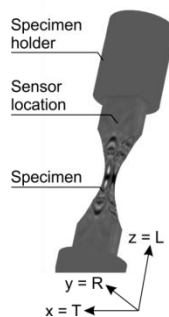
Figure 8.3 A model for visualizing wave propagation in the tested miniature specimen made of solid spruce. Original by Vergeynst et al. 2014.

The simulations will provide meaningful arguments for a conceptional discussion on the interpretation of the source, but since the morphology of wood is not included (a homogenized material is used), wood specific damage mechanisms such as trans-wall cracks or cell separation mechanisms will not definitively be proven by this. However, in principle, experimental methods could indeed help considerably, since the failure of several wood species is well known to undergo different kinds of damage. For example, carrying out further tensile tests of miniature specimens made of spruce (*Picea abies* [L.] Karst.) and yew (*Taxus baccata* L.), both loaded in the radial direction, the expected differences in damage

evolution could yield evidence for the interpretation of the low frequency cluster since the failure of yew is the consequence of comparatively more cell separation events than it is the case for spruce wood (Keunecke et al. 2007). Hence, for yew, a higher share of AE events characterized by low frequency components would be expected.

To clarify the sensitivity of the AE monitoring to the adhesives, test series of miniature specimens made of wood bonded with different adhesives should be performed. For instance, Polyurethane resins (PUR), which are more ductile than the stronger adhesives based on melamine urea formaldehyde (MUF), will probably form more damage events (AE events) than the latter. Further, shear processes will be investigated by varying the thickness of the adhesive layer, since increased shear forces occur in thicker adhesive layers under stress. However, regarding the current experiences with experiments of the bonded miniature specimens (no symmetry in layer thicknesses due to the easily damageable, manually grinded taper shape), it is proposed to develop improved specimen geometries analogous to shear test specimens typically used for studies on wood-adhesive-joints in accordance to EN 302-1 (2013) (Fig. 8.4a). The specimen geometry introduced by Dill-Langer et al. (2002) and modified by Hass et al. (2013) (Fig. 8.4b) to investigate typical failure mechanisms in adhesives may even have the potential to be scaled down to be tested with the universal micro-testing machine designed by Zauner (2014), but it would have to be monitored with the miniature sensors M31 once suitable sensor holders are also designed. However, the size effect has to be taken into account and, hence, failure patterns are assumed to differ from those obtained in laboratory scale specimens. The observation of damage evolution within the adhesive layer by means of SRμCT is assessed to be difficult, since wood matter and adhesive matter detected in the SRμCT scans are not easily separated. When using UV-fluorescent markers within the adhesive, a combination of ex-situ microscopy based on daylight-images and UV-light images of the fracture surfaces enables the evaluation of percentage wood failure and adhesive failure (Kläusler et al. 2014) which could possibly reveal a correlation with the AE activity and the AE clusters.
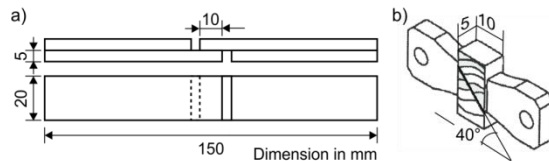
Figure 8.4 Specimen geometries to study the failure of wood-adhesive joints. a) Specimen geometry in accordance to EN 302-1 (2013), b) Specimen geometry originally designed by Dill-Langer et al. 2002 and modified by Hass et al 2013.

Concerning the studies on failure behavior of plywood it may be appropriate to design a new testing procedure at laboratory scale in accordance to the shear tests EN 314-1 (2005) or ASTM-D905 (2013). It is suggested to manufacture selected layered structures in the laboratory using industrially produced veneers, and thus to induce certain defects with known positions such as adhesive-free regions at the wood-adhesive interface or artificial crack openings oriented parallel and perpendicular to the load direction. By doing so, the AOI might match well with the dominant region of damage accumulation for the non-destructive monitoring (AE, DIC, etc.) and the evaluation and interpretation of detected results could be easier and more precise. Possibly, the experimental setup designed by Kamke et al. (2014) could be extended by AE monitoring to provide the progress in AE analysis of damage mechanisms in wood and adhesive.

Moreover, if pre-defined defects implemented in the specimen are sufficiently large enough to dominate the specimen's failure while also being small enough to allow for additional monitoring by a high-speed camera, then the detected images could provide details of crack formation. As part of the pre-trials of the present study, tensile tests on laboratory scale plywood materials were also monitored by a high speed camera. Thus, the failing structure was recorded with 25.000 images per second which was found to be insufficient to observe the crack propagation in wood. However, today's state of the art ultra-high speed cameras allow recording about 350.000 images per second (Phantom camera v2511) when monitoring the same AOI ($10x10mm^2$) with an image resolution of 128x256 pixels. Using such a new camera, the achieved time resolution of $3x10^{-6}s^{-1}$ would be close to that of the AE monitoring rather than other in-situ imaging methods and possibly, with this very high time resolution, more details of the crack propagation could be captured. However, since the obtained pixel size of 50 to $100\mu m^2$ might prove inadequate for tracking strain field formation, a combination with a CCD camera will be needed to employ DIC for further information on displacements and deformation (Müller et al 2005, Valla et al. 2011).

Regarding in-situ SRμCT monitoring of failing wood without load stops, extraordinary challenges with many problems need to be solved due to the fine microscopic structure and its spontaneous failure development and its rather unpredictable localization, especially under tensile load. Once, this predominantly technology driven method yields an adequate resolution in pixel size and time resolution, high-speed imaging systems could capture the structural changes and strain fields in the wooden tissue generated in high rate events. In the view of material characterization, this full-field approach would allow better understanding of the factors affecting the structural performance.

Finally, for the sake of completeness, other approaches concerning the investigation of the damage evolution in layered wood materials have to be mentioned, which were originally outlined within the proposal this project, but not realized due to changes in the experimental plan.

    I.   Studies on fracture toughness by tensile testing of compact tension (CT) specimens can be used to yield crack propagation or delamination along specified planes which yield a single dominant damage mechanism. To provoke dominant failure mechanisms, the tests could be carried out with different crack modes along the different planes of wood and the crack propagation could be monitored by means of AE and digital imaging. In addition, the influence of wood moisture content on the AE could be investigated for several climates.

    II.   Moreover, the tensile tests on miniature specimens presented here as well as the macroscopic CT tests described above, could be complemented by meso/micromechanical tests observed in-situ in an ESEM, perhaps again monitored with AE.

    III.   The dynamic mechanical thermal analysis (DMTA) allows measuring the viscoelastic response of the specimens, which provides insight into the structure-property relationship by applying varying mechanical loads in the linear-elastic regime. DMTA has, in some cases, proven sensitive to changes on the microscopic and even molecular scale, in particular with respect to the interaction between wood particles and adhesive. With additional humidity control accessories, DMTA equipment can explore the elastic mechanical behavior of laminated wood specimens with different levels of damage in a range of environmental conditions between dry and wet. However, the monitoring of DMTA by means of AE measurement might be a challenge in realization and would be limited by the sensors' application temperature range.

References

ASTM-D905 (2013) Standard Test Method for Strength Properties of Adhesive Bonds in Shear by Compression Loading.

Dill-Langer, G., Lütze, S., Aicher, S. (2002) Microfracture in wood monitored by confocal laser scanning microscopy. Wood Sci. Technol. 36:487-499.

DIN 52377 (1978-11) Testing of plywood; determination of modulus of elasticity in tension and of tensile strength.

EN 302-1 (2013) Adhesives for load-bearing timber structures - Test methods - Part 1: Determination of longitudinal tensile shear strength.

EN 314-1 (2005) Plywood - Bonding quality - Part 1: Test methods.

Forsberg, F. , Sjodahl, M.; Mooser, R., Hack, E., Wyss, P. (2010) Full Three-Dimensional Strain Measurements on Wood Exposed to Three-Point Bending: Analysis by Use of Digital Volume Correlation Applied to Synchrotron Radiation Micro-Computed Tomography Image Data. Strain 46(1):47-60.

Hass, P., Wittel, F.K., Niemz, P. (2013) Generic failure mechanisms in adhesive bonds. Holzforschung 67(2):207-215.

Kamke, F. A., Nairn, J.A., Muszynski, L., Paris, J.L., Schwarzkopf, M., Xiao, X. (2014) Methodology for micromechanical analysis of wood adhesive bonds using x-ray computed tomography and numerical modeling. Wood Fiber Sci. 46(1):15-28.

Keunecke, D., Sonderegger, S., Pereteanu, K., Lüthi, T., Niemz, P. (2007) Determination of Young's and shear moduli of common yew and Norway spruce by means of ultrasonic waves. Wood Sci. Technol. 41(4): 309-327.

Kläusler, O., Hass, P., Amen, C., Schlegel, S., Niemz, P. (2014) Improvement of tensile shear strength and wood failure percentage of 1C PUR bonded wooden joints at wet stage by means of DMF priming. Eur. J. Wood Prod. 72:343-354.

Müller, U., Sretenovic, A., Vincenti, A., Gindl, W. (2005) Direct measurement of strain distribution along a wood bond line. Part 1: Shear strain concentration in a lap joint specimen by means of electronic speckle pattern interferometry. Holzforschung 59(3): 300-306.

Sanabria, S.J., Zauner, M., Ritschel, F., Niemz, P. (2015) 3D morphological analysis of X-ray synchrotron tomograms of wood microstructure subjected to mechanical load for deformation measurements at the individual cell scale. In preparation.

Sause, M.G.R. (2010) Identification of failure mechanisms in hybrid materials utilizing pattern recognition techniques applied to acoustic emission signals. Dissertation, ISBN: 978-3-86664-889-0, mbv-Verlag, Berlin , 305 pp.

Valla, A., Konnerth, J., Keunecke, D., Niemz, P., Müller, U., Gindl, W. (2011) Comparison of two optical methods for contactless, full field and highly sensitive in-plane deformation measurements using the example of plywood. Wood Sci. Technol. 45(4):755-765.

Vergeynst, L.L., Sause, M.G.R., Ritschel, F., Brunner, A.J., Niemz, P., Steppe, K. (2014) Finite element modelling used to support wood failure identification based on acoustic emission signals. Proc. COST-Timber Bridges Conference, Biel/Bienne, Switzerland. pp. 141-146.

Zauner, M. (2014) In-situ synchrotron based tomographic microscopy of uniaxially loaded wood: in-situ testing device, procedures and procedures and experimental investigations. Dissertation 2012, Institute for building materials, Wood physics, ETH Zürich, 163 pp.
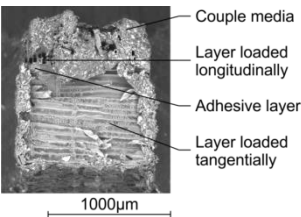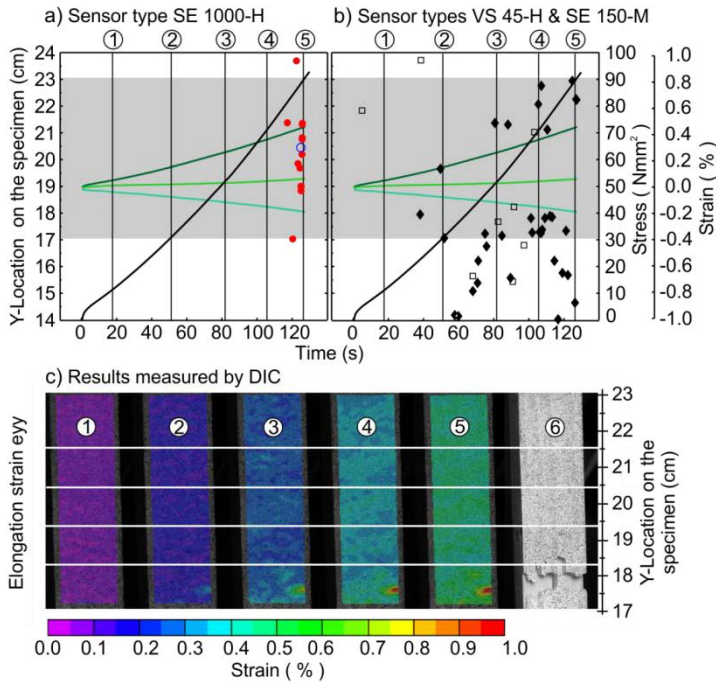
Acknowledgements

APPENDIX

Figure A.1 Fracture surface at the cross section of the tensile loaded miniature specimens TL (consists of one longitudinally and one tangentially loaded wooden layer) taken by ESEM. Surface covered with AE coupling media.
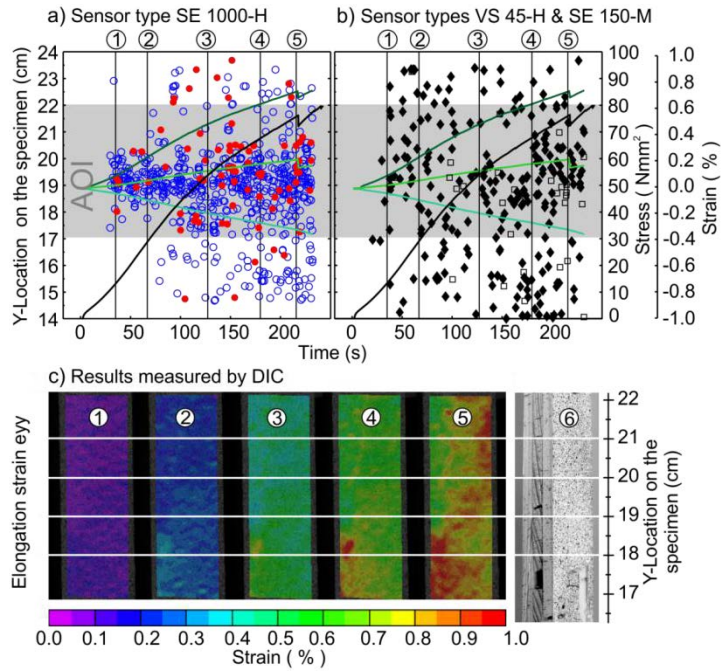
Figure A.2 Failure behavior of a selected model layered wood consisting of three clear wood laminates of spruce that are unidirectionally oriented (UD). AE detected and located by a) the sensors SE 1000-H including the clusters A (unfilled/blue) and B (filled/red) and by b) the sensors VS 45-H (filled/black diamond) and SE 150-M (unfilled/ black square). c) Selected results 1-5 determined by DIC show the elongation strain field formation at different points of progress throughout the test. The macroscopic crack path monitored by DIC is shown by the photo (c, 6).

Figure A.3 Failure behavior of a selected model layered wood consisting of three laminates of clear spruce wood with the cross oriented ply in the middle (CP). AE detected and located by a) the sensors SE 1000-H including the clusters A (unfilled/blue) and B (filled/red) and by b) the sensors VS 45-H (filled/black diamond) and SE 150-M (unfilled/ black square). c) Selected results 1-5 determined by DIC show the elongation strain field formation at different points of progress throughout the test. The macroscopic crack path monitored by DIC is shown by the photo (c, 6).

Curriculum Vitae

Dipl.-Ing. Franziska Baensch, nee Ritschel

Date of birth:	01/05/1983
Place of birth:	Riesa, Germany
Nationality:	German
Marital status:	Married
E-mail adress:	Baensch.franziska@gmail.com

Education / Profession

06/ 2010 - 12/ 2014	Doctoral candidate in the Wood Physics Group, Institute for Building Materials /Department of Civil, Environmental and Geomatic Engineering) at the ETH Zurich, Switzerland. Dissertation title: *"Damage evolution in wood and layered wood composites monitored in situ by acoustic emission, digital image correlation and synchrotron based tomographic microscopy"* under the supervision of Prof. Dr.-Ing. habil. Dr. h. c. Peter Niemz
10/2009 - 06/ 2010	Postgraduate studies in process engineering TU Dresden, Germany.
01/ 2008 - 12/2009	Management-Trainee Glunz AG, Meppen, Horn & Nettgau, Germany. Department Global Research & Development, Technical Department, Central Department for Health, Safety and Environment.
10/ 2001 - 12/ 2007	Studies of Process Technology and Engineering, specialization in engineering of wood and fiber materials TU Dresden, Germany. Diploma thesis title: "*Studies on biological resistance of reed applied in construction purposes*" under the supervision of Prof. Dr.-Ing. A. Wagenführ.
08/ 1994 - 09/ 2001	Abitur (German university entrance degree), Riesa, Germany

Publications, conference proceedings, oral presentations and posters

Publications (peer reviewed)

F. Baensch, M. Zauner, B. Pinzer, S. J. Sanabria, A.J. Brunner, M. Stampanoni, P. Niemz "Damage Evolution in Wood – X-ray micro-tomography and Complementary Evidence for Interpreting Acoustic Emission Behavior", 2015, Holzforschung (Online 02/2015), DOI: 10.1515/hf-2014-0152.

F. Baensch, M.G.R. Sause, A.J. Brunner, P. Niemz "Damage Evolution in Wood - Pattern Recognition based on Acoustic Emission Frequency Spectra", 2015, Holzforschung (Online 01/2015), DOI: 10.1515/hf-2014-0072.

F. Ritschel, Y. Zhou, T. Fillbrandt, P. Niemz "Acoustic Emission analysis of industrial plywood materials exposed to destructive tensile load", 2014, Wood Science and Technology 48:611–631.

F. Ritschel, A.J. Brunner, P. Niemz "Non-destructive evaluation of damage accumulation in tensile test specimens made from solid wood and layered wood materials", 2013, Composite structures 95, p.44-52.

Conference contributions and oral presentations

L.L. Vergeynst, M.G.R. Sause, F. Ritschel, A.J. Brunner, P. Niemz, K. Steppe „Finite element modelling used to support wood failure identification based on acoustic emission signals", COST Timber Bridge Conference, Biel (CH), 09/2014.

F. Ritschel, M.G.R. Sause, A.J. Brunner, P. Niemz "Acoustic Emission (AE) Signal Classification from Tensile Tests on Plywood and Layered Wood", 31st European conference on Acoustic Emission, Dresden (DE), 09/2014.

F. Ritschel, A.J. Brunner, P. Niemz Damage Phenomena in Wood - Acoustic Emission & Synchrotron Radiation X-Ray Tomographic Microscopy, Ph.D. Symposium, Eidgenössischen Materialprüfungs- und Forschungsanstalt, Dübendorf (CH), 03/2014.

M. Zauner, F. Ritschel "Synchrotron radiation µCT and Acoustic Emission monitoring during in-situ loading of miniature spruce wood samples", IUFRO-Division 5, Nancy (FR), 10/2013.

F. Ritschel, M. Zauner, S. J. Sanabria, A.J. Brunner, P. Niemz „Acoustic Emission and Synchrotron Radiation X-ray tomographic in situ microscopy of sub-macroscopic damage phenomena in wood", Proceedings 18th International Non-destructive Testing and Evaluation of Wood Symposium, Madison WI (USA), 09/2013.

F. Ritschel, Y. Zhou, P. Niemz „Schallemissionsanalyse von Zugversuchen an industriell gefertigten Sperrhölzern", Zerstörungsfreie Materialprüfung: Berichtsband 2013, Deutsche Gesellschaft für zerstörungsfreie Prüfung Jahrestagung 2013, Dresden (DE), 05/2013.

F. Ritschel, M. Zauner, S. J. Sanabria, A.J. Brunner, P. Niemz „In-situ Kombination von Schallemissionsanalyse und Röntgen-Mikrotomografie mit Zugversuchen an Miniatur-Prüfkörpern aus Fichtenholz", Zerstörungsfreie Materialprüfung: Berichtsband 2013, Deutsche Gesellschaft für zerstörungsfreie Prüfung Jahrestagung 2013, Dresden (DE), 05/2013.

F. Ritschel „Mikromechanik in Furnierschichtholz unter Zugbelastung", Seminar
Zerstörungsfreie Prüfung, Technische Universität München, München (DE),
01/2013.

F. Ritschel "Sub-macroscopic failure phenomena in layered wood materials by acoustic
emission", Ph.D. Symposium, Eidgenössische Materialprüfungs- und
Forschungsanstalt, Dübendorf (CH), 01/2012

F. Ritschel, P. Niemz, A.J. Brunner „Wellenformanalyse von Schallemissionssignalen
ausgewählter Zugversuche an Vollholz- und Sperrholz/LVL-Prüfkörpern", 18.
Kolloquium Schallemission, Deutsche Gesellschaft für zerstörungsfreie Prüfung,
Wetzlar (DE), 10/2011.

F. Ritschel, A.J. Brunner, P. Niemz „Damage Evolution in Layered Wood Materials
Monitored by Acoustic Emission and Optical Method", Ph.D. Symposium
(Poster), Eidgenössischen Materialprüfungs- und Forschungsanstalt, St. Gallen
(CH), 10/2011.

F. Ritschel, A.J. Brunner, P. Niemz: „Combining Image Correlation from Optical Methods
and Acoustic Emission Analysis for Investigating Damage Evolution in Plywood",
17th International Nondestructive Testing and Evaluation of Wood Symposium,
Sopron (HU), 09/2011.

F. Ritschel, A.J. Brunner, P. Niemz: „Nondestructive Evaluation of Damage Accumulation
in Tensile Test Specimens made from Solid Wood, Plywood and Laminated
Veneer Lumber (LVL)", 16th International Conference on Composite Structures,
ICCS-16, Special Session on Non-destructive Inspection Techniques for
Composite Materials and Structures, Porto (PT), 06/2011.

Supervised theses

Y. Zhou: „Untersuchungen zum Versagensverhalten von Sperrholz mittels
Schallemissionsanalyse", Referent: Prof. Dr. Dr. h.c. Gero Becker (Albert-
Ludwigs-Universität Freiburg), Korreferent: Prof. Dr.-Ing. habil. Dr. h.c. Peter
Niemz (Eidgenössische Technische Hochschule Zürich), 09/2012.